2022

Optical dosimeters for Radiotherapy with MRI-LINACs

Levi J. Madden

UNIVERSITY
OF WOLLONGONG
AUSTRALIA

Optical dosimeters for Radiotherapy with MRI-LINACs

Levi J. Madden

This thesis is presented as part of the requirements for the conferral of the degree:

Doctor of Philosophy

Supervisor:
Dr. E. Li

Co-supervisors:
Assoc. Prof. L. Holloway & Dist. Prof. A. Rosenfeld

The University of Wollongong
School of Physics

May 15, 2022

This research has been conducted with the support of an Australian Government Research Training Program Scholarship.

Contents

Acknowledgements

I am indebted to the many people who've supported me during my PhD. I'd like to acknowledge everyone who helped me and made it possible.

Firstly, I want to thank my supervisors: Enbang Li, Lois Holloway, Urszula Jelen and Anatoly Rosenfeld. Thank you all for taking me on as a student during my PhD. My time spent researching under each of you was incredibly rewarding, and the encouragement each of you provided me allowed me to thrive. I am incredibly grateful to each of you and I could not have achieved a fraction of what I did without your support.

I'm extremely grateful to the many others who've assisted me with research during my PhD. I would like to thank Bin Dong for the many hours, days and weeks you spent supervising and assisting me with my measurements with Australian MRI-LINAC. I'd like to thank Brad Oborn for providing me with the Geant4 simulations of the Australian MRI-LINAC, as well as all the support needed to get the G4MRL workflow set up and running. I'd like to thank Dean Wilkinson, Martin Carolan and Trent Causer for supervising the many nights of measurements at Wollongong Hospital. I'd also like to thank Alex Santos for providing me the opportunity to collaborate on the BeO rtOSL project, it was incredibly rewarding.

I want to thank the many peers and students who have assisted me during my studies. Firstly, thank you James Archer for enduring the ups and downs with me, assisting with measurements and reading the numerous drafts and manuscripts. Thank you also to Nuwangi Cooray for helping with the many measurements. I'd also like to thank Natalia Roberts for collaborating and assisting with the measurements made with the Australian MRI-LINAC. I also want to thank Erin Lukas for collaborating and assisting with the BeO measurements and manuscripts. I also want to express my gratitude to the staffs of CMRP, Ingham Institute, Wollongong Hospital and Liverpool Hospital that have supported myself and other students, making our research possible.

I'd like to express my gratitude for the financial support that supported this research. Thank you to the Australian Government for providing financial support of this research under the Australian Government Research and Training Program. Thank you to Liverpool Hospital and Ingham Institute for enabling my investigations with the Australian

MRI-LINAC and providing financial support under the South West Sydney Local Health District scholarship support program.

I would also like to thank my family and friends for supporting me outside of my studies, for just being there and enduring them with me. Finally, I want to express my deepest gratitude and adoration to my wife, Elle, for her love and encouragement during these studies.

Declaration

I, *Levi J. Madden*, declare that this thesis is submitted in partial fulfilment of the requirements for the conferral of the degree *Doctor of Philosophy*, from the University of Wollongong, is wholly my own work unless otherwise referenced or acknowledged. This document has not been submitted for qualifications at any other academic institution.

Levi J. Madden

May 15, 2022

List of Figures

List of Tables

Abstract

In modern radiation therapy, treatment delivery techniques are getting increasingly complex to optimise patient outcomes. In modern radiation therapy clinics, there are conditions where accurate dosimetry is challenging, yet essential to ensure that optimal treatments are being delivered. These challenging dosimetry conditions require specialised dosimeters with a set of dosimetric qualities that allow them to remain accurate in such conditions. Fibre-coupled luminescent dosimeters possess a wealth of desirable qualities that make them advantageous for a wide range of dosimetry conditions. Due to their all-optical composition (*i.e.* no electronics or wires attached to the sensitive volume) and their typically compact sensitive volume sizes, fibre-coupled luminescent dosimeters have high spatial resolutions whilst minimising the perturbations of radiation fields in water. Dosimetric properties such as water equivalence, energy independence and dose-rate independence are inherited through their luminescent sensitive volumes, allowing for the luminescent material to be chosen to suit the measurement conditions. In this thesis, two fibre-coupled luminescent dosimeters are developed and investigated for two such challenging clinical dosimetry conditions. Firstly, plastic scintillation dosimeters (PSDs) are investigated for dosimetry with MRI-LINACs, a technology that combines an MRI scanner with a linear accelerator (LINAC) to provide the opportunity for real-time image guidance with optimal soft tissue contrast during radiotherapy treatments. Secondly, an in-house fibre-coupled BeO dosimeter is investigated for it's potential as a real-time *in vivo* dosimeter during LINAC and brachytherapy treatments.

PSDs were identified as promising prospects for MRI-LINAC dosimetry given they are highly water equivalent and their responses are near-correctionless for dosimetry with LINACs. The main challenge faced when applying fibre-coupled luminescent dosimeters such as PSDs for LINAC dosimetry is that their response becomes degraded by stem signals, requiring corrections to restore the PSD's accuracy. Prior to the investigations with an MRI-LINAC, an in-house PSD was developed and optimised for it's performance with a clinical LINAC. In these investigations, novel stem signal correction methods were developed and compared against "background subtraction", a robust benchmark method for this study's measurement conditions. In this study, the stem signal reached a maximum output that was 54 % of the maximum scintillation response. Background subtraction was

determined to be the most suitable correction method investigated for LINAC dosimetry, though the novel "Non-linear least squares correction" was a suitable alternative for cases when background subtraction was unsuitable.

An in-house PSD was developed for MRI-LINAC dosimetry, with the PSD dosimetry system optimised to ensure that background subtraction remained accurate. The in-house PSD was applied to measure output factors, beam profiles and percent depth dose distributions (PDDs) with the Australian MRI-LINAC, compared with reference distributions and results for other dosimeters in the literature. The in-house PSD was conclusively demonstrated to be effective and accurate for the measurement of output factors, beam profiles, and for PDDs at field sizes 10.5 cm $\times$ 10.5 cm and 18.4 cm $\times$ 18.4 cm. However, for the PDDs at field sizes of 2.6 cm $\times$ 2.6 cm and 5.3 cm $\times$ 5.3 cm, it could not be confirmed whether the PSD was generally suitable as there were conflicting trends between the reference distributions and the in-house PSD. The presented investigations with an in-house PSD and the Australian MRI-LINAC were an important first step in demonstrating that PSDs in general are highly suitable for MRI-LINAC dosimetry. It was concluded that further work was required to verify that all PSDs in general are suitable for MRI-LINAC dosimetry, and it was recommended that PSD dosimetry systems are investigated to validate they are as accurate as is required prior to clinical MRI-LINAC dosimetry.

For real-time *in vivo* dosimetry during LINAC and brachytherapy treatments, fibre-coupled BeO dosimeters were identified as being highly suitable given their near-tissue equivalence and minimal energy dependence for photons with energies between 10 keV and 20 MeV. Further, BeO's optical stimulated luminescence response is dose-rate independent, and when this luminescence is read out in real-time using the "real-time OSL (rtOSL) technique", the measured rtOSL signals are free of stem signals. Measured rtOSL signals are typically non-linear with respect to dose, requiring a correction to restore the rtOSL dosimeter's dose-response linearity. Novel correction methods were developed to correct the measured rtOSL, compared against the prior rtOSL correction method. Two fibre-coupled BeO rtOSL dosimeters were developed and applied for measurements with a superficial X-ray unit and a clinical LINAC. The novel "deconvolution correction" significantly improved upon the performance of the prior correction method in terms of accuracy, robustness, reproducibility and uncertainty in dose-response. Through a computational simulation, the deconvolution correction was also determined to be applicable in real-time. The development of the deconvolution correction was a significant step in realising a fibre-coupled BeO dosimetry system capable of accurate, real-time *in vivo* dosimetry during LINAC and brachytherapy treatments.

Chapter 1

Introduction

It has been estimated that approximately 50 % of cancer patients would benefit from radiation therapy as part of their treatment [1, 2]. In radiation therapy, ionising radiation is used to induce damage in biological matter through the deposition of energy and radiation doses. In Australia, the most commonly applied form of radiation therapy is External Beam Radiation Therapy (EBRT). In modern EBRT, a linear accelerator (LINAC) is typically used to produce a beam of ionising radiation that is shaped to tumour volumes. Modern EBRT treatments are capable of reproducibly delivering high radiation doses to small, complex tumour volumes within the human body, whilst sparing the surrounding healthy tissues. For this precision to be realised, treatments are planned using accurate knowledge of the LINAC's radiation beam and the patient's anatomy. Through routine quality assurance (QA) dosimetry, measurements are made with radiation detectors (referred to as dosimeters) to monitor the characteristics of the LINAC's radiation beam in order to ensure that it remains consistent, thereby mitigating dose delivery errors. Many QA measurements are made by placing the dosimeter in a volume of water (or water equivalent material), irradiating the dosimeter, and converting it's response to an absorbed dose in water. In modern radiation therapy clinics, there are conditions where accurate dosimetry is challenging, yet essential to ensure that optimal treatments are being delivered. These challenging dosimetry conditions require specialised dosimeters with a set of dosimetric qualities that allow them to remain accurate in such conditions. Fibre-coupled luminescent dosimeters possess a wealth of desirable qualities that make them advantageous for a wide range of dosimetry conditions. In this thesis, two fibre-coupled luminescent dosimeters are investigated for their efficacy in two specific challenging dosimetry conditions. An in-house plastic scintillation dosimeter (PSD) is investigated for MRI-LINAC dosimetry, and fibre-coupled BeO dosimetry systems are investigated for their potential as real-time *in vivo* dosimeters for orthovoltage therapy and LINAC treatments.

Fibre-coupled luminescent dosimeters

Fibre-coupled luminescent dosimetry systems consist of a luminescent material volume that is optically coupled to an optical fibre, and a photodetector that is connected to the opposite end of the optical fibre. When the luminescent material is irradiated, it produces photon emissions that are collected by the optical fibre, and these photon emissions are subsequently measured by the photodetector. The number of photons emitted by the luminescent material is related to the dose-deposited in the luminescent material volume. Fibre-coupled luminescent dosimetry systems inherit many of their dosimetric properties through the luminescent material. There exists many luminescent materials with a variety of dosimetric properties, and so the luminescent material can be chosen to suit specific irradiation conditions. Their luminescent sensitive volumes can be manufactured to be small in size so that these dosimeters have high spatial resolutions. No cables or electronics are required around the luminescent material for it's operation, reducing the perturbation of radiation fields in water during dosimetric measurements. Additionally, the luminescence response can be produced in real-time, providing the opportunity for fibre-coupled luminescent dosimeters to be applied for real-time dosimetry. Each of these qualities are extremely advantageous for measurements in a number of challenging dosimetry conditions.

Fibre-coupled luminescent dosimeters face one main challenge that has limited their application as clinical dosimeters. When the optical fibre is irradiated by high energy photons and electrons, the optical fibre produces it's own photon emissions that are also measured by the photodetector. These photon emissions, referred to as the stem signal, are independent of the dose deposited in the luminescent material, thereby reducing the dosimeter's accuracy. Many stem signal correction methods have been developed to overcome this challenge, with each method having it's own advantages and limitations. In this thesis, the efficacy of existing and novel stem signal correction methods will be investigated for an in-house fibre-coupled plastic scintillation dosimeter.

MRI-LINAC dosimetry

Hybrid MRI-LINAC systems combine an MRI-scanner and a LINAC, with the MRI-scanner providing superior soft tissue contrast and image quality to current standard of imaging available on LINACs for those common tumour sites [3–5]. Hybrid MRI-LINAC systems therefore allow for improved target tracking at these sites, with the potential for improved targeting of tumour volumes during treatments. However, the MRI's magnetic field imparts a Lorentz force on charged particles, causing them to follow curved trajectories. This effect alters the dose distribution delivered to patients and target volumes, therefore dosimetry for the MRI-LINAC must be performed in the presence of the magnetic field. The curved trajectory taken through a material depends on the material's den-

sity and electronic stopping power. The trajectories taken through volumes of non water equivalent materials will deviate from the trajectories taken through matching volumes of water. As a result, there is the potential for dosimeters comprised of non water equivalent materials to misrepresent the dose distributions that are deposited in water, complicating MRI-LINAC dosimetry. Conversely, for highly water equivalent materials, the trajectories taken through the material will closely match those taken through water. Dosimeters that are comprised of highly water equivalent materials can be expected to more closely reproduce the dose distributions deposited in water during MRI-LINAC dosimetry and avoid the aforementioned effects that can perturb non-water equivalent dosimeters.

PSDs are comprised of highly water equivalent materials and their response is near-correctionless for dosimetry with clinical LINACs [6]. The plastic scintillator materials comprising the PSD's sensitive volumes are engineered to make their physical densities, electron densities and effective atomic numbers match those of water and tissue. Consequently, PSDs do not perturb the homogeneity of water media during dosimetry with a LINAC. Therefore, PSD measured dose distributions should closely match the dose distributions deposited in water, making them promising candidates for MRI-LINAC dosimetry. However, there have been no studies in the literature where the feasibility of PSDs are investigated for MRI-LINAC dosimetry. A primary motivation for this thesis was to investigate the feasibility and characterise the accuracy of PSDs as MRI-LINAC dosimeters.

Real-time *in vivo* dosimetry

In vivo dosimetry is the process of measuring radiation doses during a patient's treatment. Such a process provides feedback of the treatment to clinicians in real-time, enabling clinicians to intervene when delivered treatments deviate from planned treatments. The dosimetric qualities required for *in vivo* dosimetry varies with the treatment modality. For LINAC and brachytherapy treatments, many of the desirable qualities of fibre-coupled luminescent dosimeters are highly advantageous for *in vivo* dosimetry. For example, a fibre-coupled luminescent dosimeter's compact size and all-optical composition (*i.e.* no electronics or wires around the sensitive volume) ensures that the dosimeter's presence does not alter the treatment being delivered. Dosimetric properties such as tissue equivalence, energy independence and dose-rate independence are inherited through the luminescent material. The luminescent material BeO is near-tissue equivalent for the high energy photons and electrons produced by brachytherapy sources and LINACs, and it's optically stimulated luminescence (OSL) response is energy independent and dose-rate independent [7]. Additionally, BeO's OSL can be read out in real-time through a measurement scheme referred to as "the real-time OSL (rtOSL) technique", which also corrects the optical fibre's stem signal in real-time. Given this wealth of qualities, fibre-

coupled BeO dosimeters are promising prospects for real-time *in vivo* dosimetry during orthovoltage therapy, brachytherapy and LINAC treatments.

When the OSL is read out in real-time using the rtOSL technique, the measured rtOSL signal is non-linear with respect to the absorbed dose. Currently, only one correction exists to restore the linearity between the measured rtOSL and the absorbed dose. This correction method is theoretically derived, however, it exacerbates measurement noise and causes noisy rtOSL signals to become increasingly uncertain as measurement duration increases. Due to the non-linear nature of rtOSL signals, heavy signal averaging distorts the real-time response of the measured rtOSL, making this approach of noise reduction unsuitable. To take advantage of a fibre-coupled BeO dosimeter's advantageous dosimetric qualities, an alternative non-linearity correction may be required to reduce the rtOSL dose-response uncertainty. A secondary aim of this thesis is to investigate novel correction methods for the rtOSL's non-linearity.

1.1 Thesis aims

The aims of this thesis are:

1. To investigate novel and established PSD stem signal correction methods that are applicable with clinical LINACs. From these investigations, determine which of the available correction methods are most suitable for applications with the Australian MRI-LINAC.

2. To apply an in-house PSD for dosimetry with the Australian MRI-LINAC. From these measurements, determine whether the in-house PSD was suitable for MRI-LINAC dosimetry, and make recommendations for other PSD dosimetry systems based off these results.

3. To investigate novel and established correction methods for a fibre-coupled BeO rtOSL dosimetry system in order to reduce the system's dose-response uncertainty.

1.2 Thesis outline

In Chapter 2, the literature is reviewed with regards to radiation induced luminescence, luminescent dosimeters and dosimetry with LINACs and MRI-LINACs. The first thesis aim is addressed in Chapter 3, where novel temporal stem signal correction methods are investigated, along with the existing "background subtraction" method. An in-house PSD is applied to measure beam profiles with a clinical LINAC, and each correction method's

resultant beam profiles are evaluated with respect to reference data. In Chapter 4, the second thesis aim is addressed, where an in-house PSD is applied for MRI-LINAC dosimetry using the most suitable stem signal correction method. In this chapter, output factors, beam profiles and percent depth dose distributions are measured using the in-house PSD, compared against reference distributions and results for other dosimeters in the literature. In Chapter 5, the final thesis aim is addressed, where fibre-coupled BeO dosimeters are applied for dose-rate dependence measurements with a superficial X-ray unit and a clinical LINAC. In this chapter, novel rtOSL correction methods are presented, and their performance is compared against that of the existing correction method. In Chapter 6, the potential avenues for future works are discussed, and concluding remarks are given.

1.3 Contributions and publications

Publications

L. Madden, J. Archer, E. Li, D. Wilkinson, A. Rosenfeld. Temporal separation of Cerenkov radiation and scintillation using artificial neural networks in Clinical LINACs. *Phys. Medica.* 2018; 54:131-136. 10.1016/j.ejmp.2018.10.007.

L. Madden, J. Archer, E. Li, D. Wilkinson, A. Rosenfeld. Temporal separation of Cerenkov radiation and scintillation using a Clinical LINAC and artificial intelligence. *Phys. Med. Biol.* 2018; 63(22):225004. 10.1088/1361-6560/aae938.

L. Madden, J. Archer, E. Li, U. Jelen, B. Dong, N. Roberts, L. Holloway, A. Rosenfeld. First measurements with a plastic scintillation dosimeter at the Australian MRI-LINAC. *Phys. Med. Biol.* 2019; 64(17):175015. 10.1088/1361-6560/ab324b.

L. Madden, J. Archer, E. Li, U. Jelen, B. Dong, L. Holloway, A. Rosenfeld. MRI-LINAC beam profile measurements using a plastic scintillation dosimeter. *Phys. Medica.* 2020; 73:111-116. 10.1016/j.ejmp.2020.04.016.

L. Madden, A. Santos, E. Li, R. Gowda, E. Bezak, S. Asfaar, A. Rosenfeld. Technical note: Temporal modelling of beryllium oxide ceramics' real-time OSL for dosimetry with a superficial 140 kVp X-ray beam. *Phys. Medica.* 2020; 80:17-22. 10.1016/j.ejmp.2020.10.003.

L. Madden, N. Roberts, U. Jelen, B. Dong, L. Holloway, P. Metcalfe, A. Rosenfeld, E. Li. In-line MRI-LINAC depth dose measurements using an in-house plastic scintillation dosimeter. *Biomed. Phys. Eng. Express.* 2021; 7(2):025012. 10.1088/2057-1976/abe295.

L. Madden, E. Lukas, A. Santos, M. Ganija, P. Veitch, A. Rosenfeld, E. Li. Deconvolution analysis improves real-time OSL of BeO ceramic. *Radiat. Meas.* 2021; 149:106680. 10.1016/j.radmeas.2021.106680.

L.Madden, L. Holloway, A. Rosenfeld, E. Li. Mini-review: Fibre-optic dosimetry with MRI-LINACs. *Front.Phys.* 2021. 10.3389/fphy.2022.879624.

J. Archer, **L. Madden**, E. Li, M. Carolan, M. Petasecca, P. Metcalfe, A. Rosenfeld. Technical note: Temporally separating Cherenkov radiation in a scintillator probe exposed to a pulsed X-ray beam. *Phys. Medica.* 2017; 42:185-188. 10.1016/j.ejmp.2017.09.134.

J. Archer, **L. Madden**, E. Li, M. Carolan, A. Rosenfeld. A comparison of temporal Cherenkov radiation separation techniques in pulse signal scintillator dosimetry. *Biomed. Phys. Eng. Express.* 2018; 4(4):044003. 10.1088/2057-1976/aacf56.

J. Archer, **L. Madden**, E. Li, D. Wilkinson, A. Rosenfeld. An algorithmic approach to single probe Cherenkov removal in pulsed X-ray beams. *Med. Phys.* 2019; 46(4):1833-1839. 10.1002/mp.13383.

J. Archer, **L. Madden**, E. Li, D. Wilkinson, A. Rosenfeld. 2D photon dosimetry with a scintillation fibre optic dosimeter. *Radiat. Phys. Chem.* 2019; 166:108490. 10.1016/j.radphyschem.2019.108490.

Conference presentations

L. Madden, J. Archer, E. Li, D. Wilkinson, A. Rosenfeld. Temporal Separation of Cerenkov Radiation and Scintillation Using Convolutional Neural Networks. *3^{rd} Translational Cancer Research Workshop*. Austinmer, Australia. October 2018.

L. Madden, J. Archer, E. Li, D. Wilkinson, A. Rosenfeld. Plastic scintillation dosimetry with clinical LINACs and a convolutional neural network. *4^{th} Mathematical Modelling in Medicine and Biology*. Wollongong, Australia. November 2018.

L. Madden, J. Archer, E. Li, D. Wilkinson, A. Rosenfeld. Plastic scintillation dosimetry with a Clinical LINAC and convolutional neural network. *ACPSEM MedPhys18 (NSW/ACT branch)*. Sydney, Australia. December 2018.

L. Madden, J. Archer, E. Li, D. Wilkinson, A. Rosenfeld. LINAC photon beam dosimetry using a plastic scintillation dosimeter and a convolutional neural network. *1^{st} Australian MR in Radiotherapy Meeting*. Wollongong, Australia. December 2018.

L. Madden, J. Archer, E. Li, U. Jelen, B. Dong, L. Holloway, A. Rosenfeld. A plastic scintillation dosimeter for MRI-LINAC dosimetry. *19^{th} International Conference on Solid State Dosimetry*. Hiroshima, Japan. September 2019.

L. Madden, J. Archer, E. Li, U. Jelen, B. Dong, L. Holloway, A. Rosenfeld. MRI-LINAC relative dosimetry with an in-house plastic scintillation dosimeter. *Mini- Micro- Nano- Dosimetry 2020*. Wollongong, Australia. February 2020.

L. Madden, J. Archer, E. Li, U. Jelen, B. Dong, N. Roberts, L. Holloway, A. Rosenfeld. Feasibility of plastic scintillation dosimeters for MRI-LINAC dosimetry. *ACPSEM MedPhys20 (NSW/ACT branch)*. Sydney, Australia. December 2020.

Chapter 2

Literature review

Radiation dosimetry involves the measurement of quantities of ionising radiation. The radiation quantity of interest for the work in this thesis is absorbed dose, defined as the mean energy imparted per unit mass of a material [8]. Instruments that measure radiation doses are referred to as dosimeters, operating on the principle that energy depositions within their sensitive volume produces a measurable response. In the scope of radiation therapy, the dose absorbed by a volume of water is the desirable quantity [9, 10]; radiation therapy dosimetry aims to measure the absorbed dose in volumes of water equivalent material at known locations in a patient or phantom [9, 10].

In typical modern EBRT treatments, the LINAC outputs a high energy photon beam [8]; this is also the case for many of the developed MRI-LINAC systems to date [11]. The high energy photons produced by LINACs can undergo three main interactions with matter: the photoelectric effect, the Compton effect and pair production. For water, tissue and water equivalent materials, the Compton effect is the dominant interaction for the LINAC's high energy photons [12]. In the Compton effect, an orbital electron absorbs an incident photon, emits a scattered photon with some fraction of the absorbed energy, and the orbital electron is ejected from it's orbital with the remainder of the absorbed energy as kinetic energy. As energetic free electrons traverse through matter, they transfer fractions of their energy to other orbital electrons, resulting in the ionisation and excitation of orbital electrons in matter. In biological matter, the ionisation of orbital electrons produces biological damage, either by ionisation of the molecules in the DNA or through the production of free radicals in molecules that diffuse and interact with DNA [8]. The severity of biological damage to irradiated tissues depends on the absorbed dose within that tissue, where increasing radiation dose causes increasingly severe biological damage.

2.1 Luminescence

In the scope of radiation measurement and dosimetry, luminescence is a phenomenon where ionising radiation deposits energy in a material and the irradiated material emits photons [13]. Materials capable of radiation induced luminescence include inorganic crystals and ceramics, organic molecules and single atom gases[a]. Inorganic crystals and ceramics produce luminescence emissions via optically stimulated luminescence (OSL), thermoluminescence (TL) and inorganic scintillation (often referred to as radioluminescence in the literature[b]). For inorganic materials, the luminescence mechanisms arise due to the ionisation of valence electrons within a crystalline lattice [14]. Due to the presence of defects and impurities in the crystalline structure, free charges can be trapped, thus inorganic luminescent materials are capable of both prompt luminescence and stimulated luminescence. Organic molecules produce luminescence emissions via the organic scintillation and phosphorescence mechanisms. For organic molecules, the luminescence mechanisms arise due to the excitation of organic molecules with π electronic structures [13]. A crystalline lattice is not required for organic molecules to produce luminescence emissions, however these molecules are only capable of prompt luminescence such as organic scintillation and phosphorescence.

For radiation dosimetry with luminescent dosimeters, photodetectors are used to measure the typically weak photon emissions and convert these photon-intensity signals to electrical signals [15]. Measured luminescence signals are then analysed to determine the energy that is deposited into the luminescent material. Photodetectors are typically operated in one of two main measurement modes, referred to as current and pulse operation modes [15]. In current mode, the response is continuously integrated. The measured signal is directly related to the energy deposited in the detector's sensitive volume as a function of time [15]. This operation mode is typically used by the detection systems employed for the measurement of absorbed dose and absorbed dose-rate. In pulse mode, the detector's response to each individual radiation event is recorded [15]. The integral of each signal is directly related to the energy deposited in the sensitive volume for that event; the statistical analysis of these measured events is directly related to the incident radiation's energy spectrum. This approach is difficult to employ for measurements in radiation fields with high fluences, such as with LINACs [15]. All measurements presented in this thesis operate the photodetectors in current mode; for the remainder of this thesis, it is assumed that radiation detectors are operated in current mode.

[a] Gaseous scintillation will not be reviewed in this thesis; the reader is referred to Birks' The Theory and Practice of Scintillation Counting [13].

[b] It should be noted that radioluminescence collectively describes all mechanisms that result in the prompt emission of photons in response to ionising radiation, including scintillation, phosphorescence and delayed fluorescence, but not Cerenkov radiation.

2.1.1 Luminescence of inorganic materials

The luminescence of inorganic materials can be predicted by modelling the transport of charges throughout the crystalline material's band structure [14, 15]. With regards to the band structure, energy absorption by the luminescent material causes valence band electrons to excite to the conduction band, leaving a "hole" in the valence band [14, 15]. These electrons and holes can move freely throughout their respective bands in the inorganic crystal. Impurities and lattice defects in the luminescent material are present for many inorganic materials. These impurities and defects can capture the free electrons and holes created during irradiation. In the literature, these impurities and defects are referred to as trapping centres if electrons are captured, and recombination centres if holes are captured [14].

The allowed transitions for electrons are shown in Figure 2.1. These transitions include capture from the conduction band by trapping centres, release from trapping centres to the conduction band and recombination with a captured hole [14, 15]. Stimulation is typically required to release trapped electrons from trapping centres [14]. Holes are limited to capture from the valence band by recombination centres and recombination with a conduction band electron. In this model, luminescence photons are emitted when free electrons are captured by trapped holes at recombination centres [14, 16]. Luminescence emissions occurring without stimulation are referred to as radioluminescence [15]; emissions occurring as a result of optical or thermal stimulus are referred to as optically stimulated luminescence and thermoluminescence, respectively [14, 16].

Kinetics of inorganic luminescence

The intensity of luminescence photon emissions is proportional to the rate of recombination of electrons and holes. Through kinetic modelling of the charge traffic between energy states, the electron-hole recombination rate can be modelled mathematically as a function of time, and an expected time-dependent intensity of luminescence can be determined [14, 16]. The following kinetic modelling is adapted from Kitis *et al.* [17], used to model radioluminescence and OSL, but not TL[c]. For a simple material with one trapping centre species, one recombination centre species and one deep trap species as shown in Figure 2.1, the rates equations describe the post-irradiation traffic of charges throughout the material:

[c]The reader is referred to McKeever and Chen [14] for advanced kinetic models of OSL and TL.

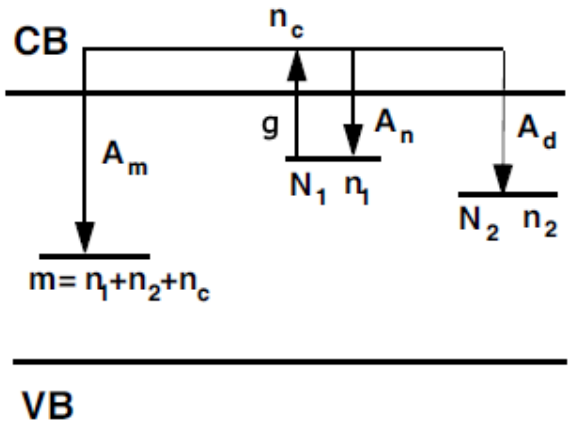

Figure 2.1: Kinetic model of a material with one species of optically active trapping centre, one species of recombination centre and one species of deep trap. In the diagram, CB is the conduction band, VB is the valence band, N_1 is the maximum population of the trapping centre and N_2 is the maximum population of the deep trap. Additionally, n_c is the population of the conduction band, n_1 is the population of the trapping centre, n_2 is the population of the deep trap and m is the population of the recombination centre. The rates A_n, A_d and A_m are the probabilities of free electron capture by trapping centres, deep traps and recombination centres, respectively. Finally, the rate g is the optical stimulus rate. Adapted from Kitis *et al.* [17].

$$\frac{dn_c}{dt} = -n_1 g(t) + n_c(N_1 - n_1)A_n \tag{2.1}$$

$$\frac{dn_1}{dt} = n_c(N_2 - n_2)A_d \tag{2.2}$$

$$\frac{dn_2}{dt} = n_1 g(t) - n_c(N_1 - n_1)A_n - n_c(N_2 - n_2)A_d - n_c(n_1 + n_2 + n_c)A_m \tag{2.3}$$

$$I = -\frac{dn_c}{dt} - \frac{dn_1}{dt} - \frac{dn_2}{dt} \tag{2.4}$$

The parameters n_1, n_2, n_c, m and g are defined in the caption of Figure 2.1. These population parameters are time-dependent and the solution to this model yields the expected time-dependent intensity of post-irradiation luminescence emissions as a function of time. This simple kinetic model can be generalised to contain multiple species of each type of centre; when the number of species of each trap is known for a material, the kinetic model can be adapted to predict the post-irradiation luminescence of the material [d]. For inorganic luminescent materials, there exists a complementary relationship between the light output for radioluminescence and the light output for stimulated luminescence, such that inorganic materials with relatively high scintillation yields possess relatively

[d]It should be noted that other transitions can be modelled, leading to different predicted luminescence functions. The choice of kinetic model and the transitions modelled are important for accurate prediction of a material's luminescence. The reader is referred to McKeever and Chen [14] and Kitis *et al.* [17] for derivations of analytical solutions to the simple model and more advanced models.

low stimulated luminescence yields, and vice versa [18, 19]. This relationship arises as trapping centres compete with recombination centres to capture free electrons, with relatively high concentrations of trapping centres in the inorganic materials promoting trapping of free electrons and stimulated luminescence. Further, the competition between the numerous species of centres can make the luminescence responses of some inorganic materials non-linear with respect to the absorbed dose [20]. The following subsections review the characteristics of thermoluminescence, optically stimulated luminescence and radioluminescence.

Thermoluminescence Thermoluminescence dosimetry applies heating to an irradiated inorganic material to release the charges stored in trapping centres [14]. Typically, the material is heated uniformly, such that the material's temperature increases linearly as a function of time [21]. The maximum temperature reached by the material is chosen to be below the temperature at which the material glows incandescently [21]. The intensity of thermoluminescence is proportional to the rate of the recombination of free electrons and holes, dependent on the rate at which trapped charges are thermally liberated [14, 21]. The probability that a trapped charge is thermally liberated, $p(T)$, follows the Arrhenius rate law [14, 21]:

$$p(T) = s(T)e^{\frac{-E}{kT}} \tag{2.5}$$

Where $s(T)$ is a weakly temperature dependent factor related to the vibration of the trapped charge in a potential well, E is the thermal activation energy of the trapping centre, k is Boltzmann's constant and T is the material's temperature (in Kelvin) [14, 21]. During readout, the thermoluminescence intensity is measured and recorded as a function of time. The resultant intensity-time spectrum is converted to an intensity-temperature spectrum, referred to as a glow curve. The kinetic model for charge transport can be modified to analytically determine the expected glow curve produced in response to a given linear heating rate [14, 21]. It should be noted that the heating rate affects the shape of the measured glow curve [14]. After readout, the thermoluminescent material is heated to high temperatures (in excess of 600 °C) to empty any remaining filled traps in a process referred to as annealing [22]. The annealing process affects the thermoluminescence dose-response, thus reproducible annealing procedures are required to ensure accurate dosimetry with thermoluminescent dosimeters [23]. For many thermoluminescent materials, the total number of photons emitted during readout is increasingly supra-linear as absorbed dose increases; the supra-linear behaviour can become significant for absorbed doses exceeding orders of 1 Gy, though this is material dependent [23].

Optically stimulated luminescence Similar to thermoluminescence, the total number of photons emitted during readout is increasingly supra-linear as absorbed dose increases

[22, 24]. This supra-linear behaviour is material dependent; for BeO, the supra-linearity is insignificant for doses below 10 Gy [7]. In optically stimulated luminescence dosimetry, an optical stimulus such as a laser is applied to the irradiated inorganic material to liberate trapped charges. The light source is chosen to have a photon energy that is tuned to the activation energy of the optically active trapping centres. To ensure accurate OSL dosimetry, the OSL dosimeters undergo a post-readout exposure to intense optical stimulus (referred to as bleaching). Bleaching is required to optically liberate any remaining filled traps after readout to ensure reproducible dosimetric characteristics, serving the same purpose as the annealing process for thermoluminescent dosimeters. The rate at which trapped charges are optically liberated is given by [17]:

$$g(t) = \sigma\phi(t) \tag{2.6}$$

Where σ is the material's photo-ionisation cross section (at the photon's energy) and $\phi(t)$ is the time-dependent intensity of the laser. OSL dosimetry methods typically apply spectral filtration to avoid measuring stimulus photons whilst measuring OSL emissions [25, 26]. In the literature, 3 main stimulation schemes are used for the readout of optically stimulated luminescence: these schemes are the continuous-wave [27], the linear-modulated [28] and the pulsed stimulation schemes [29]. In the continuous-wave stimulation scheme the intensity of the laser is fixed, and the kinetic model in Equation 2.1 reduces to a first order system of differential equations. Consequently, traps are emptied following an exponential decay with respect to time and the intensity of OSL emissions follows an exponential decay with respect to time. This form of kinetic model and it's resultant exponential decay are referred to as first order kinetics [17]. In the linear-modulated stimulation scheme, the laser intensity is increased linearly as a function of time [17, 28]. Optically active trapping centres are emptied following second order kinetics, resulting in a time-dependent OSL intensity that follows a quasi-exponential rise and decay with respect to time [17]. In the pulsed stimulus scheme, the laser stimulus is periodically pulsed on and off following a square wave. For post-irradiation readout, the pulse duration is typically chosen to be less than the decay constant of luminescence, and the stimulation's period is chosen to be approximately 10 to 20 times longer than the decay constant of luminescence [26]. The corresponding time-dependent luminescence follows an exponential rise and decay as a function of time [17].

A variation of the pulsed stimulus scheme allows for the real-time measurement of optically stimulated luminescence, referred to as the real-time OSL technique [29, 30]. While the inorganic material is irradiated, it continuously produces prompt luminescence emissions. For materials with relatively short luminescence decay constants, OSL is only measurable while the optical stimulus is applied. The difference between the luminescence signal measured with and without the stimulus corresponds to the OSL signal in

real-time. It should be noted that traps may not get completely emptied by the optical stimulus during each stimulation period, leading to a convoluted relationship between the absorbed dose and total number of OSL photons emitted during irradiation. When traps are not completely emptied in a single stimulus pulse, the measured rtOSL is non-linear with respect to the absorbed dose [29, 30]. Currently, the only method to correct the non-linear relationship between absorbed dose and rtOSL emissions applies a non-linear correction function to linearise the measured rtOSL signal with respect to absorbed dose [29, 30].

Radioluminescence The relationship between absorbed dose and radioluminescence emissions is dependent on the material being irradiated. For inorganic materials that have low concentrations of trapping centres, the intensity of scintillation is proportional to the absorbed dose-rate in the material [31]. For materials with high concentrations of trapping centres, the scintillation dose-response can be dependent on the absorbed dose in the crystal [32]. This occurs as recombination centres and trapping centres compete to capture conduction electrons. As the accumulated dose increases, the number of unoccupied trapping centres decreases, increasing the probability that a conduction electron is captured by a recombination centre [32]. This increased recombination probability results in an increased sensitivity to absorbed dose as the accumulated dose increases [32, 33]. This sensitivity dependence has been referred to as the "memory effect" in the literature. Materials with high concentrations of trapping centres such as Al_2O_3:C suffer from this effect, such that Al_2O_3:C requires a method that mitigates or corrects the increasing sensitivity of the dosimeter [33–35]. The gold standard memory effect correction method pre-irradiates the inorganic crystal prior to the dosimetric measurements [34]. In this method, the inorganic crystal is irradiated with a significantly high radiation dose that completely fills the trapping centres, eliminating the free capture mechanism for trapping centres, thus stabilising the scintillation sensitivity for the dosimetric measurements. Alternatively, some inorganic crystals are engineered to have minimal concentrations of trapping centres at room temperature, making their sensitivity stable without needing prior irradiation [31]. In other methods, the inorganic crystal is not pre-irradiated; instead the time-dependent intensity of scintillation is measured and analysed to correct for the memory effect. Andersen *et al.* iteratively corrected Al_2O_3:C's RL by multiplying the measured scintillation by a sensitivity correction function [33]. Magne *et al.* implicitly corrected Al_2O_3:C's RL by transforming the measured signal to the integral dose through the application of kinetic modelling [35]. With the memory effect corrected or avoided, the total number of photons emitted is proportional to the absorbed dose [31, 33–35].

2.1.2 Luminescence of organic materials

The luminescence of organic materials can be predicted by modelling the populations of molecules throughout each available energy state as a function of time [15]; the following paragraphs are adapted from Knoll [15]. The absorption of energy by organic molecules with π electronic structures causes the molecule to excite and vibrate to excited energy states [15]. Typical energy states of a luminescent organic molecule is shown in the Jablonski diagram in Figure 2.2. Each energy state corresponds to a different configuration of the molecule's orbital electrons. In the Jablonski diagram, two subscripts are used to classify each energy state into levels and sub-levels. Energy levels are typically separated by the order of 1 eV (*e.g.* S_{00}, S_{10}, S_{20} and S_{30}). Energy sublevels are more narrowly separated by the order of 0.1 eV (*e.g.* S_{00}, S_{01}, S_{02} and S_{03}). These sublevels correspond to vibrational energy states of the level, where sublevels with second index greater than 0 have excess vibrational energy for that energy level.

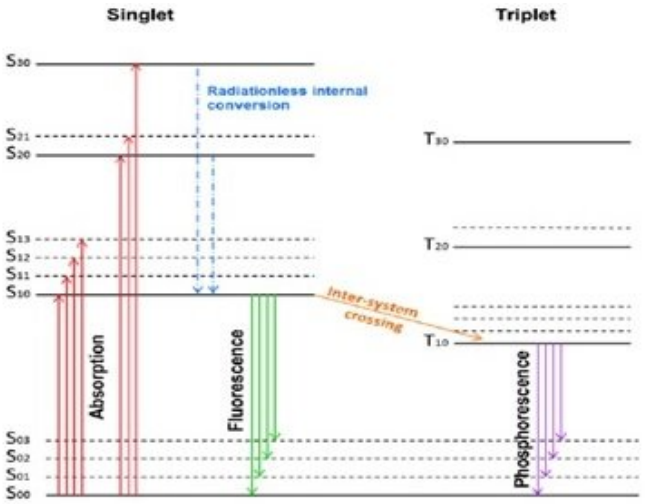

Figure 2.2: Energy levels of π orbitals in organic scintillators. S states correspond to singlet states (electron configuration with spin equal to 0) and T states correspond to triplet states (electron configuration with spin equal to 1). The first subscript denotes the energy level of the molecule, and the second subscript denotes a vibrational energy state at that level. Finally, the S_{00} state corresponds to ground state for the molecule. Diagram from Mdhluli *et al.* [36], adapted from Knoll [15].

The absorption of energy by molecules in the ground state, S_{00}, causes them to excite to the higher energy levels S_1, S_2 and S_3. Through a process known as radiationless internal conversion, the unstable energy states S_2 and S_3 relax to the metastable S_1 states with no photon emissions. The vibrational states with excess energy (*e.g.* S_{11}, S_{12} and S_{13}) dissipate their excess vibrational energy via radiationless interactions and relax to the S_{10} state. Relaxation from the S_{10} excited state to S_{00} ground state occurs with prompt photon emissions, referred to as scintillation. Through the inter-system crossing phenomena, excited singlet states can transition to excited triplet states with lesser energy; the relaxation of excited triplet states to the ground singlet state produces luminescence emissions that

are referred to as phosphorescence. The excited triplet states can absorb vibrational energy and heat energy from neighbouring molecules and transition to excited singlet states, resulting in the phenomena known as delayed fluorescence.

In general, the intensity of organic luminescence typically follows a multi-exponential rise and decay, comprised of "fast" and "slow" components with short and long decay constants. For the high energy photons and electrons produced by LINACs, the population of excited singlet states dominates the population of excited triplet states and the "fast" component of luminescence dominates the "slow" component. In this case, a mono-exponential rise and decay suffices to describe measured luminescence. However, for radiation with high linear energy transfers (LETs) such as slow neutrons and alpha particles, many organic scintillators exhibit luminescence where the slower component is significant and non-negligible. This occurs as the higher LET radiations cause significant population of the triplet states associated with the "slow" component of organic luminescence [15]; organic luminescence in response to these high LET radiations are described by a multi-exponential rise and decay with respect to time. Due to the intrinsic dependence of luminescence emissions on LET, organic scintillators have been used for discrimination of high LET and low LET particles in mixed radiation fields such as neutron-gamma mixed fields.

Kinetics of organic scintillation

The intensity of luminescence emissions is proportional to the rate of relaxation of excited singlet and triplet states to the ground singlet states. The deposition of energy by ionising radiation causes a net population shift of molecules from the S_0 ground state to the S_1 excited state due to the near instantaneous radiationless conversion. The net shift in population to the S_1 state is characterised by an exponential rise time constant, τ_r [13, 15]. The relaxation of S_1 molecules to the S_0 ground state occurs spontaneously, and is characterised by an exponential decay constant, τ_d [13, 15]. In response to a Dirac delta pulse of irradiation, $\delta(t)$, the expected luminescence, $h(t)$, is given by [15]:

$$h(t) \propto e^{(-\frac{t}{\tau_d})} - e^{(-\frac{t}{\tau_r})} \tag{2.7}$$

For the case where the linear energy transfer of incident radiation is significantly low, the total number of photons emitted is proportional to the absorbed dose in the organic scintillator. In the scope of the work presented in this thesis, the LET of high energy photons and electrons is low, such that quenching has negligible impact on the presented measurements.

2.1.3 Time-resolved methods for fluorescence and luminescence

Time-resolved methods measure the fluorescence and luminescence of materials in response to ultra-fast stimulation pulses with high temporal resolution photodetectors [37–39]. Through analysis of these responses, the fluorescence and luminescence lifetimes can be determined [37]; these characteristics can then be correlated with the kinetics and physical processes occurring in the material [40, 41]. Time-resolved methods are most frequently applied for fluorescence microscopy in chemistry, allowing for improved discrimination of the physical processes occurring in organic molecules, biological matter and chemical reactions [41, 42]. These methods have also recently been applied during pulsed OSL measurements for both dosimetry [38] and investigations into the kinetics occurring in desirable materials [40]. In the time-resolved fluorescence literature, the measured fluorescence, $I(t)$ is characterised by the convolution equation [43]:

$$I(t) = h(t) * p(t) * L(t) \tag{2.8}$$

Where $h(t)$ is the material's fluorescence impulse response function (fIRF), $p(t)$ is the photodetector's impulse response function and $L(t)$ is the stimulation profile [43]. It should be noted that the fIRF is the material's hypothetical response to an ideal Dirac δ pulse stimulus, an equivalent function to $h(t)$ in Equation 2.7 for the case of organic scintillators [15]. The stimulation profile describes the time-dependent intensity of the stimulation source [43]. The photodetector's impulse response function describes it's ability to temporally resolve measured signals. It should be noted that the relationship in Equation 2.8 precisely models the components in a real-time fibre-coupled luminescence dosimetry system: a luminescent material is stimulated by a radiation source, producing a luminescence signal that is measured by a photodetector. In the scope of fibre-coupled luminescence dosimetry, the component $h(t)$ corresponds to the luminescent material's impulse response function, $L(t)$ corresponds to the dose-rate as a function of time, and $p(t)$ corresponds to the photodetector's response function. Often in modern time-resolved fluorescence literature, the convolution of the photodetector response function, $p(t)$ and the stimulation profile, $L(t)$ are combined into a single term referred to as the instrument response function, $x(t)$ [44]. Equation 2.8 is thus often stated as:

$$I(t) = h(t) * x(t) \tag{2.9}$$

2.2 Dosimetry with LINACs

In radiation therapy, quality assurance (QA) is the process of measuring and validating the geometric and dosimetric accuracies in the planned radiation therapy treatments [45, 46]. Dosimetry plays an important role in EBRT QA, performed routinely with the LINAC as a

means to ensure that the planned dose distribution is delivered accurately to the patient as intended. In these QA measurements, dose distributions are delivered to a volume of water (simulating the tissue of the human body, referred to as a phantom) housing a dosimeter at some known position within the water volume [9, 10, 12]. In these measurements, the LINAC's output is measured under specific conditions and compared against the expected output under these conditions. This process provides a means for verification that the output and functionality of the LINAC remains within acceptable limits (based off studies and recommendations in the literature) [9, 10, 12]. When the LINAC's output deviates outside the acceptable limits, treatments can result in poor patient outcomes.

Modern EBRT treatments have become increasingly complex in order to improve dose confinement and patient outcomes, with treatment techniques advancing from fixed field 3D conformal radiation therapy (3DCRT), to dynamic field intensity modulated radiation therapy (IMRT) and volumetric modulated arc therapy (VMAT). This trend where increasing dose confinement is achieved through increased treatment complexity is expected to continue with the realisation of 4π therapy in the near future [47]. In these treatments techniques with modern LINACs, the gantry, multileaf collimators (MLCs) and patient couch can be moved dynamically. Through the coordination of these components, more optimal dose confinements and reduced treatment speeds can be achieved, with the potential for further improvements to patient outcome [46]. With the increasing treatment complexity, there exists an increased likelihood for errors in delivered treatments, with increased risks of poor treatment outcomes [46]. This trend of increasing treatment complexity makes QA dosimetry more important than ever as other previously established methods make it difficult for a clinician to detect treatment errors and avoid mistreatments.

The QA dosimetry process requires reliable dosimeters with well characterised responses to achieve the desired levels of accuracy in measured doses. There exists many types of dosimeters, each with their own dosimetric properties that can affect the dosimeters response to radiation doses [48]. There are no ideal dosimeters that suit all measurement conditions for LINACs, especially when considering the qualities required for verification of highly conformal dose distributions. Consequently, dosimeters must be selected to suit the measurement conditions. Certain dosimetric properties are generally desirable for measurements with LINACs. Desirable properties for LINAC dosimetry include: water equivalence of the sensitive volume, energy independence, a linear response with dose, dose-rate independence, directional independence, radiation hardness, real-time response, high spatial resolution, minimal perturbation of the homogeneity of water media, high accuracy and reproducibility, and independence of ambient conditions [8]. The following section provides an overview of the common LINAC dosimeters, their advantages and disadvantages in the scope of LINAC dosimetry.

2.2.1 Ionisation chambers

Ionisation chambers are gas-filled cavity dosimeters that use high voltages to produce electric fields across their cavity volume. They operate on the principle that energy depositions in the gaseous volume (typically air) produce electron-ion pairs, such that the charge collected is proportional to the dose deposited in the gaseous volume. Ionisation chambers are routinely used for QA dosimetry in radiation therapy clinics, owing to their linear response with dose, dose-rate independence and energy independent sensitivity. Ionisation chambers are capable of calibration against a national standard, enabling their use for direct measurement of the absorbed dose in water for a wide range of beam qualities. Because of this, ionisation chambers are frequently used to cross-calibrate the response of other dosimeters for relative dosimetry measurements. Ionisation chamber volumes for EBRT QA dosimetry range from the order of $0.1\,\mathrm{cm}^3$ for typical Farmer chambers to $0.001\,\mathrm{cm}^3$ for micro-ionisation chambers. Farmer chambers are recommended by the IAEA codes of practice for measurements of absorbed dose in water for the high energy photon and electron beams produced by clinical LINACs [9, 10]. Small volume ionisation chambers are recommended for dosimetry in small fields and steep dose gradients [12].

2.2.2 Diode detectors

Diode detectors have sensitive volumes comprised of silicon, operating on the principle that energy depositions within the silicon sensitive volume produce a measurable charge proportional to the absorbed dose (in silicon). Diodes have sensitivities to radiation that are approximately 18000 times greater than the sensitivity of equivalent volume ionisation chambers, and their sensitive volumes are typically of the order of $0.1\,\mathrm{mm}^3$. The diode's sensitivity however depends on factors such as temperature, beam direction, photon beam energy and dose-rate [49]. The dependence on temperature arises from variations in the band structure of silicon with temperature, reported to range from 0.05 %/°C to 0.5 %/°C [50, 51]. This effect is easily mitigated through stabilisation of the diode's temperature. Their directional dependence arises due to the non symmetrical geometry and construction of the diode and it's packaging; several geometries of diodes have been developed to negate this directional dependence [52, 53]. The sensitivity of diodes to electrons remains flat for the high energy electrons produced by LINACs. However, a diode's sensitivity to photons is energy dependent, where diodes over-respond to low energy photons [49]. To mitigate this over-response to low energy photons, shielding with heavy metals may be used as a means to attenuate the low energy photons (diodes with shielding are referred to as shielded diodes; diodes without shielding are referred to as unshielded diodes). Small volume unshielded diodes are recommended for measurements in small fields by a dedicated code of practice [12, 54], however their response requires correction for conversion

from absorbed dose in silicon to absorbed dose in water due to their energy dependent sensitivity for low energy photons.

2.2.3 Diamond detectors

Diamond detectors operate on a similar principle to diode detectors, such that energy depositions in the sensitive volume produces a measurable change in the voltage across it's sensitive volume, proportional to the absorbed dose-rate in diamond. The diamond sensitive volume is water equivalent for the high energy photons and electrons produced by LINACs [55], and it's response is real-time and typically directionally independent. Typically, their sensitive volumes are of the order of 0.1 mm^3, making them desirable for measurements in steep dose gradients and small fields [55]. However, diamond detectors can suffer from an energy dependent sensitivity, arising from the perturbation of low energy photons by the diamond's casing and electric contacts [56].

The diamond detector, PTW60019 microDiamond detector (referred to as the microDiamond detector from this point onwards), is of particular interest for dosimetry with modern LINACs [57]. The microDiamond detector has been engineered to have a cylindrical sensitive volume with 2.2 mm diameter and 1 μm thickness, giving the microDiamond high spatial resolutions and a directionally dependent sensitivity [58]. It's diamond sensitive volume is synthetically grown to ensure high reproducibility in it's dosimetric properties and characteristics. The microDiamond is characterised by a linear response with dose and dose-rate. The microDiamond thus has a set of qualities that are attractive for small field dosimetry. For use in small fields, a field size dependent correction is required for the energy dependent sensitivity due to perturbations from the packing and contacts [56]. With correction, the microDiamond detector has been recommended in the small field dosimetry code of practice TR483 for measurement of lateral beam profiles in small fields [12].

2.2.4 Metal Oxide Semiconductor Field Effect Transistors (MOSFETs)

MOSFET dosimeters operate on the principle that energy depositions in their sensitive volume produce a shift in threshold voltage, proportional to the absorbed dose in their silicon dioxide sensitive volume [59]. Their sensitive volumes are approximately 1 μm thick, and their response is able to be read out in real-time. Their sensitivity is directionally dependent, arising from asymmetrical geometries of material and packaging [60]. The sensitivity shows weak temperature dependence that does not typically warrant correction [49]. An energy dependent correction may be required to convert the absorbed dose in silicon dioxide to absorbed dose in water for conditions where significant fluences of low energy photons are present [61]. Given these qualities, they are appealing

for photon and electron beam dosimetry in high spatial dose gradients [62], as well as *in vivo* skin dosimetry [63]. In general, MOSFETS are not recommended in small fields [12]; however, the MoSkin^{TM} (CMRP, UOW, Australia) MOSFET is suitable for use in small fields, engineered with advanced packaging that provides a skin equivalent depth of measurement [64].

2.2.5 Radiochromic film

Radiochromic films are two dimensional dosimeters with a thin sensitive volume layer (approximately 30 μm). Their sensitive volumes contain radiation sensitive monomers that are distributed throughout a polymer matrix [65, 66]. Energy depositions in their sensitive volume induce the polymerisation of these monomers, forming coloured dyes at the site of the energy deposition. Due to this operation principle, radiochromic films are self developing, have intrinsically high spatial resolutions, and are single use only. Their dose-response is read out as a function of optical density using a flat-bed scanner or densitometer [65, 66]. This response is non-linear as a function of absorbed dose in water and requires calibration to correct for it's non-linearity. The commercial radiochromic film, GafChromic EBT3 (Ashland Inc, USA), has been optimised for clinical LINAC dosimetry, designed to be highly water equivalent, directionally independent and dose-rate independent for high energy photons and electrons [65, 66]. The main source of uncertainties in radiochromic film measurements arise from limits in the uniformity of films, variations between different batches of film, variations in the readout of these films by flat-bed scanners and conversion of their non-linear responses to absorbed dose [67, 68]. GafChromic EBT3 film has been recommended for relative dosimetry measurements of small fields, and broad photon and electron beams [9, 12, 69], however it is not recommended for absolute dosimetry measurements.

2.2.6 Fibre-coupled luminescent dosimeters

Fibre-coupled luminescent dosimeters are comprised of a luminescent material volume that is optically coupled to an optical fibre, with the optical fibre connected to a photodetector. The luminescence dosimetry process can be summarised as follows: the luminescent dosimeter is irradiated, a luminescence signal is generated, the luminescence signal is measured using a photodetector and the measured signal is analysed to determine the dose absorbed in the luminescent material. A fibre-coupled luminescent dosimeter's all-optical composition (*i.e.* no electronics or wires around the sensitive volume) and typically compact dosimeter size minimises the perturbation of the radiation field in water during dosimetry, advantageous in many clinical dosimetry conditions. However, fibre-coupled luminescent dosimeters encounter one main challenge that has limited their use as clinical dosimeters: stem signals.

Stem signals and correction methods

When the fibre-coupled luminescent dosimeter's optical fibre is irradiated by high energy photons and electrons, the optical fibre produces it's own photon emissions. These photon emissions, referred to as stem signals, are subsequently measured by the photodetectors and are effectively noise with respect to the desired luminescent signals. These stem signals are comprised of two independent components, being Cerenkov radiation and the luminescence of the optical fibre [70]. For dosimetry with LINACs, Cerenkov radiation is the dominant component of the optical fibre's stem signals [70]. Cerenkov radiation is produced when a charged particle traverses through an optical medium at a speed greater than the local speed of light in that optical medium [71]. Cerenkov radiation is directionally dependent [71], and the magnitude of Cerenkov radiation that is collected by the optical fibre depends on the orientation of the optical fibre with respect to the radiation beam [72]. For common plastic optical materials, the photon and electron energy thresholds for Cerenkov radiation generation are of the order of hundreds of kiloelectron-volts [73]. Clinical LINACs typically produce photon and electron beams with average energies of the order of megaelectron-volts [73], making the generation of Cerenkov radiation and stem signals unavoidable. As a result of these stem signals, the response of the fibre-coupled luminescent dosimeters is perturbed, increasing their uncertainties. Fibre-coupled luminescence dosimetry methods must therefore correct the stem signal to ensure that the dosimeter remains accurate in it's measured dose-response [72, 74]. The following section reviews the existing stem signal correction methods for fibre-coupled luminescent dosimeters; a summary of the correction methods is provided in Table 2.1.

	Advantages	Disadvantages
Background Subtraction	Robust and accurate in fields with low dose gradients	Accuracy degraded in fields with high dose gradients
Chromatic Removal	Gold standard, robust and accurate	-
Air Core	No Cerenkov radiation generated in optical fibre	Fragile, significant attenuation of optical signals
Temporal Filtration	Avoids measuring Cerenkov radiation	Significant reduction in scintillation, pulsed sources only
Remote Imaging	Minimal Cerenkov radiation, capable of 2D and 3D dosimetry	Requires calibrated scientific CCD camera
Real-time OSL	Real-time, permits use of many inorganic luminescent materials	Requires repeatable post measurement bleaching

Table 2.1: Table summarising the advantages and disadvantages of the stem signal correction methods for fibre-coupled luminescent dosimeters.

Background subtraction The original correction method, background subtraction, applies a second optical fibre with no scintillator (referred to as the reference probe) to measure only stem signals [75]. It should be noted that the reference probe has dimensions, materials and construction that matches the dosimeter's optical fibre. In the experimental setup, the fibre-coupled luminescent dosimeter and reference probe are positioned abreast to one another, and are aligned so that equal lengths of optical fibre are irradiated. With this setup, approximately equal magnitudes of stem signal will be produced by the dosimeter and the reference probe. Consequently, the luminescence response can be corrected for stem signals by taking the difference between the measured fibre-coupled luminescent dosimeter's signal and the reference probe's signal. It should be noted that the approximate equality is invalid when there are high spatial dose gradients between the dosimeter and the reference probe [76]. Most LINAC dosimetry occurs in radiation fields with low spatial dose gradients [76], enabling the use of background subtraction with LINACs. Other stem signal correction methods have been developed to avoid the high dose gradients limitations of background subtraction.

Chromatic removal In the chromatic removal method, a bifurcated optical fibre is used to produce two identical signals from the fibre-coupled luminescent dosimeter [74]. Different optical filtration is applied to the two optical signals. The first set of optical filtration is designed to filter out as much stem signal and preserve as much scintillation as possible, and the second set of filtration is designed to filter a significantly different set of wavelengths to the first filter. Through analysis of the optical signals under these two differing filtration schemes, the stem signal and the luminescence signal can be separated [74]. Chromatic removal method has achieved marginally superior accuracies compared to background subtraction [76], and is applicable in radiation fields with high spatial dose-gradients, making chromatic removal superior to background subtraction.

Temporal filtration Another set of approaches to correct for stem signals present in measured luminescence signals uses scintillators with long decay constants (*i.e.* in the order of hundreds of nanoseconds to milliseconds and longer) for dosimetry with pulsed radiation sources. It should be noted that Cerenkov radiation is produced near-instantaneously and decays with sub nanosecond half lives [77], such that Cerenkov radiation can only be measured as the optical fibre is irradiated. To take advantage of this difference in lifetimes, [78–80], temporal pulse gating is used to wait for the Cerenkov radiation to subside, so that only scintillation remains after the pulse gating. It should be noted that no reference probe is required for temporal filtration, however this method is not applicable with continuous radiation sources. This method has been highly successful with slow inorganic scintillators such as Al_2O_3:C [33], Al_2O_3:CrO_3 [78] and SiO_2:Cu [80]. However, temporal filtration was suboptimal when investigated for use with the slow plastic scintillator

BC444G (Saint Gobain, France) and a clinical LINAC [76, 79]. This result occurred as a large portion of the plastic scintillators signal was emitted prior to the pulse gating, increasing the PSD's uncertainty.

Air core optical fibres An interesting take on dealing with stem signals avoids their production by replacing the solid-core optical fibres with air-core optical fibres [81, 82]. Air-core optical fibres use a mirrored inner surface to reflect photons through the length of the optical fibre. Air can not produce Cerenkov radiation for electron energies below 20 MeV, thus they avoid producing Cerenkov radiation in their core during dosimetry with modern LINACs [81]. Air-core optical fibres face practical drawbacks that make them more difficult to implement in clinics such as high attenuation of optical signals per unit length and the fragility of the air-core fibre.

Remote imaging Another worthwhile luminescence dosimetry method obviates the use of an optical fibre to transport scintillation signals, instead imaging the scintillation from a distance with a scientific charge coupled device type camera [83–85]. It should be noted that 3D scintillation imaging is possible if the luminescent material is transparent, allowing for reconstruction from orthogonal views. The spatial and temporal resolutions of calculated dose distributions are only limited by the corresponding resolutions of the camera, and enable such a dosimetry system to measure 2D and 3D dose distributions with high spatial and temporal resolutions. Given these qualities, this approach has been applied for real-time 2D dosimetry with LINACs [86], 3D dosimetry with proton beams [83, 84] and real-time 3D dosimetry (coined "4D dosimetry") with an MRI-LINAC [85]. Cerenkov radiation is still produced in the scintillator block when this method is applied for LINAC dosimetry, though the intensity of Cerenkov radiation is reported to have an amplitude less than 0.5 % of the scintillation in these blocks [85].

The rtOSL technique The rtOSL technique was discussed in Section 2.1.1 with regards to the kinetics of OSL, and is only applicable with inorganic materials that have relatively high concentrations of optically active traps. In the rtOSL technique, a pulsed optical stimulus is applied as the luminescent material is irradiated [24, 29]. The luminescence signals measured during the stimulation consist of OSL, RL and stem signals. Conversely, the luminescence signals measured without stimulation consist of only RL and stem signals assuming that the RL, OSL and stem signals are significantly faster than the temporal resolution of the photodetector. In the rtOSL technique, the difference between the signals measured with and without stimulation corresponds to pure OSL, which is free of stem signals.

Luminescent materials

With stem signals corrected, the fibre-coupled luminescent dosimeter preserves it's accuracy and desirable dosimetric properties. Many of these properties are inherited through the luminescent materials used by fibre-coupled luminescent dosimeters. Desirable properties such as water and tissue equivalence or energy independence are material dependent. Therefore, which luminescent material is used by a fibre-coupled luminescent dosimeter is often dictated by the qualities required for accurate dosimetry in the desired conditions. The following sections presents a review of the particularly advantageous luminescent materials for the dosimetry of high energy photons and electrons.

Plastic scintillators Plastic scintillators have been shown to possess many qualities and properties that make fibre-coupled plastic scintillation dosimeters (PSDs) near correctionless for use with clinical LINACs [6, 34]. Through Burlin cavity theory, many commercially available plastic scintillator materials have been calculated to be water equivalent across the therapeutic energy range for photons and electrons [75, 87], making their response proportional to the absorbed dose in water [87, 88]. It should be noted that plastic scintillators suffer from an under-response to photons with energies below 100 keV, arising from their reduced effective atomic of $Z_{\text{eff}} \approx 5.7$ when compared to water's effective atomic number of $Z_{\text{eff}} \approx 7.4$. The scintillation mechanism is isotropic, and so PSDs have angular independent scintillation responses [89, 90]. For the high energy photons and electrons produced by LINACs, a plastic scintillators response is independent of beam energy [88] and dose-rate [88]. Plastic scintillator materials can suffer response quenching [91] when track structures are dense, as is the case for proton and heavy ion beams [92]; however, scintillator quenching is of negligible effect for LINAC radiation [88]. Being entirely plastic, PSDs are water proof. Each of these qualities makes plastic scintillators well suited to relative LINAC dosimetry with LINACs [6].

Although there exists much research interest for PSDs, there are currently only two commercial PSD systems available: the Exradin W1 (Standard Imaging, USA) and Exradin W2 (Standard Imaging, USA). Most of the literature available for PSDs are results from studies with in-house systems. The Exradin W1 was studied by Beierholm *et al.*, shown to be dose-rate independent [93]. Exradin W1's Cerenkov radiation removal was shown to be accurate within 1.1 %, and the relative response was accurate within a 1.5 % relative response of measurements made by ionisation chambers [93].

Early research with PSDs evaluated their performance for dosimetry in large field photon and electron beams [88, 94, 95]. These research groups measured photon and electron beam dose distributions such as percent depth dose distributions, beam profiles and output factors, comparing them with the respective reference dosimeters for those distributions

[88, 94, 95]. In these early measurements, the PSD was shown to be accurate for relative dose measurements of absorbed to water. In more recent work, *in vivo* measurements were made with PSDs. These measurements aimed to validate treatment planning system distributions and determine uncertainty budgets in highly conformal radiation conditions [96, 97]. In these treatment planning system evaluations, the PSD was found to be within 1 % of the treatment planning system measured doses.

Dosimetry in small fields and fields with steep dose gradients requires dosimeters with small sensitive volumes or high spatial resolution [98–101]. In these conditions, other physical effects such as volume averaging, source occlusion and loss of charged particle equilibrium can increase a dosimeter's uncertainty [102–104]. A PSD's sensitive volume is defined by the volume of it's plastic scintillator, thus the plastic scintillator volumes can be manufactured to sub-millimetric volumes to give them high spatial resolutions [6, 105, 106]. Studies have shown that PSDs with small sensitive volumes mitigate these small field effects [102–104], while other small field dosimeters such as micro-ionisation chambers require corrections for these effects [103, 104].

Al_2O_3:C Al_2O_3:C possesses many desirable qualities that are inherent to plastic scintillators [34], though it is not as water equivalent as plastic scintillators. Through Burlin cavity theory, Al_2O_3:C is water equivalent for photons with energy greater than approximately 1 MeV. However, Al_2O_3:C becomes less water equivalent as photon energy decreases below 1 MeV [107, 108]. As photon energies decrease below 100 keV, Al_2O_3:C suffers from an over-response that is approximately 3.5 times greater than the response per unit absorbed dose expected at 1 MeV [107, 108]. This arises from Al_2O_3:C's increased effective atomic number of $Z_{\text{eff}} \approx 11.3$ when compared to water's effective atomic number of $Z_{\text{eff}} \approx 7.4$. This energy dependence makes Al_2O_3:C less suitable for dosimetry in radiation fields where there are high fluences of photons with energies less than 1 MeV [107, 108].

Al_2O_3:C's RL has a dose dependent sensitivity that requires correction to restore the linearity between it's response and the absorbed dose [31, 33–35]. When corrected, Al_2O_3:C's RL is proportional to the absorbed dose-rate in Al_2O_3:C and it's integral RL response is dose-rate independent [35]. Al_2O_3:C can also be optically stimulated to produce OSL, which provide secondary means for a fibre-coupled Al_2O_3:C dosimeter to determine the absorbed dose post-irradiation [24, 34]. Al_2O_3:C's OSL has been demonstrated to be dose-rate independent, with this secondary means of dose calculation advantageous for clinical dosimetry [24]. Alternatively, when Al_2O_3:C's OSL is read out using the rtOSL technique, this rtOSL signal is also dose-rate independent [24, 109]. It should be noted that rtOSL signal is non-linear with respect to absorbed dose due to complex kinetics inherent to this technique; these kinetics were described in Section 2.1.1. The luminescence

mechanism is isotropic in nature, thus fibre-coupled Al_2O_3:C dosimeters have negligible directional dependences. Although Al_2O_3:C dosimeters face additional challenges when compared against plastic scintillation dosimeters, Al_2O_3:C possesses a similar set of desirable qualities that makes them suitable for dosimetry with LINACs [34].

BeO ceramics BeO has not received as much attention as have plastic scintillators or Al_2O_3:C for fibre-coupled luminescence dosimetry. However, BeO possesses a similar set of dosimetric qualities to plastic scintillators and Al_2O_3:C. Through Burlin cavity theory, it is near-tissue equivalent for the high energy photons and electrons produced by LINACs [110]. Through it's effective atomic number of $Z_{\text{eff}} \approx 7.3$, BeO has a significantly reduced energy dependence for photons with energy between 10 keV and 20 MeV, experiencing a maximum deviation of 13 % in it's relative response across this energy range [110]. In comparison, plastic scintillators experience a maximum deviation approaching 60 % in it's relative response in this energy range, and Al_2O_3:C experiences maximum deviations approaching 250 % in it's relative response across these energies. Given this quality, BeO is well suited for dosimetry when minimal energy dependences are required such as high dose-rate brachytherapy dosimetry [111].

A fibre-coupled BeO dosimeter was characterised for use as a high dose-rate brachytherapy dosimeter, investigated for both it's RL and OSL. BeO's RL response was linear with dose, and it's RL did not appear to suffer from the non-linear deep trap sensitisation effects [7]. Additionally, BeO's real-time RL is proportional to the dose-rate, and the integral RL response is independent of the dose-rate [7]. BeO's OSL was demonstrated to be dose-rate independent, but it exhibited a supra-linear response with respect to absorbed dose that becomes significant as doses increase above approximately 10 Gy [7]. Due to the fibre-coupled BeO dosimeter's compact size, it was capable of being inserted into catheter. However, a second optical fibre was required for stem signal correction by background subtraction, thus it was concluded that the OSL was more suitable for *in vivo* dosimetry during brachytherapy treatments. Following this investigation, BeO's OSL was investigated for it's feasibility when read out using the rtOSL technique. BeO's rtOSL was characterised by the same non-linear response as Al_2O_3:C [30]. In the single investigation of BeO's rtOSL in the literature, the uncertainty in the dose-response was significantly increased when compared against the performance of Al_2O_3:C and it's rtOSL dose response [30]. From these investigations, it was concluded that the fibre-coupled BeO rtOSL dosimeter required optimisation to reduce it's uncertainties.

It should be noted that BeO is toxic when inhaled in powdered form [112]. When inhaled, the beryllium in BeO can cause Chronic Beryllium Disease, which results in hypersensitivity and severe inflammation of the tissues in the lungs. BeO in it's ceramic form does not present this health risk [113], thus BeO should be used in it's ceramic form

for fibre-coupled luminescence dosimetry.

2.2.7 Monte Carlo simulation toolkits

In the scope of radiation therapy, Monte Carlo simulations are considered the gold standard method for calculating radiation doses from radiation sources [114]. The software for these Monte Carlo simulations are toolkits, such that the user is required to define geometries in an experimental setup, as well as a radiation source where primary particles are generated, and the interactions particles can undergo. In these simulations, individual particles are stepped iteratively and tracked throughout the simulation geometry. The secondary particles generated through the interaction of primary particles are also tracked. Random number sampling is applied to determine the interactions taken at each step. Typically, a voxelised scoring mesh is defined to score the energy depositions deposited in each voxel; radiation dose is subsequently calculated by normalising the energy deposited in each voxel by the voxel's mass. Through the simulation of several primary particles, statistical analysis yields the desired dose distribution for a modelled target volume. The Geant4 simulation toolkit [115] will be used in this thesis to calculate reference dose distributions in water for the Australian MRI-LINAC.

2.3 Dosimetry with MRI-LINACs

MRI-LINAC systems combine an MRI scanner with a LINAC. The combination of these technologies presents many engineering challenges that affects the operation of the LINAC and the MRI, such that LINAC components can affect MRI scanner's functionality and the magnetic field affects the operation of the LINAC. In terms of the LINAC's operation, the MRI scanner typically has fringe fields that can permeate into the LINAC's components, imparting a Lorentz force on electrons as they are transported throughout the LINAC, resulting in reduced outputs [116]. To overcome the magnetic field's permeation into the LINAC, the affected components can be designed to account for the effect of magnetic field permeation [117], or magnetic shielding can be used [118]. In terms of MRI imaging, the LINAC's components can cause distortions in the magnetic field [119]; magnetic shielding can exacerbate this distortion. Irradiation of the MRI's coils leads to the formation of radiation induced currents in the coils, degrading image qualities [120, 121]. Several techniques and solutions have been developed to synergise and integrate the MRI and LINAC technologies [122–126].

Dosimetry for the MRI-LINAC is impacted by the presence of the MRI's magnetic field as a Lorentz force is imparted on charged particles traversing through the magnetic field. The Compton interaction is the dominant interaction for photons produced by the LINAC, thus dose distributions are altered by the magnetic field at a macroscopic level [11, 127,

128]. For dosimetry, the changes to dose distributions are dependent upon the orientation of the MRI's magnetic field with respect to it's photon beam [11]. Two orientations are used by MRI-LINAC systems, with each orientation producing their own characteristic changes in the dose distributions. These orientations are the in-line orientation where the photon beam is aligned parallel to the magnetic field [11, 124], and the perpendicular orientation where the photon beam is aligned perpendicular to the magnetic field [127, 129].

For the in-line orientation, the Lorentz force imparted on charged particles causes them to follow helical trajectories [11, 124]. As a result, electron penetration depth and lateral spreading of electrons are reduced. At the macroscopic level, this produces narrowed penumbras [130], and enhanced doses in low density media like lung [131]. Additionally, the presence of an in-line fringe field causes electrons created between the LINAC and the patient to be directed towards the isocentre. These electrons typically have low energies, created in the air volume between LINAC or patient, or are contaminant electrons from the LINAC's target. The focusing of these low energy electrons results in increased entrance doses and high dose gradients in the entrance region, with the magnitude of these effects dependent on field size and strength of the fringe field [132, 133]. This electron focusing effect is significant for the Australian MRI-LINAC, where the entrance dose for a 3 cm $\times$ 3 cm field is approximately 300 % of the dose at the classical depth of maximum dose for a 6 MV beam [133, 134].

In the perpendicular orientation, the Lorentz force imparted on secondary electrons causes secondary electrons to follow a circular-curved trajectory with an axis of gyration orthogonal to the photon beam and magnetic field directions [127]. As a result, electron penetration depth is reduced, and the resultant dose kernel experiences a lateral shift and reduced penetration depths [127, 129]. At the macroscopic level, the dose distributions are asymmetric and laterally shifted [127, 135]. Dose enhancements occur at interfaces of high and low densities [127, 129, 135], with increased doses in the high density media (referred to as the electron return effect). With the photon beam orientated perpendicular to the MRI's magnetic field, fringe fields are unable to influence the LINAC or cause the focusing of electrons as occurs for in-line orientation MRI-LINACs [126, 127].

Dosimeters used for MRI-LINAC dosimetry can be affected by an MRI's magnetic field in several ways [136]. Dosimeters with directionally dependent sensitivities can have their accuracy degraded as the charged particles follow curved trajectories through the dosimeter's sensitive volumes [137, 138]. Many dosimeters experience directional dependences due to asymmetrical geometries and packing, including ionisation chambers [137, 138], PTW microDiamond [138] and many diode detectors [139]. Dosimeters that perturb the homogeneity of water cause secondary electrons to follow a different trajectory than that

expected through water. This effect can cause non-water equivalent dosimeters to misrepresent the dose distributions that are deposited in water [137, 138], and can be problematic if not corrected for absolute dosimetry measurements with ionisation chambers [140, 141]. For perpendicular orientations, this inhomogeneity induced effect produces variations in the measured lateral shift and asymmetry of profiles, where high density dosimeters such as diodes underestimate the lateral shift and low density dosimeters such as ionisation chambers overestimate the lateral shift [135]. This inhomogeneity effect can also increase uncertainties when using water equivalent plastic phantoms such as Solid Water (Gammex RMI), as the presence of air gaps around dosimeters can lead to inaccuracies in measured doses [142, 143].

2.3.1 Ionisation chambers

The magnetic field alters the trajectories of secondary electrons, significant for the low density air cavities of ionisation chambers. Consequently, the dose-response of an ionisation chamber is influenced by the magnetic field [127]. When the MRI-LINAC concept was first conceived, it was suspected that an ionisation chamber's dosimetric characteristics could also be influenced. Early work into MRI-LINAC dosimetry investigated the dosimetric characteristics of ionisation chambers in the magnetic field [144]. The ionisation chamber retained it's linearity with respect to monitor unit output for a perpendicular 1.5 T MRI-LINAC system [144]. The ionisation chamber's sensitivity was studied for it's orientation dependence with a perpendicular MRI-LINAC. For perpendicular MRI-LINACs, the chamber's orientation dependence was concluded to be dependent on the chamber cavity's geometry; cylindrical chambers were most effective for MRI-LINAC dosimetry when orientated perpendicular to the magnetic field and photon beam [144, 145]. The orientation dependence of similar cylindrical chambers was mitigated for an in-line MRI-LINAC setup [145, 146]. Several groups demonstrated that for cylindrical geometry ionisation chambers [140, 141, 145], the correction factors for polarity and recombination were unaffected, regardless of magnetic field strength and orientation. The ionisation chamber's change in response due to the magnetic field was therefore determined to arise as a result of the curved trajectories followed by charged particles [144]. To account for this response change during absolute dosimetry, a new correction factor was proposed, being strongly magnetic field strength and orientation dependent [140, 141, 145].

Due to the ionisation chamber's low density sensitive volume, the effective point of measurement (EPOM) of an ionisation chamber is positioned upstream of the geometric centre of the cavity volume. For a Farmer chamber or cylindrical chamber with no magnetic field present, the EPOM is positioned three fifths of the chamber's radius upstream of the chamber's geometric centre [9]. However, the EPOM shifts in the presence of the

MRI's magnetic field [135, 137, 147]. For perpendicular MRI-LINACs, the EPOM shifts downstream towards the geometrical centre, as well as laterally [135, 137, 147]; for in-line MRI-LINACs, the EPOM shifts downstream towards the geometrical centre, but not laterally [145].

Measurements with ionisation chambers in Solid Water phantoms can be problematic as small air gaps surrounding the ionisation chamber cause non-negligible deviations in the absorbed dose [142, 143]. From simulation studies, an asymmetric 0.2 mm air gap surrounding the chamber caused a 1.6 % change in dose compared to the case with no air gap [142]. The severity of this effect was reduced to less than 0.5 % when the air gap was symmetric. The authors of this study concluded that this resulted from a reduction of energy depositions by electrons produced within the air gap [142].

Ionisation chambers remain an important tool for QA dosimetry with MRI-LINACs. Several groups used ionisation chambers with scanning water tanks for the commissioning of MRI-LINACs [148]. Scanning water tank measurements were also used to validate the dose calculation algorithm of an MRI-LINAC's treatment planning system [147]. With accurate magnetic field corrections, their use as absolute dosimeters are vital for the commissioning and routine QA of beam output validation [134].

2.3.2 Diodes

As with all dosimeters in magnetic fields, diodes experience response changes due to the curved trajectories followed by charged particles. In perpendicular magnetic fields, measured dose profiles and distributions are shifted laterally as a result of the curved trajectories. This lateral shift in perpendicular magnetic fields was experienced by all investigated dosimeters in a simulation study, where it's magnitude was dependent on the dosimeter's density [135]. It was found that dosimeters with near-water densities experience a shift that matches the deposited distribution in water. Due to the increased density of silicon with respect to the density of water, diodes underestimated the lateral shift that occurred in water [135].

As a consequence of the secondary electrons' curved trajectories, a diode's directional dependence can be exacerbated in the presence of magnetic fields. In perpendicular magnetic fields, unshielded diodes are reported to experience changes in response up to the order of 20 % [149]. For measurements of perpendicular MRI-LINAC beam profiles, unshielded diodes misrepresented the penumbras when their response was converted to absorb dose in water by up to 14 % [149]. For in-line magnetic fields, the change in response was limited to less than 1 % [150]. Unshielded point diodes were demonstrated to be acceptable for near surface depth dose measurements with a perpendicular MRI-

LINAC [151]. However, it has been recommended that unshielded diodes not be used for measurements of perpendicular MRI-LINAC output factors or beam profiles [137].

Shielded diodes have been observed to be less susceptible to the magnetic field induced effects than unshielded diodes as their shielding perturbs the external magnetic field. The local magnetic field across their sensitive volume is weakened, such that shielded diodes significantly misrepresent the absorbed dose distributions in water, appearing more symmetric than the dose distribution that is absorbed by water [137]. Consequently, shielded diodes are not recommended for dosimetry measurements with perpendicular orientation MRI-LINACs [137].

Diode arrays have been demonstrated accurate and effective for measurements with both in-line and perpendicular orientation MRI-LINACs. The high resolution 2D diode array, MagicPlate-512, achieved agreement within 0.5 mm of GafChromic EBT3 film in both MRI-LINAC orientations for beam profiles measured in Solid Water [152]. The MagicPlate-512 was also accurate for real-time 2D dosimetry during an MRI image sequence, verified against film [153]. The 3D diode array, ArcCheck-MR was shown to be accurate for 3D dose distribution measurements with a perpendicular MRI-LINAC [154].

2.3.3 Diamond detectors

Similar to diodes, diamond detectors experience response changes in the presence of perpendicular magnetic fields. For the natural diamond detector, PTW60003, changes in response up to 20 % were experienced [149]. Similar to the diode, the PTW60003 measured beam profiles had misrepresented the penumbral regions of expected profiles in water for a perpendicular MRI-LINAC [149]. Additionally, the PTW60003 experiences a lateral EPOM shift when in perpendicular magnetic fields [135]. Similar to the diode, the lateral shift underestimates the shift that occurs in water [135], problematic for central axis measurements.

The synthetic diamond detector, PTW60019 microDiamond, was shown to be accurate for scanning water tank measurements in small fields for perpendicular orientation MRI-LINACs by several groups [137, 147]. The microDiamond detector has been demonstrated to be accurate for depth dose measurements and output factor measurements with perpendicular MRI-LINACs [138, 147, 151]. It possesses a significant orientation dependence with perpendicular MRI-LINACs, where correction would be required for scanning measurements in large radiation fields [137]. The orientation dependence of microDiamond is minimised for in-line orientation MRI-LINACs [149]. In-line orientation output factors measured with microDiamond were in close agreement with those measured by ionisation chambers [134]. Additionally, the microDiamond detector was used to charac-

terise the high entrance doses characteristic of the in-line MRI Australian MRI-LINAC, in close agreement with radiochromic film and MOSFET dosimeters [133].

2.3.4 MOSFETs

MOSFETs have been investigated extensively for dosimetry with perpendicular MRI-LINACs. For measurements at depth in phantoms, MOSFETS possess sensitivities independent of their orientation in perpendicular magnetic fields [155]. The linearity of MOSFETs remains unaffected by external magnetic fields [155]. However, MOSFETs experienced an approximate 5 % increase of response in the presence of perpendicular magnetic fields, requiring special calibration for measurements of absorbed dose in water [156]. For measurements of surface doses, MOSFETs were unaffected by the electron return effect as their 1 μm sensitive volume was much shorter than the average gyration radius of electrons at the surface of the phantom [133, 157]. These qualities make MOSFETs attractive for *in vivo* dosimetry measurements during MRI-LINAC treatments [157].

For relative dosimetry measurements with MRI-LINACs, the magnetic field has been demonstrated to have negligible effect on the accuracy of MoSkin [133, 158]. MOSFETs have been demonstrated to be accurate for PDD measurements with MRI-LINACs [157, 158]. The response of the commercially available MOSFET dosimeters (Best Medical, Canada) were in agreement with ionisation chambers for output factor measurements [157]. The commercial MOSkin dosimeter was used for characterisation of the high entrance doses and electron contamination of the Australian MRI-LINAC [133]. MOSFET dosimeters remain desirable for relative dosimetry measurements with MRI-LINACs.

2.3.5 Radiochromic film

The radiochromic film, GafChromic EBT3 (Ashland Inc., USA), has been investigated thoroughly for it's efficacy in magnetic fields. The sensitivity of EBT3 film to absorbed dose is reduced in the presence of magnetic fields [159], however, it's relative response is unaffected by magnetic fields [129, 160]. As it retains it's desirable qualities for relative dosimetry, it has been used in the commissioning, validation and QA of several MRI-LINAC systems [134, 147, 161, 162].

2.3.6 Plastic scintillation dosimeters

Dosimeters that possess directional independence and water homogeneous volumes are desirable for dosimetry with MRI-LINACs [137, 138, 160, 163]. PSDs possess these qualities, however limited literature is available on the use PSDs with MRI-LINACs.

Therriault-Proulx *et al.* studied how a magnetic field's magnetic flux density affected the magnitude of scintillation and Cerenkov radiation responses for an in-house PSD and the Exradin W1 PSD [164]. In the study, both Exradin W1 and an in-house PSD were found to increase at most by 2.4 % (relative to their 0 T response) for the various magnetic flux densities tested, while the Cerenkov radiation signal in a bare optical fibre increased by up to 80 % relative to it's 0 T response. A similar study was performed by Stefanowicz *et al.* and a 7 % increase in scintillation signal was observed for their two in-house PSDs [165]. PSDs are relative dosimeters, such that they are inherently immune to sensitivity changes in the presence of the magnetic field. The directional dependence of the Exradin W1 PSD was investigated by Yoon *et al.* [166]. The results of their study demonstrated that Exradin W1 retained it's directional independent sensitive. Yoon *et al.* measured MRI-LINAC output factors with Exradin W1, finding that Exradin W1 suffered an under-response for large field sizes [166].

Another method successful for MRI-LINAC dosimetry is remote scintillation imaging, where volumes of plastic scintillator are simultaneously irradiated and imaged. Bruza *et al.* demonstrated high dosimetric accuracy using the time resolved scintillation imaging to measure an MRI-LINAC's IMRT C-shape treatment plan [85]. Alexander *et al.* performed 2D transmission imaging of a thin scintillator sheet to measure 2D dose distributions with their perpendicular MRI-LINAC, shown to be acceptable with respect to film [167]; the main source of uncertainty arose due to the oblique angle of the scintillator sheet with respect to the camera.

Chapter 3

Novel stem signal correction methods for PSDs

This chapter presents the investigations into temporal stem signal correction methods with an in-house PSD and a clinical LINAC. The in-house PSD uses the slow plastic scintillator, BC444 (Saint Gobain, France), allowing for novel temporal stem signal correction methods to be investigated. The time-resolved convolutional model described in Section 2.1.3 is applied in a least squares curve-fitting algorithm to identify the scintillation present in the measured PSD signals. Neural network based stem signal correction methods are also investigated. These proposed stem signal correction methods were compared against background subtraction. Some of the results from this chapter have been presented in peer reviewed journal articles:

L. Madden, J. Archer, E. Li, D. Wilkinson, A. Rosenfeld. Temporal separation of Cerenkov radiation and scintillation using artificial neural networks in Clinical LINACs. *Phys. Medica.* 2018; 54:131-136. 10.1016/j.ejmp.2018.10.007.

L. Madden, J. Archer, E. Li, D. Wilkinson, A. Rosenfeld. Temporal separation of Cerenkov radiation and scintillation using a Clinical LINAC and artificial intelligence. *Phys. Med. Biol.* 2018; 63(22):225004. 10.1088/1361-6560/aae938.

J. Archer, **L. Madden**, E. Li, D. Wilkinson, A. Rosenfeld. An algorithmic approach to single probe Cherenkov removal in pulsed X-ray beams. *Med. Phys.* 2019; 46(4):1833-1839. 10.1002/mp.13383.

3.1 Introduction

PSDs possess a wealth of desirable qualities for dosimetry with LINACs. These qualities include water equivalence for therapeutic energy photons and electrons, a linear response

with dose, and a response that is independent of conditions such as dose-rate, beam energy, temperature or pressure. Further, their plastic scintillators can be manufactured to have sub-millimetre dimensions, minimising the perturbations of water media during dosimetric measurements. However, during LINAC dosimetry, a PSD's scintillation signals are degraded by Cerenkov radiation. The light output produced by the optical fibre is dependent on the volume of optical fibre irradiated, and the Cerenkov radiation measured depends on the irradiation angle between the optical fibre and the radiation beam. Given these dependences, the magnitude of Cerenkov radiation varies significantly depending on the irradiation conditions, thus a correction method must be applied to identify the magnitude of Cerenkov radiation measured by the photodetector and remove this estimate from the measured PSD signals.

Existing correction methods for PSDs were reviewed briefly in Section 2.2.6. Existing temporal methods use pulse gating and slow plastic scintillators to temporally avoid Cerenkov radiation; these methods have not been able to achieve accuracies comparable to background subtraction and chromatic removal as a large portion of the scintillation is emitted prior to the pulse gating threshold [76, 79]. Of the existing PSD stem signal correction methods, chromatic removal is the most robust and accurate method for dosimetry with LINACs [6]. Background subtraction achieves comparable accuracies to chromatic removal in radiation fields with low spatial dose gradients. However, when background subtraction is applied in radiation fields with high spatial dose gradients, the PSD's uncertainties are inflated [6]. As such, novel temporal stem signal correction methods are investigated with the aim of achieving accuracies superior to background subtraction and chromatic removal, whilst avoiding the increases in dose-uncertainty when being applied in high dose gradient fields.

In Section 2.1.3, it was posited that the luminescence signals measured during radiation dosimetry could be modelled by the convolution of the time-dependent dose-rate and a luminescence impulse response function (LIRF). In this chapter, this luminescence model is incorporated into novel temporal Cerenkov radiation correction methods. Two subsets of temporal methods are investigated, with one subset using least squares curve-fitting, and the other using neural networks. The proposed correction methods are compared against background subtraction in favourable conditions *i.e.* radiation fields with low spatial dose gradients. Corrected PSD responses are compared with reference data to quantify the accuracy of the proposed correction methods.

3.2 Materials and methods

Beam profiles were measured using a Varian Clinac 21iX LINAC (Varian, USA) at Illawarra Cancer Care Centre, Wollongong Hospital. Measurements were made using the LINAC's

photon beam at energies of 6 MV and 10 MV, and for field sizes of 3 cm × 3 cm, 5 cm × 5 cm and 10 cm × 10 cm. For all measurements, the repetition rate was fixed at 600 MU/min. All fields were jaw-defined, measured with an in-house PSD and a compact ionisation chamber (CC13, Scanditronix/Wellhofer, Germany). For the 3 cm × 3 cm and 5 cm × 5 cm field sizes, beam profiles were measured along the cross-plane axis. For the 10 cm × 10 cm field size, beam profiles were measured along the cross-plane and in-plane axes. Gammex RMI-457 Solid Water was used as the phantom material for measurements with the in-house PSD. Two linear translation stages (LTS150, Thorlabs Inc., USA) were used to control the off-axis position of the PSD along the in-plane and cross-plane axes. A scanning water tank (Blue Phantom 2, IBA Dosimetry, Germany) was used as the water phantom for measurements with the ionisation chamber, with the chamber orientated so that it's central axis was parallel to the in-plane axis. The PSD and cylindrical chamber were set up so that their effective point of measurements were aligned to depths of 1.5 cm for the 6 MV beam and 2.1 cm for the 10 MV beam.

3.2.1 The PSD dosimetry system

The in-house PSD consisted of a cylindrical volume of BC444 plastic scintillator (Saint Gobain, France) optically coupled to a plastic optical fibre (Eska CK-40, Mitsubishi Chemical Co., Japan). The plastic scintillator had a length of 0.5 mm and a diameter of 2 mm. The optical fibre had an approximate length of 20 m, an inner core diameter of (0.98 ± 0.06) mm, a cladding diameter of (1.00 ± 0.06) mm and a jacket diameter of 2.0 mm. The reference probe consisted of a bare Eska CK-40 plastic optical fibre with matching dimensions and materials to the PSD's optical fibre, with no scintillator attached so that only Cerenkov radiation could be measured. The tip of the PSD (*i.e.* the scintillator and adjacent fibre) and the tip of the reference probe were coated with a diffusive reflective paint (BC620, Saint Gobain, France) to make the probes light tight and increase the scintillation collection efficiency of the PSD. At the opposite end of the PSD and reference probe, the optical fibres were fitted with male FC optical connectors for reproducible connection to the photodetectors.

The PSD and reference probe were read out by two matching photomultiplier tubes (PMTs; RCA-4526, RCA Corporation, USA). These PMTs had a rise time of 2.5 ns, adequate to temporally resolve BC444's scintillation. For all measurements, the PMTs were operated in DC mode at their maximum gain. A digital oscilloscope (PicoScope PS6404D, PicoTech, USA) was used to simultaneously record both the PSD and reference probe signals as voltage-time waveforms. The digital oscilloscope's resistance was set to 1 MΩ, and it's bandwidth to 500 MHz. For all measurements, the digital oscilloscope sampled the PMT outputs at 625 MHz with each waveform consisting of 10000 samples. The LINAC's synchronisation pulse was used to trigger the digital oscilloscope, allowing

for reproducible temporal measurements of the PSD and reference probe signals. Signal averaging was used to reduce the magnitude of measurement noise in measured signals, such that recorded waveforms consisted of the average response from 100 consecutive LINAC pulses. The averaged PSD and reference probe signals were saved to a personal laptop; all stem signal corrections were applied post-measurement.

For measurements in Solid Water, a perspex housing aperture was used to protect the PSD and reference probe from mechanical damage. The housing aperture consisted of a 1 cm thick sheet of PMMA with 30 cm $\times$ 30 cm cross section, machined with a 2.2 mm wide $\times$ 4.4 mm deep groove. Prior to placing the PSD and reference probe in the housing aperture's groove, the housing groove was filled with ultrasound gel (Aquasonic 100, Parker Laboratories Inc., USA) to prevent the formation of air gaps around the PSD during measurements. The PSD and reference probe were then placed in the housing groove with the reference probe downstream from the PSD, aligned so that equal lengths of optical material were irradiated during the measurements. The perspex housing was then sandwiched between 10 cm of Solid Water downstream of the housing, and the 1.4 cm and 2.0 cm thickness of Solid Water upstream of the housing to achieve the required measurement depth. This Solid Water-perspex sandwich was placed on the linear translation stage for the measurement of beam profiles. For the 3 cm $\times$ 3 cm and 5 cm $\times$ 5 cm field sizes, profiles were measured along the cross-plane axis with the PSD orientated so that it's optical fibre was aligned parallel to the cross-plane axis. For the 10 cm $\times$ 10 cm field size, both cross-plane and in-plane profiles were measured, with the PSD aligned so that the optical fibre was aligned parallel to the cross-plane axis. The PSD beam profiles were measured using a step and measure methodology, such that the PSD was moved 1 mm and the PSD's response at this position was recorded.

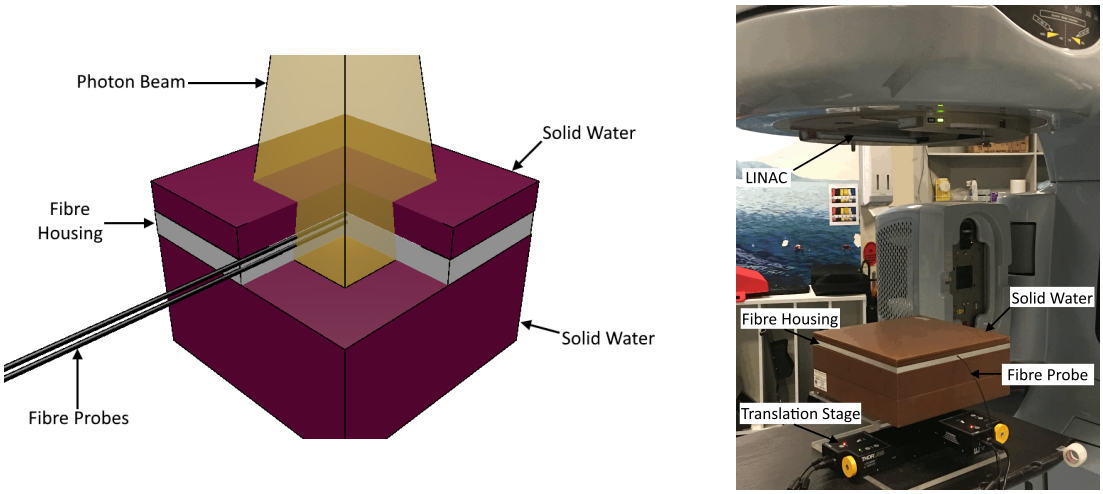

Figure 3.1: Left: 3D model of the PSD in the Solid Water phantom. Right: corresponding picture of the experimental setup. Published in Madden *et al.* 2018 [168]

3.2.2 Background subtraction

The PSD and reference probe were set up in the optical fibre housing so they were abreast and aligned with their central axis parallel to one another. The PMTs were cross calibrated prior to each beam profile scan to ensure that the Cerenkov radiation measured with one PMT matched that measured by the other. The cross calibration measurements were performed by measuring the PSD and reference probe responses at the centre of each profile's radiation field, disconnecting them from their PMTs, connecting them to each-other's prior PMTs and remeasuring their responses. From these measurements, the cross calibration factor, Cal, was calculated as:

$$Cal = \sqrt{\frac{S_1}{S_2} \cdot \frac{C_1}{C_2}} \tag{3.1}$$

Where S_1 and C_1 were the PSD and reference probe signals measured with the PSD's PMT, and S_2 and C_2 were the PSD and reference probe signals measured with the reference probe's PMT. The Cerenkov radiation of the PSD was then corrected by multiplying the reference probe signal by the calibration factor and subtracting this from the PSD measured signal. The dose deposited in the scintillator was calculated by integrating this corrected PSD signal.

3.2.3 Least squares corrections

Measured PSD signals are comprised solely of scintillation and Cerenkov radiation. Thus, measured PSD signals can be modelled as a linear combination of a scintillation signal, $S(t)$, and a Cerenkov radiation signal, $C(t)$. The corresponding least squares model given this information is given by:

$$\hat{y}(t) = aS(t) + bC(t) + c \quad \text{s.t.} \quad a, b \geq 0 \tag{3.2}$$

Where $\hat{y}(t)$ is the modelled PSD signal[a], a and b are scaling coefficients for the modelled scintillation and Cerenkov radiation, respectively, and c is a bias coefficient related to the PMT's voltage offset. From the review of time-resolved fluorescence literature in Section 2.1.3, the expected scintillation can be modelled as the convolution of a time-dependent stimulus with an impulse response function. For the time-resolved scintillation measurements presented in this chapter, the time-dependent stimulus corresponds to the LINAC's time-dependent dose-rate of the photon beam, $\dot{\mathrm{D}}(t)$. Organic scintillators such as the BC444 plastic scintillator follow a mono-exponential rise and decay in response to a single radiation event [15]; this mono-exponential rise and decay corresponds to BC444's

[a]The notation where $\hat{}$ is used above a variable, *e.g.* $\hat{y}(t)$, denotes that this is an estimator or a model of the corresponding variable, *e.g.* $y(t)$. In this case, $\hat{y}(t)$ is the modelled rtOSL signal and $y(t)$ is the measured rtOSL signal.

impulse response function for scintillation. Given this, BC444's scintillation impulse response function, $h(t)$, can be defined as in Equation 3.3. The expected scintillation, $S(t)$, produced in response to a time-dependent dose-rate, $\dot{\mathrm{D}}(t)$ can be modelled as:

$$S(t) = \dot{\mathrm{D}}(t) * h(t) \quad \text{s.t.} \quad h(t) = e^{\left(-\frac{t}{\tau_d}\right)} - e^{\left(-\frac{t}{\tau_r}\right)} \tag{3.3}$$

Where τ_d is BC444's exponential decay constant, τ_r is it's exponential rise constant and $*$ is the linear convolution operation. Conveniently, Cerenkov radiation has a sub-nanosecond exponential decay constant [169], and so measured Cerenkov radiation signals are proportional to the LINAC's time-dependent dose-rate during beam delivery[b]. The time-dependent Cerenkov radiation, $C(t)$, is measured by the reference probe, and can be measured simultaneously with the PSD signal as in the background subtraction method. It should be noted that the time-dependence of the measured Cerenkov radiation will not depend on the position of the optical fibres given that this time-dependence is proportional only to the instantaneous dose-rate of the LINAC. Given that there is no dependence on where the reference probe is positioned, these least squares corrections avoid the high spatial dose gradient constraint inherent to background subtraction. Substituting $C(t)$ for $\dot{\mathrm{D}}(t)$, the least squares problem is stated as:

$$\text{minimise} \left(||\hat{y}(t) - y(t)||^2 \right) \quad \text{s.t.} \quad \hat{y}(t) = a\big(C(t) * h(t)\big) + bC(t) + c \tag{3.4}$$

Where $y(t)$ is the measured PSD signal. It should be noted that the non-negativity constraints for a and b are omitted from the least squares problem to increase computation speed. The coefficients a, b and c can be determined through ordinary least squares (OLS), provided τ_d's and τ_r's nominal values are known and treated as constants. Saint Gobain lists BC444's exponential decay constant as $\tau_d = 285\,\text{ns}$, and BC444's exponential rise constant as $\tau_r = 19.5\,\text{ns}$. Alternatively, τ_d and τ_r can be optimised during the fitting process via non-linear least squares (NLLS), with the potential for reduced uncertainties in the fitted model of the PSD signal. Both the OLS and NLLS approaches are investigated in this chapter.

OLS correction

Though the OLS scheme allows for a fast analytical calculation of the coefficients a, b and c, noisy regression variables can cause these coefficients to be incorrectly estimated via the analytical OLS solution [170]. For the measurements presented in this chapter, measured Cerenkov radiation signals, $C(t)$, have significant measurement noise, thus the analytical solution for the coefficients a, b and c are not taken as the optimal solution. Instead, gradient descent is applied to iteratively optimise these coefficients using the

[b]This result is true if and only if Cerenkov radiation's decay constant is much shorter the PMT's rise constant; the RCA-4526 PMTs have a 2.5 ns rise constant.

sum of the squared errors as the cost function. Initial estimates for the coefficients a_0, b_0 and c_0 were calculated using this OLS analytical solution. Defining $\beta = [a_0\ b_0\ c_0]^T$, the OLS analytical solution is given by:

$$\beta = \left(X^T X\right)^{-1} X^T \tilde{y} \quad \text{s.t.} \quad X = [\tilde{S}\ \tilde{C}\ \tilde{1}] \tag{3.5}$$

Where $\tilde{S}$ is the expected scintillation $S(t)$ in column vector form[c], $\tilde{C}$ is the measured Cerenkov radiation $C(t)$ in column vector form, $\tilde{1}$ is column vector of 1s with equivalent length to $\tilde{S}$ and $\tilde{C}$, and $\tilde{y}$ is the measured PSD signal in column vector form. At the i^{th} iteration, the sum of the squared errors, SSE_i, was calculated as:

$$\text{SSE}_i = \sum_t \left(\hat{y}_i(t) - y(t)\right)^2 \tag{3.6}$$

Where $\hat{y}_i(t)$ was the modelled PSD signal at the i^{th} iteration, calculated as in Equation 3.4 using the i^{th} estimates of the coefficients a, b and c. The derivatives of the SSE with respect to the coefficients are calculated at each iteration, defined at the i^{th} iteration as:

$$\begin{aligned}
\frac{d\text{SSE}_i}{da_i} &= 2\sum_t S(t) \cdot \left(\hat{y}_i(t) - y(t)\right) \\
\frac{d\text{SSE}_i}{db_i} &= 2\sum_t C(t) \cdot \left(\hat{y}_i(t) - y(t)\right) \\
\frac{d\text{SSE}_i}{dc_i} &= 2\sum_t \left(\hat{y}_i(t) - y(t)\right)
\end{aligned} \tag{3.7}$$

Where $\cdot$ denotes element-wise multiplication (also referred to as the Hadamard product). At the i^{th} iteration, the coefficients were updated:

$$\begin{aligned}
a_{i+1} &= a_i - \eta \frac{d\text{SSE}_i}{da_i} \\
b_{i+1} &= b_i - \eta \frac{d\text{SSE}_i}{db_i} \\
c_{i+1} &= c_i - \eta \frac{d\text{SSE}_i}{dc_i}
\end{aligned} \tag{3.8}$$

Where η was the step length for gradient descent, set initially as 0.01. A backtracking line search was used to evaluate whether proposed step lengths were too large, employed to improve computational efficiency. It should be noted that the line search does not affect the optimal values of a, b and c determined through gradient descent. The stopping condition for gradient descent was chosen as: "if $\text{SSE}_i \geq 0.9999\ \text{SSE}_{i-1}$, stop". Defining the

[c]The notation where ˜is used above a variable, *e.g.* $\tilde{S}$ denotes that the corresponding variable, *e.g.* $S(t)$ is in vector form: $\tilde{S} \triangleq [S(0)\ S(1)\ \ldots\ S(N-1)]^T$.

optimised coefficients as $\hat{a}$, $\hat{b}$ and $\hat{c}$, the corrected PSD signal is calculated simply as $\hat{a}S(t)$. From a temporal perspective, background subtraction would calculated the corrected PSD signal as $y(t) - \hat{b}C(t) - \hat{c}$. Given both expressions, the PSD's corrected dose-response, R can be calculated as:

$$R = \frac{1}{2}\int \left(\hat{a}S(t) + y(t) - \hat{b}C(t) - \hat{c}\right)dt \tag{3.9}$$

Full MATLAB code of the OLS gradient descent algorithm is presented in Appendix A.1. For brevity, pseudocode of the OLS gradient descent algorithm is presented below[d]:

$h(t) \leftarrow e^{\left(-\frac{t}{\tau_d}\right)} - e^{\left(-\frac{t}{\tau_r}\right)}$
$S(t) \leftarrow C(t) * h(t)$
Calculate a_0, b_0, c_0
while true **do**
    $\hat{y}_i \leftarrow a_i\tilde{S} + b_i\tilde{C} + c_i$
    $\text{SSE}_i \leftarrow \sum \left(\hat{y}_i - y\right)^2$
    if $\text{SSE}_i \geq 0.9999\ \text{SSE}_{i-1}$ **then**
        Stop iterating
    end if
    Calculate $\frac{d\text{SSE}_i}{da_i}$, $\frac{d\text{SSE}_i}{db_i}$, $\frac{d\text{SSE}_i}{dc_i}$
    Update a_{i+1}, b_{i+1}, c_{i+1}
end while
Calculate R

NLLS correction

In the NLLS method, the exponential coefficients τ_d and τ_r are optimised simultaneously with the coefficients a, b and c. As for the OLS model, gradient descent was used to optimise the fitting coefficients with respect to the SSE (defined previously in Equation 3.6). It should be noted that the NLLS gradient descent algorithm follows the same flow in logic as in the OLS algorithm.

Initial estimates for the exponential coefficients were $\tau_{d_0} = 285\,\text{ns}$, $\tau_{r_0} = 19.5\,\text{ns}$; the initial estimates a_0, b_0 and c_0 were calculated using the OLS analytical solution in Equation 3.5 with values τ_{d_0} and τ_{r_0} substituted to calculate the expected scintillation, $S(t)$, in Equation 3.3. At the i^{th} iteration, the modelled PSD signal, $\hat{y}_i(t)$, was calculated as in Equation 3.4, substituting a_i, b_i, c_i, τ_{d_i} and τ_{r_i} for a, b, c, τ_d and τ_r. Following this, the i^{th} iteration's SSE was calculated as in Equation 3.6. Derivatives of the SSE with respect to a_i, b_i, c_i, τ_{d_i} and τ_{r_i} were calculated for each iteration; the derivatives $\frac{d\text{SSE}_i}{da_i}$, $\frac{d\text{SSE}_i}{db_i}$ and

[d]The notation $x \leftarrow 1$ means set the value of x to 1.

$\frac{d\text{SSE}_i}{dc_i}$ match those calculated for the OLS model, defined in Equation 3.7. The derivatives $\frac{d\text{SSE}_i}{d\tau_{d_i}}$ and $\frac{d\text{SSE}_i}{d\tau_{r_i}}$ are defined below in Equation 3.10:

$$\begin{aligned}\frac{d\text{SSE}}{d\tau_{d_i}} &= 2\sum_t \left(\left(C(t) * \frac{t \cdot e^{\frac{-t}{\tau_{d_i}}}}{{\tau_{d_i}}^2} \right) \cdot \left(\hat{y}_i(t) - y(t) \right) \right) \\ \frac{d\text{SSE}}{d\tau_{r_i}} &= -2\sum_t \left(\left(C(t) * \frac{t \cdot e^{\frac{-t}{\tau_{r_i}}}}{{\tau_{r_i}}^2} \right) \cdot \left(\hat{y}_i(t) - y(t) \right) \right)\end{aligned} \tag{3.10}$$

Where $\hat{y}_i(t)$ was the modelled PSD signal at the i^{th} iteration. At the i^{th} iteration, τ_{d_i} and τ_{r_i} were updated as in Equation 3.11, and the coefficients a_i, b_i and c_i were updated as in Equation 3.8.

$$\begin{aligned}\tau_{d_{i+1}} &= \tau_{d_i} - \eta \cdot \frac{d\text{SSE}_i}{d\tau_{d_i}} \\ \tau_{r_{i+1}} &= \tau_{r_i} - \eta \cdot \frac{d\text{SSE}_i}{d\tau_{r_i}}\end{aligned} \tag{3.11}$$

Where η was the step length for gradient descent, set to 0.01 initially. As for the OLS optimisation algorithm, a backtracking line search was used to optimise the step length prior to coefficient updates. The stopping criteria for the NLLS algorithm was: "stop if $\text{SSE}_i \geq 0.9999\ \text{SSE}_{i-1}$", matching that for the OLS algorithm. The corrected dose-response, R, was calculated the same as in the OLS algorithm, with R defined in Equation 3.9. Pseudocode for the NLLS algorithm is presented below; the full MATLAB implementation is presented in Appendix A.2.

$h(t) \leftarrow e^{\left(-\frac{t}{\tau_{d_0}}\right)} - e^{\left(-\frac{t}{\tau_{r_0}}\right)}$
$S(t) \leftarrow C(t) * h(t)$
Calculate a_0, b_0, c_0
while true **do**
    $h(t) \leftarrow e^{\left(-\frac{t}{\tau_{d_i}}\right)} - e^{\left(-\frac{t}{\tau_{r_i}}\right)}$
    $S(t) \leftarrow C(t) * h(t)$
    $\hat{y}_i \leftarrow a_i\tilde{S} + b_i\tilde{C} + c_i$
    $\text{SSE}_i \leftarrow \sum \left(\hat{y}_i - y\right)^2$
    if $\text{SSE}_i \geq 0.9999\ \text{SSE}_{i-1}$ **then**
        Stop iterating
    end if
    Calculate $\frac{d\text{SSE}_i}{da_i}$, $\frac{d\text{SSE}_i}{db_i}$, $\frac{d\text{SSE}_i}{dc_i}$, $\frac{d\text{SSE}}{d\tau_{d_i}}$, $\frac{d\text{SSE}}{d\tau_{r_i}}$
    Update a_{i+1}, b_{i+1}, c_{i+1}, $\tau_{d_{i+1}}$, $\tau_{r_{i+1}}$
end while

15: Calculate R

3.2.4 Neural network corrections

Neural networks are machine learning algorithms that employ computational models inspired by the brain to mimic the brain's learning capabilities. Of the various types of neural networks, feed forward neural networks are particularly attractive due to their structured nature. In general, feed forward neural networks are universal function approximators [171, 172], capable of being trained to model complicated, abstract and non-linear relationships between input and output data. Given this ability, neural networks were trained to receive a time-dependent PSD signal as an input and predict the time-dependent Cerenkov radiation present in the input PSD signal. To train neural networks to perform such analysis, measurements of both the PSD and reference probe signals are required. However, once the neural networks are trained, no reference probe measurements are required, making these corrections free of the high spatial dose gradient constraints of background subtraction. Two types of feed forward neural network were investigated for this correction: shallow Artificial Neural Networks (ANNs) and deep Convolutional Neural Networks (CNNs). Shallow ANNs were investigated for the proof of concept, whereas deep CNNs were investigated to improve the accuracy of neural network corrections. The architectures, training methods and Cerenkov radiation corrections for each type of neural network are described below.

Shallow ANNs

Architecture The shallow ANNs were multilayer perceptrons consisting of a 1000 node input layer, a single hidden layer with 100 nodes and a 1000 node output layer. Batch normalisation was used to mitigate backpropagated gradients from vanishing or exploding [173]. The activation functions for these ANNs were leaky rectified linear units (leaky ReLU) with activation coefficient of 0.01, also chosen to mitigate the vanishing gradients that can be encountered when using sigmoid activation functions [174]. A diagram of the ANN architecture is shown in Figure 3.2.

Data preprocessing Data preprocessing was applied to transform the measured waveforms into a reproducible format, important for optimising the trained ANN's performance [176]. The amplitude of measured signals were dependent on the PMT's gains, therefore measured signals were dependent on the ambient temperature. Transmission through the optical fibre is affected by bends in the optical fibre, thus the amplitude of measured signals also varied with the experimental setup. Min-max normalisation was applied to the measured PSD signals to ensure that inputs to the ANN were expressed over a fixed dynamic range, making analysis robust with respect to variations in signal

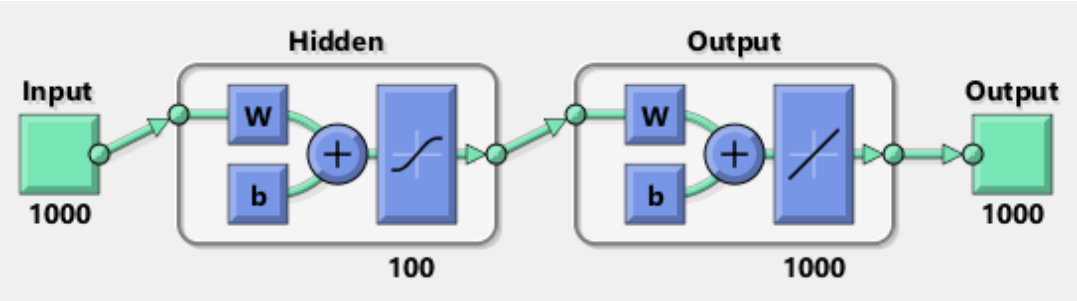

Figure 3.2: Structure of the artificial neural networks developed and trained for temporal Cerenkov radiation separation. Published in Madden *et al.* 2018 [175].

amplitude. The min-max transform is defined in Equation 3.12 [177]. By definition, min-max normalisation expresses the measured signals over the interval [0,1].

$$I_{\text{norm}}(t) = \frac{I(t) - \min(I(t))}{\max(I(t)) - \min(I(t))} \tag{3.12}$$

With $I(t)$ being the measured PSD signal and $I_{\text{norm}}(t)$ being the normalised PSD signal to be input to the ANN. Additional preprocessing was applied to shorten the normalised waveforms from lengths of 10000 samples to lengths of 1000 samples. It was expected that the trained ANNs would perform optimally when input signals were comprised maximally of scintillation, with minimal Cerenkov radiation and measurement noise. Given this belief, the scintillation decay tail was targeted for analysis with the shallow ANNs. To reproducibly shorten the measured signals, the decay tail was found by fitting a square pulse to the measured Cerenkov radiation signal, $C(t)$. The least squares fitting model was given by $\hat{C}(t)$ in Equation 3.13:

$$\hat{C}(t) = \alpha\left[\theta(t - T_1) - \theta(t - T_1 - T_{Pulse})\right] + \beta \tag{3.13}$$

Where $\theta(t)$ was the unit step function. In this model, the parameter T_1 corresponds to the time when the radiation beam delivery begins, T_{Pulse} is the duration of the radiation pulse, and α and β were the fitting coefficients. Gradient descent was applied to optimise the parameters T_1, T_{Pulse}, α and β to minimise the SSE between $\hat{C}(t)$ and $C(t)$. Once optimised, the normalised PSD signal was shortened by sampling at times $(\hat{T}_1 + \hat{T}_{Pulse})$ ns $\leq t < (\hat{T}_1 + \hat{T}_{Pulse} + 1600)$ ns, such that 1600 ns corresponds to 1000 samples. The measured waveforms are shown in Figure 3.3 (left), with the preprocessed waveforms shown in Figure 3.3 (right).

Training data synthesis The time-dependence of measured Cerenkov radiation and scintillation signals varies with beam energy, observable in Figure 3.3. To compensate for this variation, two ANNs were trained for the Cerenkov radiation correction: one ANN was trained to analyse signals measured at the 6 MV beam energy, and the other

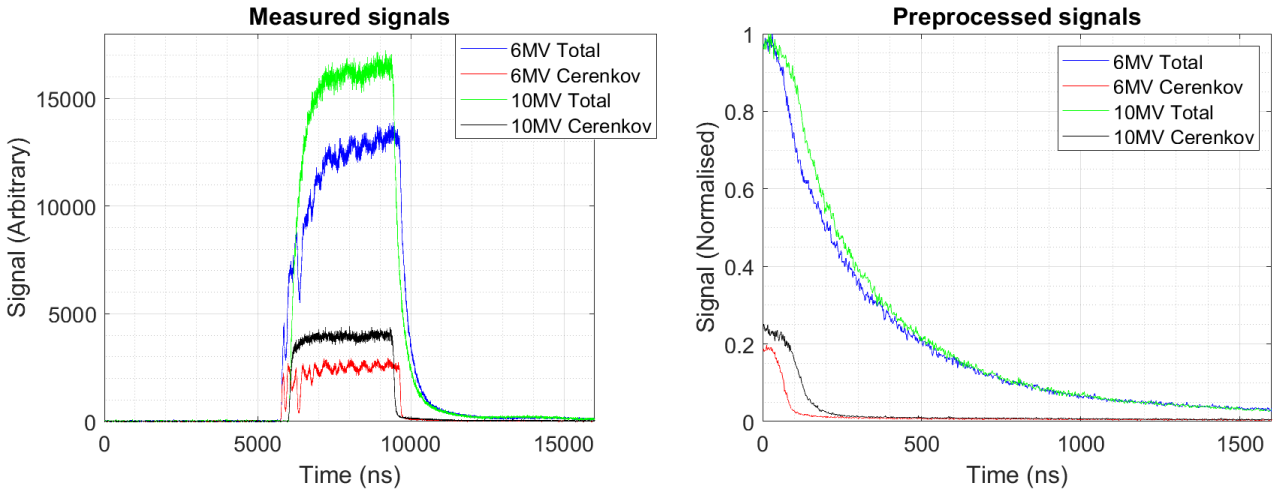

Figure 3.3: Left: measured PSD and reference probe signals for the 6 MV and 10 MV beam energies. Right: preprocessed PSD and reference probe signals for the 6 MV and 10 MV beam energies. 6 MV Total and 10 MV Total are the combined scintillation and Cerenkov radiation signals for the 6 MV and 10 MV beam energies, respectively. 6 MV Cerenkov and 10 MV Cerenkov are the sole Cerenkov radiation signals at the 6 MV and 10 MV beam energies, respectively. The responses shown were measured with the scintillator tip positioned at the centre of a 10 cm $\times$ 10 cm field. Published in Madden *et al.* 2018 [175].

was trained for analysis at the 10 MV beam energy. Both ANNs were trained in MATLAB 2018a using the Deep Learning Toolbox. Mixed scintillation and Cerenkov radiation signals were the input data, and corresponding Cerenkov radiation signals were the target data for training.

Typically in machine learning problems, impractically large quantities of training data are required to train these algorithms to high accuracies. For the ANNs developed, it was expected that a minimum of tens of thousands of input-output pairs would be required to train the shallow ANN to sufficient accuracy; too large to be measured. To achieve such a large training data size, the training data was generated synthetically from a secondary set of measured data, different from those used to test the ANN. The secondary dataset was measured using the same setup as described in Section 3.2.1. This secondary dataset was acquired by scanning the LINAC's photon beam in 2 dimensions, similar to the methodology described in Archer *et al.* 2020 [178]. The measured data set consisted of a 2D scan of a 1 cm $\times$ 1 cm field and a 2D scan of a 3 cm $\times$ 3 cm field. The secondary dataset consisted of a total of 1117 measured PSD and reference probe signals. The algorithm for developing training data for the shallow ANNs was as follows:

1. Perform background subtraction to determine the sole scintillation response for a corresponding Cerenkov radiation response.

2. For each sole scintillation and Cerenkov radiation response, record the minimum and maximum signal levels, as well as the amplitude (defined as the difference

between the maximum and minimum signal levels of a sole response). Determine the global minimum and maximum signal levels for the set of sole scintillation responses; repeat for the set of Cerenkov radiation responses. Record the maximum and minimum amplitudes of scintillation and Cerenkov radiation signals.

3. Apply min-max normalisation to each sole scintillation response using the global minimum and maximum signal levels of scintillation. Repeat for each Cerenkov radiation response using the global minimum and maximum signal levels of Cerenkov radiation. These normalised responses serve as models for the expected Cerenkov radiation and scintillation responses.

4. Scintillation and Cerenkov radiation dose-response profiles are modelled with the hypothetical PSD orientated parallel to the scanning axis. An empirical model is used to approximate the scintillation dose-response profile, as in Equation 3.14. The Cerenkov radiation response profile is the theoretical response of the optical fibre to the photon beam whose profile is equivalent to the scintillator response profile, as in Equation 3.15:

$$S(x,FS) = \frac{S_{min}}{S_{min}+S_{max}} + \frac{S_{max}}{S_{min}+S_{max}} \cdot \frac{1}{1+exp(-4\sqrt{2}\cdot|x+0.5FS|)} \tag{3.14}$$

$$C(x,FS) = \frac{C_{min}}{C_{min}+C_{max}} + \frac{C_{max}}{C_{min}+C_{max}} \cdot \int_{-\infty}^{x} \frac{S(x',FS)dx'}{FS_{rel}} \tag{3.15}$$

$S(x,FS)$ and $C(x,FS)$ are the relative dose-responses of scintillation and Cerenkov radiation as a function of PSD position, x, and the width of the modelled photon beam, FS. S_{min} and S_{max} are the minimum and maximum scintillation signal amplitudes, while C_{min} and C_{max} are the minimum and maximum Cerenkov radiation signal amplitudes. FS_{rel} is the maximum width of experimentally measured beam profiles, compensating for the linear relationship between the length of optical fibre irradiated and the magnitude of measured Cerenkov radiation responses [73]. The constant $4\sqrt{2}$ in Equation 3.14 was empirically chosen so that the synthetic dose profiles had a penumbra width of 5 mm. The modelled dose profiles for the 6 MV, 5 cm $\times$ 5 cm and 10 cm $\times$ 10 cm field sizes are plotted against the measured 6 MV, 5 cm $\times$ 5 cm and 10 cm $\times$ 10 cm dose profiles in Figure 3.4.

5. Dose profiles are modelled for FS = (1, 1.2, 1.4, ..., 14.6, 14.8, 15) cm. The modelled profiles are sampled for their relative dose across the positions x = (-1.5FS, -1.48FS, -1.46FS, ..., 1.46FS, 1.48FS, 1.5FS).

6. A random pair of normalised sole scintillation and Cerenkov radiation responses (as

in step 3) are chosen for each combination of position and modelled photon beam width. The random pair of sole responses are scaled by their respective relative doses (as in step 4) and their respective maximum signal amplitude (as in step 2). These resultant scaled responses are the sole scintillation and Cerenkov radiation responses that are expected to be produced experimentally.

7. A training input waveform is synthesised by adding the sole synthetic scintillation response, the sole synthetic Cerenkov radiation response and Gaussian noise. A training Cerenkov radiation waveform is synthesised by adding zero mean Gaussian noise to the sole synthetic Cerenkov radiation response. The training set is developed by synthesising training waveforms across the 10721 combinations of FS and x.

The model for the scintillator dose profile in Equation 3.14 was an empirical model that uses the sigmoid distribution to approximate the shape of experimentally measured relative dose profiles. The modelled relative Cerenkov radiation dose profile, $C(x,FS)$ in Equation 3.15 is the theoretical integral response of the irradiated fibre to the modelled photon beam with dose profile, $S(x,FS)$. The modelled relative dose profiles and experimentally measured dose profiles are plotted in Figure 3.4 for comparison with the modelled profiles.

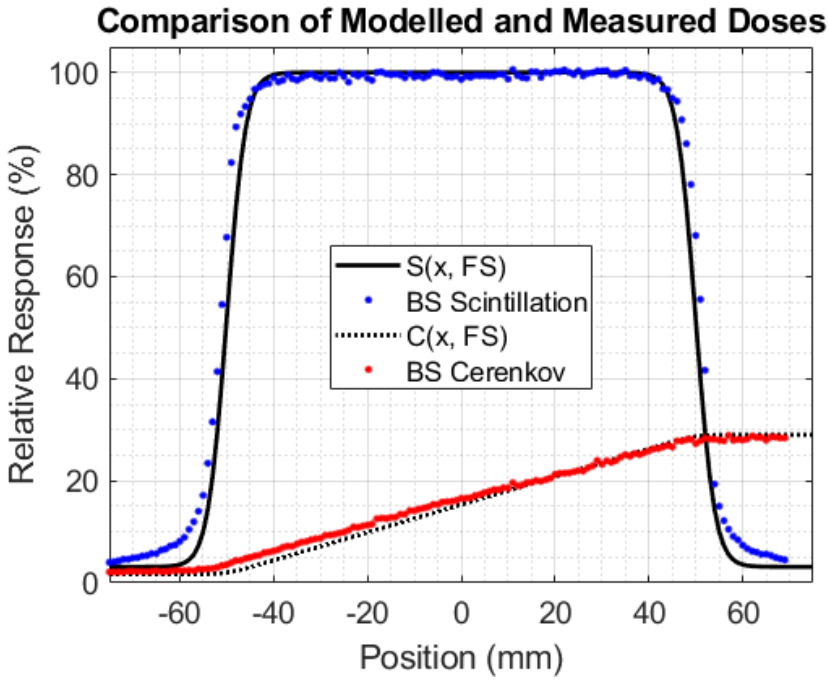

Figure 3.4: S(x, FS) and C(x, FS) are the modelled scintillation and Cerenkov radiation responses for a 10 cm × 10 cm modelled beam using Equations 1 and 2, respectively, while BS Scintillation and BS Cerenkov are the corresponding experimentally measured scintillator and Cerenkov radiation dose profiles at an energy of 10 MV. Published in Madden *et al.* 2018 [175]

Training conditions The shallow ANNs were modelled in MATLAB 2018a using the Deep Learning Toolbox. The shallow ANNs were trained using stochastic gradient descent with a minibatch size of 100. The initial learning rate was set to 0.005. The learning rate was decreased by a factor of 0.9 every epoch (108 iterations). $L2$ weight decay was applied with a weight decay factor of 0.001. Weights were initialised randomly using Glorot initialisation for the fully connected layers [179]. The synthetically produced data was used as the training dataset, and the secondary set of measured data that generated the synthetic dataset was used as the validation set during training. The mean squared error was used as the loss function during training.

Early stopping was used to terminate training before the ANNs had overfitted to the synthetic training data. The ANNs were evaluated on the validation dataset every 25 iterations. The mean squared error for the validation set was recorded every evaluation. Similarly, the values of the ANN's weights were recorded for every evaluation on the validation dataset. Training of the ANNs was terminated after 20 consecutive failures on the validation set, *i.e.* when the validation set error did not decrease below a minimum validation set error for 20 consecutive validation evaluations. Once training was terminated, the ANN's optimal weights were chosen to be those that achieved the lowest validation set error.

Cerenkov radiation correction The ANN correction used the optimal values for the weights founding during training. The preprocessed PSD signals from the testing set were input to the ANN. The ANN's output corresponded to the predicted Cerenkov radiation present in the input PSD signals. Cerenkov radiation was corrected by subtracting the ANN's output from the input PSD signal and multiplying by the value C_{max} obtained during preprocessing. This ANN corrected signal was integrated to obtain the ANN corrected PSD response.

Convolutional Neural Networks

Architecture The architecture of the deep CNNs was modelled around that of AlexNet [180] and VGGNet [181], both of which achieved their state of the art accuracy with a simple, deep structure. In this work, the CNN's structures were optimised for their performance by varying the types of layers used, the order of the layers, layer size and network depth. The optimal structure found is presented in Figure 3.5, modelled in MATLAB 2018a using the Deep Learning toolbox.

The CNN's input size was 3500×1. The CNN's first layer was an average pooling layer with a span of 21 and a stride of 1, smoothing input signals to improve the robustness of the CNN with respect to noise. From the 2^{nd} to 21^{st} layers, 5 stacks of convolutional

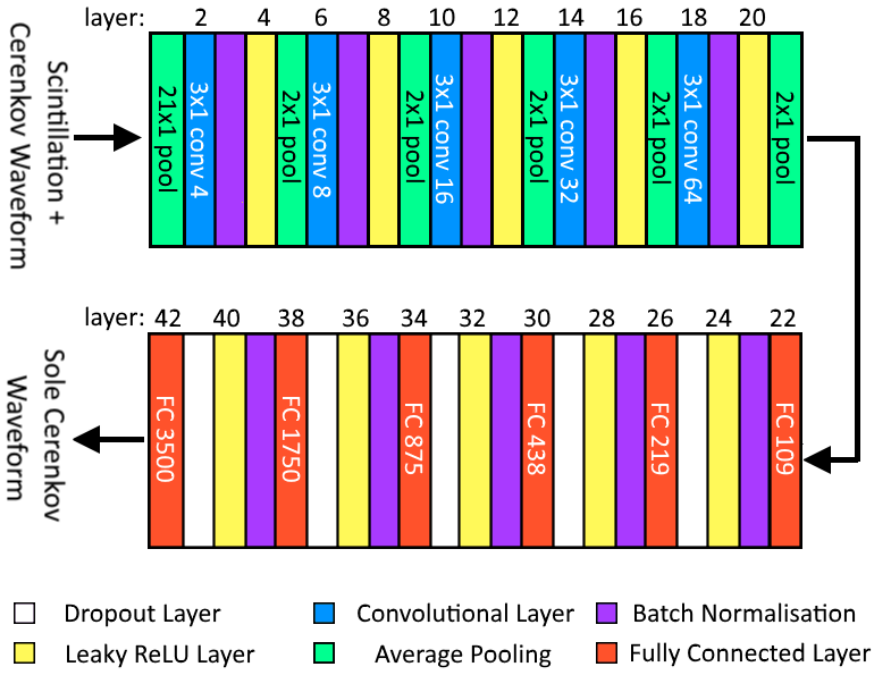

Figure 3.5: Architecture of the developed CNNs. The notation 3×1 conv 4 at layer 2 denotes that four 3x1 convolutions are independently applied to the incoming 3500×1 array, with the output being a $3500 \times 1 \times 4$ array. The average pooling layers at layers 5, 9, 13, 17 and 21 downsample the incoming waveforms by a factor of 2. The activation parameter for each leaky ReLU layer was 0.1. The dropout rate for each dropout layer was 0.15 for the 6 MV energy and 0.1 for the 10 MV energy. Published in Madden *et al.* 2018 [168].

layers, normalisation layers, activation layers and pooling layers were implemented. Convolutional layers were limited to 3×1 array sizes and a stride of 1. Similar to in VGGNet, the number of convolutional filters per layer increased as the depth increased, with 4, 8, 16, 32 and 64 filters used in layers 2, 6, 10, 14 and 18, respectively [181]. Batch normalisation was applied prior to each of the activation layers to mitigate gradient vanishing and gradient explosion during training[e] [173]. Leaky rectified linear units (Leaky ReLU) were used as the activation function. The optimal leaky ReLU activation coefficient was found to be 0.1. Local average pooling layers with a size of 2×1 and a stride of 2 were used to downsample each of the feature maps by a factor of 2. After the 5 stacks of convolution, normalisation, activation and pooling layers, the input 3500×1 array was mapped to 64 109×1 feature maps.

From the 22^{nd} to the 42^{nd} layers, 5 stacks of fully connected layers, normalisation layers, activation layers and dropout layers were implemented to upsample the feature maps from a 109×1 array to a 3500×1 array at the output. Batch normalisation was implemented prior to the leaky ReLU activations to mitigate vanishing and exploding gradients

[e]It is generally accepted that batch normalisation mitigates gradient vanishing and gradient explosion during the training of ANNs and CNNs. However, batch normalisation was shown to induce significant gradient explosion in deep networks at the beginning of training [182].

during training. The optimal leaky ReLU activation coefficient was 0.1. Dropout layers were implemented to improve the accuracy and generalisation of trained CNNs. The optimal dropout probability was 0.15 [183].

Data preprocessing As for the ANNs, preprocessing was applied to transform the measured waveforms into a reproducible format. Measured PSD signals were normalised using the min-max normalisation in Equation 3.12. The 10000 sample length measured signals were shortened to a length of 3500 samples, using the same fitting model as in Equation 3.13 as for the ANNs. For the CNNs, the PSD and reference probe signals were shortened for times $T_1 - 80\,\text{ns} \leq tT_1 + 5520\,\text{ns}$. The measured waveforms are shown in Figure 3.6 (left), with the preprocessed waveforms shown in Figure 3.6 (right).

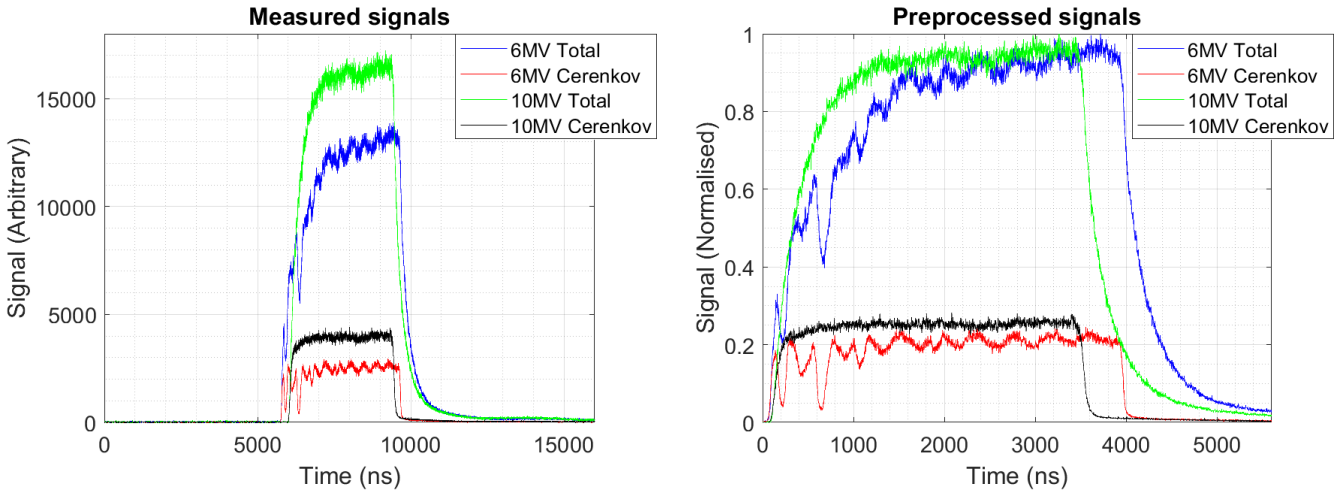

Figure 3.6: Left: measured PSD and reference probe signals for the 6 MV and 10 MV beam energies. Right: preprocessed PSD and reference probe signals for the 6 MV and 10 MV beam energies. 6 MV Total and 10 MV Total are the combined scintillation and Cerenkov radiation signals for the 6 MV and 10 MV beam energies, respectively. 6 MV Cerenkov and 10 MV Cerenkov are the sole Cerenkov radiation signals at the 6 MV and 10 MV beam energies, respectively. The responses shown were measured with the scintillator tip positioned at the centre of a 10 cm $\times$ 10 cm field. Published in Madden *et al.* 2018 [168].

Training data synthesis Two CNNs were trained for the Cerenkov radiation correction, where one CNN was trained for use with the 6 MV beam energy and the other was trained for the 10 MV beam energy. As for the ANNs, it was expected that impractically large data sizes were going to be required to train the deep CNNs to acceptable accuracies. To obtain such a large dataset, training data was synthesised from a smaller set of data measured from the same setup as described in Section 3.2.4. The same training data synthesis algorithm to that of the ANN was applied to generate training data, described in Section 3.2.4. A total of 10721 input-output pairs were synthesised for the training of each of the CNNs.

Training conditions The deep CNNs were modelled in MATLAB 2018a using the Deep Learning Toolbox. Stochastic gradient descent was applied with a minibatch size of 76. The initial learning rate was set to 0.005. The learning rate was decreased by a factor of 0.3 every epoch (every 140 iterations). L_2 weight decay was applied with a weight decay factor of 0.01. Weights in the fully connected layers were initialised randomly under Glorot initialisation conditions [179]. Convolution kernels were initialised randomly using He initialisation [184]. The synthetically produced data was used as the training set, split up into 140 minibatches. The secondary set of measured data was used as the validation set during training. The mean squared error was chosen as the cost function for training. Early stopping was used as the termination condition during training. The CNNs were evaluated on the validation set once every 20 iterations. The validation patience was set to 10, such that when 10 consecutive validation failures occurred, training was terminated. The optimal weights and convolution kernels for the CNNs were those that achieved the lowest validation error. Each CNN took approximately 4 minutes to train on a personal computer using a NVIDIA GeForce GTX 1060 graphics card.

Cerenkov radiation correction The CNN correction used the optimal values for the weights and convolution kernels found during training. The preprocessed PSD signals from the testing set were passed to the CNN as inputs. The CNN's output corresponded to the predicted Cerenkov radiation present in the input PSD signals. Cerenkov radiation was corrected by subtracting the CNN's output from the input PSD signal, and multiplying by the value C_{max} obtained during preprocessing. The CNN corrected signal was then integrated to obtain the CNN corrected PSD response.

3.2.5 Analysis

Dosimetric performance

To assess the performance of each stem signal correction method, global dose differences were calculated between each of the corrected responses and the ionisation chamber responses. Mean absolute differences (MADs) were calculated to determine the average deviation between each corrected PSD beam profiles and corresponding ionisation chamber beam profiles. Linear interpolation was used to sample the ionisation chamber profiles at positions where the PSD measurements were made. The dose differences and MADs between background subtraction corrected responses and the ionisation chamber were taken as the benchmark when evaluating the proposed temporal stem signal correction methods. The MAD for each correction method is calculated as:

$$\mathrm{MAD} = \frac{1}{N_{pos}} \sum_{x} |\mathrm{D_{PSD}}(x) - \mathrm{D_{IC}}(x)| \tag{3.16}$$

Where $D_{PSD}(x)$ is the corrected PSD dose-response at position x, $D_{IC}(x)$ is the ionisation chamber dose-response at position x, and N_{pos} are the number of measurement positions in each beam profile. It should be noted that the penumbral regions are excluded when calculating MADs due to the large dose gradient in this region. The positions included when calculating dose differences and MADs were those that occurred when the ionisation chamber's response was less than 10 %, and measurement positions within the central 80 % of the beam's width.

Comparison of time-dependent scintillation with known scintillation

Each correction method's estimate of the time-dependent scintillation should closely match that the time-dependent scintillation calculated using background subtraction. For the case of the OLS and NLLS methods, the scintillation present in the modelled PSD signal is estimated by $\hat{S} = \hat{a}S(t)$. It should be noted that gradient descent algorithm was set up to optimise the error between the modelled PSD signal, $\hat{y}(t) = \hat{a}S(t) + \hat{b}C(t) + \hat{c}$, and the measured PSD signal, $y(t)$. However, the time dependence of the estimated scintillation depends on the exponential rise and decay constants, τ_r and τ_d. As a result, $\hat{a}$, $\hat{b}$ and $\hat{c}$ implicitly depend on τ_r and τ_d, and so the modelled scintillation given by $\hat{S} = \hat{a}S(t)$ may not match the known scintillation (calculated by background subtraction). For the case of the ANN and CNN methods, the ANN and CNN were trained to estimate the time-dependent Cerenkov radiation present in input PSD signals. Consequently, the time-dependent scintillation can be estimated as the difference between the input PSD signal and the output Cerenkov radiation estimate. The performance of these ANNs and CNNs in predicting the time-dependent scintillation implicitly depends on how "well" the synthesised training data reflects the measured data. Consequently, there exists the possibility for systematic deviations between estimated scintillation and known scintillation. To identify whether there are significant systematic deviations between the estimated time-dependent scintillation and known scintillation, relative mean differences (RMDs) are calculated for the out of field regions and central regions (as defined above in Section 3.2.5). The relative mean difference is calculated as in Equation 3.17:

$$\text{RMD} = \frac{1}{\max(S_{BS})} \sum \frac{\hat{S} - S_{BS}}{N} \tag{3.17}$$

Where $\hat{S}$ is the estimate for the scintillation, S_{BS} is the scintillation calculated by background subtraction and N is the length of the scintillation signals. To quantify how far on average the modelled scintillation signals deviated from the known scintillation signals, relative mean absolute differences (RMADs) between the modelled and known scintillation signals are calculated. These RMADs are defined in Equation 3.18 below:

$$\text{RMAD} = \frac{1}{\max(S_{BS})} \sum \frac{|\hat{S} - S_{BS}|}{N} \tag{3.18}$$

Through comparison of each method's calculated RMDs with it's RMADs, the significance of systematic trends can be quantified. Direct comparison of one correction method's RMADs with another correction method's are problematic, as the ANN and CNN analyse a fraction of the measured waveforms, whereas the OLS and NLLS signals analyse the entire duration of measured waveforms. To enable direct comparison of the OLS and NLLS estimates with the ANN, the OLS and NLLS estimates of scintillation were cropped to match the fraction of the waveform that the ANN had used. To enable direct comparison of the OLS and NLLS estimates of scintillation with the CNN's estimate of scintillation, the OLS and NLLS estimates of scintillation were cropped to match the segment of the waveform that the CNN had used. Through comparison of each methods RMADs with those calculated by other methods, the methods can be quantified in terms of their ability to model the time-dependent scintillation.

3.3 Results

3.3.1 Dosimetric performance

The 7 measured beam profiles are presented in Figures 3.7−3.13, with corresponding global dose-differences presented below each profile. The MADs between each of the corrected PSD profiles and corresponding ionisation chamber profiles are presented in Table 3.1, along with the global MAD for each of the correction methods. For Figures 3.7−3.9 and Figures 3.11−3.12, the PSD was orientated so that it's optical fibre was aligned parallel to the scanning axis of the beam profile. For Figures 3.10 and 3.13, the PSD was orientated so that it's optical fibre was aligned perpendicular to the scanning axis of the beam profile.

For the 6 MV, 3 cm × 3 cm profile presented in Figure 3.7, the PSD's penumbras were narrower than those measured by the ionisation chamber as the PSD's spatial resolution was significantly greater than the ionisation chamber's spatial resolution. As a result, there were significant disagreements between the PSD and ionisation chamber in the penumbral regions. On average, the background subtraction corrected responses (referred to as BS corrected responses for the remainder of this chapter) remained within 1.1 % of the ionisation chamber. The OLS and NLLS responses had MADs of 1.1 %, matching that of the BS correction. The ANN and CNN corrections performed marginally poorer, with the ANN having a MAD of 1.2 % and the CNN having a MAD of 1.3 %. For the ANN, the main source of error had occurred in the central region with respect to the ionisation chamber, underestimating the dose at +9.4 mm by 4.5 %, attributed to a random fluctua-

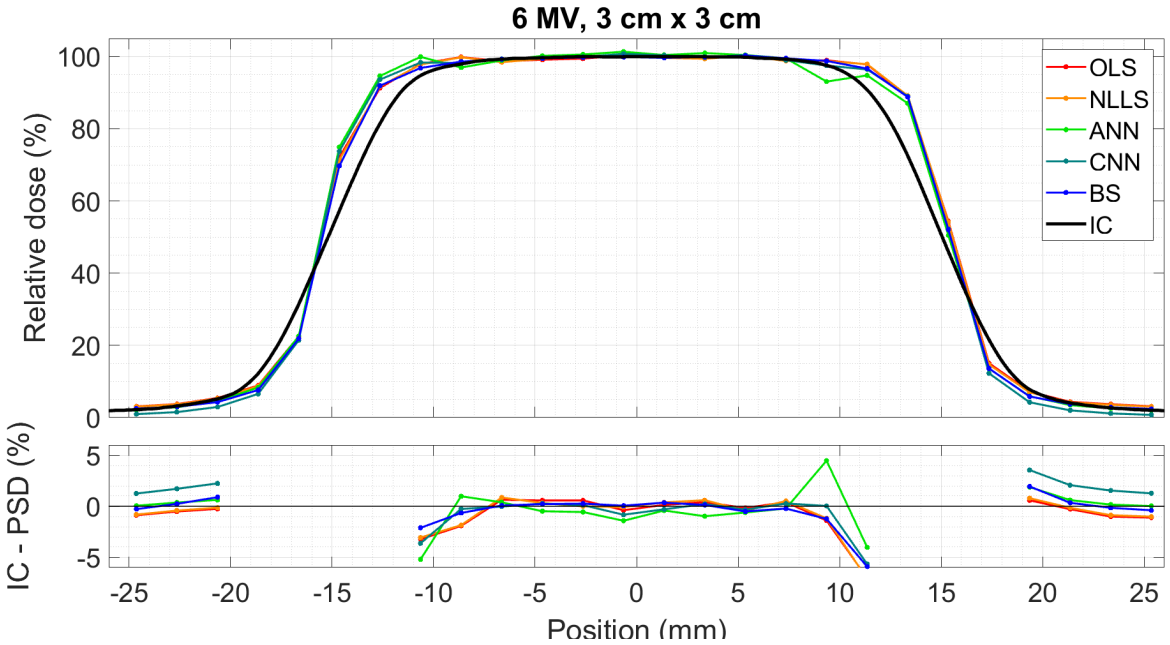

Figure 3.7: Top: Cross-plane beam profile at 6 MV, 3 cm × 3 cm. Bottom: dose differences between each of the corrected PSD responses with respect to the ionisation chamber. In the legend, OLS is the PSD response corrected using the OLS correction method, NLLS is the PSD response corrected using the NLLS correction, ANN is the PSD response corrected using the ANN correction, CNN is the PSD response corrected using the CNN correction, BS is the PSD response corrected using background subtraction and IC is the ionisation chamber response. Results for BS, IC and CNN published in [168].

tion. For the case of the CNN, the source of the inflated error was poor performance in the out of field regions, such that the CNN had systematically under-responded by an average value of 1.9 % with respect to the ionisation chamber.

For the 6 MV, 5 cm × 5 cm profile presented in Figure 3.8, there are significant slants in the central region of the BS, OLS and NLLS profiles (*i.e.* for positions between −20 mm and +20 mm). For the BS, OLS and NLLS corrections, this slant was attributed to gain drift that had occurred in the PSD's PMT. When scanning the PSD through the radiation field, the PSD had originated from the +55 mm position and finished at the −55 mm position. The LINAC was set to continuously deliver it's photon beam during the scan, with the PMTs consistently in operation for the duration of the scan. As a result, the PMTs consistently produced waste heat, and so the PMT's dynodes increased in temperature as the scan progressed. Consequently, the PMT's sensitivity increased as the PSD was scanned from +55 mm to −55 mm. For the OLS and NLLS corrections, the gradient descent optimisation process negates the effects of PMT gain drift that stems from the reference probe's PMT by adjusting the value calculated for $\hat{b}$. However, gain drift stemming from the PSD's PMT causes the OLS and NLLS estimates of scintillation to increase, causing the OLS and NLLS profiles to suffer from the same dosimetric trends as

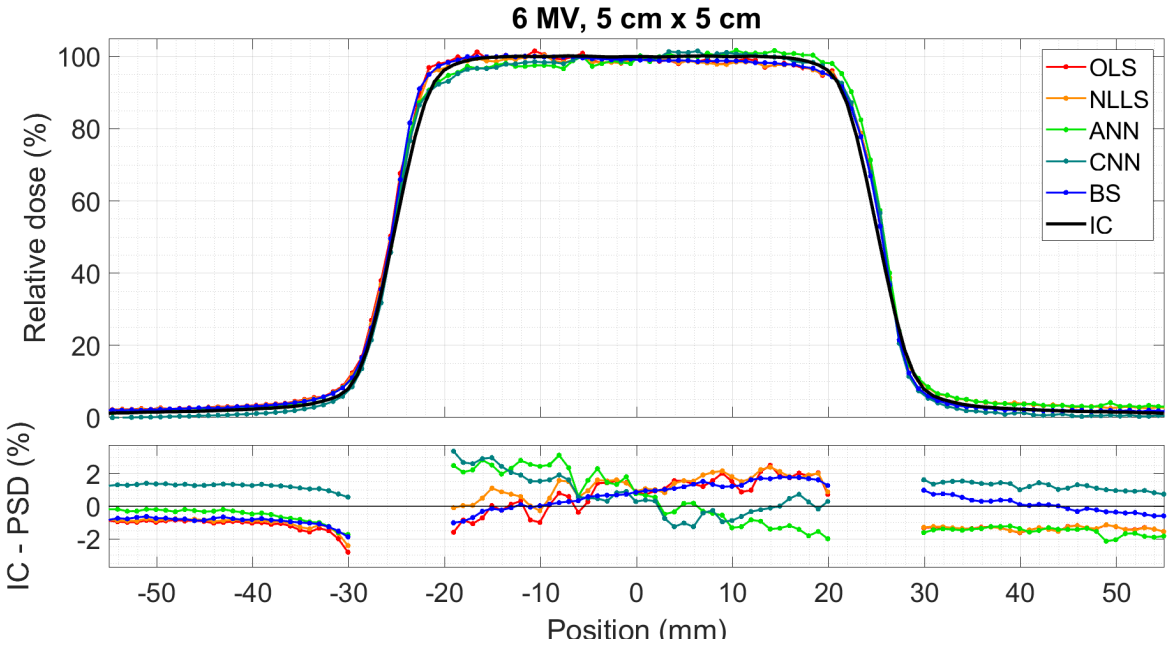

Figure 3.8: Top: Cross-plane beam profile at 6 MV, 5 cm × 5 cm. Bottom: dose differences between each of the corrected PSD responses with respect to the ionisation chamber. In the legend: OLS, NLLS, ANN, CNN, BS and IC are defined as in Figure 3.7. Results for BS, ANN, CNN and IC were published in Madden *et al.* 2018 [168, 175].

the BS profile. As a result of these gain drift effects, the BS dose differences ranged from an overestimation of 1.0 % at the −19 mm position to an underestimation of 1.7 % at the +19 mm position with respect to the ionisation chamber. The OLS and NLLS corrections experienced exacerbated overestimation and underestimations when compared with the BS correction as the OLS and NLLS corrections were less reproducible, having increased magnitudes of random fluctuations in their profiles. The OLS and NLLS corrections had a maximum overestimation of 1.6 % at the −19 mm position, and a maximum underestimation of 2.5 % at the +19 mm position. For the central region in this profile, the MADs for BS, OLS and NLLS were 0.8 %, 1.0 % and 0.9 %, respectively.

For the ANN and CNN in Figure 3.8, the slant runs in the opposite direction to that of the BS, OLS and NLLS corrections. The source of this disagreement between the neural networks corrections and the BS, OLS and NLLS corrections was attributed to a systematically poor performance of the neural networks when estimating Cerenkov radiation present in measured PSD signals. The ANN and CNN profiles have significant fluctuations in their calculated doses for the central region of the profile, suggesting suboptimal reproducibility of the ANNs and CNNs under these conditions. Conversely, the fluctuations are near negligible in the out of field regions, suggesting the ANN's and CNN's performance was more reproducible in the out of field regions than the central regions.

In the out of field regions in Figure 3.8 (*i.e.* at positions more than 30 mm away from

the centre of the field), each of the correction method's responses systematically deviated from the ionisation chamber by maximum values of 1.9 % for BS, 2.8 % for OLS, 2.4 % for NLLS, 2.1 % for the ANN and 1.6 % for the CNN. BS remained within 1 % of the ionisation chamber at the positive out of field positions *i.e.* for positions greater than +30 mm. BS overestimated the dose with respect to the ionisation chamber by an average value of 0.8 % for the negative out of field positions *i.e.* positions less than −30 mm. This deviation arose due to the aforementioned PMT gain drift. The OLS and NLLS corrections performed similarly in the out of field regions, systematically over-estimating the dose measured by the ionisation chamber with an average value of 1.4 %. The ANN correction systematically overestimated the dose with respect to the ionisation chamber by an average value of 0.9 % for these out of field regions. The CNN correction systematically underestimated the dose with respect to the ionisation chamber by an average value of 1.0 % for these out of field regions.

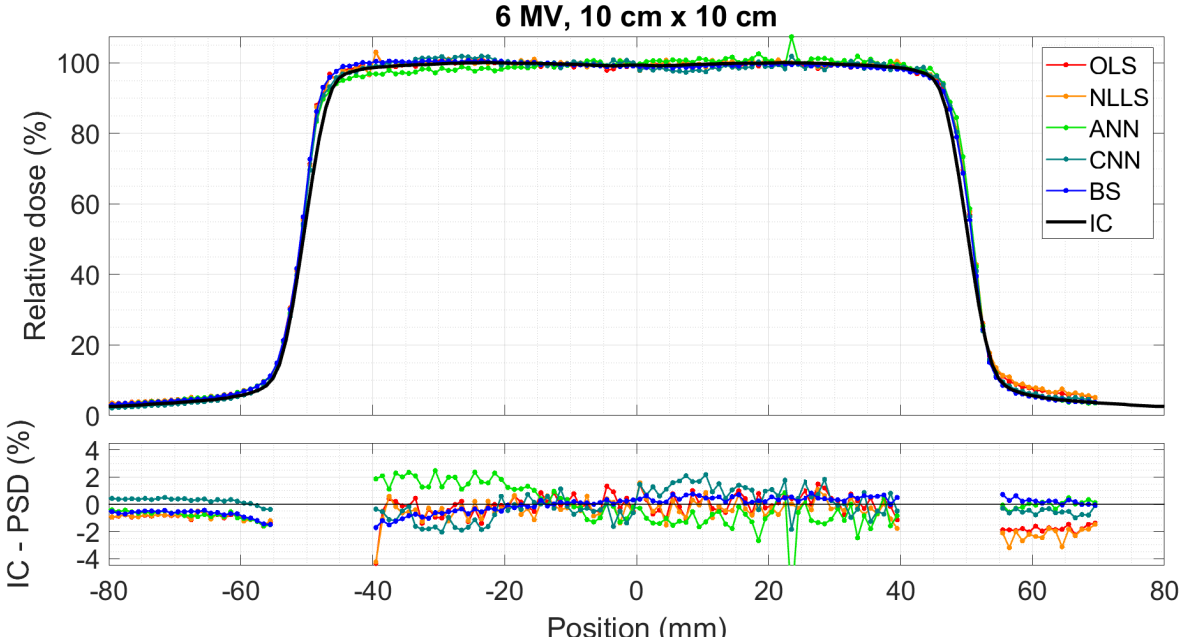

Figure 3.9: Top: Cross-plane beam profile at 6 MV, 10 cm × 10 cm. Bottom: dose differences between each of the corrected PSD responses with respect to the ionisation chamber. In the legend: OLS, NLLS, ANN, CNN, BS and IC are defined as in Figure 3.7. Results for BS, ANN, CNN and IC were published in Madden *et al.* 2018 [168, 175].

For the 6 MV, 10 cm × 10 cm cross-plane profile presented in Figure 3.9, no slants were observed in the central regions of the PSD profiles, unlike those in Figure 3.8. In the central regions (*i.e.* for positions between −40 mm and +40 mm), the BS corrected profiles remained within 1.7 % of the ionisation chamber, having a MAD of 0.5 %. The OLS and NLLS corrections performed similarly to the BS correction in the central regions, each having MADs of 0.6 %. However, the OLS and NLLS corrections had maximum dose

differences of 4.3 %, inflated as they had decreased reproducibilities and increased fluctuations in the central regions of their profiles observable in Figure 3.8. The ANN profile in Figure 3.9 had inflated deviations with respect to the ionisation chamber in the central region, attributed to suboptimal performance of the ANN. As a result, the ANN's MAD was 1.2 % in the central region, having a maximum difference in dose of 7.4 %. The CNN correction reproduced the trends of the BS correction in the profile's central region. The CNN had a MAD of 1.0 % and a maximum dose difference of 2.2 % in the central region, inflated above BS due to the random fluctuations present in the CNN profile.

For the out of field regions in Figure 3.9 (*i.e.* for positions more than 56 mm from the centre of the field), BS remained within 1.5 % of the ionisation chamber, and had a MAD of 0.5 %. The OLS and NLLS corrections performed similarly to each other in the out of field regions, having MADs of 1.2 % and 1.4 %, and maximum dose differences of 2.3 % and 3.2 %, respectively. The ANN and CNN corrections reproduced the trends of the BS profiles in the out of field regions. The ANN had a MAD of 0.6 % and a maximum difference in dose of 1.6 %. Similarly, the CNN had a MAD of of 0.4 % and a maximum difference in dose of 1.0 %. Each of the correction methods were reproducible in the out of field regions, such that the dose differences plotted in Figure 3.9 had reduced random fluctuations when compared against their corresponding differences in the central region.

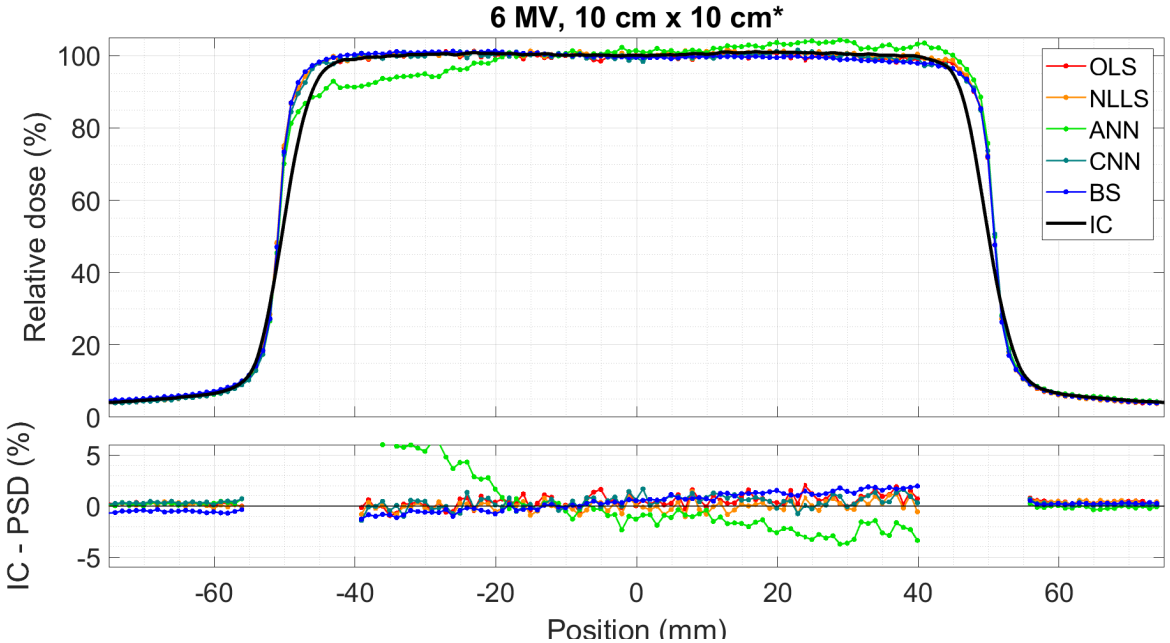

Figure 3.10: Top: In-plane beam profile at 6 MV, 10 cm × 10 cm. Bottom: dose differences between each of the corrected PSD responses with respect to the ionisation chamber. In the legend: OLS, NLLS, ANN, CNN, BS and IC are defined as in Figure 3.7. Results for BS, ANN, CNN and IC were published in Madden *et al.* 2018 [168, 175].

For the 6 MV, 10 cm × 10 cm in-plane profile presented in Figure 3.10, the PSD was

orientated so that it's optical fibre was perpendicular to the in-plane axis. Central regions occurred for positions between -40 mm and $+40$ mm. The BS profile had a slant in it's central region that did not appear in the corresponding OLS and NLLS profiles. When compared against the ionisation chamber, BS overestimated the dose by 1.3 % at -39 mm to an underestimated the dose by 2.0 % at $+39$ mm. As outlined earlier, the OLS and NLLS corrections mitigate the effects of gain drift in the reference probe's PMT, but these methods are unable to mitigate gain drift effects stemming from the PSD's PMT. Given that this slant is only observed for the BS profile, it was determined that the reference probe's PMT had be affected by gain drift. In the central region, BS had a MAD of 0.9 %, OLS had a MAD of 0.6 %, NLLS had a MAD of 0.4 % and the CNN had a MAD of 0.6 %. The ANN performed poorly in the central region, reproducing the trends present in the ANN profiles in Figures 3.8 and 3.9.

For the out of field regions in Figure 3.10 (*i.e.* for positions more than 56 mm from the centre of the field), all corrected PSD profiles remained in close agreement with the ionisation chamber. On average, the BS corrected profiles remained within 0.4 % of the ionisation chamber, and had a maximum dose difference of 0.7 %. The OLS correction had a MAD of 0.3 % and had a maximum dose difference of 0.8 % with respect to the ionisation chamber. Similarly, the NLLS correction had a MAD of 0.3 % with respect to the ionisation chamber, and a maximum disagreement of 0.6 %. The ANN and CNN performed similarly to the other correction methods, remaining in close agreement with the ionisation chamber. The ANN correction had a MAD of 0.2 % and a maximum disagreement of 0.7 %, and the CNN correction had a MAD of 0.3 % and a maximum disagreement of 0.7 %.

For the 10 MV, 5 cm $\times$ 5 cm profile presented in Figure 3.11, the BS, OLS and NLLS profiles had matching slants in their central regions (*i.e.* for positions between -20 mm and $+20$ mm). Following the same logic outlined for the profile presented in Figure 3.8, the source of these slants was gain drift that affected the PSD's PMT. The BS correction had a MAD of 0.9 % and a maximum difference in dose of 2.5 % with respect to the ionisation chamber, exacerbated due to the PMT gain drift during the measurement of this profile. The OLS and NLLS corrections had MADs of 0.7 % and 0.9 %, and maximum differences in dose of 1.7 % and 2.8 % with respect to the ionisation chamber in this region. The ANN and CNN profiles did not possess any slants in their central region, however there were significant random fluctuations, suggesting their reproducibility was poor for these measurement conditions. As a result of their suboptimal performances in these measurement conditions, the ANN and CNN corrections had MADs of 1.4 % and 1.0 %, and maximum differences in dose of 4.7 % and 4.3 % with respect to ionisation chamber, respectively.

For the out of field regions in Figure 3.11 (*i.e.* for positions more than 31 mm from

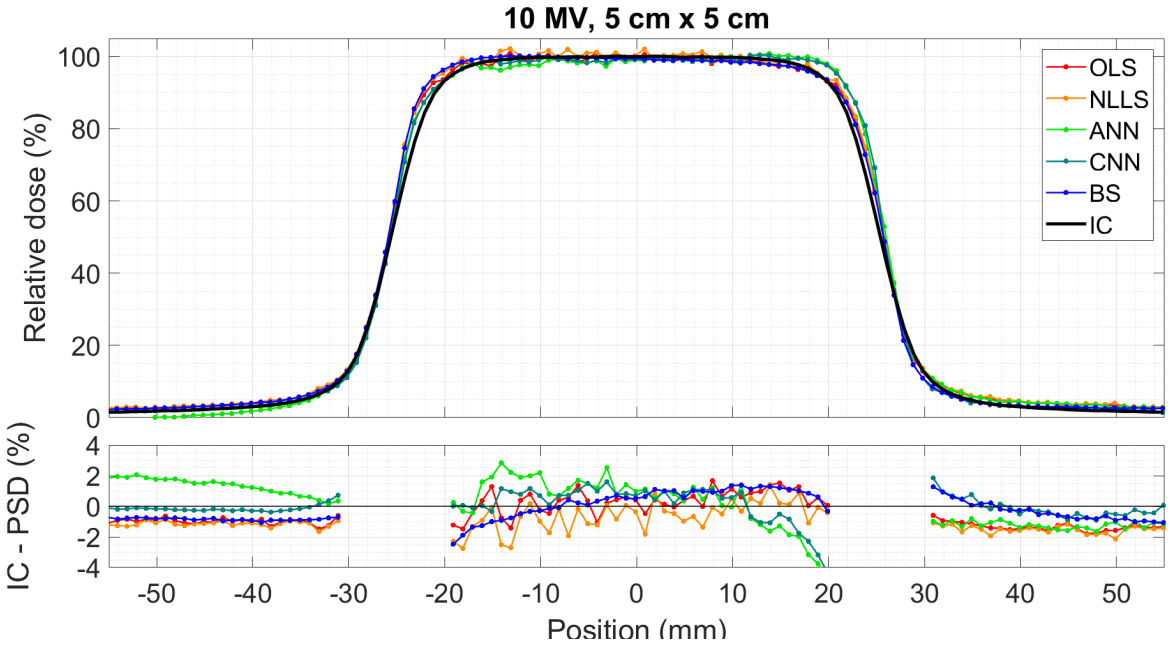

Figure 3.11: Top: Cross-plane beam profile at 10 MV, 5 cm × 5 cm. Bottom: dose differences between each of the corrected PSD responses with respect to the ionisation chamber. In the legend: OLS, NLLS, ANN, CNN, BS and IC are defined as in Figure 3.7. Results for BS, ANN, CNN and IC were published in Madden *et al.* 2018 [168, 175].

the centre of the field), the BS corrected profiles remained within 1.3 % of the ionisation chamber, having a MAD of 0.7 %. The OLS corrected profile remained within 1.8 % of the ionisation chamber, overestimating the out of field dose on average by 1.2 %. Similarly, the NLLS corrected profile remained within 2.1 % of the ionisation chamber in the out of field regions, systematically overestimating the dose measured by the ionisation chamber by an average value of 1.3 %. The ANN correction systematically underestimated the dose at the negative out of field positions by a maximum of 2.0 %. Consequently, the ANN correction had a MAD of 1.3 % in these out of field regions. The CNN corrected profiles remained within 1.8 % of the ionisation chamber for the out of field positions, having a MAD of 0.4 % in the out of field region.

For the 10 MV, 10 cm × 10 cm cross-plane profile presented in Figure 3.12, the PSD was orientated so it's optical fibre was aligned parallel to the cross plane axis. No slants were present in the central region of the BS, OLS, NLLS or CNN corrected profiles (*i.e.* at for positions between −40 mm and +40 mm), however a slant was present in the ANN profile. The BS corrected profile remained in close agreement with the ionisation chamber, having a MAD of 0.3 % and a maximum dose difference of 0.8 %. The OLS and NLLS corrections had inflated MADs and maximum dose differences when compared against the BS correction, arising from the increased random fluctuations in the OLS and NLLS profiles. The corresponding MAD was 0.5 % for both the OLS and NLLS correc-

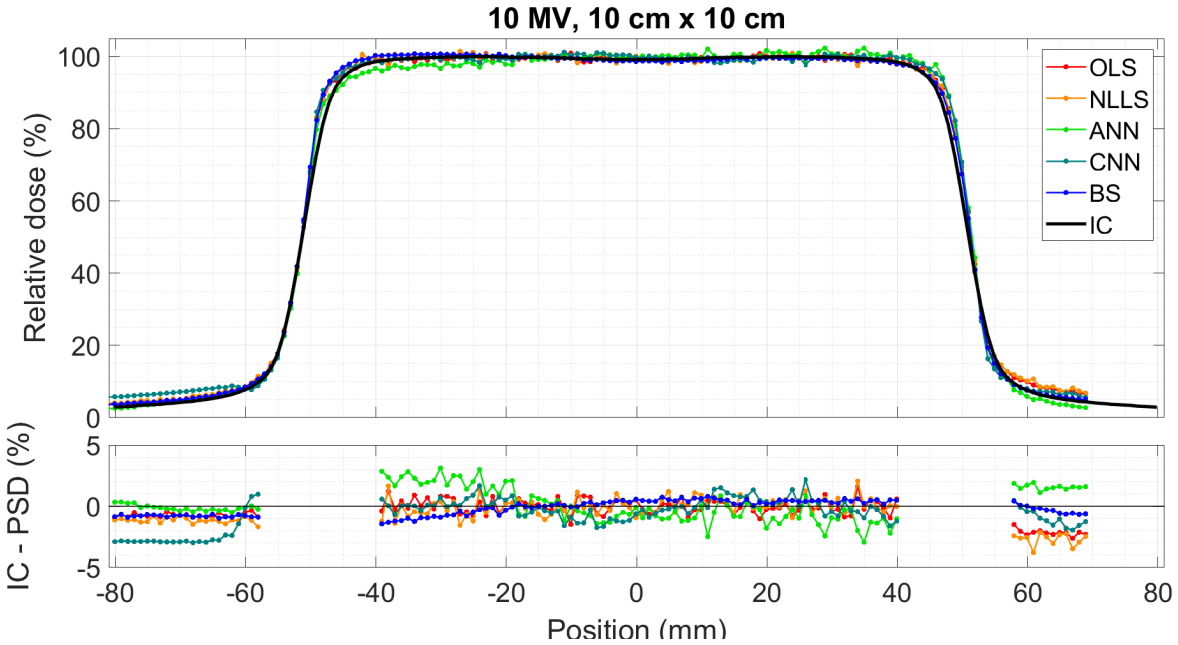

Figure 3.12: Top: Cross-plane beam profile at 10 MV, 10 cm × 10 cm. Bottom: dose differences between each of the corrected PSD responses with respect to the ionisation chamber. In the legend: OLS, NLLS, ANN, CNN, BS and IC are defined as in Figure 3.7. Results for BS, ANN, CNN and IC were published in Madden *et al.* 2018 [168, 175].

tions, and the maximum differences were 1.5 % for the OLS correction and 1.2 % for the NLLS correction. The ANN corrected profile was slanted in the central region, exacerbating the ANN correction's MAD to 0.8 % and it's maximum dose difference to 2.5 %. The CNN corrected profile had significant random fluctuations in it's central region, leading to an increased MAD of 0.8 % and an increased maximum dose difference of 1.7 % when compared against the BS, OLS and NLLS corrections.

For the out of field region in Figure 3.12 (*i.e.* for positions further than 57 mm away from the centre of the field), the BS corrected profile remained within 1.0 % of the ionisation chamber. The BS correction overestimated the out of field dose with respect to the ionisation chamber by an average value of 0.7 %. The OLS correction had overestimated the dose by an average value of 1.2 %, with a maximum difference of 2.6 % with respect to the ionisation chamber. Similar to the OLS correction, the NLLS correction had overestimated the dose by an average value of 1.7 %, with a maximum difference of 3.8 %. Comparing the OLS and NLLS profiles, the NLLS's inflated MAD and maximum difference are attributed to the NLLS correction having significant random fluctuations in the out of field region. For the negative out of field region in Figure 3.12, the ANN corrected profile remained close to the ionisation chamber, having a maximum difference of 0.5 % in this region. However, the ANN correction systematically under-estimated the dose with respect to the ionisation chamber at the positive out of field regions by an aver-

age value of 1.6 %. Conversely, the CNN correction overestimated the dose in the out of field regions. At the negative out of field positions, the CNN correction overestimated the dose with respect to the ionisation chamber by an average value of 2.5 %; at the positive out of field region, the CNN correction overestimated the dose by an average value of 1.1 %.

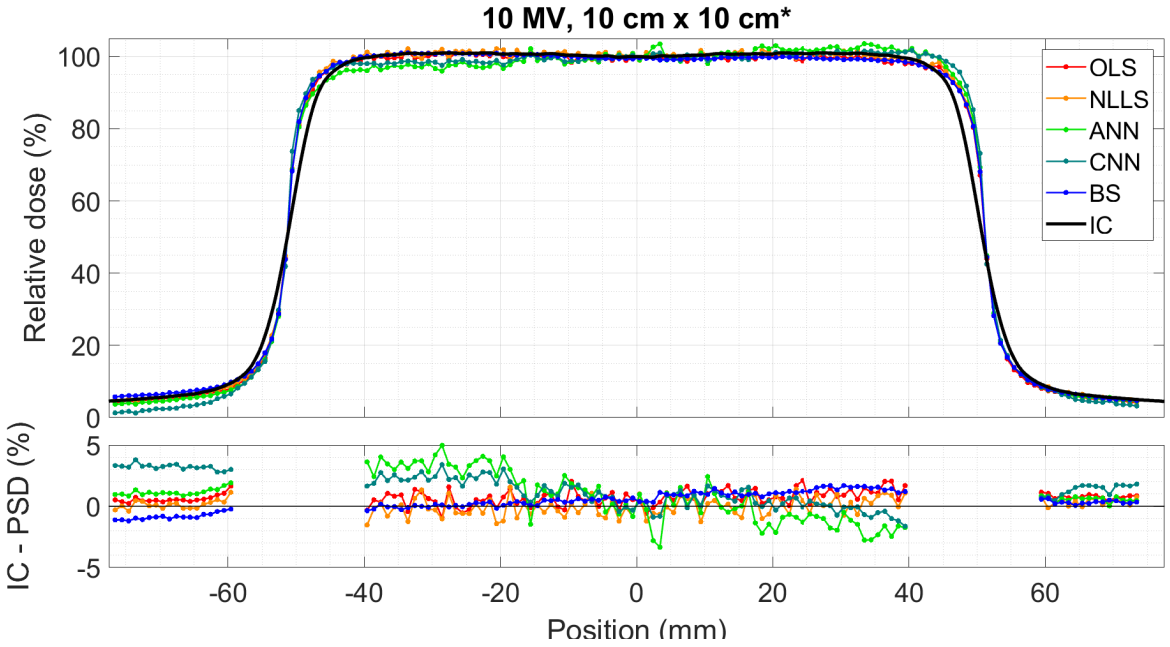

Figure 3.13: Top: In-plane beam profile at 10 MV, 10 cm × 10 cm. Bottom: dose differences between each of the corrected PSD responses with respect to the ionisation chamber. In the legend: OLS, NLLS, ANN, CNN, BS and IC are defined as in Figure 3.7. Results for BS, ANN, CNN and IC were published in Madden *et al.* 2018 [168, 175].

For the 10 MV, 10 cm × 10 cm in-plane profile 3.13, the PSD was orientated so that it's optical fibre was aligned perpendicular to the in-plane axis. Central regions occurred for positions between −40 mm and +40 mm. A slant was present in the central region of the BS, OLS and NLLS profiles, suggesting gain drift had occurred in the PSD's PMT during the measurement of this profile. As for all previously discussed profiles, the OLS and NLLS profiles had increased random fluctuations when compared against corresponding BS profiles. In this profile's central region, the BS correction had a MAD of 0.7 % and a maximum dose difference of 1.4 % with respect to the ionisation chamber. The OLS correction had a MAD of 0.7 % and a maximum dose difference of 1.7 %. The NLLS correction performed similarly to the OLS correction, having a 0.7 % MAD, and a maximum dose difference of 1.6 %. The ANN and CNN corrected profiles had slants and significant random fluctuations in the central regions, increasing their maximum dose differences above those of the BS, OLS and NLLS corrected profiles. In the central regions, the ANN corrected profiles had a maximum difference in dose of 4.0 %, and the CNN corrected

profiles had a maximum difference in dose 3.0 %.

For the out of field regions in Figure 3.13 (*i.e.* for positions further away than 57 mm from the centre of field), the BS correction systematically deviated from the ionisation chamber. For the negative out of field positions, the BS correction overestimated the dose by an average value of 0.8 %; however, the BS corrected profiles remained within 0.6 % of the ionisation chamber for the positive out of field positions. The OLS correction overestimated the dose by an average value of 0.7 % in the out of field regions, with a maximum difference in dose of 1.7 %. The NLLS corrected profile was in the best agreement with the ionisation chamber, having a MAD of 0.3 % and a maximum difference in dose of 1.1 %. The ANN correction had a MAD of 0.9 % and a maximum difference in dose of 1.9 %. The CNN correction performed poorly in the negative out of field region, systematically under-estimating the dose with respect to the ionisation chamber by an average value of 2.4 %. The maximum dose differences for the ANN and CNN corrections in the out of field regions were 1.9 % and 3.8 %, respectively.

Beam energy, Field size	BS (%)	OLS (%)	NLLS (%)	ANN (%)	CNN (%)
6 MV, $3 \times 3\,cm^2$	0.8	1.1	1.1	1.2	1.3
6 MV, $5 \times 5\,cm^2$	0.8	1.2	1.2	1.2	1.2
6 MV, $10 \times 10\,cm^2$	0.5	0.8	0.9	1.0	0.8
6 MV, $10 \times 10\,cm^2$*	0.7	0.5	0.4	1.7	0.5
10 MV, $5 \times 5\,cm^2$	0.8	1.0	1.1	1.3	0.6
10 MV, $10 \times 10\,cm^2$	0.5	0.7	0.9	1.1	1.1
10 MV, $10 \times 10\,cm^2$*	0.7	0.8	0.6	1.6	1.5
Global MAD	0.7	0.8	0.8	1.3	1.0

Table 3.1: In this table, MADs between the ionisation chamber and the corrected PSD responses are are reported for each beam profile. Global MAD corresponds to the global MAD between the ionisation chamber responses and the corrected PSD dose-responses. In the top row, BS corresponds to the MADs of the background subtraction correction, OLS corresponds to the MADs of the temporal OLS correction, NLLS corresponds to the MADs of the NLLS correction, ANN corresponds to the MADs of the ANN correction and CNN corresponds to the MADs of the CNN correction. In the first column, * denotes that profiles were measured along the in-plane axis, whereas an absence of * denotes that profiles were measured along the cross-plane axis. Results for BS, ANN, CNN and IC were published in Madden *et al.* 2018 [168, 175].

From the MAD statistics in Table 3.1, the BS correction was the most robust and accurate correction method investigated, having a global MAD of 0.7 %. The OLS and NLLS corrections were the next best performing correction methods, both having global MADs of 0.8 %. The BS correction's most significant source of error was PMT gain drift, which caused systematic deviations between the corrected PSD response and the ionisation chamber. Statistically, the ANN and CNN corrections had the poorest performance

of the investigated corrections. Both the ANN and CNN correction had consistently performed poorly in the central regions of the profiles, systematically deviating from the BS, OLS and NLLS corrections.

With regards to the central regions of the presented profiles, the BS, OLS and NLLS corrections all had global MADs of 0.7 %. From the profiles presented in Figures 3.7−3.13, the BS correction was statistically the most robust and reproducible correction in the central, with the BS corrected profiles being spatially smooth. In comparison, the OLS and NLLS corrections were less reproducible, having noticeable fluctuations present in the central regions of their profiles. Though suffering from a reduced reproducibility, the performance of the OLS and NLLS corrections matched the performance of the BS correction as the BS correction was affected by PMT gain drift for 4 of the 7 profiles measured. It should be noted that the OLS and NLLS correction methods were less prone to PMT gain drift as they mitigate the effects of gain drift stemming from the reference probe's PMT, though these corrections were still susceptible to PMT gain drift stemming from the PSD's PMT.

With regards to the out of field regions, the BS correction tended to systematically deviate from the ionisation chamber when gain drift had occurred in either of the PMTs. Similar to the central regions, the BS corrected profiles were spatially smooth in the out of field regions. The performance of the OLS and NLLS corrections was inconsistent from one profile to another. For the profiles in Figures 3.7, 3.10 and 3.13, the OLS and NLLS profiles remained close to the ionisation chamber in the out of field regions. However, for the profiles in Figures 3.8, 3.9, 3.11 and 3.12, the OLS and NLLS corrections systematically overestimated the dose with respect to the ionisation chamber by average values of 1.2 % and 1.4 % respectively. The ANN and CNN corrections performed inconsistently from one profile to another, often deviating systematically from the ionisation chamber. The global MADs for the out of field region were 0.6 % for BS, 1.0 % for OLS, 1.1 % for NLLS, 0.8 % for the ANN correction and 1.1 % for the CNN correction. These results suggest that the BS correction was most suitable correction in the out of field region, provided that gain drift effects are mitigated.

3.3.2 Comparison of estimated scintillation with known scintillation

RMDs and RMADs between each correction method's estimated scintillation and the known scintillation were calculated using Equations 3.17 and 3.18. The OLS and NLLS estimates of scintillation and the known scintillation were cropped to match the temporal regions used by the ANN and CNN, enabling for direct comparisons with the ANN and CNN estimates of scintillation. The calculated RMADs and RMDs are presented in Table

3.2. Examples of each correction method's estimated scintillation signal and corresponding known scintillation signal are shown in Figures 3.14 and 3.15.

	Central			Out of field		
	RMD (%)	RMAD (%)	$\frac{RMD}{RMAD}$ (%)	RMD (%)	RMAD (%)	$\frac{RMD}{RMAD}$ (%)
OLS	−0.5	2.1	−26	-0.5	7.8	−5.9
NLLS	−0.3	1.9	−18	-0.2	8.3	−2.2
ANN	3.3	3.8	87	19	25	79
OLS	−2.4	5.4	−44	5.7	13	43
NLLS	1.8	3.6	50	10	16	66
CNN	5.0	11	46	14	47	29

Table 3.2: Relative mean differences and relative mean absolute differences calculated between estimated scintillation and known scintillation. In the top row, Central and Out of field corresponds to the global average RMD and RMAD calculated for the central and out of field regions, respectively (as defined in Section 3.2.5). In the second row of the first column: OLS, NLLS and ANN corresponds to the RMDs and RMADs calculated for the ANN's temporal region of interest. In the bottom row of the first column: OLS, NLLS and CNN corresponds to the RMDs and RMADs calculated for the CNN's temporal region of interest.

Estimates of the scintillation are shown for the ANN's temporal region of interest in Figure 3.14. For this temporal region of interest (*i.e.* the scintillation decay tail), the OLS and NLLS estimates of scintillation were closer to the known scintillation than the ANN's estimate of the scintillation in the central regions of measured profiles. For these central regions, the NLLS estimate of scintillation had best matched the known scintillation, having a RMAD of 1.9 %. The OLS estimate of scintillation was marginally poorer, having a mean RMAD of 2.1 % with respect to the known scintillation. From the RMDs in the central region, the OLS correction underestimated the scintillation present on average by 0.5 % relative to the amplitude of the scintillation pulse. The NLLS correction reproduced this trend, systematically underestimating the scintillation present on average by 0.3 % with respect to the amplitude of the scintillation signal. The ANN correction produced the least accurate estimate of the known scintillation when analysing the scintillation decay tail, having a RMAD of 3.8 %. The ANN correction systematically overestimated the scintillation present in the central region, having a RMD that was 87 % of it's RMAD. The ANN's systematic overestimation of the scintillation can be observed in the top left corner of Figure 3.14.

Similar trends were observed for the out of field region for the ANN's temporal region of interest. The OLS and NLLS corrections performed similarly to one another, with the OLS correction having a RMAD of 7.8 % and the NLLS correction having a RMAD of 8.3 %. Comparing the RMDs with the RMADs, the OLS and NLLS corrections appeared

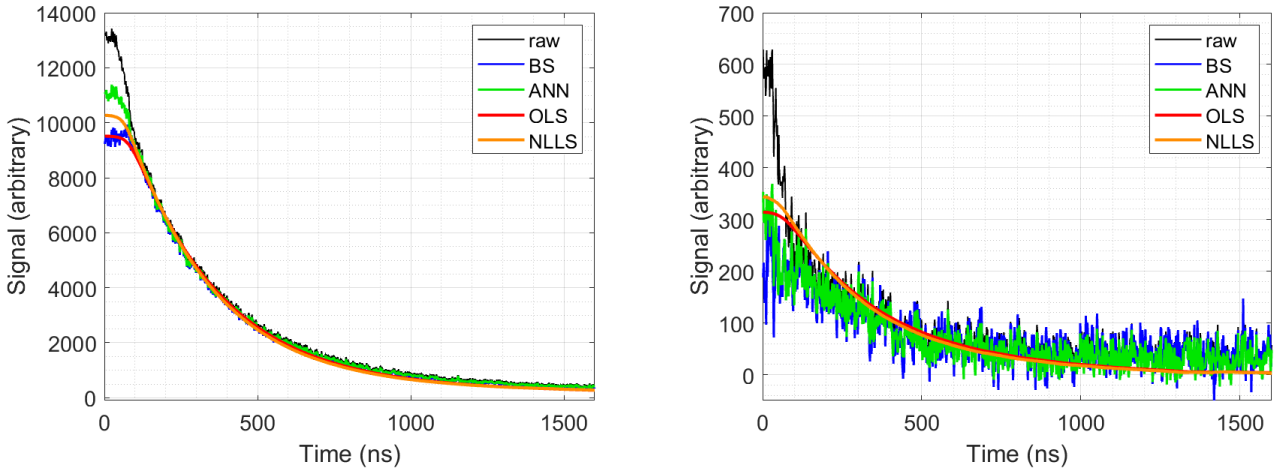

Figure 3.14: Left: measured and estimated signals recorded at the centre of the 6 MV, 10 cm × 10 cm field. Right: measured and estimated signals recorded at a position of −80 mm for the 6 MV, 10 cm × 10 cm field (corresponding to 30 mm outside the 10 cm × 10 cm field). In the legends, raw corresponds to the measured PSD signal, and BS, OLS, NLLS and CNN correspond to their calculated scintillation signals.

to be free of systematic over-estimation or underestimation trends in the out of field regions as their RMDs were less than 0.5 % of the amplitude of known scintillation signals. With reference to the measured PSD signals in Figure 3.14, increased magnitudes of noise are present in the known scintillation measured in the out of field region, compared to the known scintillation measured in the central region. These inflated RMADs for the out of field region arise partially due to the poor signal to noise ratio of the measured PSD signals in the out of field region. The ANN correction was the worst descriptor of the scintillation present, having and RMAD of 25 % with respect to the amplitude of the scintillation present. The ANN's increased RMAD when comparing the central region against the out of field region can be partially attributed to the increased measurement noise in this region. However, through comparison of the RMD and RMAD, the most significant source of the ANN's inflated RMAD resulted from a systematic underestimation the scintillation present by an average value of 19 % relative to the amplitude of scintillation.

Estimated scintillation signals for the CNN's temporal region of interest are shown in Figure 3.15. For the CNN's temporal region of interest, the OLS and NLLS estimates of scintillation were superior to corresponding CNN estimates of scintillation. In the central region, the NLLS estimate best matched the known scintillation, having a RMAD of 3.6 % relative to the amplitude of the scintillation. The OLS correction performed marginally poorer than the NLLS correction, having a RMAD of 5.4 %. From the RMDs, the OLS correction tended to systematically underestimate the scintillation by an average value of 2.4 % in the central region of the profiles. Conversely, the NLLS correction tended to systematically overestimate the scintillation signal by an average value of 1.8 % in the central region. The CNN correction was the poorest model of the time-dependent

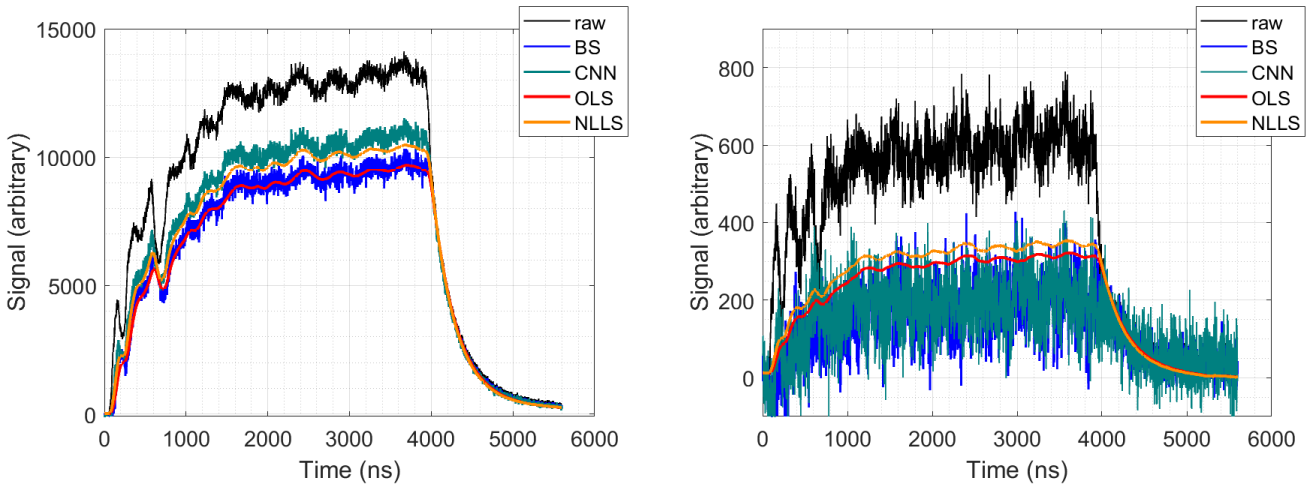

Figure 3.15: Left column: measured and estimated signals recorded at the centre of the 6 MV, 10 cm × 10 cm field. Right column: measured and estimated signals recorded at a position of −80 mm for the 6 MV, 10 cm × 10 cm field (corresponding to 30 mm outside the 10 cm × 10 cm field). In the legends, raw corresponds to the measured PSD signal, and BS, OLS, NLLS and CNN correspond to their calculated scintillation signal.

scintillation in the central region, having a RMAD of 11 % with respect to the amplitude of the known scintillation. From it's RMD, the CNN correction systematically overestimated the scintillation by an average value of 5.0 % relative to the amplitude of scintillation. These systematic trends of the OLS, NLLS and CNN corrections are observable in the bottom left corner of Figure 3.15.

For the out of field regions in the scope of the CNN's temporal region of interest, each of the correction methods systematically overestimated the scintillation present. The OLS estimate of scintillation was on average the best descriptor of the known scintillation, having a RMAD of 13 %. The NLLS estimate of scintillation was a poorer descriptor of the known scintillation than the OLS estimate, having a RMAD of 16 % relative to the amplitude of the known scintillation. Through comparison of RMD with RMADs, the systematic overestimation trend was least significant for the OLS correction, with OLS having a RMD of 5.7 %. Comparatively, the NLLS correction had on average overestimated the scintillation by 10 % relative to the known scintillation's amplitude. The CNN's estimate was the worst descriptor of the time-dependent scintillation. From the RMDs, the CNN systematically overestimated the scintillation by a value of 14 % relative to the known scintillation. It should be noted that the CNN's estimates were noisy in the out of field regions, leading to an inflation of it's RMAD to 47 %. The overestimation trends are present in the bottom right graph in Figure 3.15.

3.4 Discussion

In terms of dosimetric performance, background subtraction was the most effective correction method investigated in this chapter. Background subtraction was characterised by a global MAD of 0.7 % in the central regions of profiles and a global MAD of 0.6 % for the out of field regions. The most significant source of systematic error was PMT gain drift, which could not be corrected when analysing the measured PSD and reference probe signals. Despite these gain drift effects, the BS profiles remained within 2.5 % of the ionisation chamber in the central regions, and 1.9 % of the ionisation chamber for the out of field regions (excluding the 6 MV, 3 cm $\times$ 3 cm profile). Comparatively, the next best performing correction, the OLS correction had a global MAD of 0.7 % in the central region and 0.8 % in the out of field region. However, the OLS correction had maximum discrepancies of 4.3 % and 2.8 % for the central and out of field regions, respectively. The NLLS correction had performed similarly to the OLS correction for all profiles measured, however it's global MAD had increased to 0.8 % for the out of field region. Comparing the BS correction against the other corrections, the BS corrected profiles tended to remain spatially smooth, whereas the other corrections produced profiles with significant spatial fluctuations. Given the analytic nature of the OLS, NLLS, ANN and CNN corrections, the spatial fluctuations were expected to arise as a consequence of the significant measurement noise present in the measured signals.

PMT gain drift could not be corrected for during the analysis of the beam profiles in this chapter. To correct for PMT gain drift in the beam profiles, multiple calibration measurements must be taken immediately before and after the profiles are scan. These multiple calibration measurements were not taken during the measurement of the presented beam profiles, omitted at the time of measurement. This omission occurred as negligible PMT gain drift was expected to occur in the approximate 9 minutes taken to measure each profile. It should be noted that the majority of other reported PSD dosimetry systems in the literature are not susceptible to PMT gain drift effects as the majority of the reported PSD dosimetry systems utilise other types of photodetectors that are much less temperature sensitive than the PMTs used in this work. For example, the commercial PSD dosimetry systems Exradin W1 and Exradin W2 (Standard Imaging, USA) use photodiodes as their photodetector [185]. Research groups investigating spectral Cerenkov radiation correction methods typically utilise charged coupled devices [74]. Alternatively, there exists PMTs that have integrated cooling systems that control the PMT's temperature; these PMTs mitigate the PMT gain drift phenomenon.

When calculating RMDs and RMADs, the known scintillation was calculated using background subtraction, and was assumed to be correct and certain. However, this assumption was invalid when PMT gain drift occurred, as in Figures 3.8, 3.10, 3.11 and

3.13. Calculated RMDs and RMADs were uncertain as a result. For this reason, the correction methods were not classified as being successful or unsuccessful models of the time-dependent scintillation. Instead, the RMDs and RMADs were used to determine which estimates best matched BS, where BS had performed superior to all other estimates for dosimetry.

Through comparison of the known scintillation with those estimated by the proposed methods, the NLLS estimate of scintillation was a better descriptor of the known scintillation than the OLS estimate of scintillation in the central region of the beam profiles. For the out of field regions, measured signals suffered from significant quantities of measurement noise, and both the OLS and NLLS estimates of scintillation were comparatively poorer descriptors of the known scintillation than in the central regions. For the central regions, it seems intuitive that the NLLS correction was the better estimator of the time-dependent scintillation given the NLLS correction could optimise the parameters τ_d and τ_r, whereas the OLS correction had used fixed values of $\tau_d = 285\,\text{ns}$ and $\tau_r = 19.5\,\text{ns}$. The optimal values for τ_d and τ_r are plotted in Figure 3.16 as a function of measurement position for each of the NLLS profiles measured in the $10\,\text{cm} \times 10\,\text{cm}$ fields. From these distributions of τ_d and τ_r, mean values and standard deviations were calculated, limited to the central regions of the profiles. For the 6 MV beam energy, τ_d had a mean value of $(272 \pm 5)\,\text{ns}$ and τ_r had a mean value of $(0.53 \pm 0.13)\,\text{ns}$, taking 2 standard deviations as the uncertainty. For the 10 MV beam energy, τ_d had a mean value of $(275 \pm 6)\,\text{ns}$ and τ_r had a mean value of $(0.85 \pm 0.43)\,\text{ns}$. Given the difference between the NLLS optimised values of τ_d and τ_r and the expected values of $\tau_d = 285\,\text{ns}$ and $\tau_r = 19.5\,\text{ns}$ supplied by Saint Gobain, these results indicate that the OLS estimate calculated a sub-optimal time-dependent scintillation.

Curiously, the OLS and NLLS estimates of the total PSD signals closely match one another, as well as the measured PSD signal in spite of the OLS's suboptimal estimate of the time-dependent scintillation. This agreement is observable in Figure 3.17, where BS total is the measured scintillation, OLS total is the OLS's estimate of the PSD signal and NLLS total is the NLLS's estimate of the PSD signal. It should be noted that the OLS estimate of scintillation (OLS scint) does not reproduce the sharp spikes of the known scintillation (BS scint) that occur between 5800 ns and 6500 ns in Figure 3.17. Conversely, the NLLS estimate of scintillation (NLLS scint) successfully reproduces these sharp spikes of the known scintillation signal between 5800 ns and 6500 ns. Given that the OLS and NLLS estimates of the total signal closely match the measured PSD signal, it is expected that the OLS algorithm systematically underestimates the value of $\hat{a}$ and overestimates the value of $\hat{b}$ to compensate for the less temporally resolved estimate of the time-dependent scintillation (calculated using $\tau_d = 285\,\text{ns}$ and $\tau_r = 19.5\,\text{ns}$). This tendency explains the difference between the NLLS RMD and OLS RMD in the central regions, where the OLS

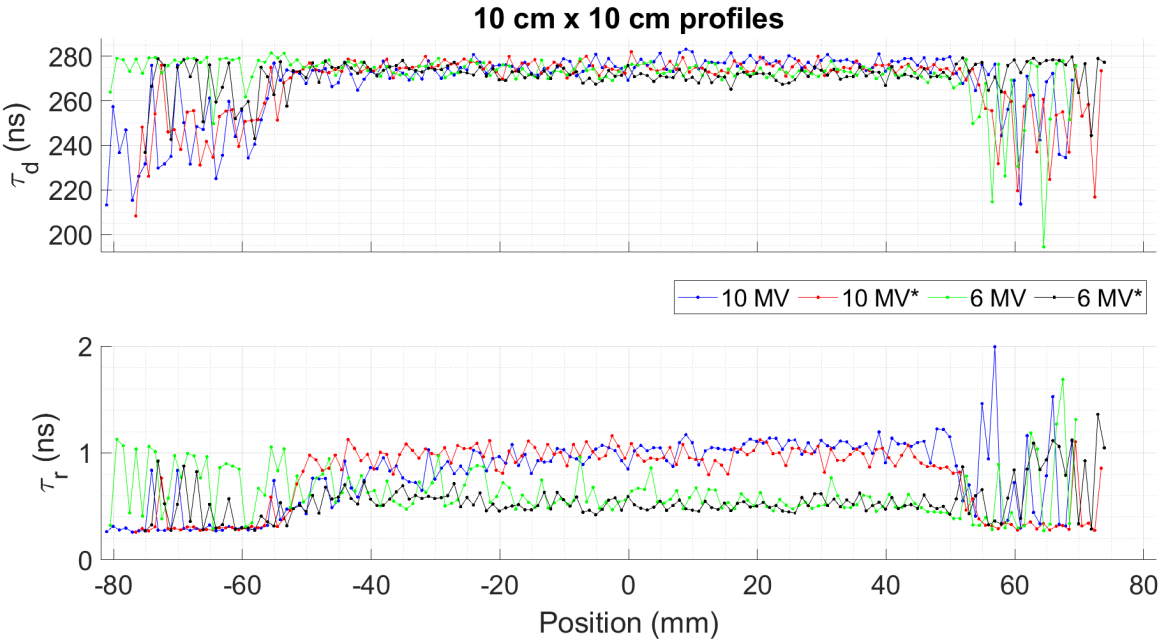

Figure 3.16: Top: values for τ_d for the 10 cm $\times$ 10 cm fields optimised during the NLLS method, plotted as a function of measurement position. Bottom: corresponding values for τ_d optimised through the NLLS method plotted as a function of measurement. In the legend, * denotes that the profile was measured along the in-plane axis and the absence of * denotes the profile was measured along the cross-plane axis, as in Table 3.1, and Figures 3.10 and 3.13.

estimate of scintillation systematically underestimates the NLLS estimate of scintillation by a value of 4.2 % relative to the amplitude of the known scintillation. For this reason, the NLLS corrections should be used in preference to the OLS corrections when the exponential constants of the scintillator have not been verified experimentally.

Each of the ANNs and CNNs had comparatively poor performances with regards to the BS, OLS and NLLS corrections. The ANN had performed worse than the CNN for dosimetry, having increased MADs for all profiles except the 3 cm $\times$ 3 cm profile profile presented in Figure 3.7. In all profiles except the 3 cm $\times$ 3 cm profile, the central regions of the ANN profile possessed significant slants. These slants appeared in the corresponding CNN profiles of Figures 3.8, 3.11 and 3.13, however the CNN did not reproduce these trends in Figures 3.9, 3.10 or 3.12. Given that these slants were reproduced in some of the CNN profiles but not all CNN profiles, and these slants appeared for profiles at both beam energies, these slants arose partially due to some sub-optimal aspect of the training methodology common to both the ANNs and CNNs methods. One likely sub-optimal aspect was the generative model used to synthesise the training data for the ANNs and CNNs. The generative model assumed that the sole scintillation responses calculated by BS were exactly correct, having subtracted the exact magnitude of Cerenkov radiation present from the total PSD signal. This assumption would be voided PMT gain drift during the measurement of the PSD and reference probe signals. In retrospect, the

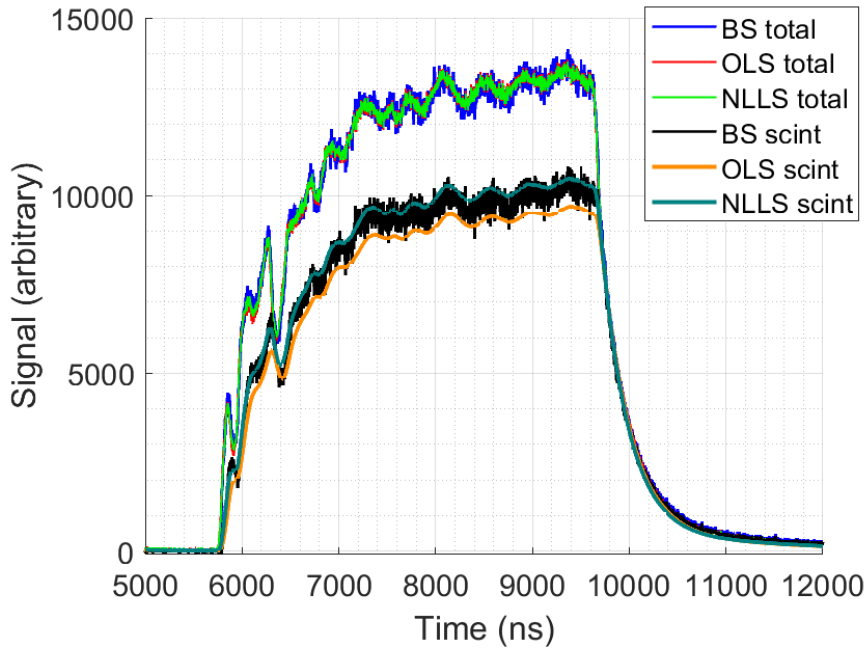

Figure 3.17: OLS and NLLS estimates of the total PSD signal and the scintillation, compared against the measured PSD signal and known scintillation. In the legend, BS total is the measured PSD signal, OLS total is the OLS estimate of the modelled PSD signal, NLLS total is the NLLS estimate of the modelled PSD signal, BS scint is the scintillation calculated using BS, OLS scint is the OLS's estimate of scintillation and NLLS scint is the NLLS's estimate of scintillation.

PMTs were susceptible to PMT gain drift, with gain drift affecting 4 of 7 measured profiles. Consequently, it is likely that the synthesised training data had incorrect estimates of the scintillation and Cerenkov radiation present in the preprocessed training data signals. As a result, the trained ANNs and CNNs would be prone to systematic deviations when analysing real data. Such a result would cause the ANN's and CNN's calculated RMDs and RMADs to be inflated above those of the OLS and NLLS, as was observed. To improve the performance of the ANN and CNNs, a better generative model would be required to synthesise the training data.

The translation of trained ANNs and CNNs for analysis with other LINACs or PSD dosimetry systems is not recommended. For the case of the single Varian 21iX Clinac that was used for all measurement in this chapter, there was significant variation in the time dependence of Cerenkov radiation at beam energies of 6 MV and 10 MV. Given this, there is likely to be significant variations in the time dependences of scintillation and Cerenkov radiation signals when comparing measured PSD signals from one LINAC against those from another LINAC. The CNN's performance is expected to be degraded when analysing PSD signals measured with different LINACs to those that were used to generate their training data. For the case of translation with other PSD dosimetry systems, the time dependence of the scintillation will vary in the event other scintillator materials

are used.

The training data was synthesised using theoretical beam profiles to closely match the distribution of the testing dataset. It is expected that the trained ANNs and CNNs would perform poorly in significantly different measurement conditions as the training distribution was highly specific, modelling the dose profiles of the testing dataset. Additionally, the training dataset was limited to a size of 10721 training samples due to CPU and GPU memory constraints at the time of training. Bends in the optical fibres affect the collection and transmission of optical signals, which consequently affects the intensity of measured scintillation and Cerenkov radiation signals. For the training data synthesis framework presented in this chapter, variations in the setup of the optical fibres are not accounted for. To train the ANNs and CNNs to for improved generalisation with regards to variations in setup, it is recommended that the scaling factors be sampled from a random uniform distribution with a minimum value of 0 and maximum value greater than S_{max} and C_{max} instead of the modelled dose profiles used in this work. Additionally, for improved performance, it is recommended that the networks be trained on a larger training dataset.

In the literature, the most popular alternative to the BS correction is the chromatic removal method, having been investigated thoroughly by several research groups [74, 76, 186]. Of all the publications in the literature, only one direct comparison of the BS correction and chromatic removal is reported. Archambault *et al.* compared the chromatic removal and background subtraction corrections, evaluating their corrected responses with respect to an ionisation chamber [76]. For the few photon beam PDDs measured, chromatic removal had a MAD of 0.52 % and BS had a MAD of 0.67 %. The global MAD for BS reported in this chapter was 0.7 %, matching that reported by Archambault *et al.* [76]. Though comparisons between BS and chromatic removal are limited, the performance of chromatic removal method appears superior to the OLS and NLLS corrections.

In future work, it is anticipated that the proposed NLLS and CNN corrections will be investigated further. The implementation of gain drift correction methods would benefit each of these corrections. For the case of the NLLS correction, the corrected profiles would not have had slants in their central regions as in Figures 3.8, 3.11 and 3.13, leading to reduced MADs and maximum discrepancies. For the case of the CNN correction, the training data would have better reflected the real data used to test the CNN, and it is anticipated that the CNN would be free of it's systematic deviations with respect to the ionisation chamber. Additionally, the PSD dosimetry system should be optimised to increase the signal to noise ratio of measured signals. Archambault *et al.* had reported that optical filtration had improved the signal to noise ratio of both BS's and chromatic removal's estimates of scintillation [76]. Consequently, each of the presented correction methods may benefit from the use optical filtration, reducing the random fluctuations

in the presented profiles. With these optimisations, the performance of the NLLS and CNN corrections are expected to improve, potentially matching that of chromatic removal reported in the literature.

3.5 Conclusions

From the MAD statistics calculated, the BS correction was determined to be the most accurate stem signal correction method that can be applied with the developed in-house PSD dosimetry system. The OLS and NLLS corrections had performed at a similar level of accuracy to BS when compared with the ionisation chamber in the central regions of profiles, however the BS correction's performance was superior to the OLS and NLLS corrections in the out of field regions of the profiles. Providing that the PSD is not being used in radiation fields with high spatial dose gradients, the BS correction is recommended over the current temporal methods. For measurements in radiation fields with high spatial dose gradients, the NLLS correction is recommended as an alternative to the BS correction. This recommendation is given as NLLS correction's performance matched the BS correction's performance in the central region, and the NLLS estimate of scintillation was semantically better than OLS. In general, the trained ANNs performed poorly as they were unable to reproducibly identify the time-dependent Cerenkov radiation present in the scintillation decay tail; consequently, the proposed ANN correction is not recommended. In general, the trained CNNs had generally poor performances, being trained on synthetic data that could not accurately represent the real data. However, the CNN had uncharacteristically outperformed the BS correction for the profile presented in Figure 3.10. If the CNN was trained with suitable training data, the results of Figure 3.10 suggests that the CNN correction could also be a worthwhile alternative to the BS correction for measurements in high spatial dose gradients.

Chapter 4

Feasibility of PSDs for MRI-LINAC dosimetry

This chapter presents the experimental investigations with an in-house plastic scintillation dosimeter (PSD) and the Australian MRI-LINAC. The PSD dosimetry system used the same photomultiplier tubes (PMTs) and digital oscilloscope as for the measurements in Chapter 3. However, the PSD was different from that used in the temporal stem signal correction investigations in Chapter 3. Output factors measured with the Farmer chamber and microDiamond detector were published in Madden *et al.* 2019 [106]. However, the PSD output factors presented in this chapter differed from those published in Madden *et al.* 2019 [106], re-measured using the daisy chain methodology described in Section 4.2.3 to avoid the effects of PMT gain drift. Presented beam profiles for the PSD and film were published in Madden *et al.* 2020 [187]. The presented percent depth dose distributions (PDDs) for the PSD, film and Farmer chamber were published in Madden *et al.* 2021 [188]. Monte Carlo simulations were built and run using the Geant4 simulation toolkit post-publication to provide additional reference data.

L. Madden, J. Archer, E. Li, U. Jelen, B. Dong, N. Roberts, L. Holloway, A. Rosenfeld. First measurements with a plastic scintillation dosimeter at the Australian MRI-LINAC. *Phys. Med. Biol.* 2019; 64(17):175015. 10.1088/1361-6560/ab324b. [106]

L. Madden, J. Archer, E. Li, U. Jelen, B. Dong, L. Holloway, A. Rosenfeld. MRI-LINAC beam profile measurements using a plastic scintillation dosimeter. *Phys. Medica.* 2020; 73:111-116. 10.1016/j.ejmp.2020.04.016. [187]

L. Madden, N. Roberts, U. Jelen, B. Dong, L. Holloway, P. Metcalfe, A. Rosenfeld, E. Li. In-line MRI-LINAC depth dose measurements using an in-house plastic scintillation dosimeter. *Biomed. Phys. Eng. Express.* 2021; 7(2):025012. 10.1088/2057-1976/abe295. [188]

4.1 Introduction

PSDs have a set of advantageous qualities that make them highly water equivalent for the high energy photons and electrons produced by LINACs and near-correctionless for relative dosimetry with LINACs. Given this set of qualities, PSDs were suspected to be highly suitable for relative dosimetry with MRI-LINACs. Previous studies investigating PSDs for MRI-LINAC dosimetry characterised the change in response arising with the magnetic field [164, 165], characterised their directional dependence in magnetic fields [166] and investigated how stem signals are affected by magnetic fields [189]. No studies had investigated whether PSDs remain feasible for relative dosimetry with MRI-LINACs; the work in this chapter aims to quantify how accurate PSDs are for relative dosimetry with MRI-LINACs.

4.2 Materials and methods

4.2.1 The Australian MRI-LINAC

The Australian MRI-LINAC consists of a 1 T open-bore MRI-scanner (Agilent, UK) and an industrial linear accelerator (Linatron-MP, Varex, USA). The linear accelerator is a horizontal beamline that is fitted with multileaf collimators (Millennium 120, Varian, USA) as the Linatron has no secondary collimators, and so all fields are defined with the MLCs. As discussed in Section 2.3, the Australian MRI-LINAC uses an in-line orientation such that the fringe magnetic field extends outward in the direction of the Linatron. The Linatron and MLCs were mounted on rails so that the source to isocentre distance (SID) could be varied, allowing for them to be positioned so that the fringe field's influence on beam formation and MLC operation can be mitigated. Achievable SIDs ranged from 1.869 m to 3.269 m. For all measurements, the Linatron had a nominal beam energy of 6 MV and was set to deliver pulses of radiation at a frequency of 200 Hz.

4.2.2 The PSD dosimetry system

The in-house PSD consisted of a cylindrical volume of plastic scintillator optically coupled to a plastic optical fibre, modelled in Figure 4.1. The plastic scintillator material used was BC444 (Saint Gobain, France), chosen for it's relatively slow decay constant that enables temporal based Cerenkov radiation correction methods. The plastic scintillator volume had a diameter of 2 mm and a length of 0.8 mm. The plastic optical fibre used was a jacketed Eska CK-40 (Mitsubishi Chemicals Co., Japan). The plastic optical fibre had an inner core diameter of (0.98 ± 0.06) mm, a cladding diameter of (1.00 ± 0.06) mm, a jacket diameter of 2 mm and an approximate length of 15 m. The reference probe consisted of a bare Eska CK-40 plastic optical fibre with matching dimensions and

materials to the optical fibre of the PSD, however no scintillator was attached in order to measure only Cerenkov radiation. The tip of the PSD (*i.e.* scintillator and adjacent fibre) and the reference probe was coated with black paint to make them light tight. At the distal end of the PSD and reference probe, the optical fibres were fitted with male FC optical connectors to make connections with the photodetectors fibre more reproducible.

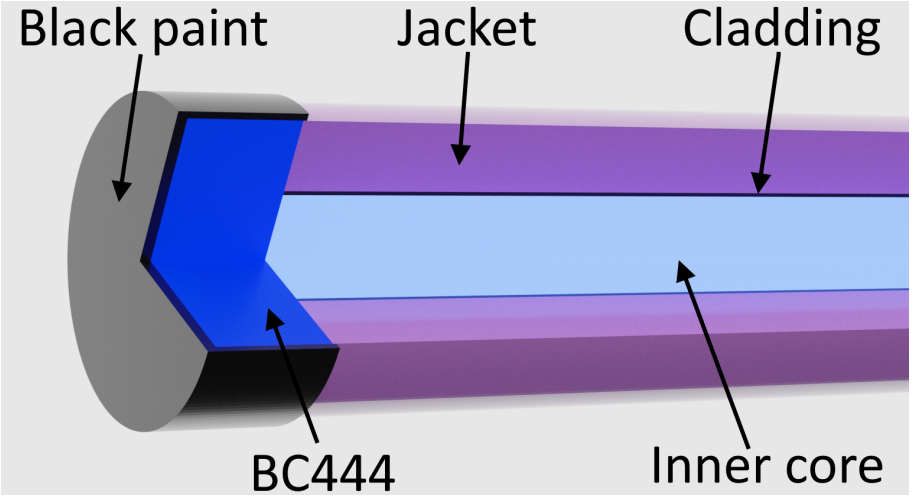

Figure 4.1: 3D model of the in-house PSD with a cutaway to show the coupling of the PSD to the optical fibre; published in Madden *et al.* 2021 [188].

Two matching PMTs (RCA-4526, RCA Corporation, USA) were used for all measurements. These PMTs had a rise time of 2.5 ns, an adequate temporal resolution to resolve the slow scintillation signal. For all measurements, the PMTs were operated in DC mode, at their maximum gain to make their operational characteristics as reproducible as possible across all experimental measurements. A digital oscilloscope (PicoScope PS6404D, PicoTech, USA) was used to simultaneously record the photoconverted PSD and reference probe signals as voltage-time waveforms, with each waveform saved on a personal computer. For all measurements, the digital oscilloscope sampled at a frequency of 625 MHz. 1 MΩ resistance was used, with a maximum available bandwidth of 500 MHz. A typical waveform recorded by the digital oscilloscope is presented in Figure 4.2.

For all measurements, a triggering signal was used to synchronise the digital oscilloscope's recorded waveforms with each pulse of radiation. No synchronisation signal was produced by the Linatron as is usually the case for clinical LINACs. Instead an external trigger signal was provided by using a "fast" dosimeter placed in the path of the radiation beam; the oscilloscope has functionality that allows for signals prior to the trigger to be included in the measured waveform[a]. For all PSD measurements, a scintillating fibre

[a]The oscilloscope continuously samples signals while waiting for the trigger and transfers them into it's memory buffers; once the trigger signal is received, the oscilloscope keeps a user-specified number of samples prior to the trigger and incorporates these samples into the desired waveform

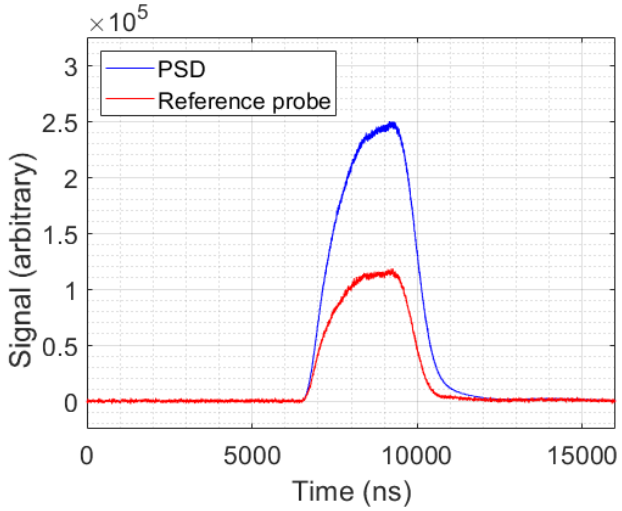

Figure 4.2: Typical PSD and reference probe waveforms produced in response to the MRI-LINAC's pulsed radiation beam. PSD signals (blue) are comprised of scintillation and Cerenkov radiation, and reference probe signals (red) are comprised purely of Cerenkov radiation. Published in Madden *et al.* 2019 [106].

(BCF-60, Saint Gobain, France) and silicon photomultipliers (MiniSM-30035, SensL, Ireland) were used to produce the trigger signal. The scintillating fibre was placed in the path of the radiation beam upstream of the MLCs, such that it would be irradiated whilst remaining out of the field shaped by the MLCs. The setup of the triggering fibre is modelled in Figure 4.5.

For all measurements, a fixed quantity of monitor units was delivered. During beam delivery, the PSD and reference probe's responses to each individual pulse of radiation were stored in the oscilloscope's memory buffer as individual waveforms. After beam delivery had terminated, the stored waveforms were summed across all radiation pulses, integrating the PSD and reference probe signals to reduce the memory required to save the data and reduce the statistical noise in measured signals.

Stem signal correction method

The background subtraction method was applied to correct for Cerenkov radiation stem effect in measured PSD signals. The implementation of the background subtraction method matches that described in the Chapter 3. The reader is referred to Section 3.2.2 for details on background subtraction's implementation.

Gain drift correction

Due to PMT gain drift, the calibration factor can vary over long measurement periods. PMT gain drift occurs as the PMT's gain is dependent on it's temperatures. As the PMTs are operated, they produce waste heat and their gains increase with increasing tempera-

ture. This effect is problematic for background subtraction, requiring corrections for the gain drift effect when measurements occur over a long period of time. For the measurement of output factors and beam profiles, an interpolation based gain drift correction was used. In the interpolation based gain drift correction, the time when each measurement was taken (from the computer's clock) was recorded along with the PSD and reference probe signals. The PMTs were cross calibrated before and after the measurements were taken, with the time of calibrations recorded. Linear interpolation was then used to predict the calibration factor that would be measured at each measurement time.

For the measurement of the presented output factors and PDDs, a daisy chaining methodology was used to improve the robustness of the interpolation based gain drift correction. In this daisy chaining methodology, a reference measurement was taken between each of the output factor and PDD measurements. For the output factors, the reference field size was chosen to be the response in the 10.5 cm $\times$ 10.5 cm field. For the PDDs, the reference depth was chosen to be the 10 cm depth. Through analysis of the change in responses at the reference point, the change in each PMT's gain was determined.

4.2.3 Experimental measurements

Output factors

Relative output factors were measured with the in-house PSD, a Farmer ionisation chamber (FC65G, Scanditronix/Wellhofer, Germany) and a microDiamond detector (PTW60019, IBA Dosimetry, Germany). Gammex RMI457 Solid Water was used as the phantom material for all output factor measurements. A 30 cm $\times$ 30 cm $\times$ 30 cm phantom size was used for all measurements, with the 10 cm depth aligned to the MRI's isocentre. The output factors were measured at an SID of 2.469 m, and at depths of 10 cm and 20 cm. Field sizes ranged between between 2.6 cm $\times$ 2.6 cm and 21.0 $\times$ 21.0 cm.

The Farmer chamber was orientated with it's central axis aligned vertically, perpendicular to the photon beam and magnetic field. The Farmer chamber was inserted into a 3 cm thick slab of Solid Water with a housing bore hole. The bore hole was filled with water prior to the Farmer chamber's insertion to prevent the formation of air gaps around the chamber. For the perpendicular chamber orientation in the 1 T in-line magnetic field, the Farmer chamber's EPOM is located 0.4 times the radius upstream from the chamber's geometric centre. The Farmer chamber's radius was 3.1 mm, such that the effective point of measurement was located approximately 1 mm upstream from the chamber's centre. This EPOM was accounted for when setting up, such that an extra 1 mm of Solid Water was used to achieve the desired depth of measurement. A perspex stand was used to hold the Solid Water slabs vertically and clamp them together to mitigate the formation of air gaps between the slabs; this stand is shown in Figure 4.3. The Farmer chamber was read

out by a reference class electrometer (DOSE-1, Scanditronix/Wellhofer, Germany) at a 300 V bias. No correction factors were applied to it's response as these are cancelled out when normalising by the response at the 10.5 cm × 10.5 cm field size for the relative output factors. The Farmer chamber's response was measured 3 times at each field size to determine the reproducibility of it's response in these conditions, serving as a benchmark for the reproducibility of the PSD.

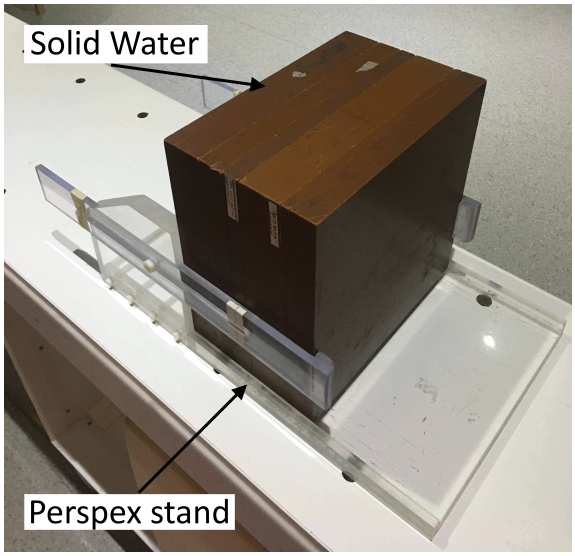

Figure 4.3: Labelled picture of the perspex stand used clamp the Solid Water together whilst stood vertically.

The microDiamond detector was orientated horizontally with it's central axis antiparallel to the photon beam and magnetic field; this setup orientation is visible in 4.4 (a). An in-house housing aperture was used to house the microDiamond detector, consisting of a 3 cm × 3 cm rectangular block of Solid Water that was machined with a bore hole. This bore hole was machined to tightly fit the microDiamond detector face on and flush to it's surface such that the formation of air gaps was mitigated; the microDiamond is shown housed in the 3 cm × 3 cm rectangular block of Solid Water in Figure 4.4 (b). Depth of measurement was controlled by shifting the microDiamond's housing back and placing machined 3 cm × 3 cm pieces of Solid Water in front of the housing. The microDiamond's EPOM was located 1 mm behind it's packaging's surface [190]; this EPOM was accounted for when setting up the microDiamond for measurements at the desired depths. The microDiamond was read out by the same electrometer as the Farmer chamber (DOSE-1, Scanditronix/Wellhofer, Germany). The microDiamond's response was measured 3 times at each field size to determine the standard deviation of it's response.

The setup for the PSD measurements of output factors is modelled in Figure 4.5. An optical fibre housing aperture was used to house the PSD and reference probe. The housing aperture consisted of a 1 cm × 30 cm × 30 cm slab of perspex with a 2 mm wide ×

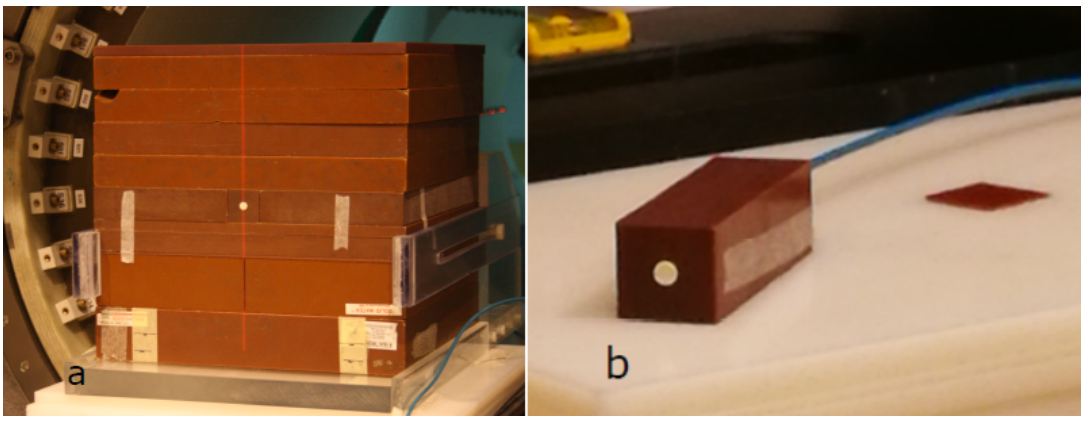

Figure 4.4: Pictures of the Solid Water setup used for the microDiamond detector. In (a), the microDiamond detector setup is shown for the measurement of output factors in Solid Water. In (b), the Solid Water housing for the microDiamond detector is show, with the microDiamond detector seated in the housing. Published in Roberts *et al.* 2019 [133].

4 mm deep housing groove machined into it's surface. The housing groove was filled with ultrasound gel (Aquasonic 100, Parker Laboratories Inc., USA) to avoid the formation of air gaps between the PSD and the perspex. The PSD and reference probe were aligned so that equal lengths of optical material were irradiated, and were placed in the housing groove. The PSD was placed so that it was upstream of the reference probe when set up in Solid Water. The optical fibre housing was stood vertically and orientated such that the PSD's and reference probe's central axes were aligned vertically as shown in Figure 4.5. The perspex stand was used to hold the slabs of Solid Water and the optical fibre housing for all measurements to prevent the formation of air gaps between the Solid Water slabs and the perspex housing. The PSD's EPOM was located at the geometric centre of the scintillator; this intrinsic 1 mm EPOM was accounted for when determining the desired measurement depth. The PSD's response was measured 3 times at each field size to determine the standard deviation in it's response, and 2 times for each reference field size to determine the standard deviation in each reference measurement.

Beam profiles

Relative beam profiles were measured with the in-house PSD and radiochromic film (GafChromic EBT3, Ashland Inc., USA). Beam profiles were measured at SIDs of 1.869 m and 2.469 m, for depths of 1 cm, 5 cm, 10 cm and 20 cm. Each phantom was set up so that the 10 cm depth was aligned to the MRI's isocentre. The nominal field size at isocentre was 1.9 cm $\times$ 1.9 cm for the 1.869 m SID and 2.6 cm $\times$ 2.6 cm at 2.469 m SID.

The PSD's setup for the measurement of beam profiles is shown in Figure 4.6. The PSD's phantom consisted of a perspex water tank filled with de-ionised water. The tank's outer dimensions were 37 cm $\times$ 30 cm $\times$ 42 cm and it's wall thickness was 8 mm. A

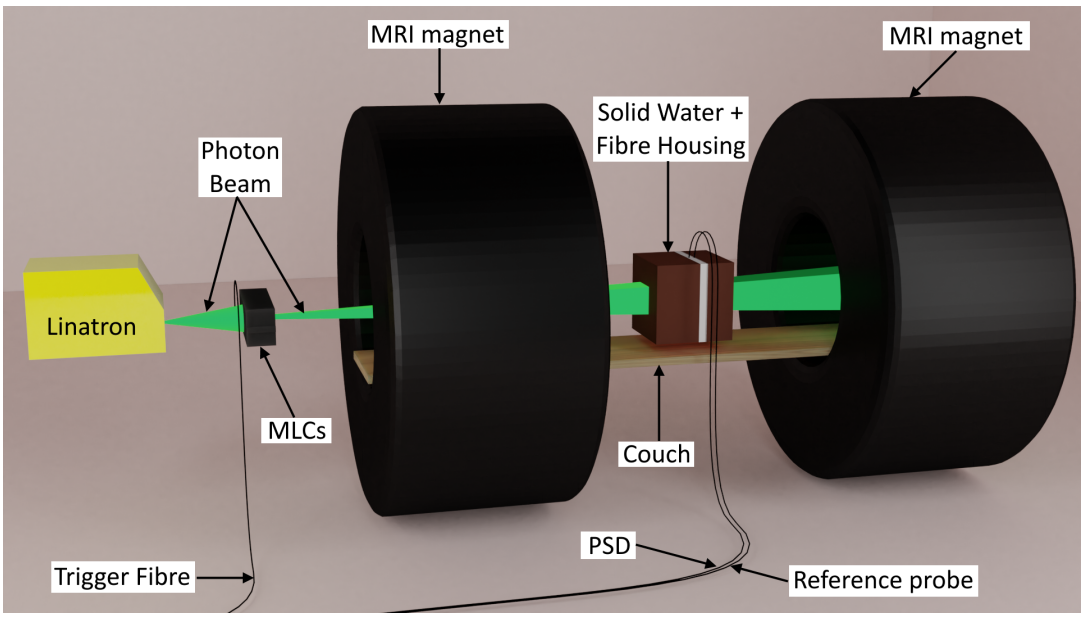

Figure 4.5: 3D model showing the Australian MRI-LINAC and the Solid Water setup used by the in-house PSD for the measurement of output factors and PDDs. Published in Madden *et al.* 2021 [188].

manual linear translation stage (MT-DDA, Med Tech Inc., USA) was used to vertically position the PSD at desired off axis positions. The translation stage's minimum step size was 0.1 mm, thus the PSD's off axis position had an uncertainty of 0.05 mm. A 1 cm $\times$ 2 cm $\times$ 16 cm piece of Solid Water was machined with a 2 mm deep $\times$ 4 mm wide housing groove to hold the PSD and reference probe while in the water tank. The PSD and reference prove were aligned and placed abreast in the housing groove such that the PSD was upstream of the reference probe. The PSD and reference probe were orientated horizontally so that their central axes were perpendicular to the photon beam and magnetic field to minimise the Cerenkov radiation collected by each optical fibre. A step size of 2.5 mm was used to sample each beam profile with the PSD. Each off axis position was measured 3 times to determine the standard deviation in the PSD's response.

Gammex RMI457 Solid Water was the phantom material for all film measurements. The film was orientated perpendicular to the photon beam and magnetic field, sandwiched between vertical slabs of Solid Water; a diagram of this setup is shown in Figure 4.7 (b). The perspex stand was used to tightly press the Solid Water slabs together in order to mitigate the formation of air gaps between the film and Solid Water slabs. The batch of films was calibrated using a 6 MV Elekta photon beam at the Liverpool Cancer Therapy Centre. The processing and handling of films followed published recommendations [69, 191]. All films were read out 24 hours after they were irradiated. Films were scanned at a resolution of 72 dpi with 48 bit RGB colour depth using an EPSON V700 Photo flat bed scanner (EPSON, Japan). All scanning corrections were turned off when scanning the films. A thin sheet of glass was placed on top of the film to prevent bowing of the films

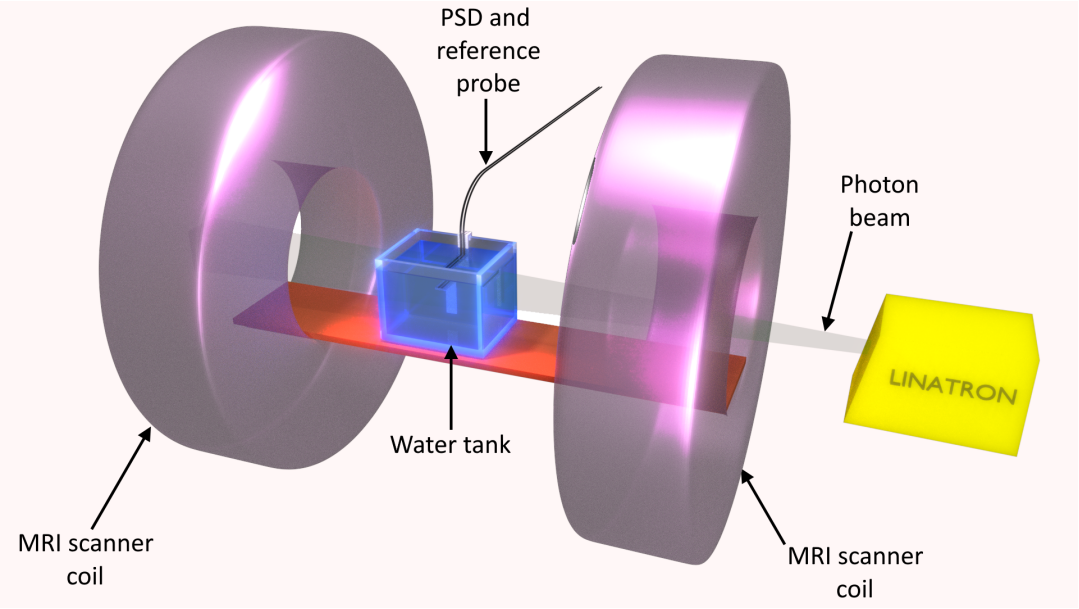

Figure 4.6: Labelled 3D model showing the Australian MRI-LINAC and the water tank setup for the measurement of vertical beam profiles with the in-house PSD. Published in Madden *et al.* 2020 [187].

during readout. A black paper sheet with a cut-out was used to reproducibly position each film on the scanner, reducing the scanner readout uncertainty due to non-uniformity. Only the red channel was used when converting the film's optical density to absorbed doses. Once converted, a 5 pixel wide moving average filter was applied to each profile to reduce statistical noise.

During analysis, the empirical penumbra model developed by Tang *et al.* was fit to each of the PSD and film profiles' penumbra [192]. This model was used to determine the positions of the 20 %, 50 % and 80 % relative dose values in each penumbra. The penumbra model was favoured over linear interpolation as the PSD's 2.5 mm step size makes linear interpolation an inaccurate method in determining the sought positions. Penumbra widths were calculated by finding the penumbral positions where the relative doses were 20 % and 80 % of the maximum dose in the fit models. The central position of each profile was calculated by taking the average of the left and right 50 % dose positions; all beam profiles were translated so that their calculated central position was aligned with the origin.

Percent depth dose distributions

Relative percent depth dose distributions were measured along the central axis with the in-house PSD, a Farmer chamber (Scanditronix/Wellhofer FC65G, Germany) and radiochromic film (GafChromic EBT3 film, Ashland Inc., USA). PDDs were measured at an SID of 2.469 m for field sizes ranging between 2.6 cm × 2.6 cm to 18.4 cm × 18.4 cm. The 10 cm depth of the phantom was aligned to the MRI's isocentre. Gammex RMI457

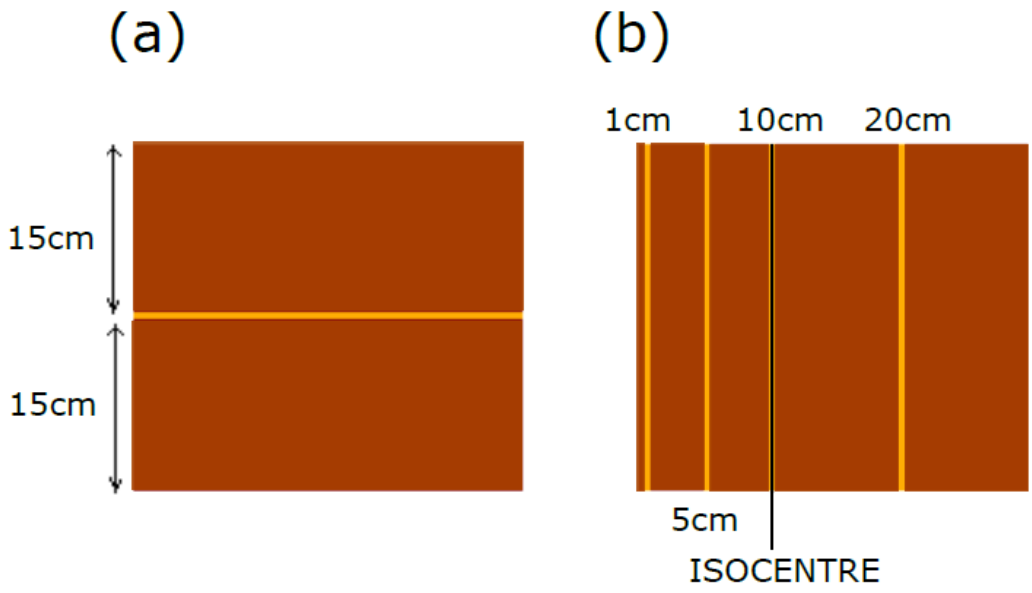

Figure 4.7: Diagram showing the film setup in Solid Water. In (a) the setup for PDD measurements is shown, and in (b) the setup for beam profile measurements are shown for each of the measurement depths. Courtesy of Natalia Roberts.

Solid Water was the phantom material for all measurements. The PSD was placed upstream of the reference probe in the optical fibre housing and orientated vertically, matching the setup described for the measurement of output factors. The optical fibre's housing groove was filled with ultrasound gel, and the Solid Water slabs were held in the perspex aperture. Similarly, the Farmer chamber was housed in the Solid Water housing used during the measurement of output factors. The bore hole was again filled with water and the Farmer chamber was orientated with it's central axis aligned vertically. For measurements with film, the film was orientated horizontally and sandwiched between two 15 cm thicknesses of Solid Water as shown in Figure 4.7. The film readout analysis procedure matched that described for the measurement of beam profiles. The film used in the measurement of PDDs belonged to the same batch as those used for the measurement of beam profiles.

4.2.4 Monte Carlo simulations

Monte Carlo simulations were built using the Geant4 simulation toolkit (version 10.7.p02). The Australian MRI-LINAC was previously modelled in Geant4 [193], with the simulation geometry optimised so that simulated beam profiles and PDDs had matched corresponding measured distributions to within $\pm 2\,\%$ [193]. This previously modelled simulation geometry of the Australian MRI-LINAC was used to obtain reference data for the experimentally measured output factors, beam profiles and percent depth dose distributions in this chapter.

In each simulation the MRI scanner, the linear accelerator's head and the MLC leaves were modelled and positioned in the world volume to match the experimental setup. The MRI scanner and it's components were modelled following vendor specifications of the scanner components and their component's materials. The linear accelerator's head was modelled based upon the vendor's specifications of materials and geometry; modelled components included the transmission target, the primary collimators, the monitor chamber and the exterior casing. For the MLCs, each individual leaf was modelled following vendor specifications for geometry and materials. The MRI's magnetic field was modelled externally in COMSOL Multiphysics (Stockholm, Sweden) using a finite element method, modelled for each simulation geometry; it should be noted that the magnetic field influences the linear accelerator's electron beam upstream of the transmission target and significantly affects secondary electron transport downstream of transmission target [194]. These resultant fringe magnetic fields are dependent on the source-isocentre distance and the potential magnetic shielding effects introduced by the MLCs [119, 195, 196], hence this magnetic field modelling was performed for each simulation geometry. Modelled magnetic fields were stored in a lookup table, and read into the simulations with identical geometries. The modelled physics processes for the simulations were the photoelectric effect, Compton scattering, pair production, internal gamma conversion, multiple scattering, bremsstrahlung, ionisation and annihilation. Range cuts were defined to be 0.1 mm for all particles, and the step limit was defined to be 1 mm.

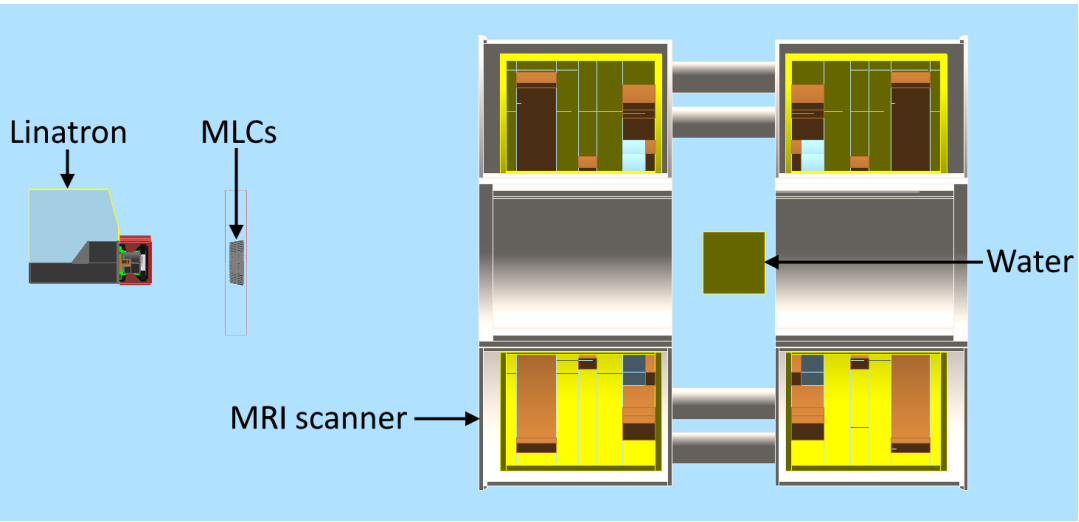

Figure 4.8: Simulation geometry of the Australian MRI-LINAC modelled in Geant4 with cutaway to show the components of the linear accelerator and MRI scanner.

Each simulation was split into two independent run stages. In the first stage, an electron beam was fired at the LINATRON's transmission target and the particles crossing a plane upstream of the MLCs were scored in a phasespace file. In the second stage of the simulations, the phasespace files were used to generate a radiation beam directed at the

MRI's isocentre. In all second stage simulations, a 30 cm cube of G4Water was placed with it's geometric centre 5 cm downstream from the MRI scanner's isocentre, such that the 10 cm depth was aligned with the MRI's isocentre. In these second stage simulations, the dose distribution deposited in this volume of water were scored in a scoring mesh with 1 mm $\times$ 1 mm $\times$ 1 mm voxel.

Each simulation geometry was split into 200 identical simulations. 10^8 primary electrons were fired in each of the first simulations to generate each phase space files, with approximately 3.3×10^6 particles scored in each phasespace file. As a result, approximately 2×10^{10} primary electrons were generated per simulation geometry and approximately 6.6×10^8 particles were scored in the 200 phasespace files. For each of the second stage simulations, the primary particles in the phasespace files were recycled by a factor of 99 so that an approximate total of 6.6×10^{10} primary particles were run for each simulation geometry. The modelled geometry of these simulations are shown in Figure 4.8.

4.2.5 Analysis

Dose differences

To assess the performance of the in-house PSD, global dose-differences were calculated between the PSD measured distributions and reference distributions. For the case of film measured and simulated dose in water distributions, linear interpolation was used to predict the dose at positions where other detector responses were measured; these interpolated distributions were used as the reference distributions when calculating the differences. Differences were calculated using Equation 4.1 (defined as ΔD) [197].

$$\Delta \mathrm{D}(r) = \mathrm{D}_E(r) - \mathrm{D}_R(r) \tag{4.1}$$

Where $\mathrm{D}_E(r)$ is the dose in the evaluated distribution at position r, $\mathrm{D}_R(r)$ is the dose in the reference distribution at position r. To determine whether dose differences between two distributions were statistically acceptable, these differences were compared against the corresponding combined uncertainty in the dose differences. For measurements with film, the batch of film used for measurements in this chapter had a relative uncertainty of 3.2 % [134]. For simulations and the measurements with the PSD, Farmer chamber and microDiamond, standard deviations were calculated in each of their responses at each measurement position. The uncertainty in each of their responses was taken as two standard deviations of the corresponding mean response at that position, as recommended by NIST primary standards for the reporting of all dosimetric quantities in medical physics [198]. The combined uncertainty in the dose differences was then taken as the sum of the corresponding two detector's uncertainties at each point in the distribution. When the magnitude of the dose difference was less than the corresponding combined uncertainty,

the dose difference was acceptable within the 95 % confidence interval.

Mean absolute differences

Mean absolute differences (MADs) were calculated between each set of measured distributions to determine the average deviation between the PSD, the reference detectors and the simulated distributions. Calculated MAD values were compared to corresponding MAD values for MRI-LINAC dosimetry published in the literature, with the aim of providing context of the performance of the PSD. MADs were calculated using Equation 4.2:

$$\mathrm{MAD} = \frac{1}{N}\sum_{i=1}^{N} |\Delta \mathrm{D}(r_i)| \tag{4.2}$$

Where $\Delta \mathrm{D}(r_i)$ is the dose difference at position r_i, and N is the number of points in the reference distribution.

Gamma index

The difference in dose metric is not suitable for comparing distributions in high spatial dose gradients, *e.g.* the penumbral regions of beam profiles. For beam profiles, global gamma indices (γ) were calculated between the in-house PSD and the reference data for a more suitable comparison of distributions that includes the penumbral regions of beam profiles. The γ metric combines the difference in dose metric with the distance to agreement metric [197]; the distance to agreement corresponds to the minimum euclidean distance between two distributions at equivalent doses. These differences in dose and distance to agreements are compared against preset criteria ($\delta \mathrm{D}$ and δr) to evaluate whether the point in the evaluated distribution lies within an acceptable error with respect to a point in the reference distribution. The formalism for calculation of the γ is:

- Calculate the difference in doses between all reference distributions (*i.e.* film and simulations) and the evaluated distribution (*i.e.* the in-house PSD).
- Calculate the distance to agreement between all reference distributions (*i.e.* film and simulations) and the evaluated distribution (*i.e.* the in-house PSD).

Defining r_R as the position in the reference distribution, r_E as the position in the evaluated distribution, the γ is calculated for each r_E using Equation 4.3:

$$\gamma(r_E) = \min\left(\sqrt{\left(\frac{r_R - r_E}{\delta r}\right)^2 + \left(\frac{\mathrm{D}(r_R) - \mathrm{D}(r_E)}{\delta \mathrm{D}}\right)^2}\right) \tag{4.3}$$

Where D(r_E) is the dose in the evaluated distribution at position r_E, δr is the distance to agreement criterion and δD is the difference in dose criterion. The rationale behind this calculation is: δr and δD form an ellipsoid about each point in the reference distribution. When points in the evaluated distribution lie within one of these ellipsoids, γ will have value ≤ 1 and the evaluated dose at this point is deemed to be passable for the δD(%)/δr(mm) criterion. From the set of $\gamma(r_E)$s calculated for evaluated distributions, the percentage of $\gamma(r_E)$ passing the criterion (referred to as the γ pass-rate) is used to determine whether the evaluated distribution is acceptable. Typically, the evaluated distribution is deemed acceptable when the pass-rate ≥ 95 % for a δD(%)/δr(mm) criterion [197]. For the beam profiles presented in this chapter, the γs and passing rates were calculated for criterion of 1 %/1 mm, 2 %/2 mm and 3 %/3 mm.

4.3 Results

4.3.1 Output factors

The output factors measured at 10 cm and 20 cm depth are presented in the top of Figures 4.9 and 4.10, respectively, with the corresponding uncertainties in the measured responses plotted at the bottom of Figures 4.9 and 4.10, respectively. Dose differences between each of the detectors are presented in the middle of Figures 4.9 and 4.10. MADs and maximum differences in dose are reported in Table 4.1. It should be noted that the Farmer chamber was susceptible to partial volume effects in the 2.6 cm $\times$ 2.6 cm field, causing an underresponse at this field size. The Farmer chamber was not used to measure the response in this 2.6 cm $\times$ 2.6 cm field.

For the 10 cm depth, the PSD, Farmer chamber and microDiamond detector were all within an average value of 0.3 % of each other. Maximum differences in dose at this depth were 0.7 % between the PSD and Farmer chamber, 0.9 % between the PSD and microDiamond detector, and 0.4 % between the Farmer chamber and microDiamond. These maximum differences were less than the corresponding uncertainty of the dose differences. No systematic trends are present when comparing the PSD, Farmer chamber and microDiamond measured output factors. Given this, differences between the output factors arise as a result of statistical measurement fluctuations. The Monte Carlo simulation results had standard deviations greater than 2 % for all field sizes, and so the simulated output factors had uncertainties greater than 4 %. Given these uncertainties, all dose differences with respect to the simulated output factors were less than the corresponding uncertainties in the dose differences. The PSD, Farmer chamber and microDiamond detector had MADs of 1.2 %, 1.7 % and 1.2 % with respect to the simulated doses in water, respectively. Maximum differences with respect to simulations were 3.0 % for the PSD, 2.1 % for the Farmer chamber, and 2.3 % for the microDiamond detector. No systematic

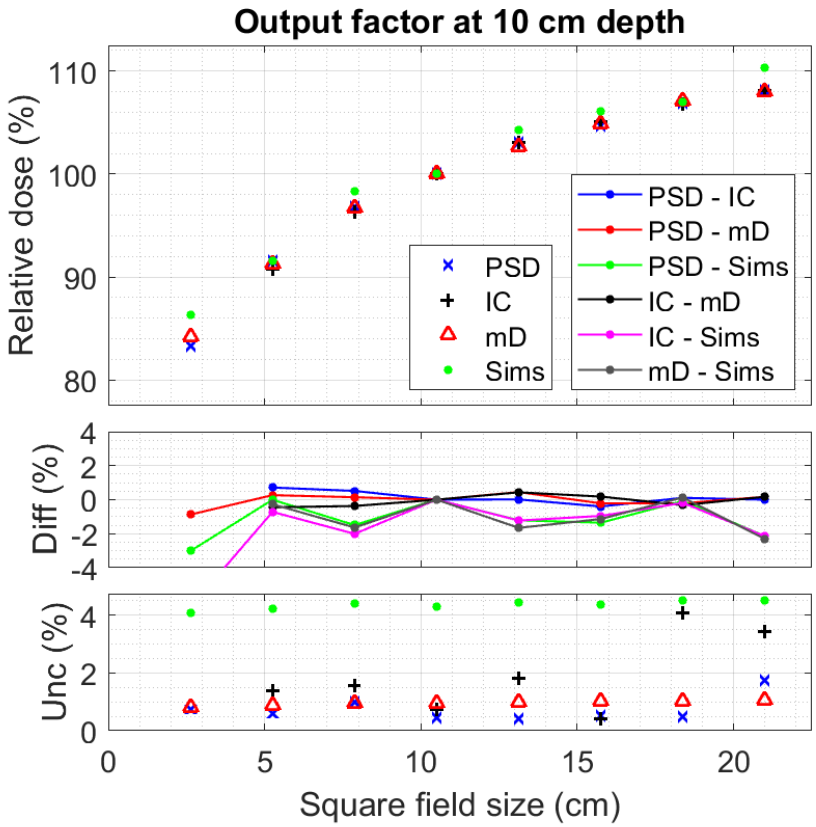

Figure 4.9: Top: output factors at the 2.469 m SID, 10 cm depth. Middle: differences in dose between each detector and the simulation. Bottom: Uncertainties in each of the output factors. In the legend, PSD is the in-house PSD, IC is the Farmer chamber, mD is the microDiamond detector and Sims are the Monte Carlo simulations.

trends were present when comparing the simulated output factors to the measured output factors, suggesting that all reported difference arose as a result of random statistical fluctuations.

The maximum differences between the simulations and the PSD, and the simulations and microDiamond detector occurred for the 2.6 cm $\times$ 2.6 cm, with the PSD and microDiamond under-responding with respect to the simulations. This under-response may be inflated by detector misalignment. For small fields such as the 2.6 cm $\times$ 2.6 cm, it is recommended that detectors are aligned to peak dose in the small field within a tolerance less than 1 mm [12]. The PSD and microDiamond were both aligned to the MRI-LINAC's isocentre projection lasers by eye, such that there was potential for misalignment that could cause a decrease in measured output factor at the 2.6 cm $\times$ 2.6 cm field size. Typically, it is recommended that the centre of the field is found using a scanning water tank for these real-time dosimeters [12]; however, this approach could not be applied at the time of measurement given no MRI compatible scanning water tank was available. Thus for measurements in the 2.6 cm $\times$ 2.6 cm field, there was the potential for misalignment induced underestimations in the small field.

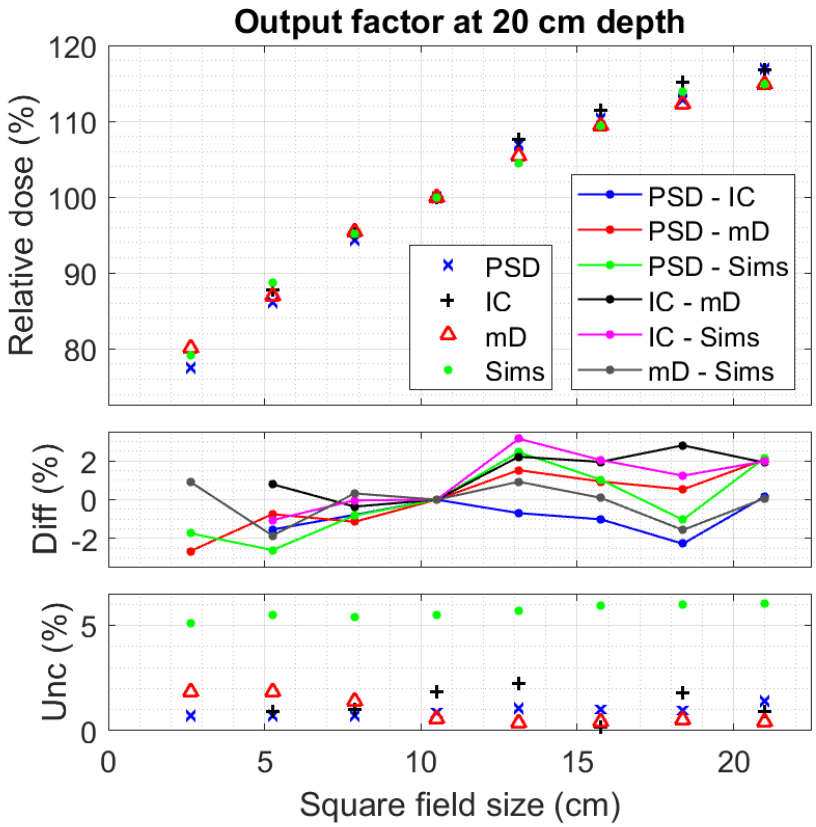

Figure 4.10: Top: output factors at the 2.469 m SID, 20 cm depth. Middle: differences in dose between each detector and the simulation. Bottom: Uncertainties in each of the output factors. As in Figure 4.9, PSD is the in-house PSD, IC is the Farmer chamber, mD is the microDiamond detector and Sims are the Monte Carlo simulations.

For the 20 cm depth, MADs were 0.9 % between the PSD and Farmer chamber, 1.2 % between the PSD, and microDiamond detector and 1.4 % between the Farmer chamber and microDiamond detector. Maximum differences were 2.3 % between the PSD and Farmer chamber, 2.6 % between the PSD and microDiamond detector and 2.8 % between the Farmer chamber and the microDiamond detector. Differences between the PSD and Farmer chamber were less than the difference's corresponding uncertainty, however, differences between the PSD and microDiamond were unacceptable for the 2.6 cm $\times$ 2.6 cm, 13.1 cm $\times$ 13.1 cm and 21.0 cm $\times$ 21.0 cm field sizes. The excessive differences at 2.6 cm $\times$ 2.6 cm may be explained by detector misalignment, however these other disagreement cannot be explained by such setup related effects. Differences between the Farmer chamber and microDiamond were unacceptable for the 3 largest field sizes, in which it appears that the microDiamond increasingly under-responded with respect to the PSD and the Farmer chamber as field size increased above 10.5 cm $\times$ 10.5 cm. It should be noted that the microDiamond's uncertainties at these field sizes had significantly decreased below it's uncertainties for field sizes below 10.5 cm $\times$ 10.5 cm, though the source of this result could not be determined. Simulated doses were on average within 1.5 %, 1.4 % and

	10 cm MAD (%)	20 cm MAD (%)	Global MAD (%)	Global max (%)
PSD - IC	0.3	0.9	0.6	2.3
PSD - mD	0.3	1.2	0.7	2.6
PSD - Sims	1.2	1.5	1.3	3.0
IC - mD	0.3	1.4	0.9	2.8
IC - Sims	1.0	1.4	1.2	3.1
mD - Sims	1.2	0.7	0.9	2.3

Table 4.1: 10 cm MAD and 20 cm MAD are the mean absolute differences for the output factors at 10 cm depth and 20 cm depth. Global MAD is the global mean of the absolute dose differences and Global max is the maximum difference in dose. As in Figures 4.9 and 4.10, PSD is the in-house PSD, IC is the Farmer chamber, mD is the microDiamond detector and Sims are the simulated doses.

0.7 % of the PSD, Farmer chamber and microDiamond detector, respectively. Standard deviations in the simulated doses ranged between 2.5 % and 3.0 %, such that all dose differences were smaller than the corresponding uncertainties in these dose differences.

In the literature, Farmer type ionisation chambers and the PTW60019 microDiamond have been studied extensively to validate their responses in the presence of magnetic fields, important for QA dosimetry with MRI-LINACs. For in-line orientation MRI-LINACs, the response of Farmer chambers remains within 1 % of their corresponding responses with no magnetic field present [199]. With the microDiamond orientated parallel to the in-line magnetic field, the response of the microDiamond detector varied by less than 1 % compared to it's corresponding response with no magnetic field present [149]. With regards to the presented output factors, calculated MADs and maximum differences were similar for the PSD, Farmer chamber and microDiamond detector. Given the Farmer chamber and microDiamond detector were valid and suitable for these output factor measurements, the PSD can be concluded to also be suitable for the measurement of output factors with the in-line MRI-LINAC.

Typically for clinical LINACs, the shape of output factors arises due to two independent effects [200]. Firstly, as field size increases, the dose deposited in the dosimeter increases due to increasing contributions of scattering radiation. Secondly, as field size increases, the dose-rate in the LINAC's monitor chamber decreases due to decreasing scattering from the secondary collimators and MLCs, and so the duration required to deliver the prescribed quantity of monitor units decreases as field size increases. In the Monte Carlo simulations, the first effect is implicitly incorporated into the simulation but the latter effect was not taken into account. The simulations are expected to remain valid due to the unique characteristics of the Australian MRI-LINAC: the LINAC has no secondary collimators and the fitted MLCs are positioned approximately 50 cm downstream from the

LINAC's transmission target. The simulated output factors were within acceptable agreement of all other detectors, hence the effect where increasing field size leads to increasing measurement duration was negligible; otherwise this effect would have caused systematic disagreements between simulated output factors and the measured output factors.

4.3.2 Beam profiles

The measured and simulated beam profiles at 1.869 m SID are presented in Figures 4.11 and 4.12. Similarly, the measured and simulated beam profiles at 2.469 m SID are presented in Figures 4.13 and 4.14. In these profiles, the error bars correspond to the uncertainty in the PSD's response, and the shaded regions correspond to the uncertainty in film's response and the simulation's doses. During the calculation of dose differences and γs, each beam profile was treated as a relative beam profile. To conserve space, the profiles in Figures 4.11−4.14 are shown scaled by the relative central axis PDD response of the PSD for corresponding depths of measurement. To calculate differences in dose between the PSD and film, and the PSD and simulations, linear interpolation was used to sample each of the film and simulated profiles at positions where corresponding PSD measurements were made. For differences between the simulated profiles and film profiles, linear interpolation was used to sample the film profiles at positions where the dose in water was simulated. MADs were calculated for the central regions of the beam profiles (*i.e.* for off-axis positions within the central 80 % of the beam's width) and out of field regions of the beam profile (positions where the relative dose was less than 10 %). Global MADs are presented in Table 4.2.

For the profiles measured at 1.869 m SID in Figures 4.11 and 4.12, the central region ranged between −7.6 mm and +7.6 mm, and the out of field regions were located for off axis positions further than +13.5 mm from the centre of the field. For the central region, the dose differences between the PSD and film were less than the corresponding uncertainty in the dose differences. Similarly, the dose differences between the PSD and simulations, and film and the simulations were less than each dose difference's uncertainties for this central region. MADs for the central region were 1.1 % between the PSD and film, 1.5 % between the PSD and simulations, and 1.2 % between the film and simulations.

For the out of field regions at 1.869 m SID, the PSD and film profiles were generally in close agreement. The dose differences between the PSD and film were less than these dose difference's uncertainties for all out of field positions in these profiles, except for the −15 mm position at 10 cm depth. This was the only disagreement, and so it was expected to be the result of a random statistical fluctuation. The dose differences between the PSD and simulations, and film and simulations had their profiles in agreement for the positions

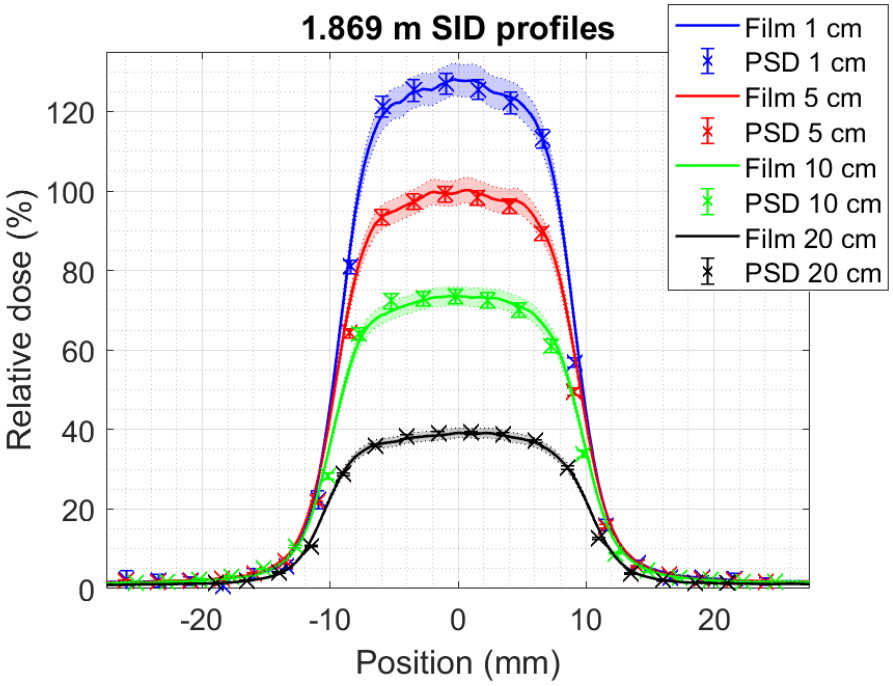

Figure 4.11: Beam profiles measured with the in-house PSD and radiochromic film, for the 1.869 m SID, 1.9 cm × 1.9 cm field. In these figures, PSD is the in-house PSD and Film is EBT3 film. Error bars correspond to the uncertainty in the PSD's response, and shaded regions corresponds to the uncertainty in film's response. Results for the PSD and film were published in Madden *et al.* 2020 [187].

further than ±15 m from the centre of the field, but fall out of agreement for positions between the ±(13.5−15) mm positions. This occurred as the simulated beam profiles had narrower full widths at half maximums (FWHMs) and penumbral widths than the PSD and film profiles. As a result, the PSD and film profiles had higher relative doses than those that were simulated between the ±(13.5−15) mm positions. These out of field dose differences between the simulations and measured doses were inflated as a result. MADs for the out of field regions were 0.4 % between the PSD and film, 0.7 % between the PSD and simulations, and 0.8 % between the simulations and film. It was expected that simulated profiles had narrowed penumbra and FWHMs due to minor differences between the modelled MLC leaves and the true MLC leaves [201].

For the 2.469 m SID profiles in Figures 4.13 and 4.14, the central region was defined between −10.4 mm and +10.4 mm, and the out of field regions occurred at positions less than −16.5 mm and positions greater than +16.5 mm. Similar to the profiles measured at 1.869 m SID, the PSD, film and simulated profiles had dose differences that were less than the corresponding uncertainty in the dose differences for the central regions of the beam profiles. MADs for the central region of these profiles were 1.0 % between the PSD and film, 1.6 % between the PSD and simulations, and 1.3 % between the film and simulations. Similar to the profiles measured at 1.869 m SID, the out of field differences were within agreement for the PSD and film, such that their dose differences were less

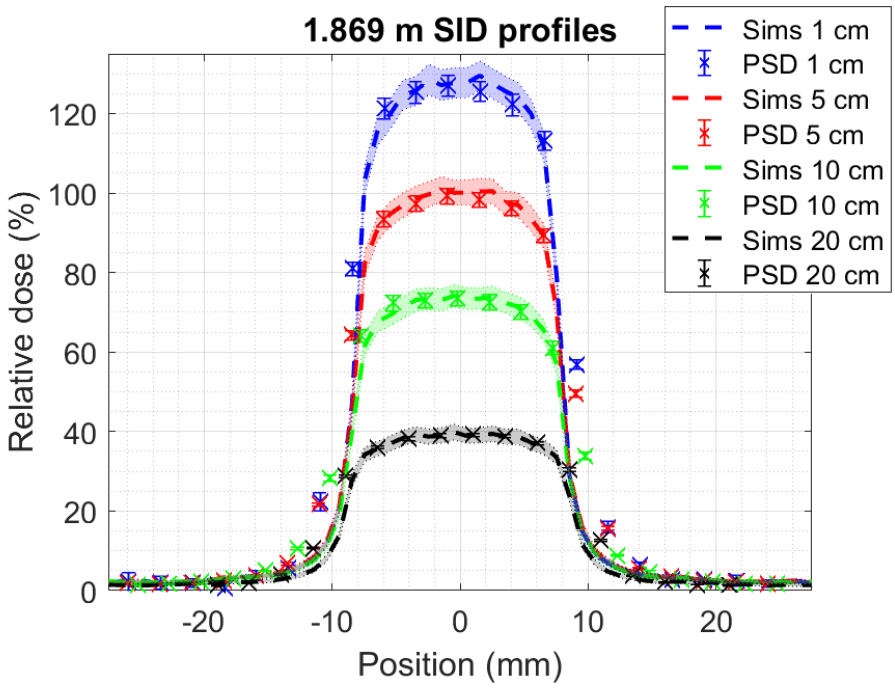

Figure 4.12: Right: Beam profiles measured for the 1.869 m SID for the 1.9 cm × 1.9 cm field, with the PSD compared against simulated beam profiles. In this figure, PSD is the in-house PSD and Sims are the simulated dose profiles. Error bars correspond to the uncertainty in the PSD's response, and shaded regions corresponds to the uncertainties in the simulated dose.

than the uncertainty in the dose differences. For the out of field region at 1 cm depth, the simulations over-estimated the dose with respect to the PSD and film. As for the simulated profiles at 1.869 m SID, the simulated profiles at 2.469 m SID had narrowed FWHMs and penumbras, causing inflation of the simulation's MADs with respect to the PSD and film. MADs for the out of field regions were 0.5 % between the PSD and film, 1.5 % between the PSD and simulations, and 1.5 % between the film and simulations.

Global γs were calculated for the 1 %/1 mm, 2 %/2 mm and 3 %/3 mm criterion with no dose threshold. The global γs shown in Figure 4.15 evaluate the PSD profiles using the film profiles. Similarly, the global γs shown in Figure 4.16 evaluate the PSD profiles using the simulations as reference distributions. Global γs shown in Figure 4.17 evaluate the simulated profiles using the film as reference distributions; film was used as the reference distribution in this case as it's spatial sampling frequency was ≈0.36 pixels/mm, smaller than the simulation's sampling frequency of 1 mm/voxel, making film the more suitable reference distribution. Global γ pass-rates are presented in Table 4.2.

For the γs evaluating the PSD with reference to film presented in Figure 4.15, the central regions and out of field regions were all within the 3 %/3 mm agreement, such that all γs were less than 1 in these regions. This result was expected given the maximum difference in dose between the PSD and film was 2.2 % in the central regions and 1.5 % in the out of

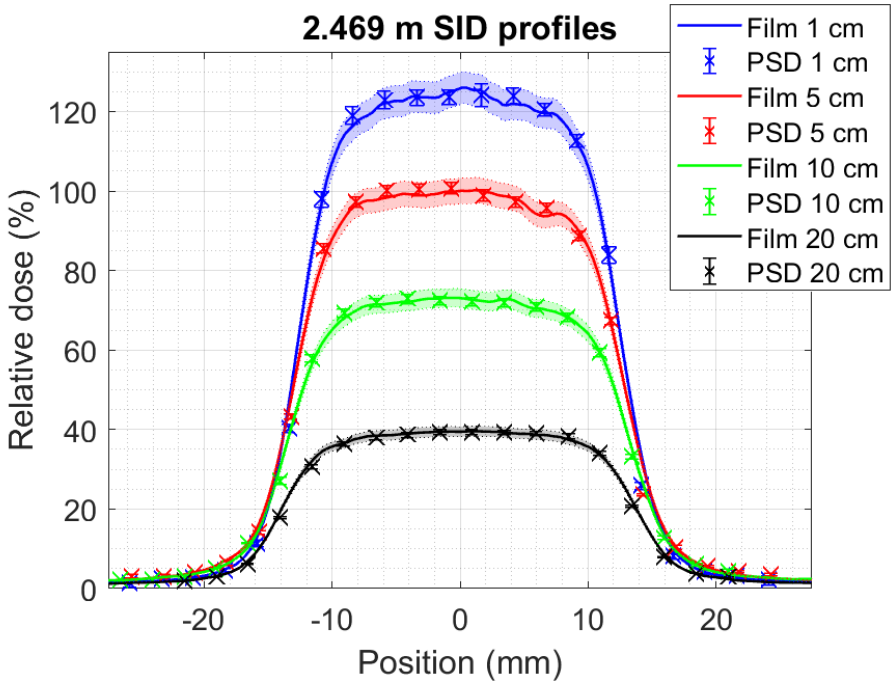

Figure 4.13: Beam profiles measured with the in-house PSD and radiochromic film, for an 2.469 m SID 2.6 cm × 2.6 cm field. In the legend, PSD is the in-house PSD and Film is EBT3 film. Error bars correspond to the uncertainty in the PSD's response, and shaded regions corresponds to the uncertainty in film's response. Results for the PSD and film were published in Madden *et al.* 2020 [187].

field regions. In the penumbral regions, all but 1 of the PSD's measurement positions were within the 3 %/3 mm agreement with film. The corresponding mean pass-rate was 99.4 %, acceptable for the 3 %/3 mm criteria. At 2 %/2 mm, the PSD remained in agreement with film for the central regions, such that all γs were less than 1 in these regions. However, there were 3 failures in the penumbral regions for the 2 %/2 mm criteria. This increased failure rate in the penumbras arose from a combination of the 0.36 mm spatial sampling frequency of film, and the high spatial dose gradient of the MRI-LINAC's penumbral widths. From previous investigations, the penumbra width in film ranged between (3.4 ± 0.4) mm and (3.9 ± 0.2) mm at 1.869 m SID in the 1.9 cm × 1.9 cm sized field, and between (4.0 ± 0.4) mm and (4.6 ± 0.9) mm at 2.469 m SID in the 2.6 cm × 2.6 cm sized field [187]. In this penumbral region, film averages a minimum relative change in response of 4.6 %/pixel. As a result, an increased failure rate occurred in the penumbral region. The mean pass-rate for the 2 %/2 mm criteria was 98.1 %, therefore the PSD was in acceptable agreement with film for the 2 %/2 mm criteria. At 1 %/1 mm, there were increased failures in each of regions. In the central region, dose differences greater than 1 % caused 6 failures, such that γ was less than one. For the out of field regions, there were 5 failures, and there were 10 failures in the penumbral regions. The number of failures in the penumbral regions was inflated due to the aforementioned combination of film's spatial sampling frequency and the narrow penumbra widths of these beam profiles.

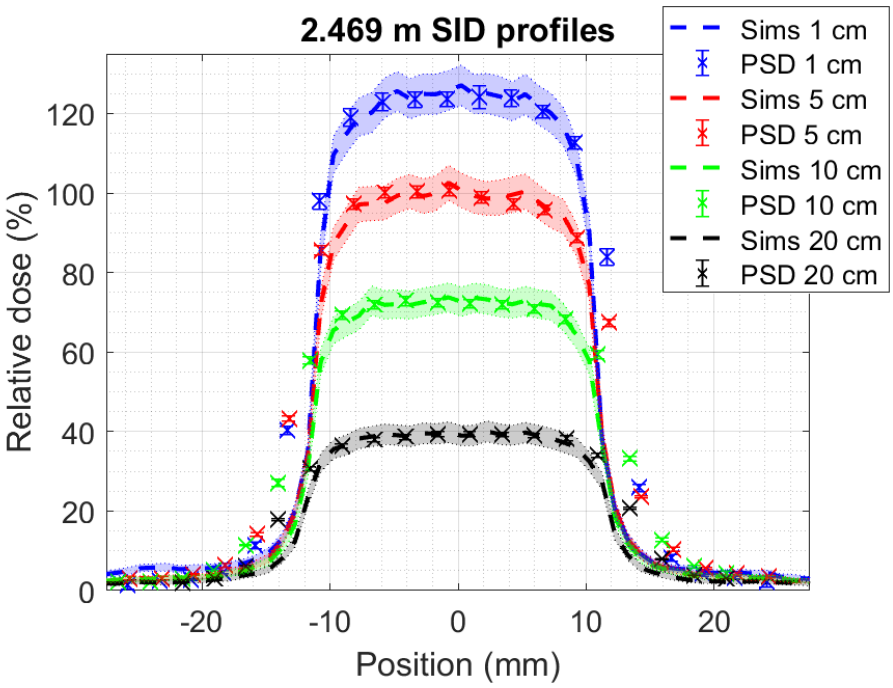

Figure 4.14: Beam profiles measured with the PSD, compared against simulated beam profiles, for an 2.469 m SID 2.6 cm × 2.6 cm field. In these figures, PSD is the in-house PSD and Sims are the simulated dose profiles. Error bars correspond to the uncertainty in the PSD's response, and shaded regions corresponds to the uncertainty in the simulated distributions.

The mean pass-rate between the PSD and film for the 1 %/1 mm criteria was 85.8 %, and therefore unacceptable given this criteria.

The γs evaluating the PSD with respect to the simulations are presented in Figure 4.16. For the 3 %/3 mm criteria, the PSD was within acceptable agreement with the simulations for the central and out of field regions, such that all γs were less than 1 in the out of field regions and all γs except one were less than one in the central regions. However, there were 25 failures in the penumbral regions, some of which have γ values that were too large to be shown in the 3 %/3 mm criteria's graph in Figure 4.16. Due to the 1 mm/voxel spatial sampling frequency of the simulations, there were increased frequencies of failures in the penumbral regions when evaluating the PSD with respect to simulations, compared to when the PSD was evaluated with respect to film. Additionally, the simulations had narrowed FWHMs and penumbras compared to the PSD and film, causing a further increase in the penumbral region's failure rate. The mean pass-rate between the PSD and simulations was 83.9 %, unacceptable within the 3 %/3 mm criteria. For the 2 %/2 mm criteria, there were increased rates of failure in the out of field and penumbral regions, whereas the number of failures in the central region remained at 1. The number of failures in the out of field increased to 7, arising as a result of the significant random statistical fluctuations associated with the high uncertainty in the out of field doses (observable in Figures 4.12 and 4.14), as well as an over-estimation in the out of field dose at 1 cm depth, 2.469 m

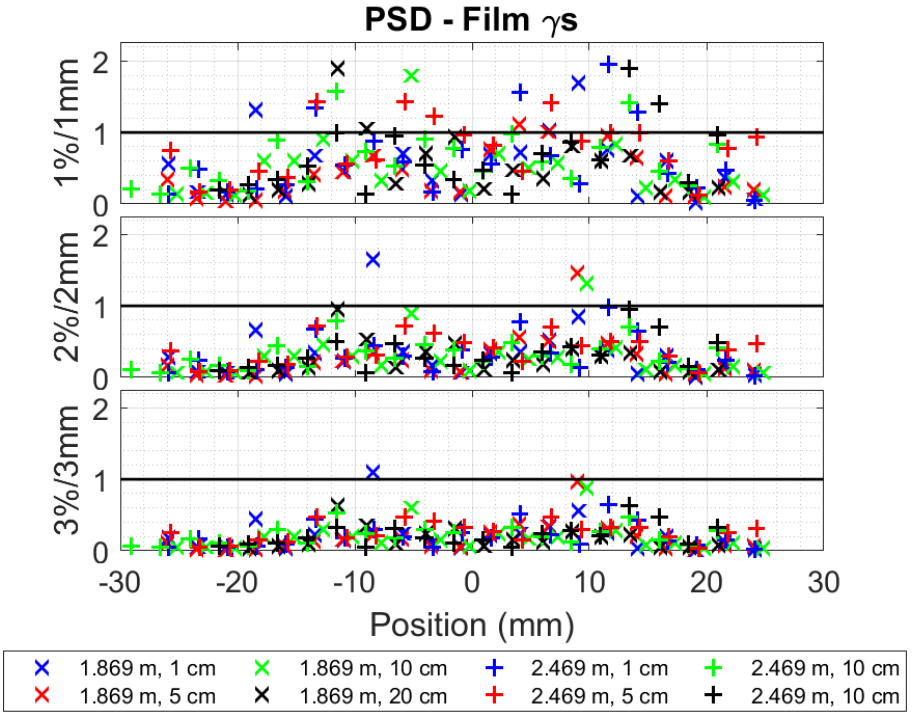

Figure 4.15: Gamma indices between PSD and film for each set of beam profiles; results were published in Madden *et al.* 2020 [187].

SID. The number of failures in the penumbral regions increased to 32. The mean pass-rate when evaluating the PSD with respect to simulations at 2 %/2 mm was 75.2 %. For the 1 %/1 mm criteria, failure rates increased in each of the regions. The increased failure rates in the central and out of field regions was exacerbated due to the significant statistical uncertainty in the simulated doses, observable in the error bars of Figures 4.12 and 4.14. At the 1 %/1 mm criteria, the PSD and simulation had a mean pass-rate of 46.0 %.

For the γs evaluating the simulations with reference to film presented in Figure 4.17, the central regions and out of field regions were all acceptable for 3 %/3 mm criteria, such that all γs were less than 1 in these regions. All instances of failures at 3 %/3 mm occurred in the penumbral regions, arising from the simulation's narrowed FWHMs and penumbral widths when compared against the PSD's and film's profiles. The mean pass-rate for the 3 %/3 mm criteria was 97.5 %, therefore the simulations were acceptable given a 3 %/3 mm criteria when evaluated with respect to film. For the 2 %/2 mm criteria, there were increased failure rates for the central, out of field and penumbral regions. The increase in failure rates for the central regions arose as dose differences exceeded 2 %, owing to the significant uncertainties in the simulation's and film's profiles in the central regions (observable as the shaded regions in Figures 4.11−4.14). Failures in the out of field region arose as the simulated dose profiles at 1 cm depth, 2.469 m SID had increased out of field doses. Increased failure rates in the penumbral region arose as many of the simulated doses in the penumbral regions caused the calculated γs to exceed 1 with a

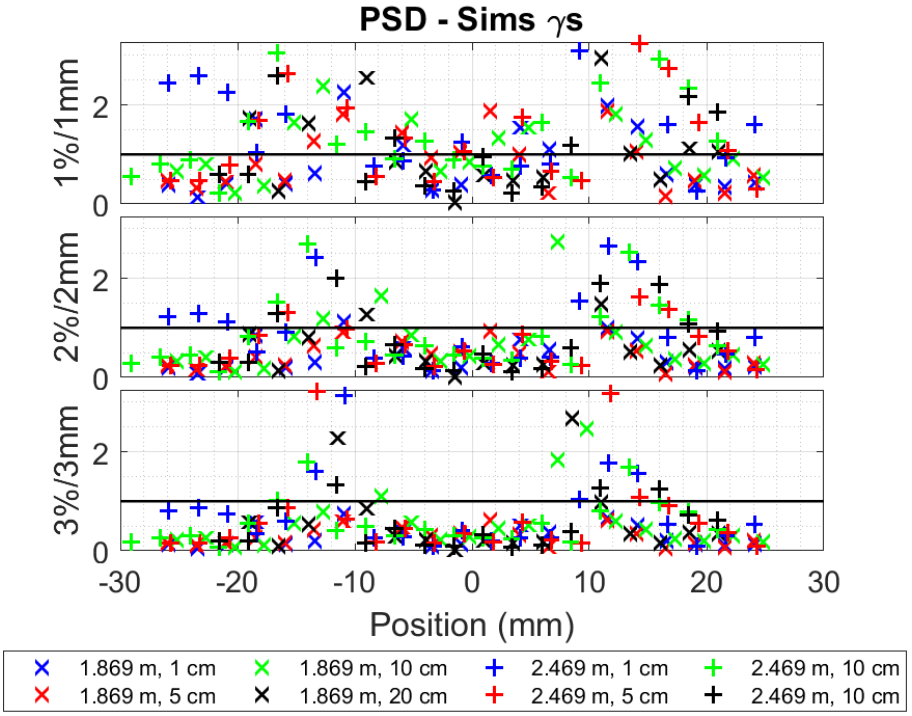

Figure 4.16: Gamma indices between the PSD and simulations for each set of beam profiles.

2 mm distance to agreement, whereas many of these simulated doses in the penumbral region were acceptable given the 3 mm distance to agreement. For the 2 %/2 mm criteria, the mean pass-rate when evaluating the simulated profiles with respect to film was 83.4 %, therefore the simulations were unacceptable within this 2 %/2 mm criteria. For the 1 %/1 mm criteria, failure rates were significantly increased in all regions of the profiles. Aforementioned disagreements were exacerbated, causing the mean pass-rate to decrease to 58.4 % at 1 %/1 mm.

The PSD's performance in the measurement of MRI-LINAC beam profiles was assessed by comparing the calculated statistics against those published in the literature for other detectors. Chen *et al.* compared beam profiles measured by a micro-ionisation

	Central MAD (%)	OOF MAD (%)	1 %/1 mm γ (%)	2 %/2 mm γ (%)	3 %/3 mm γ (%)
PSD - Film	1.1	0.4	85.8	98.1	99.4
PSD - Sims	1.5	1.1	46.0	75.2	83.9
Sims - Film	1.2	1.2	58.4	83.4	97.5

Table 4.2: Table presenting the Global MADs and γs for the measured and simulated beam profiles. Central MAD columns refer to the global MADs calculated in the central regions of the profile, and OOF MAD columns refer to the global MADs calculated in the out of field regions of each profile. Each of the γ columns reports the mean pass-rate for each of the criterion.

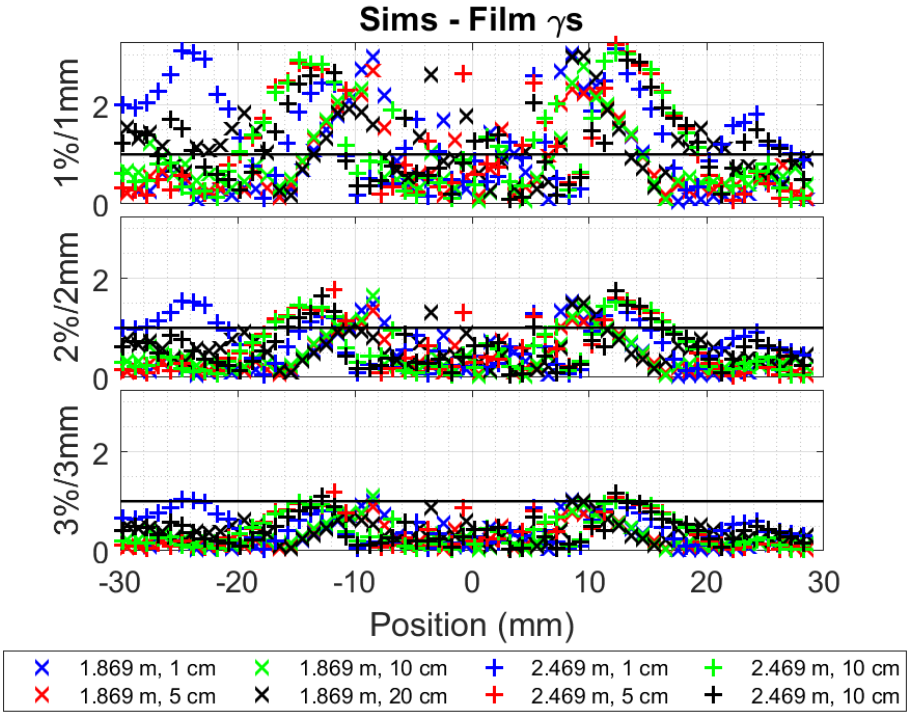

Figure 4.17: Gamma indices between the simulations and film for each set of beam profiles.

chamber, a Farmer chamber and GafChromic EBT3 film against those calculated by the MRI-LINAC's treatment planning system [147]. These detectors were found to be within 1 % global agreement for central regions and 2 % global agreement for out of field regions. For the same conditions, the PSD and film had a maximum difference of 2.2 % for the central regions and 1.5 % agreement for the out of field regions. Given these statistics, it can be concluded that the PSD performed similarly to the investigated ionisation chambers and radiochromic film. Roed *et al.* compared 1.5 T perpendicular MRI-LINAC beam profiles measured with GafChromic EBT3 film, a microDiamond detector and Fricke type gel [202]. The film and microDiamond detector profiles were within 2 % global agreement for all positions, comparable to the performance 2.2 % maximum difference between the PSD and film.

O'Brien *et al.* applied global γ analysis to evaluate beam profiles measured by a Farmer chamber, multiple micro-ionisation chambers, a microDiamond detector and multiple diode detectors for the 2 %/0.2 mm criterion [137]. Each profile was evaluated with reference to the mean of all detector's profile. The mean global pass-rate was 96.9 % with no magnetic field present, and 89.2 % in the presence of the 1.5 T perpendicular magnetic field. It was concluded that the increased failure rate arose due to varying degrees of asymmetry and lateral shift as these effects are dependent on the dosimeter's density [135]. It should be noted that the diode detectors under-estimate the lateral shift and asymmetry that occurs in water, whereas the ionisation chambers over-estimate the lateral shift and

asymmetry that occurs in water. Through taking the mean of all detector's profiles, the mean beam profiles average the lateral shifts of the diodes and the ionisation chambers. For the case of the PSD used in the presented work, it's sensitive volume had a density of 1.032 g/cm^3, and so it's expected that the PSD would have experienced a lateral shift and asymmetry matching that of water given water's density of 1 g/cm^3. Given this, the PSD could have been expected to closely match the mean beam profile calculated for the γ analysis. For the γ analysis between the PSD and film at 2 %/2 mm, the only failures occurred in the penumbral region, with these failures occurring as the film could not provide an adequate number of samples to satisfy the 2 % dose difference component of the γ analysis. Given this result and the PSD's highly water equivalent sensitive volume, it is plausible that the PSD would have remained close to the mean beam profile if it was applied in O'Brien *et al.*'s study.

4.3.3 Percent depth dose distributions

PDDs measured in the 2.6 cm × 2.6 cm, 5.3 cm × 5.3 cm, 10.5 cm × 10.5 cm and 18.4 cm × 18.4 cm fields are presented at the top of Figures 4.18−4.21, respectively. Corresponding dose differences are presented in the middle of Figures 4.18−4.21. All PDDs were normalised to the response at 5 cm depth. The Farmer chamber PDDs were not measured for the 2.6 cm × 2.6 cm sized field as the Farmer chamber suffers from partial volume effects in this small field. Uncertainties in the PDDs are presented in the bottom of Figures 4.18−4.21. MADs for each set of dose differences are presented in Table 4.3, along with the global mean MADs.

For the PDDs measured in the 2.6 cm × 2.6 cm field (presented in Figure 4.18), the PSD systematically under-responded with respect to the film PDDs between depths of 1 mm and 15 mm, with a maximum under-response of 4.0 % at the 1 mm depth. These dose differences were less than the corresponding uncertainty in the dose differences. For depths between 1 mm and 15 mm, the PSD and film under-responded when compared against the simulated dose distributions. These under-responses were most significant at the 1 mm depth, being 15.7 % between the PSD and simulations, and 11.7 % between the film and simulations. The dose differences between the PSD and simulations, and the film and simulations were unacceptable only at the 1 mm depth, with the dose differences between 3 mm and 15 mm being less than the corresponding uncertainty in the dose differences. These discrepancies in the entrance region were expected to arise due to two separate effects induced by the high lateral dose gradient of the electron focal spot [133]. Firstly, the PSD and film were aligned to the central axis by eye to the MRI-LINAC's isocentre-projection lasers. These lasers were reported to have a positioning uncertainty of 1.6 mm with respect to the MRI-LINAC's isocentre for the 2.469 m SID [134]. From previous investigations [128, 133], the focal spot also has significantly high

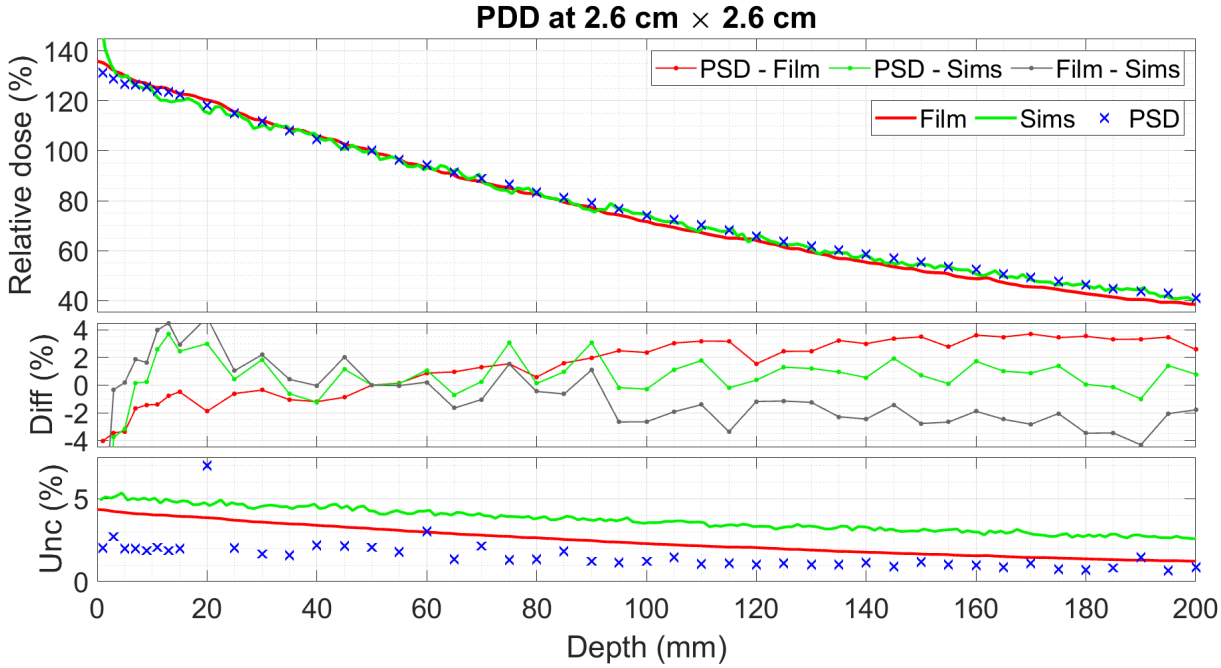

Figure 4.18: Top: central axis PDDs for the 2.469 m SID, 2.6 cm × 2.6 cm field. Bottom: dose differences between each of the PDDs. In the legend, PSD is the PSD, Film is the GafChromic EBT3 film, and Sims are the simulated dose distributions in water. Results for the PSD and film were published in Madden *et al.* 2021. [188]

spatial dose gradients orthogonal to the central depth axis. Given the alignment method for film, small offsets from the central axis would cause an underestimation of the doses in the entrance region, as observed in the 2.6 cm × 2.6 cm field. The other effect expected to cause disagreements between the PSD, film and simulations in the entrance regions are partial volume effects. The PSD's sensitive volume had a diameter of 2 mm and a length of 0.8 mm. In the simulations, the 1 mm^3 dose scoring voxels were geometrically centred at half-integer values, *e.g* $0.5, 1.5, ..., n + 0.5$. To determine the PDD responses along the central axis, the simulations were averaged across the 2 voxels × 2 voxels that intersected the central axis, effectively making the simulation's sensitive volume a 2 mm × 2 mm cross section with a 1 mm thickness. In comparison to the PSD and simulations, film's sensitive volume was approximately 30 μm × 0.36 mm, mitigating the partial volume effects for these high spatial dose gradients. Consequently, there was the potential for differing degrees of partial volume effects to perturb the entrance doses of the PSD, film and simulations.

For depths between 20 mm and 200 mm, there were no systematic over-response or under-response trends present when comparing the PSD and the simulations. All dose differences between the PSD and simulations were less than their dose difference's uncertainty for these depths. When comparing the PSD and film, and the film and simulations, there was a systematic trend where the film increasingly under-responded as depth increased beyond 50 mm. For depths greater than 15 mm, the maximum difference between

the PSD and film was 3.7 %, and the maximum difference between the simulations and film was 4.3 %. The calculated MADs for depths between 15 mm and 200 mm were 2.1 % between the PSD and film, 0.9 % between the PSD and simulations, and 1.9 % between the film and simulations. Due to the systematic deviations between the PSD and film, the dose differences between the PSD and film were unacceptable at depths greater than 135 mm, whereas depths between the simulations and film were acceptable for all depths greater than 15 mm except the 190 mm depth. Evidently, there was a systematic experimental setup uncertainty that could be not accounted for, causing systematic deviations between the PSD and film, as well as the film and simulations. For PDD measurements in small fields, angular misalignments from the depth axis are reported to be potential sources of such increasing dose differences with increasing depth. In a Monte Carlo study by Khelashvili *et al.*, a 1° misalignment between a LINAC's gantry angle and the central depth axis caused dose differences greater than 2 % at 15 cm depth in small fields [203]. Alignment for the film and PSD was performed with reference to the LINAC's isocentre projection laser; the observed trends in differences between the PSD and film could result from angular misalignment.

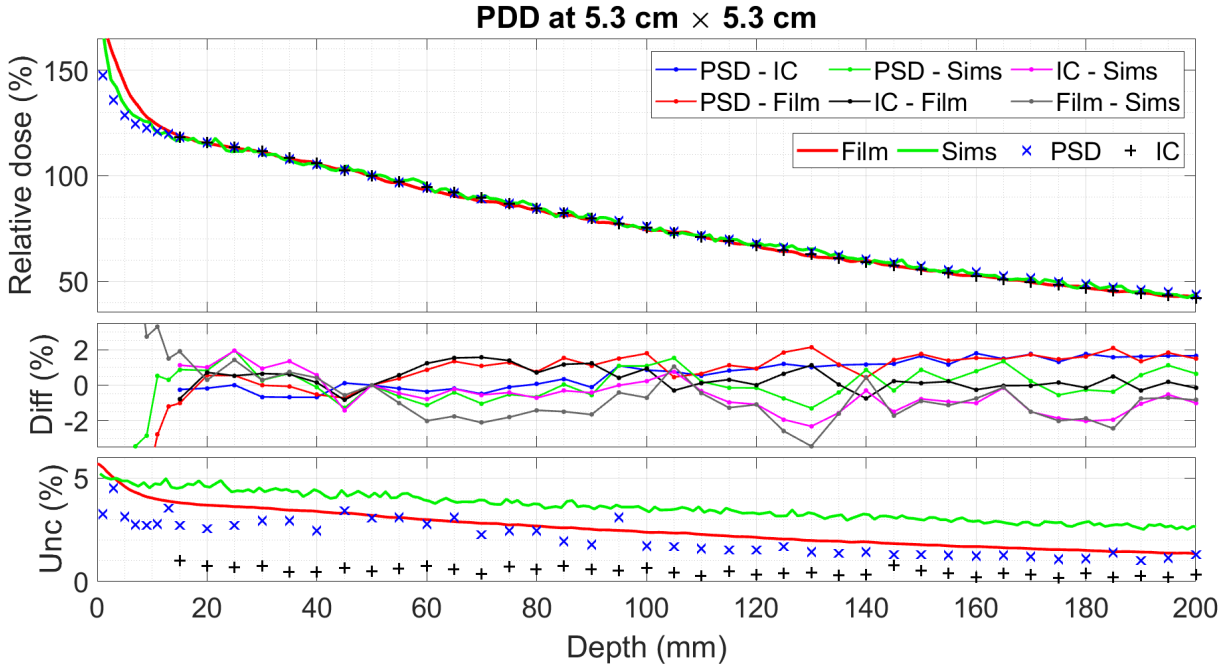

Figure 4.19: Top: central axis PDDs for the 2.469 m SID, 5.3 cm × 5.3 cm field. Bottom: dose differences between each of the PDDs. In the legend, PSD is the in-house PSD, IC is the Farmer ionisation chamber, Film is the GafChromic EBT3 film, and Sims are the simulated distributions in water. Results for the PSD, Farmer chamber and film were published in Madden *et al.* 2021 [188].

For the 5.3 cm × 5.3 cm field size PDDs presented in Figure 4.19, there were significant disagreements between the PSD, film and simulations for depths between 1 mm and 15 mm. At these depths, the PSD and film had a difference of 26.7 %, the PSD and sim-

ulations had a maximum difference of 22.3 %, and the film and simulations had a maximum difference of 13.3 %. Dose differences were unacceptable between the PSD and film for depths between 1 mm and 7 mm, acceptable between the PSD and simulations at all depths except 1 mm, and acceptable between the film and simulations for all depths except 3 mm. As discussed earlier, there were effects that were expected to systematically induce these inflated differences; these were detector misalignment and partial volume effects.

For depths between 20 mm and 200 mm, the PSD and simulations remained in close agreement, with no systematic trends present between the PSD and simulations. At these depths, the dose difference between the PSD and simulations was less than the uncertainty in the dose differences. Similarly, when comparing the Farmer chamber and film at these depths, there were no systematic differences and the corresponding dose differences were less than the uncertainty in these differences. However, when comparing the PSD and simulations with the film and Farmer chamber, there were systematic differences between the PSD and film, the PSD and the Farmer chamber, the simulations and film, and the simulations and the Farmer chamber. At the 200 mm depth, the PSD's response was 1.7 % greater than the Farmer chamber's response and 1.5 % greater than the film's response. Similarly, at 200 mm, the simulated doses were 1.0 % greater than the Farmer chamber's response and 0.8 % greater than the film's response. It should be noted that all systematic differences were less than the corresponding uncertainties in these dose differences, except between the PSD and the Farmer chamber at depths greater than or equal to 160 mm. These systematic differences may have arisen due to an angular misalignment from the central axis. The corresponding MADs are reported in Table 4.3 for depths between 15 mm and 200 mm.

For the 10.5 cm $\times$ 10.5 cm field size PDDs presented in Figure 4.20, there were systematic differences between the PSD, film and simulations for depths between 1 mm and 15 mm. Unlike the previous PDDs at field sizes of 2.6 cm $\times$ 2.6 cm, the PSD and simulations under-responded with respect to the film. The simulation's under-response arose due to partial volume effects experienced, whereas the PSD's under-response likely arose due to a combination of partial volume effects and misalignment from the central axis. At these depths, the PSD and film were not in agreement for the depths between 1 mm and 9 mm, the film and simulations were not in agreement for depths between 1 mm and 7 mm, and the PSD and simulations were in agreement for all depths except the 1 mm depth.

For the depths between 20 mm and 200 mm, all PDDs were generally within agreement, and any systematic differences between the PSD and film, the PSD and Farmer chamber, the simulations and film, and the simulations and the Farmer chamber were reduced in

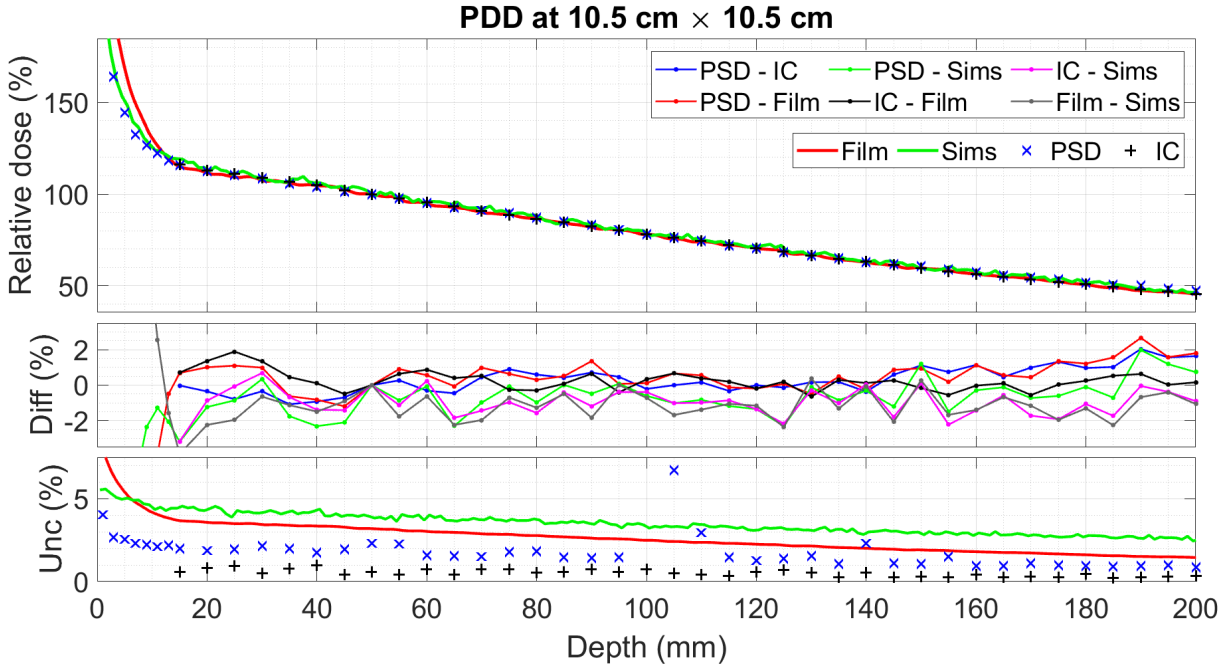

Figure 4.20: Top: central axis PDDs for the 2.469 m SID, 10.5 cm × 10.5 cm field. Bottom: dose differences between each of the PDDs. As in Figure 4.19, PSD is the in-house PSD, IC is the Farmer chamber, Film is the GafChromic EBT3 film and Sims are the simulated dose distributions in water. Results for the PSD, Farmer chamber and film were published in Madden *et al.* 2021 [188].

comparison to the trends present for the 2.6 cm × 2.6 cm and 5.3 cm × 5.3 cm fields. The only significant systematic deviation occurred between the PSD and film, and the PSD and the Farmer chamber for depths greater than 170 mm. At these depths, the maximum difference between the PSD and film was inflated to 2.7 %, and the maximum difference between the PSD and the Farmer chamber was inflated to 2.3 %. The remaining maximum differences between depths 20 mm and 200 mm were 2.0 % between the PSD and simulations, 1.9 % between the film and Farmer chamber, 2.4 % between the simulations and film, and 3.2 % between the simulations and the Farmer chamber. For the depths between 20 mm and 200 mm, dose differences between each of the PDDs were less than the corresponding difference's uncertainties, except between the PSD and the Farmer chamber for depths between 175 mm and 200 mm. Corresponding MADs are reported in Table 4.3. Angular misalignment is less severe as field size increases [203], therefore angular misalignment cannot be the sole cause of the differences between the PSD and film, and the PSD and the Farmer chamber at this field size.

For the 18.4 cm × 18.4 cm field size PDDs presented in Figure 4.21, there were significant systematic disagreements between the PSD and film, and the PSD and simulations between depths of 1 mm and 15 mm. Dose differences between the PSD and film were unacceptable for all depths between 1 mm and 15 mm, and the dose differences between the film and simulations were only acceptable at the 13 mm and 15 mm depths. For reference,

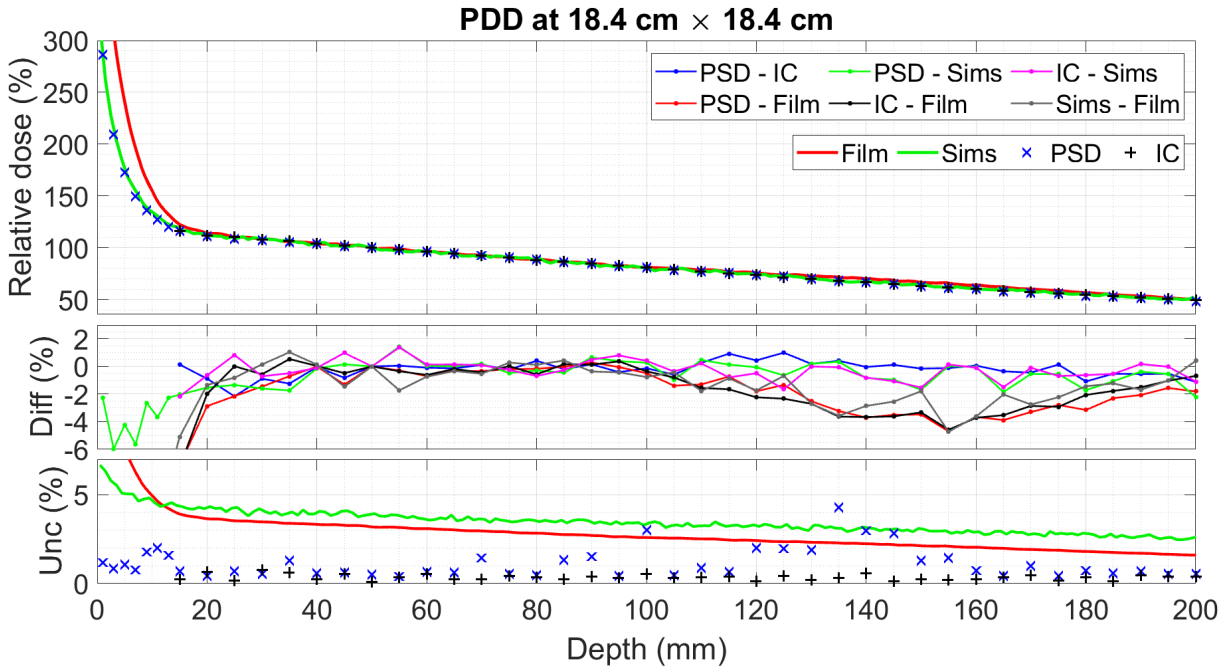

Figure 4.21: Top: central axis PDDs for the 2.469 m SID, 18.6 cm × 18.6 cm field. Bottom: dose differences between each of the PDDs. As in Figure 4.19's legend, PSD was the in-house PSD, IC was the Farmer ionisation chamber, Film was the GafChromic EBT3 film and Sims were the simulated dose distributions in water. Results for the PSD, Farmer chamber and film were published in Madden *et al.* 2021 [188].

the PSD and simulations had dose differences that were less than the corresponding uncertainty in these dose differences at all depths between 1 mm and 15 mm, except at the 7 mm depth. The disagreements at this field size were the most severe out of all the PDDs measured. As for the 2.6 cm × 2.6 cm, the 5.3 cm × 5.3 cm and 10.5 cm × 10.5 cm field sizes, the simulations under-responded as a result of partial volume effects and the PSD likely under-responded due to the combination of partial volume effects and potential misalignment from the centre of the field. These effects were most severe at the 18.4 cm × 18.4 cm as the fluence of electrons focused by the fringe magnetic field increases with field size, thereby escalating the dose in the entrance region as field size increased. It should be noted that the PSD, film and simulations were all highly water equivalent dosimeters with small sensitive volumes. In spite of these qualities the significant and unacceptable dose differences arose between each of the distributions, mainly due to partial volume effects that lead to the under-estimation of dose by the PSD and simulations. Given these results, the in-house PSD is conclusively not suitable for measurements in the electron focal spot of the Australian MRI-LINAC. This limitation could be easily addressed by reducing the PSD's sensitive volume thickness and using a scanning water tank to find the centre of the focal spot prior to measurements.

For depths between 20 mm and 200 mm in the 18.4 cm × 18.4 cm sized field, there was no under-response trend between the PSD and the Farmer chamber, and the Farmer cham-

ber and simulations. Dose differences between the PSD, Farmer chamber and simulations were all less than their dose difference's uncertainties between these depths, except for the PSD and Farmer chamber at depths of 180 mm and 200 mm. These two unacceptable differences arose as a result of random statistical fluctuations. With regards to the film measured PDDs, the film over-responded with respect to the PSD, Farmer chamber and simulations for depths between 100 mm and 200 mm. This over-response gradually increased in magnitude as depth increased from 100 mm to 155 mm, and then decreased in magnitude as depth increased from 155 mm and 200 mm. Given the nature of this trend, the film was expected to have had a significant non-uniformity when it was read out, causing this apparent trend. As a result of this trend, dose differences were unacceptable between the PSD and film from depths of 150 mm to 180 mm, and unacceptable between the Farmer chamber and film from depths between 130 mm and 175 mm. The corresponding dose differences between the simulations and film remained within agreement between depths of 20 mm and 200 m. For depths between 20 mm and 200 mm, the maximum differences were 2.2 % between the PSD and the Farmer chamber, 4.7 % between the PSD and film, 2.2 % between the PSD and simulations, 4.6 % between the Farmer chamber and film, 2.2 % between the Farmer chamber and film, and 5.1 % between the film and simulations.

To assess whether the PSD's performance was suitable, these MAD and maximum difference statistics are compared to values reported for other dosimeters in the literature. In O'Brien *et al.* [137], PDDs were measured with a 1.5 T perpendicular magnetic field using a micro-volume ionisation chamber, a thimble ionisation chamber, a microDiamond detector and multiple diode detectors. In a 2 cm $\times$ 2 cm field, the ionisation chambers and solid state detectors had a maximum disagreement approaching 2.2 % at 10 cm depth, increasing as depth increased; this trend was not observed in the 10 cm $\times$ 10 cm field, with all detectors being within 1 % of the accepted PDD. In Chen *et al.* [147], a Farmer chamber, a micro-volume ionisation chamber and a microDiamond detector were used to measure PDDs with a 1.5 T MRI-LINAC, compared against the treatment planning system's beam model. Measured PDDs were within 2 % of the beam model, reported to be within 1 % for most measurement points, acceptable for all measurement depths given the detector's and beam model's uncertainties. Galavis *et al.* [185] applied the commercial PSDs Exradin W1 and W2 (Standard Imaging, USA) for the measurement of a non-MRI LINAC's PDD in a scanning water tank. The maximum discrepancy between the PDD responses was 2.5 % relative to the response at 5 cm depth. It should be noted that the Exradin W1 and W2 PSDs have the same constituents and dimensions, thus the source of discrepancies were not related to differences in detector geometry.

For the 10.5 cm $\times$ 10.5 cm and 18.4 cm $\times$ 18.4 cm field size, it is conclusive that the PSD performed similarly to the other detectors in the literature given the calculated MADs

	2.6×2.6 cm^2 (%)	5.3×5.3 cm^2 (%)	10.5×10.5 cm^2 (%)	18.4×18.4 cm^2 (%)	Global mean (%)
PSD - IC	-	0.9	0.6	0.5	0.7
PSD - Film	2.1	1.1	0.7	1.9	1.4
PSD - Sims	0.9	0.9	1.0	0.8	0.9
IC - Film	-	0.5	0.4	1.7	1.0
IC - Sims	-	0.9	0.8	0.8	0.8
Film - Sims	1.9	1.0	0.9	2.2	1.5

Table 4.3: In this table, MADs between the PDDs are reported. In the second to fifth columns, the MADs are reported for depths between 15 mm and 200 mm for each of the field sizes. In the sixth column, the Global mean reports the mean MAD across all field sizes. In the first column, PSD, IC, Film and Sims are defined as in Figure 4.19

and maximum differences. For these field sizes, the PSD deviated by no more than 2.0 % with respect to the Farmer chamber, and dose differences were generally acceptable with reference to the simulations and film. For the 2.6 cm $\times$ 2.6 cm and 5.3 cm $\times$ 5.3 cm fields, the PDDs appeared to systematically overestimate the depth-dose response with respect to the Farmer chamber and film as depth increased. In the literature, the Farmer chamber and film have been validated for the conditions they were applied in. Curiously, the simulated PDDs matched the PSD's PDDs for these field sizes; these simulations were previously verified to match measured data within ± 2 % [193]. Given these conflicting trends between the PSD and reference distributions for the 2.6 cm $\times$ 2.6 cm and 5.3 cm $\times$ 5.3 cm field size, a definitive conclusion cannot be reached with regards to the suitability of the PSD for these measurement conditions.

4.4 Discussion

From the comparison of output factors and beam profiles, the in-house PSD was in agreement with each of the references when 2 standard deviations in each calculated dose was taken as the uncertainty. The corresponding calculated MADs and dose differences suggested that the in-house PSD performed comparably to other dosimeters in the literature that are considered accurate and suitable for MRI-LINAC dosimetry, supporting that the in-house PSD was also accurate and suitable for MRI-LINAC dosimetry. From the comparison of the PDDs, the PSD remained in agreement with the reference distributions at depths greater than 15 mm for the 10.5 cm $\times$ 10.5 cm and 18.4 cm $\times$ 18.4 cm field sizes. However, systematic disagreements were observed between the in-house PSD and some of the references at depths greater than 15 mm for the 2.6 cm $\times$ 2.6 cm and 5.3 cm $\times$ 5.3 cm field size. Detector misalignment was identified as one potential source of the systematic disagreements, though it could not be identified whether detector misalignment

had occurred for any of the measured distributions; in future studies, this could be addressed by measuring the PDDs using a scanning water tank to ensure that detectors are aligned to the central axis. Due to the plausibility of detector misalignment when measuring PDDs, conclusions about the suitability of the in-house PSD for these conditions cannot be drawn.

One promising opportunity for fibre-coupled PSDs is the measurement of detector specific correction factors with MRI-LINACs. It is expected that the PSD's response will be free from effects that increase a dosimeter's uncertainties given their high water equivalence and near-correctionless response for LINACs. Consequently, PSDs are expected to be one of the most effective detectors for this niche measurement. Unfortunately, the measurement of such detector specific correction factors could not be investigated as the PSD system was sensitive to significant changes in set up. This sensitivity arose as transmission through the optical fibre is strongly dependent on any bends in said optical fibre and their bend radius. The measurement of such detector specific correction factors can only be achieved for the Australian MRI-LINAC by significantly changing where the PSD is set up between measurements. Given that the optical fibres were each approximately 20 m long, there was a high likelihood that the optical fibre was subject to significant changes in it's bends and bending radius between measurements, compromising any correction factors measured.

With regards to the entrance region of the PDDs, the in-house PSD, film and simulations systematically disagreed with each other. It was identified that there were likely varying degrees of volume averaging given their different sensitive volume sizes, leading to disagreements between all three detectors. However, with regards to the PSD, there are likely two additional sources of effect which also perturbed it's response in this region. Firstly, in the background subtraction correction it is assumed that equal magnitudes of Cerenkov radiation were produced in each of the optical fibres. In the setup for the PDDs, the PSD and reference probe aligned upstream and downstream from one another. The assumption of equal magnitudes of Cerenkov radiation being measured by each optical fibre was invalid in the entrance region as there was a high spatial dose gradient directed depth-wise along the central axis. This potential source of uncertainty could easily be addressed through the application of an alternative correction method. Secondly, the PSD may have suffered from an under-response to low energy electrons. In the entrance region of the PDDs, the MRI's in-line fringe field directs scattered and contaminant electrons between the LINAC and isocentre towards the MRI's isocentre [128]. Plastic scintillators can suffer from ionisation quenching in response to low energy electrons given the corresponding high linear energy transfers of these electrons [204, 205]. Consequently, there may be an energy dependence in effect that caused the PSD to under-respond in the entrance region of the PDDs with the Australian MRI-LINAC. Given these three potential

sources of perturbation, the investigated in-house PSD was not suitable for measurements in the electron focal spot of the Australian MRI-LINAC.

The measurements in this chapter were limited in scope, consisting solely of measurements with the Australian MRI-LINAC. At the time of writing, many of the MRI-LINAC systems are perpendicular orientation MRI-LINACs. For these systems, the perpendicular magnetic field imparts a Lorentz force on the secondary electrons that shifts them laterally. At the macroscopic level, the perpendicular magnetic field causes dose distributions to become laterally skewed and asymmetric, whilst also reducing the penetration depth of secondary electrons. The magnitude of these effects is dependent on the medium's material density. For dosimeters that are not water equivalent, the magnitude of these magnetic field induced effects can deviate from the corresponding magnitudes experienced by water. Consequently, the dose distributions measured by non-water equivalent dosimeters can misrepresent the dose distributions that are deposited in water. Such misrepresentations have been observed for diodes, microDiamond and ionisation chambers [137, 138]. Given that PSDs are highly water equivalent, it was hypothesised that PSDs would experience similar magnitudes of these magnetic field induced effects to those experienced by water. Unfortunately, the hypothesis that PSDs would experience matching similar magnetic field induced effects to those of water for perpendicular MRI-LINACs could not be investigated as the Australian MRI-LINAC has an in-line orientation.

Another limitation of the work in this chapter was that only one in-house PSD was investigated. The plastic scintillator used in this chapter was BC444 (Saint Gobain, France), a polyvinyl toluene (PVT) based plastic scintillator with a long exponential decay constant. Many other commercial plastic scintillators exist, used by other research groups for a variety of reasons. Material properties such as water equivalence, effective atomic number and density are dominated by the plastic base of these scintillators. It should be noted that most plastic scintillators applied for dosimetry with LINACs use either PVT or polystyrene as the plastic base. PVT and polystyrene are very similar in terms of their water equivalence through Burlin cavity theory, their effective atomic number and their material densities [87, 206]. At a technical level, there exists the potential for slight differences between the performance of different plastic scintillators given that they are similar, but not identical. However, it can generally be expected that the many of the plastic scintillators would perform similarly in the scope of MRI-LINAC dosimetry given the similarities in material properties of PVT based and polystyrene based scintillators. Due to the limited scope of the investigations in this chapter, as well as the investigations by Yoon *et al.* [166] and Galavis *et al.* [185], it is recommended that PSDs are verified with an MRI-LINAC system to ensure that they are suitable and accurate in the desired conditions. To determine whether PSD systems in general are suitable for MRI-LINAC dosimetry, further study of the many other PSDs is required.

4.5 Conclusion

Given the many desirable dosimetric properties that are ubiquitous for PSDs, it was expected that all PSDs in general would be suitable for MRI-LINAC dosimetry. The presented results for the output factors and beam profiles supported this notion, such that the in-house PSD performed comparably with respect to other dosimeters that were proven suitable for relative MRI-LINAC dosimetry. For the case of PDDs, the discrepancy in trends between the film, Farmer chamber and simulations at the 2.6 cm $\times$ 2.6 cm and 5.3 cm $\times$ 5.3 cm field sizes prevented conclusions from being drawn with regards to the suitability of the PSD for measurements in these conditions. For PDD measurements in the electron focal spot with the Australian MRI-LINAC, the PSD was observed to suffer from significant partial volume effects, arising from the steep spatial dose gradients in this entrance region. From these PDD measurements, the in-house PSD was conclusively not suitable as it's sensitive volume was too large, though this result is not reflective of all PSDs and it could be mitigated by reducing the sensitive volume thickness. Given the peculiar results of Galavis *et al.* [185] where two PSDs of identical construction measured PDDs with discrepancies up to 2.5 %, conclusions about the suitability of all PSDs with MRI-LINACs should not be drawn from the results presented in this chapter alone. Instead, it is recommended that the PSDs are verified prior to measurements with an MRI-LINAC.

Chapter 5

Non-linearity correction of real-time OSL

This chapter presents the investigations into novel non-linearity corrections for real-time optically stimulated luminescence (rtOSL) signals. Experimental measurements from this chapter were carried out at Royal Adelaide Hospital using an in-house fibre-coupled BeO dosimeter, a superficial X-ray unit and a clinical LINAC. The novel non-linearity corrections were tested using the BeO's rtOSL signals. The performance of these novel corrections were compared against the only other non-linearity correction for rtOSL signals, the ΔrtOSL correction. The results from these investigations are published in the following peer-reviewed journal articles:

L. Madden, A. Santos, E. Li, R. Gowda, E. Bezak, S. Afshar, A. Rosenfeld. Temporal modelling of beryllium oxide ceramics' real-time OSL for dosimetry with a superficial 140 kVp X-ray beam. *Phys. Medica*. 2020; 80:17-22. 10.1016/j.ejmp.2020.10.003.

L. Madden, E. Lukas, A. Santos, M. Ganija, P. Veitch, A. Rosenfeld, E. Li. Deconvolution analysis improves real-time OSL of BeO ceramic. *Radiat. Meas.* 2021; 149:106680. 10.1016/j.radmeas.2021.106680

5.1 Introduction

Fibre-coupled luminescent dosimeters possess a wealth of desirable qualities that are promising for a range of challenging dosimetry conditions [30]. The luminescent materials comprising their sensitive volumes typically have high sensitivities to radiation, and these sensitive volumes can be manufactured to sub-millimetre sizes to achieve high spatial resolutions [6, 34]. The compact dosimeter size and all-optical arrangement of these dosimeters (*i.e.* no electronics or wires required around the sensitive volume) minimises the perturbation of water media during dosimetric measurements [6, 34]. Fibre-coupled

dosimetry systems utilising beryllium oxide (BeO) as the luminescent sensitive volume possess these attractive qualities and inherit BeO's near-tissue equivalence [207, 208], it's energy independent OSL response [110] and it's dose-rate independence [30]. This set of attractive qualities makes fibre-coupled BeO dosimeters promising for applications in challenging clinical dosimetry conditions such as *in vivo* dose monitoring.

However, fibre-coupled luminescent dosimeters have encountered challenges that have limited their applications as *in vivo* dosimeters. Stem signals are produced when the solid-core optical fibres of these dosimeters are irradiated. Correction methods are required to preserve a fibre-coupled luminescent dosimeter's accuracy [6, 34]. For materials that can be optically stimulated to produce luminescence such as BeO, the rtOSL technique allows for real-time stem signal correction [24, 109]. In the rtOSL technique, an optical stimulus is periodically pulsed on and off as the luminescent material is irradiated, and it is assumed that the lifetimes of the luminescence signals and stem signals are significantly shorter than the temporal resolution of the data acquisition system. Optical signals measured while the stimulus is on are assumed to be comprised of radioluminescence (RL), optically stimulated luminescence (OSL) and stem signals. Conversely, the optical signals measured while the stimulus is off are assumed to be comprised of only RL and stem signals (for the same assumptions). The rtOSL signal is calculated by taking the difference between the optical signals measured while the stimulus is on and off; a visualisation of typical signals measured with the rtOSL measurement technique is shown in Figure 5.1.

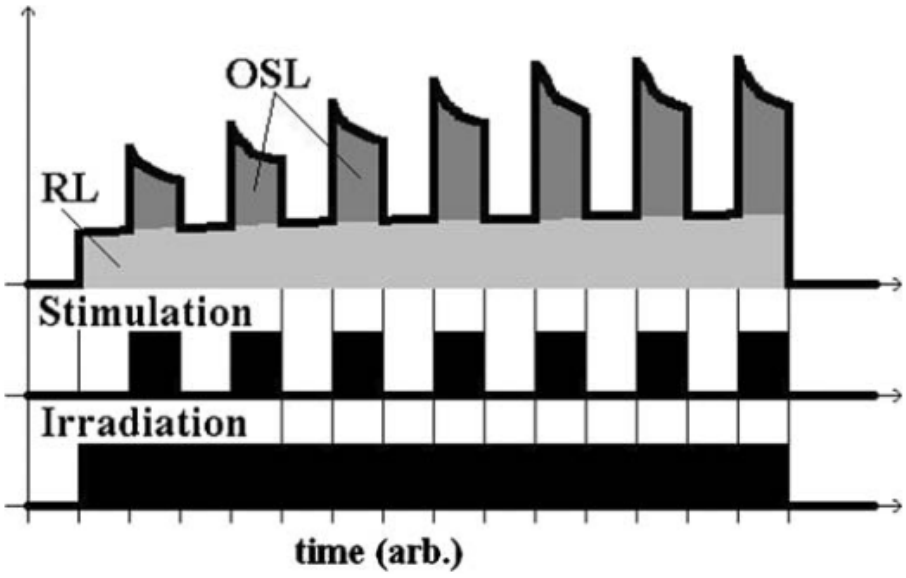

Figure 5.1: Visualisation of the OSL and RL signals measured during the rtOSL technique. Image from Gaza *et al.* 2004 [24]

Typically when OSL signals are read out post-irradiation, their OSL response is proportional to the absorbed dose [24]. However, the measured rtOSL's intensity is supra-linear

with respect to the absorbed dose [24, 30]. This supra-linearity arises due to the complex kinetics inherent to the rtOSL measurement technique [24]. Only one correction method currently exists that restores the linearity between rtOSL signals and the absorbed dose, referred to as the ΔrtOSL correction [24]. In this correction, the measured rtOSL signal is multiplied by a correction function that accounts for the partial emptying of traps during each stimulus pulse [24, 30]. This correction function is typically optimised post-measurement, where corrected rtOSL signals have been reported to be highly linear with absorbed dose [24, 109].

In this chapter, two novel alternative methods are investigated for the real-time correction of the rtOSL supra-linearity. In both proposed methods, the rtOSL signals are modelled using the convolution of a time-dependent dose-rate and a luminescence impulse response function (LIRF), as described previously in Sections 2.1.3 and 3.2.3. With the current computational power available at the time of writing, both corrections can be performed in real-time provided the LIRF is known prior to the required measurements. In the work presented, the feasibility of these correction methods are investigated post-measurement using a fibre-coupled BeO system, with the proposed corrections method compared against the ΔrtOSL correction.

5.2 Materials and methods

5.2.1 Experimental measurements

Superficial X-ray measurements

Measurements were taken with a superficial X-ray unit (Gulmay D3150, Gulmay Medical Ltd., UK) at Royal Adelaide Hospital. All measurements used the 140 kVp X-ray beam energy with 8 mm aluminium half value layer and a 5 cm beam diameter. Gammex RMI Solid Water was used as the phantom material for all measurements. For all measurements, the BeO dosimeter was positioned at the surface of 8 cm of Solid Water. This setup is modelled in Figure 5.2, with a close up of the BeO-optical fibre coupling shown in the figure's top right corner. The instantaneous dose-rate dependence of the BeO rtOSL dosimeter was investigated by varying the source-surface distances (SSDs). The rtOSL signals were measured at SSDs of 15 cm, 25 cm, 35 cm, 45 cm and 55 cm; these SSDs had nominal dose-rates (at the surface of water) of 3.88 Gy/min, 1.42 Gy/min, 0.72 Gy/min, 0.44 Gy/min and 0.29 Gy/min, respectively.

The fibre-coupled BeO dosimeter consisted of a cylindrical volume of pure BeO ceramic (Thermalox 995, Materion, USA) with a 1 mm diameter and a 1 mm length, optically coupled to two silica optical fibres. The first optical fibre (FP400URT, Thorlabs,

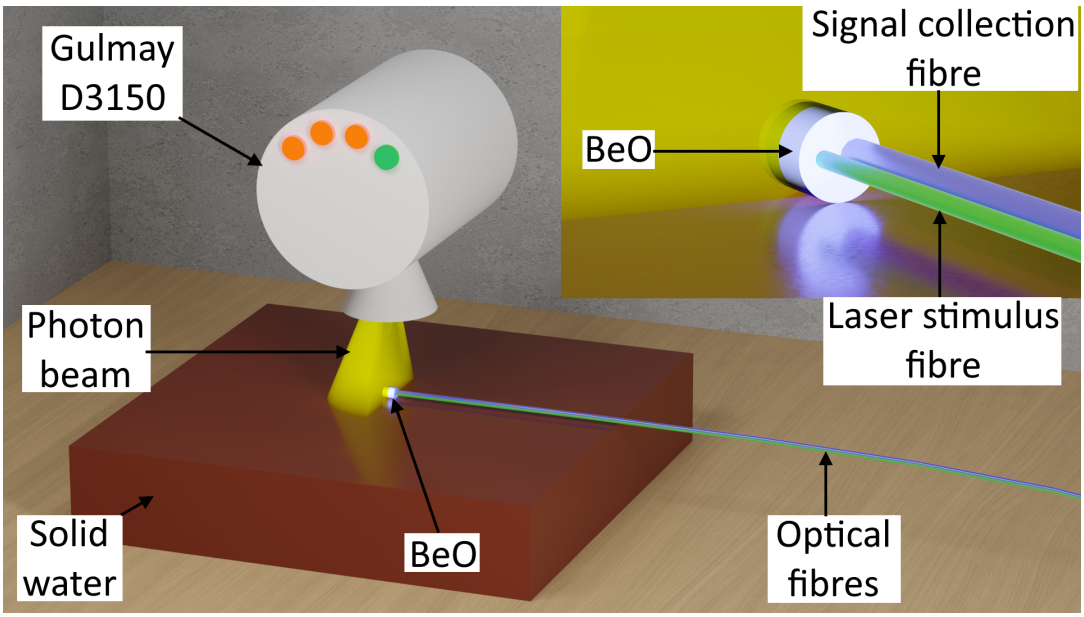

Figure 5.2: 3D model of the superficial X-ray measurement setup with a cutaway in the photon beam to show the BeO dosimeter (not to scale). Close up of the BeO ceramic volume and optical fibres is shown in the top right corner. Published in Madden *et al.* [209].

USA) was used to collect the BeO luminescence signal, and had an approximate length of 20 m, a pure silica core with 400 μm nominal diameter, a hard polymer cladding with 425 μm nominal diameter and numerical aperture of 0.50. The second optical fibre (FG200UEA, Thorlabs, USA) was used to transport the optical stimulus light to the BeO ceramic, and had an approximate length of 20 m, a pure silica core with 200 μm nominal diameter, a fluorine-doped silica cladding with 220 μm nominal diameter and a numerical aperture of 0.22. The two optical fibres were aligned parallel and positioned abreast, end-butt coupled to the BeO volume as shown in Figure 5.2. A photomultiplier tube (H7360-01, Hamamatsu, Japan) was used to measure the luminescence signals transported through the signal collection fibre. A 40 mW laser diode with 450 nm peak emission wavelength (Z-laser, Germany) was used as the optical stimulus, and was connected to the stimulus fibre. The PMT output was recorded at a sampling frequency of 1 kHz using a data acquisition card (USB-6341, National Instruments Inc., USA). The data acquisition card also controlled the laser diode optical stimulus, such that the laser diode pulsed a 2 Hz square wave with 50 % duty cycle for the rtOSL measurement scheme. For all measurements with the superficial X-ray unit, the BeO dosimeter was irradiated for 5 minutes and optically bleached for 5 minutes post-irradiation to substantially empty the optically active trapping centres. An example of the measured rtOSL, stem+RL and stem+RL+rtOSL signal is presented in Figure 5.3.

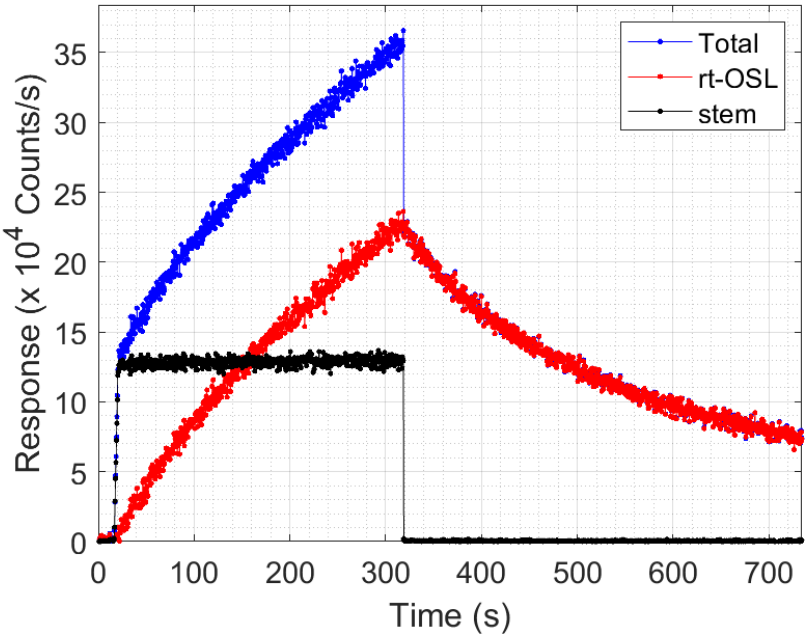

Figure 5.3: Sample measured waveform during the rtOSL measurement scheme. In the plots, Total corresponds to the laser on signal (blue), stem corresponds to the laser off signal (black) and rtOSL corresponds to the difference between the laser on and laser off signal (red). Published in Madden *et al.* 2020 [209].

Clinical LINAC measurements

Further measurements were taken with a linear accelerator (Truebeam, Varian, USA) at Royal Adelaide Hospital. All measurements used the 6 MV flattening filter free photon beam, with Gammex RMI457 Solid Water as the phantom material. To prevent mechanical damage to the dosimeter while it was sandwiched between the Solid Water slabs, the dosimeter was housed in a 4 mm thick cardboard sheet. The cardboard housing was sandwiched between 1.3 cm of Solid Water placed upstream of the dosimeter for build-up, and 12 cm of Solid Water placed downstream of the dosimeter for backscatter. This setup is modelled in Figure 5.4, with a close up of the BeO-optical fibre coupling shown in the figure's top right corner. The dose-rate dependence of BeO's rtOSL response was investigated by varying the LINAC's repetition rate and the SSD. For all measurements, a 10 cm $\times$ 10 cm jaw-defined field was used. For the repetition rate dependence measurements, 400 Monitor Units (MU) were delivered with the source-surface distance fixed at 100 cm, and the repetition rate was varied between 400 MU/min and 1400 MU/min. For the SSD measurements, the repetition rate was fixed at 800 MU/min and the SSD was varied between 62.5 cm and 143 cm.

The BeO dosimeter differed from that used for the superficial X-ray measurements, such that it was modified to improve it's signal to noise ratio. The BeO dosimeter consisted of a cylindrical volume of pure BeO ceramic (Thermalox 995, Materion, USA)

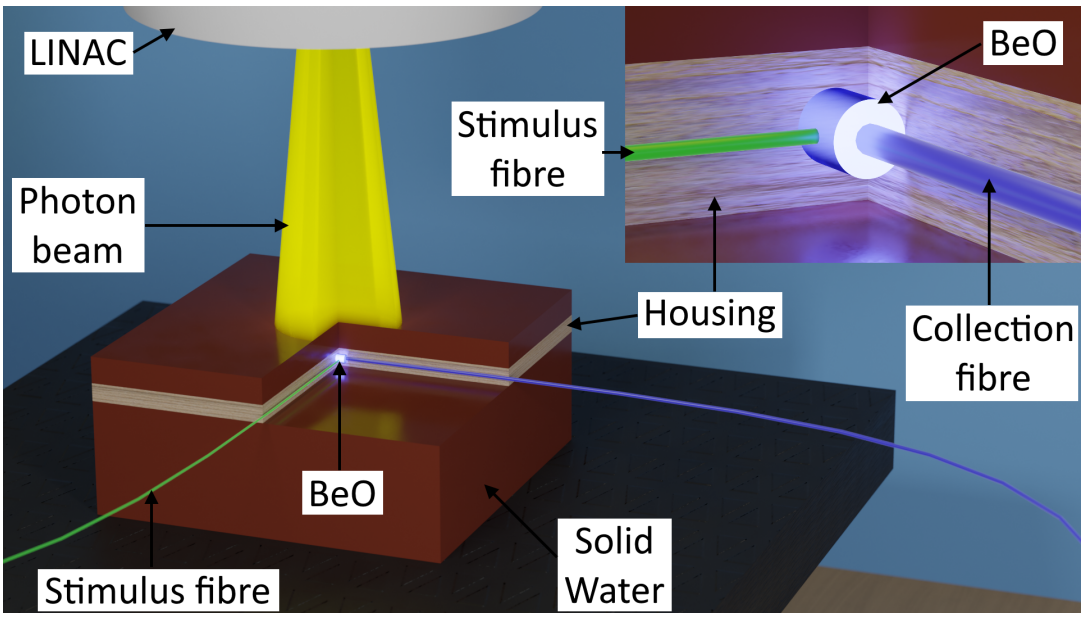

Figure 5.4: 3D model of the setup in Solid Water with a cutaway to show the BeO dosimeter. Close up of the BeO dosimeter and optical fibres are shown in the top right corner. The green optical fibre is the stimulus fibre, and the blue optical fibre is the collection fibre.

with a length of 1 mm and a diameter of 1 mm, coupled to two optical fibres. The first optical fibre (FP600URT, Thorlabs, USA) was used to collect BeO's luminescence signal, and had an approximate length of 20 m, a pure silica core with 600 μm nominal diameter, a hard polymer cladding with 630 μm nominal diameter and a numerical aperture of 0.50. The second optical fibre (SH2001, Eska, Mitsubishi Chemical Co., Japan) was not permanently coupled to the BeO ceramic, but was set up so it's tip was in contact with the ceramic during experimental measurements. This second optical fibre was used to transport the optical stimulus signal, and had an approximate length of 20 m, a PMMA core with 200 μm nominal diameter, a fluorinated polymer cladding with 220 μm nominal diameter and a numerical aperture of 0.50. The fibre-coupled BeO dosimeter used with the LINAC is shown in Figure 5.4, with a close up of the BeO-optical fibre couplings shown in the figure's top right corner. The same H3760-01 photomultiplier tube and USB data acquisition card were used to measure and record the luminescence signal at a 1 kHz sampling frequency. The same 40 mW laser diode was used to optically stimulate the BeO ceramic with a 2 Hz, 50 % duty cycle square wave. After each irradiation, the BeO volume was optically bleached for 20 minutes to substantially empty the optically active trapping centres.

5.2.2 Non-linearity correction methods

ΔrtOSL correction

The supra-linear behaviour of rtOSL signals arises due to the competing kinetics describing the filling and emptying of optically active traps during irradiation and inconsistent optical stimulation [109]. The concentration of filled optically active traps increases at a rate proportional to the dose-rate. Each stimulus pulse liberates some constant fraction of the filled optically active traps. As a result, the OSL signal measured during the n^{th} stimulus pulse is reduced in intensity due to the liberations caused by previous $n-1$ stimulus pulses. To restore proportionality between the measured OSL and the absorbed dose, the ΔrtOSL method corrects the OSL signal measured during the n^{th} stimulus pulse by correcting for the depletion effects of previous $n-1$ stimulations [24]:

$$\hat{\mathrm{D}}_{\Delta\mathrm{rtOSL}}(n) = \tilde{I}(n) + \sum_{i=1}^{n-1} \tilde{I}(i) \cdot F(D)^{n-i} \tag{5.1}$$

Where $\hat{\mathrm{D}}_{\Delta\mathrm{rtOSL}}(n)$ is the corrected rtOSL signal during the n^{th} stimulus pulse, $\tilde{I}(n)$ is the rtOSL signal measured during the n^{th} stimulus pulse, and $F(D)$ accounts for the depletion of the rtOSL signal due to previous stimulus pulses [24]. $F(D)$ is typically determined algorithmically post-measurement from the shape of the OSL curve [24], and $\hat{\mathrm{D}}_{\Delta\mathrm{rtOSL}}(n)$ has a time dependence that is proportional to the time-dependent accumulated dose in BeO. For measurements with the superficial X-ray source, the depletion correction factor was determined algorithmically with optimal value of 1.0017. For measurements with the LINAC, the depletion correction factor was similarly determined with the optimal value determined to be 1.0040. For the ΔrtOSL correction method, the integral dose in BeO was calculated as $I'(N)$, with N being the length of the measured rtOSL waveform.

Deconvolution correction

Luminescence signals can be modelled using the convolution of a time-dependent stimulus with a luminescence impulse response function (LIRF) [43]. For the measurements in this chapter, the measured rtOSL, $I(t)$, is modelled using the convolution of the time-dependent dose-rate, $\dot{\mathrm{D}}(t)$, (referred to as the dose-rate profile) and BeO's LIRF (for it's rtOSL response), $h(t)$:

$$I(t) \propto h(t) * \dot{\mathrm{D}}(t) \tag{5.2}$$

Where $*$ is the linear convolution operation. Proportionality is used in Equation 5.2 to preserve dimensionality. Equation 5.2 can be represented in discrete time using matrix multiplication, this is desirable as this representation takes the form of a least squares problem, allowing for fast computations of $h(t)$ when $\dot{\mathrm{D}}(t)$ is known and $\dot{\mathrm{D}}(t)$ when $h(t)$

[210]. For BeO, the RL and OSL have luminescence lifetimes of the order of tens of microseconds or shorter [211, 212], and so the stem+RL signal decays so fast that it appears instantaneous at the 2 Hz timescale used during the rtOSL technique in this chapter. Further, the stem signals produced by optical fibres have lifetimes that are of the order of tens of microseconds or shorter [169], also appearing instantaneous at the 2 Hz timescale used by the data acquisition card. Given these signals are so fast they appear instantaneous at the 2 Hz timescale, the measured stem+RL signal has a time-dependence that matches the time-dependent dose-rate. The stem+RL signal can be substituted for $\dot{\mathrm{D}}(t)$, and the least squares representation of Equation 5.2 is given by:

$$\begin{bmatrix} I(1) \\ I(2) \\ \vdots \\ I(N) \end{bmatrix} \propto \begin{bmatrix} \dot{\mathrm{D}}(1) & 0 & ... & 0 \\ \dot{\mathrm{D}}(2) & \dot{\mathrm{D}}(1) & ... & 0 \\ \vdots & \vdots & \ddots & \vdots \\ \dot{\mathrm{D}}(N) & \dot{\mathrm{D}}(N-1) & ... & \dot{\mathrm{D}}(1) \end{bmatrix} \cdot \begin{bmatrix} h(1) \\ h(2) \\ \vdots \\ h(N) \end{bmatrix}$$

$$\tilde{I} \propto \dot{\mathbf{D}} \cdot \tilde{h} \tag{5.3}$$

Where $\tilde{I}$ is the measured rtOSL in column vector form, N is the number of samples in measured rtOSL signals, the $N \times N$ matrix, $\dot{\mathbf{D}}$, is a lower triangular Toeplitz matrix constructed from $\dot{\mathrm{D}}(t)$, and $\tilde{h}$ is BeO's LIRF in column vector form. From classical kinetic modelling, BeO's post-irradiation OSL is given by a sum of m exponential decays, where m is the number of optically active traps in BeO [16]. BeO's LIRF can thus be modelled using a non-negative linear combination of M exponential decays, defined in discrete time in Equation 5.4:

$$\begin{bmatrix} h(1) \\ h(2) \\ \vdots \\ h(N) \end{bmatrix} = \begin{bmatrix} 1 & 1 & ... & 1 \\ e^{(-\frac{1}{\tau_1})} & e^{(-\frac{1}{\tau_2})} & ... & e^{(-\frac{1}{\tau_M})} \\ \vdots & \vdots & \vdots & \vdots \\ e^{(-\frac{N}{\tau_1})} & e^{(-\frac{N}{\tau_2})} & ... & e^{(-\frac{N}{\tau_M})} \end{bmatrix} \cdot \begin{bmatrix} a_1 \\ a_2 \\ \vdots \\ a_M \end{bmatrix}$$

$$\tilde{h} = E \cdot \hat{a} \tag{5.4}$$

Where E is the library of M exponentials and $\hat{a}$ are the fitting coefficients. The exponential decay parameters remained fixed at predefined values to reduce computation times whilst avoiding the more cumbersome non-linear least squares optimisation. The fitting coefficients, a_1, a_2, ..., a_M were constrained to non-negative values to enforce sparsity and prevent overfitting of a_1, a_2, ..., a_M to noise in the measured rtOSL signals. The non-negative least squares problem to be solved for the optimal coefficients of $\hat{a}$:

$$\min\left(||\tilde{I} - \dot{\mathbf{D}} \cdot E \cdot \hat{a}||^2\right) \quad \text{s.t.} \quad \hat{a} \succeq 0 \tag{5.5}$$

In this work, MATLAB's built-in non-negative least squares solver **lsqnonneg** was used to determine $\hat{a}$ in Equation 5.5. For rtOSL signals, the rate at which traps are emptied depends on the optical stimulus' intensity [24, 109], therefore the LIRF and $\hat{a}$ are affected by LASER intensity. The BeO dosimetry system varied between measurements with the superficial X-ray unit and the LINAC, hence $\hat{a}$ varies between these measurements. From the 5 rtOSL signals measured with the superficial X-ray unit, $\hat{a}$ was calculated, normalised so that $\Sigma\hat{a} = 1$ and averaged to determine the optimal fitting coefficients $\hat{a}$ for the BeO dosimetry system used with the superficial X-ray measurements. Similarly, from the 11 rtOSL signals measured with the LINAC, $\hat{a}$ was calculated, normalised so that $\Sigma\hat{a} = 1$ and averaged to determine the optimal fitting coefficients for the BeO dosimetry system used with the LINAC. Full MATLAB code of this LIRF calculation is presented in Appendix A.3.

With the two optimal $\hat{a}$s calculated, $h(t)$ was calculated as in Equation 5.4. Equation 5.3 can be reformulated with the lower-triangular Toeplitz matrix constructed using $\tilde{h}$, the LIRF. Defining $\mathbf{H}$ as the lower triangular Toeplitz matrix constructed using $\tilde{h}$, the convolutional model of luminescence can be expressed as in 5.6:

$$\begin{bmatrix} I(1) \\ I(2) \\ \vdots \\ I(N) \end{bmatrix} = \begin{bmatrix} h(1) & 0 & \dots & 0 \\ h(2) & h(1) & \dots & 0 \\ \vdots & \vdots & \ddots & \vdots \\ h(N) & h(N-1) & \dots & h(1) \end{bmatrix} \cdot \begin{bmatrix} \dot{\mathrm{D}}(1) \\ \dot{\mathrm{D}}(2) \\ \vdots \\ \dot{\mathrm{D}}(N) \end{bmatrix}$$
$$\tilde{I} = \mathbf{H} \cdot \dot{\mathrm{D}} \tag{5.6}$$

From this expression of the expected luminescence, the ordinary least squares solution for an unknown $\dot{\mathrm{D}}_{\mathrm{OLS}}$ is given by $\dot{\mathrm{D}}_{\mathrm{OLS}}$ in Equation 5.7:

$$\dot{\mathrm{D}}_{\mathrm{OLS}} = (\mathbf{H}^T\mathbf{H})^{-1}\mathbf{H}^T\tilde{I} \tag{5.7}$$

The ordinary least squares solution to deconvolution problems are known to exacerbates measurement noise and produce estimates with sub-optimal signal qualities [213], hence $\dot{\mathrm{D}}_{\mathrm{OLS}}$ was not taken as the optimal solution. Instead, Tikhonov regularised least squares was applied to enforce smooth solutions of $\dot{\mathrm{D}}$ in the deconvolution problem in Equation 5.6. The regularised least squares problem for smooth solutions of $\dot{\mathrm{D}}$ was [213]:

$$\min\left(||\tilde{I} - \mathbf{H} \cdot \dot{\mathrm{D}}||^2 + \alpha||L\dot{\mathrm{D}}||^2\right) \tag{5.8}$$

Where α is the regularisation hyperparameter and L was chosen to be the first-order finite difference matrix (defined in [214]) for smoothness of $\dot{\mathrm{D}}$ [213]. The Tikhonov regularised least squares solution for the dose-rate profile in BeO is given by $\dot{\mathrm{D}}_{\mathrm{RLS}}$ in Equation 5.9 [213]:

$$\dot{\mathrm{D}}_{\mathrm{RLS}} = \left(\mathbf{H}^T\mathbf{H} + \alpha L^T L\right)^{-1}\mathbf{H}^T\tilde{I} \tag{5.9}$$

α's value influences the estimated $\dot{\mathrm{D}}_{\mathrm{RLS}}(t)$, with increasing values of α leading to increasingly biased solutions. An equivalent minimisation problem to that in Equation 5.8 can be achieved under a Bayesian framework for Tikhonov regularised least squares [215]. The Tikhonov least squares estimator $\dot{\mathrm{D}}_{\mathrm{RLS}}$ is equivalent to the posterior mean estimator for $\dot{\mathrm{D}}$ when imposing a Gaussian smoothness prior on $\dot{\mathrm{D}}$ [215]. Under this framework, the Maximum A Posteriori solution for $\dot{\mathrm{D}}(t)$ uses $\alpha = \hat{\alpha}$ in Equation 5.10 [215]:

$$\hat{\alpha} = \frac{\sigma_I^2}{\sigma_D^2} \quad \text{s.t.} \quad \sigma_I^2 = \mathrm{var}\left(\tilde{I} - \mathbf{H}\cdot\dot{\mathrm{D}}_{\mathrm{OLS}}\right), \quad \sigma_D^2 = \mathrm{var}\left(L\dot{\mathrm{D}}_{\mathrm{OLS}}\right) \tag{5.10}$$

Where σ_I^2 are the variance of the ordinary least squares residual given by $(\tilde{I} - \mathbf{H}\cdot\dot{\mathrm{D}}_{\mathrm{OLS}})$ and σ_D^2 is the variance of the first order time derivative of $\mathrm{D}_{\mathrm{OLS}}$. This value of $\hat{\alpha}$ was chosen as it analytically determines an optimal trade off between the smoothness of $\dot{\mathrm{D}}_{\mathrm{OLS}}$ and the fit of $\mathbf{H}\cdot\dot{\mathrm{D}}_{\mathrm{RLS}}$ to measured rtOSL signals, $\tilde{I}$ [215], effectively de-noising the $\dot{\mathrm{D}}_{\mathrm{RLS}}$ without degrading the time-dependence of $\dot{\mathrm{D}}_{\mathrm{RLS}}$. The regularised least squares estimate, $\dot{\mathrm{D}}_{\mathrm{RLS}}$, was calculated using $\hat{\alpha}$. The accumulated dose signal, $\hat{\mathrm{D}}_{\mathrm{RLS}}$ was calculated by integrating $\dot{\mathrm{D}}_{\mathrm{RLS}}$ with respect to time, with the boundary condition that the dose in BeO at time $t = 0$ is zero:

$$\hat{\mathrm{D}}_{\mathrm{RLS}}(t) = \int_0^t \dot{\mathrm{D}}_{\mathrm{RLS}}(t')dt' \quad \text{s.t.} \quad \hat{\mathrm{D}}_{\mathrm{RLS}}(t=0) = 0 \tag{5.11}$$

The dose deposited in BeO is given by $\hat{\mathrm{D}}_{\mathrm{RLS}}(t = t_N)$ where t_N is the last time when the rtOSL was measured. MATLAB code for the deconvolution correction method is presented in Appendix A.4

Exponential correction

An rtOSL signal's supra-linearity arises as a result of the opposition between the filling and emptying of traps [24, 109]. The concentration of filled traps increases at a rate proportional to the dose-rate, and the concentration of filled traps decreases at a rate proportional to the concentration of filled traps. The population of filled traps can be crudely modelled as:

$$\frac{dn(t)}{dt} = k_1\dot{\mathrm{D}}(t) - k_2 n(t) \tag{5.12}$$

Where $\frac{dn}{dt}$ is the rate of change of the filled traps, $\dot{\mathrm{D}}(t)$ is the time-dependent dose-rate, n is the filled trap population, and k_1 and k_2 are constants. The kinetics modelled in Equation 5.12 are non-linear, but are approximately first order in nature. The rtOSL signal experiences a depletion that is approximately first order with respect to time. These depletion effects can be empirically cancelled out through multiplication with an exponential function to restore linearity with the accumulated dose:

$$\tilde{I(t)} \cdot e^{F(D)t} = \mathrm{D}(t) \cdot \text{constant} \tag{5.13}$$

Where $\tilde{I(t)}$ is the measured rtOSL, $F(D)$ is a coefficient to correct for the approximately first order depletion effects inherent to the rtOSL, and $\mathrm{D}(t)$ is the accumulated dose as a function of time. Rearranging the terms in this expression, the exponential constant $F(D)$ can be determined analytically:

$$\ln\left(\frac{\mathrm{D}(t)}{\tilde{I}(t)}\right) = F(D)t + \text{constant} \tag{5.14}$$

Where $F(D)$ corresponds to the slope when $\ln\left(\frac{\mathrm{D}(t)}{\tilde{I}(t)}\right)$ is plotted as a function time, hence linear regression can be used to determine this slope. Though the accumulated dose is not known, the stem+RL signal has a time dependence matching the time-dependent dose-rate as the stem signal, RL and OSL have short luminescence lifetimes. The accumulated dose can be modelled by the integral of the stem+RL signal with respect to time, provided the field size and irradiation angle remain constant during the irradiation. The degradation effects of measurement noise can be mitigated through substitution of the measured rtOSL signal with a noiseless model of the rtOSL signal. Substituting the optimal LIRF calculated previously for $h(t)$ in the deconvolution correction, and the stem+RL signal for $\dot{\mathrm{D}}(t)$, a noiseless model of the rtOSL, $I(t)$ can be calculated as in Equation 5.2. Substituting the noiseless model of the rtOSL $I(t)$ for the measured rtOSL $\tilde{I}(t)$, $F(D)$ is calculated as:

$$F(D) = \text{slope}\left(\ln\left(\frac{\mathrm{D}(t)}{I(t)}\right)\right) \tag{5.15}$$

The measured rtOSL is corrected by multiplying the measured rtOSL by the exponential correction function:

$$\hat{\mathrm{D}}_{exp}(t) = \tilde{I}(t) \cdot e^{F(D)t} \tag{5.16}$$

As in the ΔrtOSL correction method, the corrected rtOSL, $\hat{\mathrm{D}}_{exp}(t)$, has a time-dependence proportional to the time-dependent accumulated dose in BeO. The integral dose in BeO

was calculated as the final value of the corrected rtOSL signal, $\hat{\mathrm{D}}_{exp}(t_N)$, where t_N was the final time in the measured rtOSL signal.

5.2.3 Analysis

Time-dependence of corrected rtOSL

Given the stem+RL signal has a time-dependence matching $\dot{\mathrm{D}}$, the integral of the stem+RL signal has a time dependence matching the accumulated dose in BeO as a function of time, $\mathrm{D}(t)$. Through curve fitting, the integral stem+RL signal can be fit to each of the corrected rtOSL signals using the ordinary least squares model:

$$\min\left(||\hat{\mathrm{D}}(t) - Y(t)||^2\right) \quad \text{s.t.} \quad Y(t) = b \cdot \int \text{stem+RL}(t)dt + c \tag{5.17}$$

Where $\hat{\mathrm{D}}(t)$ are each of the corrected rtOSL signals, stem+RL(t) is the measured stem+RL signal and b and c are fitting coefficients. The uncertainty in each of the fits of $Y(t)$ to each of the corrected rtOSL signals, $\hat{\mathrm{D}}(t)$ is given by the root mean squared error (RMSE) between $Y(t)$ and $\hat{\mathrm{D}}(t)$ [216]:

$$\text{RMSE} = \sqrt{\frac{1}{N}\sum\left(\hat{\mathrm{D}}(t) - Y(t)\right)^2} \tag{5.18}$$

Where N is the length of the corrected rtOSL signal $\hat{\mathrm{D}}(t)$.

Dosimetry

BeO's OSL and rtOSL are dose-rate independent [7, 30]. During the repetition rate measurements with the LINAC, the same nominal dose was delivered and so the corrected rtOSL responses can be compared directly. For these measurements, the corrected responses were normalised so that the mean response corresponded to a relative dose of 100 %. With these corrected responses normalised to a mean relative dose of 100 %, mean absolute doses (MADs) can be calculated as in Equation 5.19 to quantify how the average corrected response deviated from the mean:

$$\text{MAD} = \frac{1}{N_{meas}} \sum_{i=1}^{N_{meas}} |\hat{\mathrm{D}}_i - 100\%| \tag{5.19}$$

Where $\hat{\mathrm{D}}_i$ is the corrected rtOSL response and N_{meas} are the number of measured responses. Similarly, standard deviations can be calculated as an additional measure of how dispersed the corrected rtOSL responses are about a relative dose of 100 %. During the SSD measurements with the LINAC, 800 MU was delivered by the LINAC at 800 MU/min, such that the BeO dosimeter was irradiated for 1 minute. Similarly for the SSD measurements with the superficial X-ray unit, the BeO dosimeter was irradiated for

5 minutes during each measurement. For each of the measurements with the SSD, the corrected rtOSL responses can be normalised by the inverse squared SSD to account for the change in dose deposited in BeO due to the variation of the SSD. The normalised responses can be further normalised so that their mean corresponds to a relative dose of 100 %, and mean MADs and SDs can be calculated.

To determine how measurement noise affected the corrected rtOSL responses, each of the correction methods were applied independently to the measured and fitted rtOSL signals. Measured rtOSL signals were inherently noisy, whereas fitted rtOSL signals were noiseless. Comparisons of the MADs and standard deviations calculated from the measured rtOSL signals allow for the robustness of each correction method to be established in the presence of measurement noise. Conversely, the MADs, standard deviations and RMSEs calculated from the fitted rtOSL signals serve as the estimates of each method's accuracy in optimal conditions.

5.2.4 Simulation of real-time deconvolution

The exponential and deconvolution corrections can be performed in real-time, provided that the optimal LIRF is known prior to the real-time measurements. However, the exponential correction requires the stem+RL signal for correction of the rtOSL. The stem+RL signal can vary with field size and irradiation angle, the stem+RL signal has the potential to deviate from the dose-rate profile when the field size or irradiation angle varies. As the field size and irradiation angle have the potential to vary during *in vivo* dosimetry, the exponential correction may not be viable for *in vivo*, real-time dosimetry measurements.

A computational simulation was performed to simulate the deconvolution correction in real-time and determine the time required to compute the corrected rtOSL signal. In this simulation, the measured rtOSL signal was sampled from it's first point to it's i^{th} point, with i iterated from 2 to N (the length of the rtOSL signal) to simulate the real-time measurement of rtOSL. Similarly, the time array was sampled from 1 to i at each iteration, and was used to calculate the LIRF from Equation 5.4 in real-time (with the optimal fitting coefficients known prior to the simulation). The calculated LIRF and sampled rtOSL was then used for the deconvolution analysis at each iteration. The time taken to compute the LIRF and perform each correction was recorded at each iteration to determine the feasibility of deconvolution as a real-time rtOSL correction.

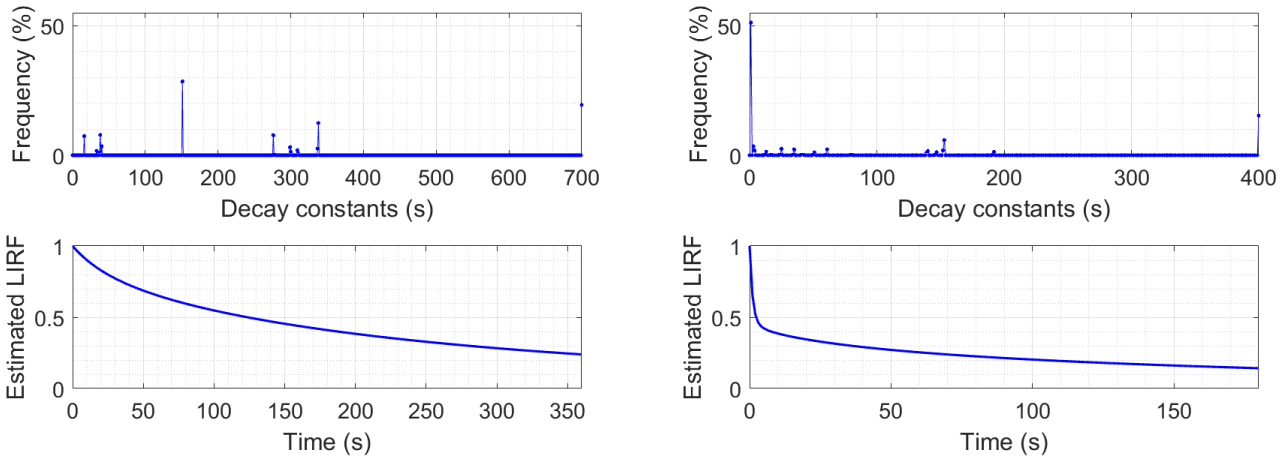

Figure 5.5: Left column: Lifetime distribution and corresponding LIRFs from measurements with the superficial X-ray unit. Right column: Lifetime distribution and corresponding LIRFs from measurements with the LINAC. Top: distribution of exponential lifetimes for BeO's rtOSL LIRF, normalised by the sum of all fitting coefficients in the distribution. Bottom: Optimal LIRF for measured rtOSL signals.

5.3 Results

5.3.1 Fitting an LIRF to measured rtOSL

For the signals measured using the superficial X-ray unit, the exponential decay parameters (τ_1, τ_2, ..., τ_M) were set to (ε, 1, 2, ..., 700) s with ε being a machine epsilon to avoid division by zero. The optimum fitting coefficients, $\hat{a}$, were calculated for each rtOSL signal measured with the superficial X-ray unit, averaged to find the global optimum fitting coefficients. The global fitting coefficients are presented in Figure 5.5 (top), corresponding to the distribution of exponential lifetimes for BeO's real-time optically stimulated luminescence. The most significant lifetimes for these measurements occurred for decay constants of 151 s and 700 s, comprising 28 % and 19 % of the total distribution. There was also a cluster of constants between 16 s and 40 s, with this cluster comprising 21 % of the total distribution. A more widely distributed cluster of lifetimes occurred for decay constants between 276 s and 338 s, comprising 31 % of the total distribution.

Similarly, the exponential decay parameters (τ_1, τ_2, ..., τ_M) were set to (ε, 1, 2, ..., 400) s for the rtOSL signals measured using the LINAC. The optimal fitting coefficients, $\hat{a}$, were calculated for each rtOSL signal measured with the LINAC, averaged to find the global optimum fitting coefficients. The global fitting coefficients are presented in Figure 5.5 (top), corresponding to the distribution of exponentials for BeO's rtOSL. The most significant clusters of lifetimes in the optimal LIRF occur for decay constants between 1 s and 10 s, comprising 56 %, and 400 s, comprising 15 % of the total distribution. There also exists a cluster of decay constants spanning between 138 and 152 s comprising 12 % of

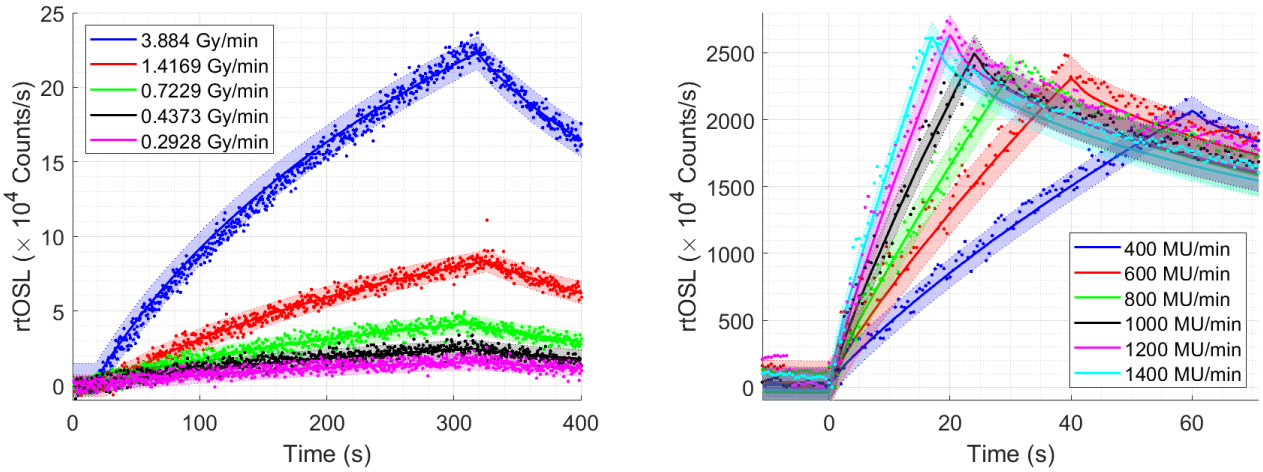

Figure 5.6: Left column: Fit and measured rtOSL signals from measurements with the superficial X-ray unit. Right column: Fit and measured rtOSL signals from the repetition rate measurements with the LINAC. Points correspond to the measured rtOSL signals, solid lines correspond to the fitted rtOSL signals, and shading corresponds to 2 standard deviations in the fitted rtOSL signals.

the lifetime distribution, and a more sparsely populated cluster for constants between 10 s and 62 s comprising 14 % of the lifetime distribution. The global optimal LIRF was calculated using Equation 5.4, substituting the global optimal fitting coefficients for $\hat{a}$. The global LIRF calculated from the distribution of lifetimes is shown in Figure 5.5 (bottom), normalised to the LIRF at time $t = 0$ s.

$I(t)$ was calculated using Equation 5.2, substituting the optimal LIRFs shown in Figure 5.5 for $h(t)$ and the measured stem+RL signals for $\dot{D}(t)$. $I(t)$ was fit to the measured rtOSL using the ordinary least squares fitting model:

$$\min\left(||\tilde{I}(t) - \hat{I}||^2\right) \quad \text{s.t.} \quad \hat{I} = eI(t) + f \tag{5.20}$$

Where $\hat{I}$ was the fitted rtOSL, $\tilde{I}(t)$ was the measured rtOSL, and e and f are fitting coefficients. The fitted rtOSL signals, $\hat{I}(t)$, and the corresponding measured rtOSL signals, $\tilde{I}(t)$, from the superficial X-ray unit shown in Figure 5.6 (left); the fit and measured rtOSL signals for the repetition rate measurements with the LINAC are shown in Figure 5.6 (right). Shading corresponds to the 95 % confidence interval in each of the fitted rtOSL signals. As can be seen in Figure 5.6, the fitted rtOSL qualitatively closely matched the measured rtOSL.

5.3.2 Calculation of F(D) using exponential correction

The fitted rtOSL $\hat{I}(t)$ was plotted as a function of the accumulated dose, shown in Figure 5.7 (left) for the measurements with the superficial X-ray unit. The corresponding natural log of the accumulated dose divided by the fitted rtOSL was plotted against time, shown

in Figure 5.7 (right). The expected linearity trend was not observed in the first 30 seconds of irradiation; for this reason, the first 30 seconds of each fit was excluded when fitting the linear trend. From Equation 5.15, the rtOSL decay correction $F(D)$ was calculated by fitting a linear trend-line to the natural log of the accumulated dose divided by the rtOSL, and the time axis. The optimal value of $F(D)$ was calculated to be $(1.9\times10^{-3} \pm 5.8\times10^{-5})\ s^{-1}$. The same analysis was repeated for the rtOSL signals measured with the LINAC. The optimal value for the depletion factor, $F(D)$ was calculated to be $(7.0\times10^{-3} \pm 2.1\times10^{-4})\ s^{-1}$.

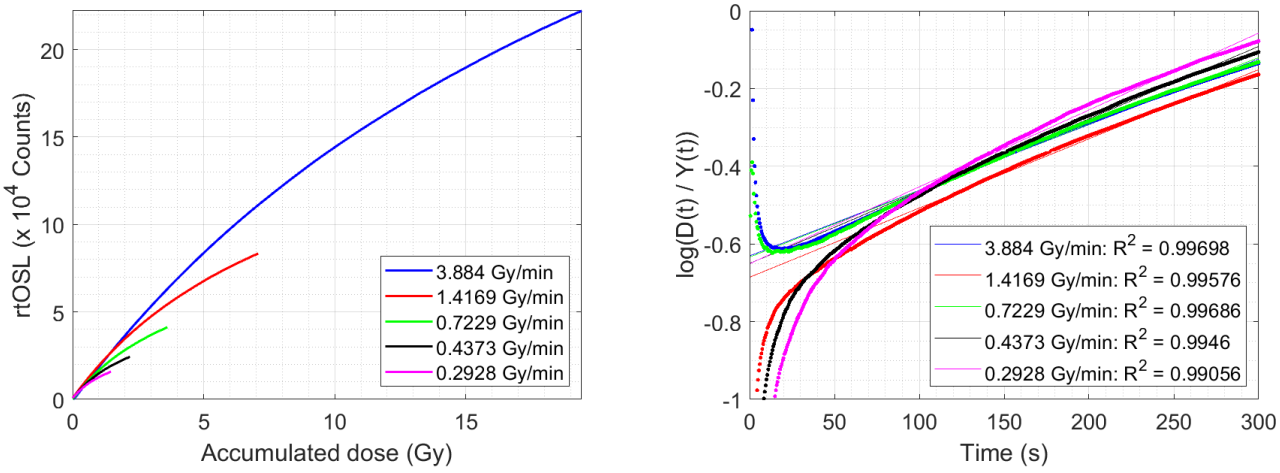

Figure 5.7: Left: Fitted rtOSL signal plotted as a function of accumulated dose (corresponding to duration of irradiation multiplied by each nominal dose-rate). Right: Plot of $\ln\left(\frac{D(t)}{Y(t)}\right)$ as a function of time for calculation of $F(D)$. Linear trend lines are fit to $\left(\frac{D(t)}{Y(t)}\right)$ versus time to determine each rtOSL's $F(D)$. Published in Madden *et al.* [209].

5.3.3 Time dependence of corrected rtOSL

The measured rtOSL signals were corrected using the aforementioned correction methods. A sample of the measured and corrected rtOSL signals are plotted in Figure 5.8, measured using the LINAC. In the presented waveform, the LINAC's beam delivery began at 11 s and concluded at 71 s; these are marked with the magenta dashed line in Figure 5.8. Each of the corrected rtOSL signals increases linearly during irradiation, proportional to the accumulated dose in BeO. During the post-irradiation readout, the ΔrtOSL and exponential corrected signals were approximately stable with time, whereas the deconvolution corrected signal was more stable during this period.

The stem+RL signal was integrated and fitted to the corrected rtOSL signals as described in Equation 5.17, with the fit of the integral stem+RL signal to each correction method's corrected rtOSL shown in Figure 5.9. Each of the corrected rtOSL signals have time-dependence matching that of the integral stem+RL signal, plotted in black for each

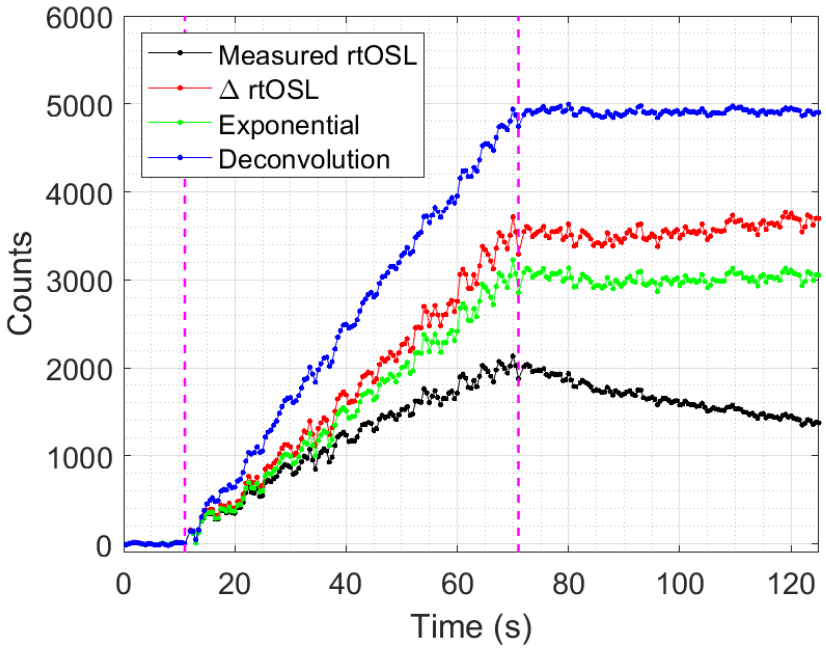

Figure 5.8: Example of measured and corrected rtOSL signals, measured using the LINAC. The measured rtOSL is uncorrected, ΔrtOSL is the corrected rtOSL using the ΔrtOSL method, Exponential is the corrected rtOSL using the exponential correction and Deconvolution is the corrected rtOSL using the deconvolution correction.

of the correction methods. The deconvolution corrected rtOSL signal had an observably smaller magnitude of noise than the ΔrtOSL and exponential corrected rtOSL signals, with the $\hat{\alpha}$ regularisation parameter acting as a smoothing operator. The uncertainty of each fit is given by two times the RMSE between the fit integral stem+RL signal and the corrected rtOSL as defined in Equation 5.18. In Figure 5.9, the 95 % confidence interval is plotted as the magenta shaded region (2 times the RMSE), too small to be seen for the deconvolution method given it's improved SNR. Deconvolution's global RMSE was smallest, indicating the deconvolution corrected rtOSL was the best descriptor for the absorbed dose in BeO as a function of time.

5.3.4 Dosimetry

The correction methods were applied to the measured rtOSL signals and the fitted rtOSL signals. Responses were calculated for each of the correction methods using the measured rtOSL signals and the resultant dose-rate dependences are plotted in Figures 5.10 and 5.11. For the responses calculated with the fitted rtOSL signals, the resultant dose-rate dependences are plotted in Figures 5.12 and 5.13. RMSEs for each of the corrected responses were plotted at the bottom of Figures 5.10−5.13. From each of the dose-rate dependences, MADs and standard deviations were calculated, reported in Tables 5.1 and 5.2. The global mean RMSEs for each correction method are also reported in Tables 5.1

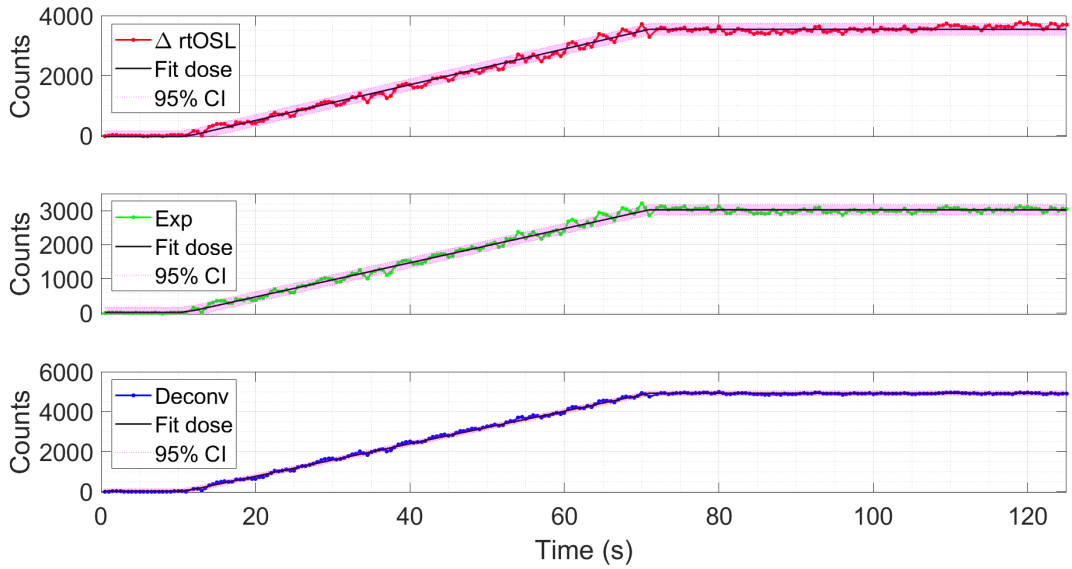

Figure 5.9: Fits of the integral stem+RL signal to each corrected rtOSL signal. In each of the plots, Fit dose corresponds to the fit integral stem+RL signal to the corrected rtOSL, 95 % CI corresponds to the 95 % confidence interval (equal to 2 times the RMSE) and ΔrtOSL, Exp and Deconv correspond to the ΔrtOSL, exponential and deconvolution correction methods.

and 5.2.

Performance of correction methods using measured signals

	Global MAD	Global SD	Global RMSE
ΔrtOSL: SXR	10.2 %	16.5 %	5.9 %
Exponential: SXR	10.6 %	16.6 %	10.5 %
Deconvolution: SXR	6.2 %	7.4 %	4.6 %
ΔrtOSL: LINAC	4.4 %	6.4 %	7.3 %
Exponential: LINAC	4.1 %	5.4 %	4.6 %
Deconvolution: LINAC	1.5 %	1.9 %	2.0 %

Table 5.1: Table reporting the performance of rtOSL correction methods with measured rtOSL signals. In the top row, Global MAD is the global mean of the absolute dose differences for each correction method, Global SD is the standard deviation of the integral responses, and Global RMSE is the average of the root mean squared error for the fit of the integral stem+RL signals to the corrected rtOSL signals. In the left column, SXR corresponds to the statistics calculated from measurements with the superficial X-ray unit, LINAC corresponds to the statistics calculated from measurements with the LINAC.

Corrected responses calculated from the rtOSL signals measured with the superficial X-ray unit are shown in Figure 5.10. The ΔrtOSL corrected responses remained close to the expected 100 % mean relative dose for dose-rates of 0.2928 Gy/min, 1.4169 Gy/min and 3.884 Gy/min, however the ΔrtOSL corrected responses overestimated the mean 100 %

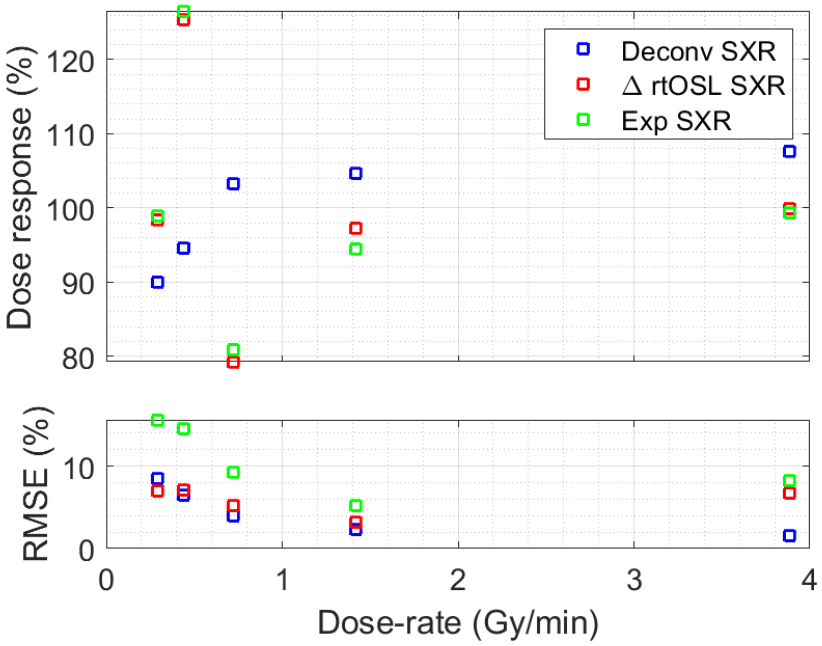

Figure 5.10: Top: Integral responses for the superficial X-ray unit using measured rtOSL signals. In the legend, ΔrtOSL, Exp and Deconv corresponds to the ΔrtOSL, exponential and deconvolution correction methods. Bottom: the RMSE in each integral response is plotted, calculated between the fit accumulated dose to the corrected rtOSL signals.

response by 25.4 % at 0.4373 Gy/min and underestimated the mean 100 % response by 20.9 % at 0.7229 Gy/min. A matching trend is observed for the corresponding exponential corrected responses, hence this overestimation and underestimation at the 0.4373 Gy/min and 0.7229 Gy/min dose-rates were expected to arise as a result of the significant measurement noise present in these measured rtOSL signals. As a result of these significant deviations in the corrected responses at 0.4373 Gy/min and 0.7229 Gy/min, the ΔrtOSL corrected responses had a MAD of 10.2 %; excluding the responses at 0.4373 Gy/min and 0.7229 Gy/min, the ΔrtOSL corrected responses reduced the MAD to 1.5 %. Similarly, the exponential corrected responses had a MAD of 10.6 % when including the responses at 0.4373 Gy/min and 0.7229 Gy/min, and 2.4 % excluding the responses at 0.4373 Gy/min and 0.7229 Gy/min. On average, the ΔrtOSL correction was characterised by a mean RMSE of 5.9 % in it's corrected responses, whereas the exponential correction had a mean uncertainty of 10.5 % in it's corrected responses.

Unlike the ΔrtOSL and exponential corrected responses from the superficial X-ray unit, the deconvolution corrected responses did not suffer from the overestimation at 0.4373 Gy/min and the underestimation at 0.7229 Gy/min. The deconvolution corrected responses systematically underestimated the dose in BeO as dose-rate decreased. This trend arose from a combination of two factors: regularisation during the least squares deconvolution, and the decreasing SNRs of measured rtOSL signals with decreasing dose-rate observable in Figure 5.6. For the Tikhonov regularised least squares approach to

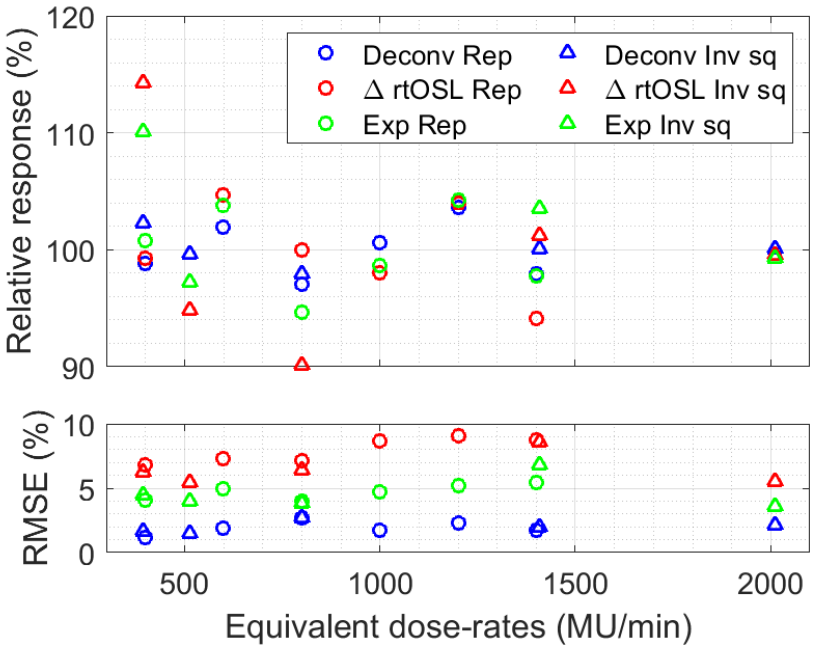

Figure 5.11: Top: Integral responses for the LINAC using measured rtOSL signals. In the legend, ΔrtOSL, Exp and Deconv corresponds to the ΔrtOSL, exponential and deconvolution correction methods. The suffix Rep corresponds to the dose-rate dependencies measured with varying repetition rate, and the suffix Inv sq corresponds to the dose-rate dependencies measured by varying the SSD. Bottom: the RMSEs in each integral response is plotted, calculated between the fit accumulated dose to the corrected rtOSL signals.

deconvolution used in this work, the regularisation biases estimates of $\dot{D}_{RLS}$ towards being temporally smooth. Increasing values of $\hat{\alpha}$ causes estimates of $\dot{D}_{RLS}$ to become increasingly smooth, but less sensitive to small changes in the measured rtOSL signal [216, 217]. As a result, the calculated $\hat{\dot{D}}_{RLS}(t)$ had a reduced amplitude relative to what would have been expected by the ordinary least squares model. Due to the decreasing SNRs with dose-rate, the value of $\hat{\alpha}$ calculated using Equation 5.10 increased as the dose-rate decreased. The deconvolution corrected responses had a MAD of 6.2 % when normalised to the mean response, improving on the 10.2 % and 10.6 % MADs for the ΔrtOSL and exponential corrections. Deconvolution's RMSEs decreased as the dose-rate increased, reaching a minimum of 1.6 % at 3.884 Gy/min. Globally, deconvolution corrected rtOSL signals had a mean RMSE of 4.6 %, improving upon the 5.9 % mean RMSE of the ΔrtOSL correction and 10.5 % mean RMSE of the exponential correction. From the statistics calculated from the 5 measured rtOSL signals, the deconvolution correction was more robust than the ΔrtOSL and exponential corrections.

Corrected responses calculated from the rtOSL signals measured with the LINAC are shown in Figure 5.11. There were no systematic trends for any of the correction methods as a function of dose-rate. The deconvolution corrected responses had a global MAD

of 1.5 %, whereas the ΔrtOSL and exponential corrected responses had global MADs of 4.4 % and 4.1 % respectively. The deconvolution corrected responses had a maximum deviation from the mean of 3.3 %, less than the MADs of the ΔrtOSL and exponential corrected responses with these signals. for these corrected signals. The deconvolution correction achieved the lowest MAD, standard deviation and RMSE for these 11 noisy rtOSL signals, such that the deconvolution correction was more accurate and reproducible than the ΔrtOSL and exponential corrections for the LINAC's rtOSL signals. From the integral responses in Figures 5.10 and 5.11, and the statistics in Table 5.1, it is conclusive that the deconvolution correction improves upon the performance of ΔrtOSL correction method with noisy rtOSL signals.

Performance of correction methods using fitted signals

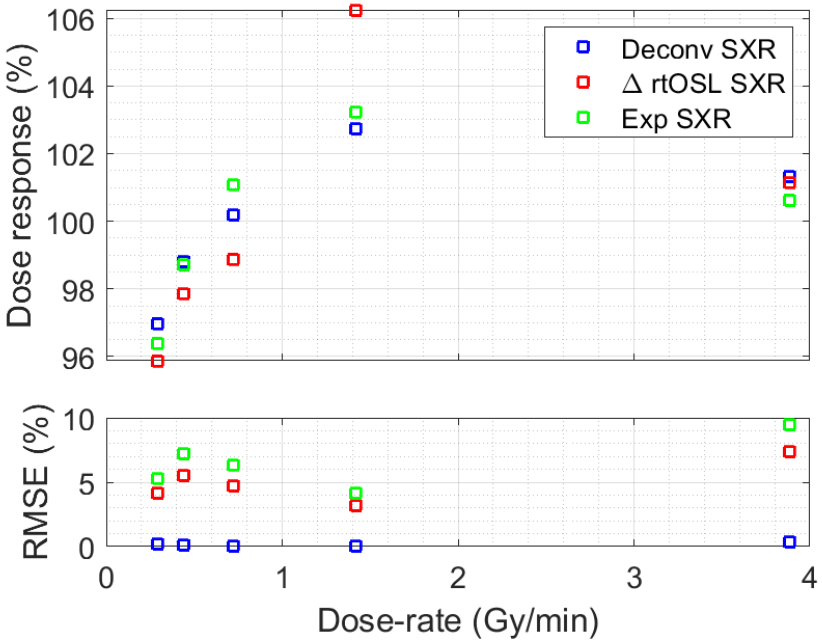

Figure 5.12: Top: Integral responses for the superficial X-ray unit using fitted rtOSL signals. In the legend, ΔrtOSL, Exp and Deconv corresponds to the ΔrtOSL, exponential and deconvolution correction methods. Bottom: the RMSEs in each integral response is plotted, calculated between the fit accumulated dose to the corrected rtOSL signals. Results for the exponential correction published in Madden *et al.* [209].

The corrected responses calculated using the fitted rtOSL signals with the superficial X-ray unit are show in Figure 5.12. There were no systematic trends present in the corrected responses with respect to the dose-rate. The deconvolution corrected responses were characterised by a MAD of 1.7 %, and a standard deviation of 2.2 %. The exponential corrected response were the next best correction with these fitted rtOSL signals, where the exponential corrected responses had a MAD of 2.0 % and a standard deviation of 2.6 %. The ΔrtOSL correction had the poorest performance with the fitted rtOSL

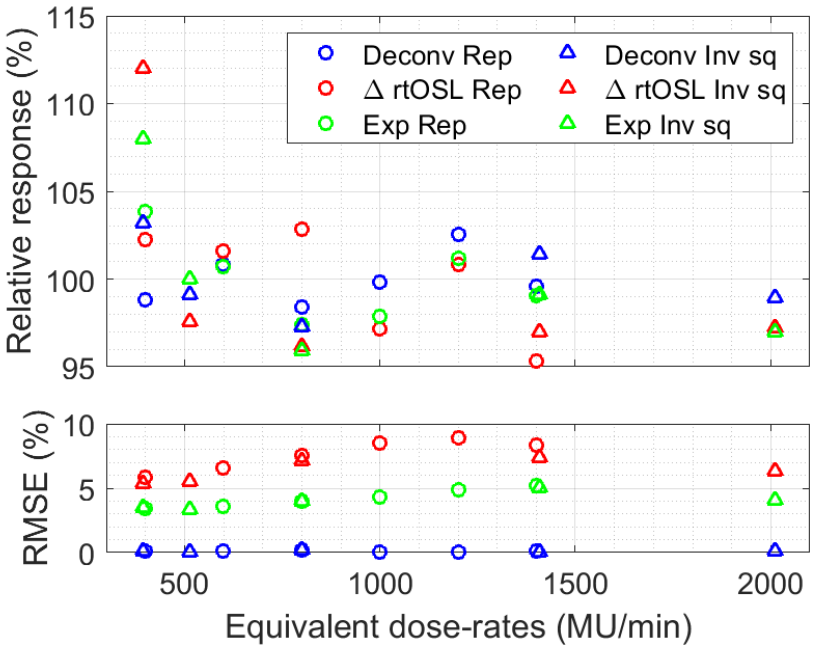

Figure 5.13: Top: Integral responses for the LINAC using measured rtOSL signals. In the legend, ΔrtOSL, Exp and Deconv corresponds to the ΔrtOSL, exponential and deconvolution correction methods; the suffix Rep corresponds to the dose-rate dependencies measured with varying repetition rate, and the suffix Inv sq corresponds to the dose-rate dependencies measured by varying the SSD. Bottom: the RMSEs in each integral response is plotted, calculated between the fit accumulated dose to the corrected rtOSL signals.

signals, such that the ΔrtOSL corrected responses had a MAD of 3.0 % and a standard deviation of 4.0 %. For the corrected responses in Figure 5.12, the deconvolution method was the most accurate correction method when using fitted rtOSL signals. It should be noted that the deconvolution corrected rtOSL had an average RMSE of 0.1 %. When applying the deconvolution correction to the fitted rtOSL signals, the distortion effect of the LIRF gets cancelled out and the integral stem+RL signal remains. The integral stem+RL signal was also used as the time-dependent accumulated dose when calculating the RMSE, hence the resultant RMSE approaches zero. Given this, the RMSEs calculated for the deconvolution correction are misleading when compared to the RMSEs calculated from the fitted signals using the ΔrtOSL and exponential corrections.

The corrected responses calculated using the fitted rtOSL signals from the LINAC are shown in Figure 5.13. There were no systematic trends present for the corrected rtOSL responses as a function of dose-rate. The deconvolution correction was the most effective method for these fitted rtOSL signals, such that the deconvolution corrected responses had a MAD of 1.5 % and a standard deviation 1.8 %. The exponential correction was the next most accurate correction method, with the exponential corrected responses having a MAD of 2.5 % and a standard deviation of 3.5 %. The ΔrtOSL correction had the poorest

	Global MAD	Global SD	Global RMSE
ΔrtOSL: SXR	3.0 %	4.0 %	5.0 %
Exponential: SXR	2.0 %	2.6 %	6.5 %
Deconvolution: SXR	1.7 %	2.2 %	0.1 %
ΔrtOSL: LINAC	3.6 %	4.8 %	7.0 %
Exponential: LINAC	2.5 %	3.5 %	4.1 %
Deconvolution: LINAC	1.5 %	1.8 %	0.1 %

Table 5.2: Table reporting the performance of rtOSL correction methods with fitted rtOSL signals. In the top row, Global MAD is the global mean of the absolute dose differences for each correction method, Global SD is the standard deviation of the integral responses, and Global RMSE is the average of the root mean squared error for the fit of the integral stem+RL signals to the corrected rtOSL signals. In the left column, SXR corresponds to the statistics calculated from measurements with the superficial X-ray unit, LINAC corresponds to the statistics calculated from measurements with the LINAC.

performance, where the ΔrtOSL corrected responses had a MAD of 3.6 % and a standard deviation of 4.8 %.

The MADs, standard deviations and RMSEs achieved with the fitted rtOSL signals are reported in Table 5.2. Each correction method achieved reduced MADs, standard deviations and RMSEs when correcting the fitted rtOSL signals, compared against their corresponding statistics from the measured rtOSL signals reported in Table 5.1. This improvement of performance was most significant for the rtOSL signals from the superficial X-ray unit. Comparing the results from the superficial X-ray unit's measured and fitted signals, the ΔrtOSL correction's MAD was reduced from 10.2 % to 3.0 %, the exponential correction's MAD was reduced from 10.6 % to 2.0 %, and the deconvolution correction's MAD was reduced from 6.2 % to 1.5 %; similar improvements occurred for their standard deviations. Improvements in performance of the correction methods was reduced when comparing the statistics calculated from the LINAC's measured and fitted rtOSL signals. This reduced improvement arose due to a number of setup related factors. Firstly, the BeO dosimetry system had been optimised to reduce measurement noise in measured rtOSL signals. Additionally, the LINAC's dose-rate was significantly higher than the dose-rate from the superficial X-ray unit, hence the LINAC's measured rtOSL signals had greater signal levels. It should be noted that the deconvolution corrected responses had a MAD of 1.5 % and a standard deviation of 1.9 % when correcting the measured rtOSL signals from the LINAC as in Figure 5.11. From these comparisons between measured rtOSL signals and fitted rtOSL signals, it is recommended that rtOSL dosimetry systems should be optimised for reduced measurement noise in order to minimise the uncertainties in corrected rtOSL responses.

5.3.5 Simulation of real-time deconvolution

The real-time simulation of the deconvolution correction is presented in Figure 5.14. In this file, each iteration is plotted as a single frame, with the computation time for deconvolution plotted in the bottom section. The simulation was performed in MATLAB 2021a on a 64 bit desktop computer with a 3.5 GHz Intel Core i7 CPU and 16 GB of installed RAM. The maximum time to calculate the LIRF and the deconvolution correction in a given iteration was approximately 18 ms, promising for real-time measurements where the time between measured rtOSL samples is 500 ms. The time to compute the deconvolution correction increased as the number of samples in the rtOSL increased, seen in the bottom section.

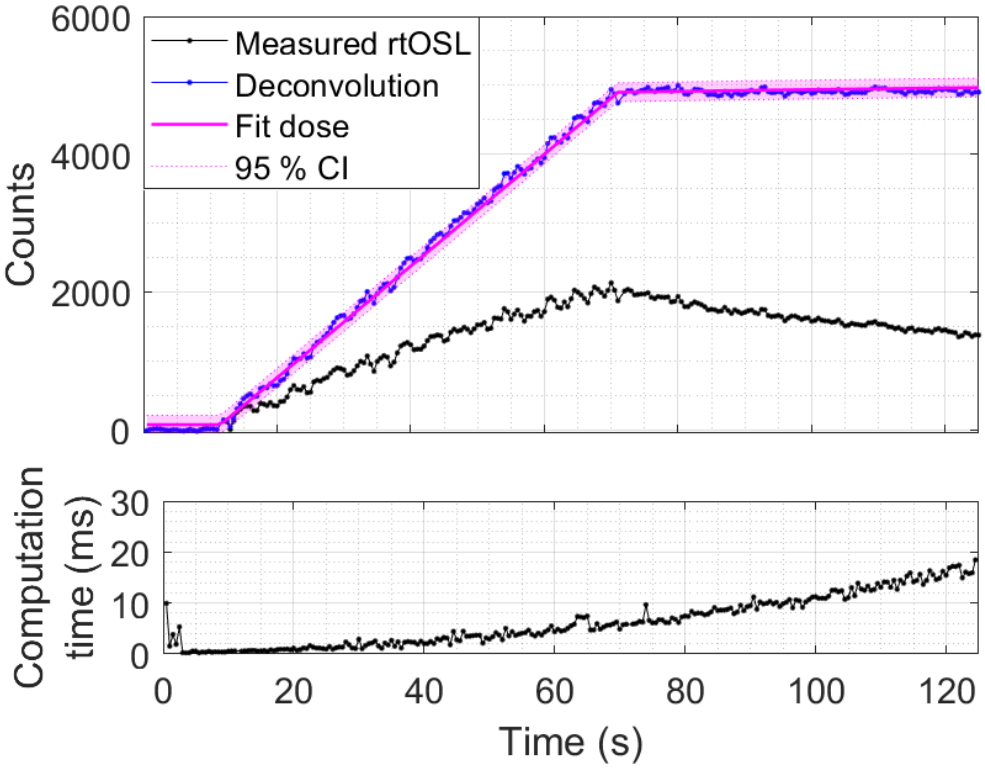

Figure 5.14: Simulation of the deconvolution correction applied for real-time use. Top: Measured rtOSL is the measured rtOSL signal (in black), Deconvolution is the deconvolution corrected rtOSL signal (in blue), Fit dose is the absorbed dose model fit to the corrected rtOSL (in magenta) and the magenta shading is the 95 % confidence interval in the fit dose. Bottom: the computation time required to calculate the deconvolution correction during each iteration.

5.4 Discussion

5.4.1 General discussion

From the results presented in Figures 5.10−5.13 and Tables 5.1 and 5.2, it is conclusive that the deconvolution correction was the most robust and accurate rtOSL correction method investigated. For all sets of measured and fitted rtOSL signals, the deconvolution achieved the lowest MAD and standard deviation in it's corrected responses. However, the deconvolution correction suffered from a systematic underestimation of the absorbed dose in BeO as the SNR decreased; this was observed in the analysis of the measured rtOSL signals with the superficial X-ray unit, but not the LINAC. This systematic underestimation arose as the optimal regularisation parameter, $\hat{\alpha}$, was determined algorithmically and increased in value as the SNR decreased. To mitigate this systematic trend, a number of approaches could be taken to increase the SNR of measured rtOSL signals, including optimisation of the measurement system, signal de-noising, and the application of increasingly robust deconvolution methods. Alternatively, direct correction of the amplitude may be achievable by performing singular value decomposition on $\dot{\mathrm{D}}_{\mathrm{RLS}}$ and scaling it's singular values [218].

From the comparison of the performances of each correction with measured and fitted responses, improvement of the SNRs lead to significant improvements in performance. With regards to the translation of rtOSL dosimeters to real-time dosimetry measurements, the rtOSL dosimeter's uncertainties may be inflated due to poor SNRs, especially when the dose-rate is expected to be low. The SNR of measured rtOSL signals could be improved by increasing the stimulus intensity, *e.g.* by using a more powerful laser diode and improving the optical coupling between the laser diode and stimulus fibre. Additionally, by increasing the diameter of the collection fibre or using a single fibre for both stimulus and collection, the measured rtOSL signal's intensity is increased. With regards to translating rtOSL dosimeters for real-time dosimetry, the rtOSL system's hardware should be optimised to improve it's SNR to ensure accuracy of corrected rtOSL signals and reduce dosimetric uncertainties to clinically acceptable standards, regardless of which correction method is applied.

In terms of robustness with respect to noise, the deconvolution corrected rtOSL was the best time-dependent descriptor of the time-dependent accumulated dose for measured rtOSL signals, having the lowest RMSE of each of the corrections in Table 5.1. Deconvolution's improved robustness with respect to noise arises as Tikhonov regularisation effectively de-noises the measured rtOSL as it is corrected. It should be noted that deconvolution is unable to completely recover the time-dependent absorbed dose from measured rtOSL signals due to the degradations caused by measurement noise.

From the real-time simulation of the deconvolution correction, the maximum time taken to compute the optimal LIRF and the correct the rtOSL was 18 ms, sufficiently short to allow for the deconvolution correction to be applied in real-time. The ΔrtOSL and exponential correction methods are more difficult to apply algorithmically in real-time as the ΔrtOSL requires prior knowledge of the value of $F(D)$ and the exponential correction requires that there is no change in field size or irradiation angle. However, both corrections could be implemented in real-time if a pre-irradiation measurement were performed, allowing for both methods to determine their required $F(D)$s prior to the real-time measurements. Due to the simplicity of the ΔrtOSL and exponential corrections, it is expected that they would also be feasible for real-time correction if $F(D)$ was known prior to real-time dosimetric measurements.

With regards to the exponential correction, the relationship between $\ln\left(\frac{\mathrm{D}(t)}{I(t)}\right)$ and time in Figure 5.7 was non-linear as the kinetics of rtOSL bleaching are non-first order in nature [219, 220]. Given that the assumption is approximately true, but not theoretically true, the exponential correction had it's MADs and uncertainties inflated. Conversely, the ΔrtOSL correction is a theoretically derived correction, and should not suffer from such increases in MADs and uncertainties. However, the exponential correction typically had reduced MADs, standard deviations and RMSEs when compared to the ΔrtOSL correction. The comparatively poorer performance of the ΔrtOSL correction is attributed to several factors. $F(D)$'s optimal value can not be determined analytically in the ΔrtOSL correction. The value of $F(D)$ for the ΔrtOSL correction can be optimised numerically using the measured rtOSL signal. However, measurement noise is increasingly exacerbated as signal lengths increase. It should be noted that heavy signal averaging has been applied to measured rtOSL signals in the literature to reduce measurement noise, however, this technique inflates the uncertainties in measured rtOSL signals [30] as it heavily blurs and temporally distorts the measured rtOSL signals. In the exponential correction, $F(D)$ is calculated using a fitted rtOSL signal. Given this, it proposed that $F(D)$ could be optimised numerically using a fitted rtOSL signal for the ΔrtOSL correction. Alternatively, approaches improving the SNR could be applied, such as signal de-noising or optimisation of the measurement system.

The exponential library approach was chosen to model the LIRF as it assumed no information about BeO's kinetics or the kinetics of real-time optically stimulated luminescence. At the time of writing, the transitions occurring in BeO's band structure are uncertain [221], and so BeO's kinetics are uncertain given that the theoretically predicted LIRF implicitly depends on the transitions modelled throughout BeO's band structure [221]. The kinetics of rtOSL depends upon many factors, including the intensity of the stimulus light and the band structure of the luminescent material [109]. Additionally, the concentration of trapping species in this material can vary between multiple samples of

the same luminescent material, leading to variations between their rtOSL responses. The exponential library approach avoided assumptions about kinetics, and allows for direct translation of the deconvolution method to other materials that produce OSL. Additionally, the optimal coefficients fit to the exponential library may provide insight into the kinetics of a material such as BeO whose kinetics are uncertain.

5.4.2 Inference of kinetics from the LIRF

The LIRF characterises the rate at which holes and electrons recombine after being stimulated. This rate depends on two processes: the stimulation of trapped electrons, and the recombination of free electrons and holes. For a single trapping species, these two processes can be described simply using Bateman equations with three species. The measured OSL in response to continuous stimulation is given by:

$$\mathrm{OSL}(t) \propto \frac{e^{-\lambda_1 t}}{\lambda_2 - \lambda_1} + \frac{e^{-\lambda_2 t}}{\lambda_1 - \lambda_2} \tag{5.21}$$

where λ_1 is the stimulation rate of trapped charges and λ_2 is the spontaneous recombination rate of free electrons and holes. It should be noted that these decay rates, λ_1 and λ_2, are equivalent the inverse of corresponding exponential decay constants. From the literature on time-resolved OSL measurements with BeO, the decay constants characterising spontaneous recombination of free electrons and holes are short-lived, up to an order of tens of μs [212]. When fitting the LIRF, we noted that all components had exponential decay constants much greater than 1 s, hence it can be concluded that $\lambda_2 \gg \lambda_1$. Therefore, the LIRF is dominated by the relatively slow stimulation rate of traps, and so the mono-exponential $e^{-\lambda_1 t}$ models the OSL from a single trapping species. Assuming that each trapping species is independent from other trapping species, this mono-exponential models the OSL of each of the optically active traps.

The distribution of fitting coefficients, $\hat{a}$, indirectly models the distribution of optically active trapping species in BeO. The total number of photons emitted by each trapping centre is proportional to the total number of optically active traps stimulated. An important consideration when inferring kinetics from the modelled LIRF is that the total number of photons emitted during an exponential decay is dependent on the lifetime of luminescence [222, 223]. The area under each exponential in the exponential library is given by $\int_0^\infty e^{-\frac{t}{\tau_i}} dt = \tau_i$, therefore the concentration of optically active traps stimulated with a decay constant τ_i is proportional to $\frac{\hat{a}_i}{\tau_i}$. From this relationship, the relative concentration of each trapping species can be inferred from the LIRF.

As stimulus intensity increases by a factor of k, the recombination rate increases by a factor of k and the decay constants of the fitted LIRF will be reduced by a factor of k^{-1}. In terms of universality of the results of the LIRF, the spread of the distribution of $\frac{\hat{a}_i}{\tau_i}$ will

also narrow by a factor of k^{-1} as stimulus intensity increases by a factor of k. Given these properties, the distribution of $\frac{\hat{a}_i}{\tau_i}$ is expected to be scale invariant, and so the distribution of $\frac{\hat{a}_i}{\tau_i}$ may be able to be correlated with distributions of trapping centres in a material. This hypothesis can be tested directly by comparing the distribution of $\frac{\hat{a}_i}{\tau_i}$ versus τ_i for the fitted SXR's and LINAC's fitted LIRFs in Figure 5.5. Shown in Figure 5.15 are log-log graphs of $\frac{\hat{a}_i}{\tau_i}$ versus τ_i for the fitted SXR's and LINAC's fitted LIRFs, where the log-log graph was used for scale invariance.

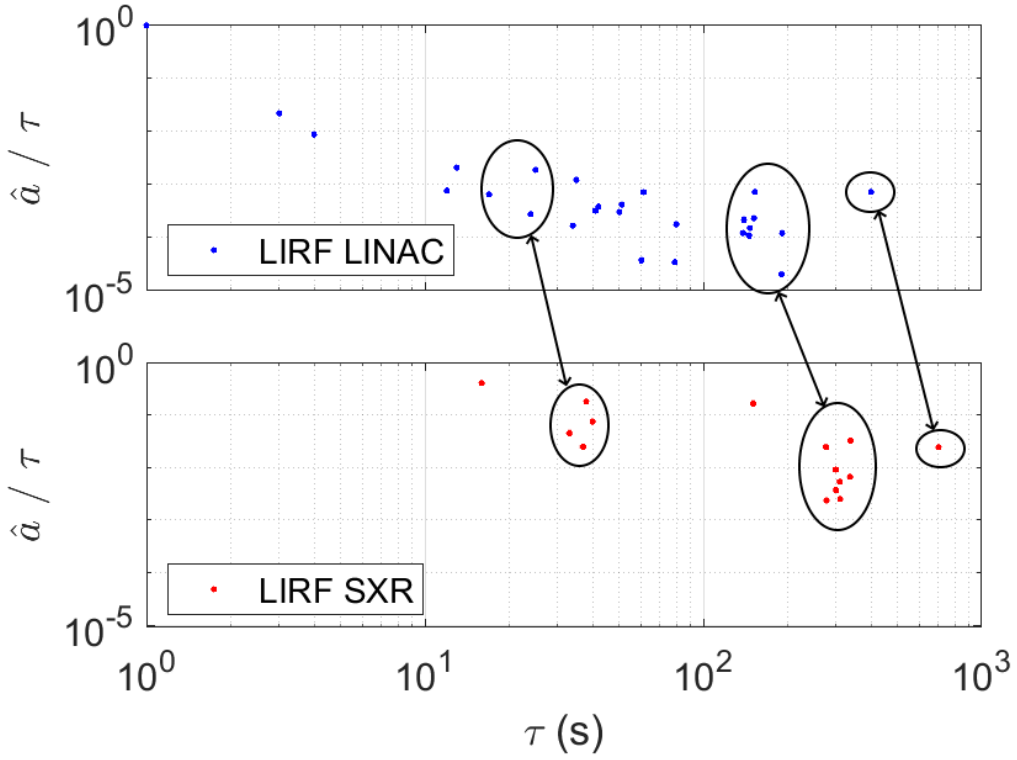

Figure 5.15: Comparison of fitted LIRF's $\frac{\hat{a}_i}{\tau_i}$ versus τ_i. Top: $\frac{\hat{a}_i}{\tau_i}$ versus τ_i for the LINAC's LIRF. Bottom: $\frac{\hat{a}_i}{\tau_i}$ versus τ_i for the SXR's LIRF. Correlated clusters of lifetimes in $\frac{\hat{a}_i}{\tau_i}$ versus τ_i have been circled, and are hypothesised to be related to trapping centre species in BeO.

In Figure 5.15, there are matching clusters in each of the $\frac{\hat{a}_i}{\tau_i}$ versus τ_i distributions; these clusters have been circled and linked. There were significant differences between the irradiation conditions and stimulus conditions when measuring rtOSL with the SXR and the LINAC. The only aspect that remained consistent was that the BeO ceramic was the same for both measurements. Therefore, this result supports the hypothesis that the distribution of $\frac{\hat{a}_i}{\tau_i}$ versus τ_i from a fitted LIRF can be correlated with traps in a material. Further work is required to investigate which lifetimes correlate with which trapping centre species, and to determine why the components of $\frac{\hat{a}_i}{\tau_i}$ versus τ_i that were not circled had differed significantly.

5.4.3 Translation of theory, algorithm and results

The convolutional model of luminescence is a model for predicting the time-dependent luminescence produced in response to a time-dependent source that induces luminescence. In this model, the LIRF is effectively a transfer function between the stimulus and the produced luminescence, describing how the luminescent material temporally distorts the time-dependent stimulus when it produces its luminescence. This model is also capable of predicting the time-resolved organic scintillation, radioluminescence, and post-irradiation OSL. For time-resolved organic scintillation measurements, the stimulus corresponds to the dose-rate, and the fitted coefficients $\hat{a}$ characterise the distribution of scintillating molecules. For time-resolved inorganic radioluminescence measurements, the stimulus corresponds to the dose-rate, and the fitted coefficients $\hat{a}$ characterise the distribution of recombination centres in the luminescent material. For post-irradiation OSL measurements, the stimulus is not the absorbed dose-rate, but the time-dependent optical stimulus, and the fitting coefficients $\hat{a}$ characterise the two step process recombination of stimulated trapped charges. The convolutional model of luminescence and the ability to infer kinetics from fitted LIRFs could be important tools considering the increasing interest in luminescent dosimetry. Furthermore, these techniques may prove useful for the high dose-rate modality, FLASH radiation therapy given that high temporal resolutions are required to resolve the absorbed dose-rate.

When translating this theory for use with other inorganic materials, deep traps may cause changes in sensitivity as the luminescent dosimeter is irradiated [20]; the severity and occurrence of such deep trap sensitisation effects is material dependent. When deep trap sensitisation effects are significant, it is expected that the convolutional model of luminescence will not properly model the time-dependent luminescence measured due to the complicated, non-linear kinetics that give rise to these non-linearities. Similarly, it is expected that the deconvolved luminescence may require correction for these non-linearities.

With regards to the design of the exponential library, the exponential library approximates a continuous distribution of exponential decays. To ensure that the LIRF can accurately model the distribution of trapping centres of a material, the graduations between the decay constants in the exponential library must be "small enough" and the span of the library should be "wide enough" to approximate a continuous distribution. In this work, integer graduations (*i.e.* $\tau = (\varepsilon,\ 1,\ 2,\ ...)$ s) and the 401 s span were sufficient to model BeO's LIRF. When aiming to translate this theory to other time-dependent luminescence measurements, these graduations and spans should be adjusted as necessary to optimise the fit of the expected luminescence to the measured luminescence. When calculating an LIRF for a given material, several rtOSL signals should be measured and averaged. Each fitted LIRF is effectively a probably distribution of trapping centres in the material; with

more data, the fitted distribution of trapping centres can be expected to more accurately reflect the distribution of trapping centres in the luminescent material. If the distribution of trapping centres were known to follow a well-defined structure like a Gaussian mixture model with a known number of components, fewer measurements of the rtOSL would be required.

5.5 Conclusion

From the dose-rate dependence measurements in this chapter, deconvolution was quantified to be the most robust and accurate correction method for rtOSL dosimetry. The deconvolution correction was demonstrated to be feasible for real-time applications, requiring at most 18 ms to correct the measured rtOSL signal. From these results, the deconvolution correction is recommended for the correction of rtOSL signals. The exponential correction was the next most robust and accurate correction method investigated, improving upon the performance of the ΔrtOSL correction. From the comparisons of each correction method's performance using measured and fitted rtOSL signals, measurement noise was demonstrated to inflate the uncertainties of corrected rtOSL signals. Therefore, it is recommended that rtOSL dosimetry systems are optimised for minimal measurement noise in order to ensure the accuracy of corrected rtOSL signals. Heavy signal averaging should be avoided as it temporally distorts the time-dependence of rtOSL signals and inflates the uncertainty of corrected rtOSL responses. Other de-noising approaches may be suitable provided the rtOSL's time-dependence remains unaffected. Alternatively, the convolutional model of luminescence can be applied to fit a model of the rtOSL signal to the measured rtOSL signals, such that the fitted rtOSL signal is a noiseless estimate of the measured rtOSL signal.

The convolutional model of luminescence and LIRF fitting technique is a simple linear model than can be used for other luminescence measurements, such as time-resolved scintillation, time-resolved radioluminescence, and time-resolved OSL. In this work, it was hypothesised that the distribution of trapping centres in a material could be inferred from a fitted LIRF. From the comparison of the two LIRFs in this work, there were correlations between clusters of lifetimes in the distributions of $\frac{\hat{a}_i}{\tau_i}$ versus τ_i; this result was taken as evidence to support the hypothesis. Further work is required to verify that distributions of trapping centres in a material can be inferred from the distributions of $\frac{\hat{a}_i}{\tau_i}$ versus τ_i, as well as limitations of such inferences.

Chapter 6

Conclusions and future work

6.1 Conclusion

This thesis presented the investigations into fibre-coupled luminescent dosimeters as potential solutions for two specific challenging cases of dosimetry in modern radiation therapy clinics: MRI-LINAC dosimetry and real-time *in vivo* dosimetry. With fibre-coupled luminescent dosimeters being entirely optical in nature whilst having compact sensitive sizes, dosimeter induced perturbations are minimised during dosimetric measurements. These qualities are particularly advantageous when the perturbation of water leads to increased uncertainties in the measured dose, as can be the case during MRI-LINAC dosimetry and real-time *in vivo* dosimetry.

PSDs were identified as promising candidates for MRI-LINAC dosimetry given their highly water equivalent compositions and their near-correctionless performance with clinical LINACs. In Chapter 2 the literature on radiation induced luminescence, PSD dosimetry and dosimetry with LINACs and MRI-LINACs was reviewed. During the review, the Cerenkov radiation stem effect was identified to be of particular concern during dosimetry with LINACs, requiring a dedicated correction method to preserve the PSD's accuracy. In Chapter 3, novel and existing stem signal correction methods were investigated for their reliability and their performance during dosimetry with LINACs. From these measurements, it was determined that background subtraction was the most suitable correction investigated provided that PMT gain drift could be mitigated. For measurements in conditions where background subtraction's accuracy could not be guaranteed, the non-linear least squares correction was the most suitable alternative correction method investigated, being on an average 0.1 % less accurate than background subtraction. Optimisation of the PSD dosimetry system was expected to further improve the performance of the investigated corrections.

In Chapter 4, an in-house PSD was applied for MRI-LINAC dosimetry with the Australian MRI-LINAC. In these measurements, background subtraction was applied to cor-

rect the stem effect, with PMT gain drift correction methods integrated into these experimental measurements. Output factors, beam profiles and PDDs were measured using the in-house PSD and various other dosimeters known to be accurate and valid with in-line MRI-LINACs. Monte Carlo simulations were also built and run to provide additional reference data. Comparing the performance of the PSD to other dosimeters in the literature, the in-house PSD achieved similar performances to these other dosimeters in the literature for the measurement of output factors and beam profiles, suggesting that the in-house PSD remained accurate for MRI-LINAC dosimetry. For the PDDs, there were systematic disagreements between the reference detectors, preventing conclusions from being drawn with regards to the suitability of the PSD in these measurement conditions. Further investigations with other PSD systems are required to verified that PSDs are inherently accurate and reliable for dosimetry with MRI-LINACs. These investigations were a significant first step in demonstrating that PSDs in general are effective for relative MRI-LINAC dosimetry.

Fibre-coupled luminescent dosimeters have many of the qualities required for accurate real-time *in vivo* dosimetry during LINAC and brachytherapy treatments. In Chapter 2, the literature on fibre-coupled luminescence dosimetry and desirable luminescent materials was reviewed. BeO was identified as a desirable luminescent material for real-time *in vivo* dosimetry during both LINAC and brachytherapy treatments given it's near-tissue equivalence and minimal energy dependence over both the brachytherapy and LINAC energy ranges. As with PSDs, the fibre-coupled BeO dosimeter required an accurate stem signal correction method to preserve the accuracy of it's luminescence response. With the long term aim of applying the fibre-coupled BeO dosimeter for real-time *in vivo* dosimetry, it was identified that the fibre-coupled BeO dosimeter could only use one optical fibre, otherwise the dosimeter would not fit into a catheter. For this reason, the rtOSL technique was identified as the most suitable correction method for a fibre-coupled BeO dosimeter intended as a real-time *in vivo* dosimeter.

In previous investigations of such a fibre-coupled BeO rtOSL dosimeter, the dosimeter had unacceptable uncertainties in it's dose-response. These uncertainties were inflated during the correction of the non-linear measured rtOSL signal, which was non-linear with respect to the absorbed dose. In order to reduce the uncertainties in the BeO dosimeter, novel rtOSL correction methods were developed. These novel correction methods were presented and applied in Chapter 5. From measurements with a superficial X-ray unit and a clinical LINAC, the deconvolution correction was determined to be a superior correction method to the prior correction method, significantly improving upon it's performance for all investigations. The novel deconvolution correction was also demonstrated to be applicable in real-time, making it highly suitable for use during real-time dosimetry. The deconvolution correction was therefore recommended for the correction of rtOSL sig-

nals. From investigations using noiseless models of the time-dependent rtOSL, it was determined that all of the correction methods had significantly improved performances when no measurement noise was present in the rtOSL signals. From this result, it was also recommended that fibre-coupled dosimetry systems should be optimised to increase the signal to noise ratio to ensure accurate dosimetry with rtOSL dosimeters. These investigations were a significant step in realising an accurate and reliable fibre-coupled BeO dosimeter that can be applied for real-time *in vivo* dosimetry during LINAC and brachytherapy treatments.

For the translation of the fibre-coupled luminescence dosimeters and stem signal correction methods reported in this thesis, these dosimeters and stem signal correction methods face a limitation with regards to their setup. The accuracy of fibre-coupled luminescent dosimeters with LINACs is partially dependent on the setup of the dosimeter relative to the radiation beam. In Chapters 3 and 4, the in-house PSD was set up orthogonal to the radiation beam to minimise the production and collection of Cerenkov radiation. A stem signal correction method's accuracy is expected to be degraded when the PSD is aligned parallel to the radiation beam given that the length of irradiated optical fibre increases and the collection efficiency increases due to the strong directional dependence of Cerenkov radiation emissions. Consequently, it is expected that the PSD's accuracy will become degraded when the PSD is orientated parallel to the photon beam during dosimetric measurements. Given this limitation, for LINAC and MRI-LINAC dosimetry, it is recommended that other PSDs and fibre-coupled luminescence dosimeters be orientated perpendicular to the radiation beam to optimise the dosimeter's accuracy.

6.2 Future work

To further improve the accuracy of the stem signal correction methods investigated in Chapter 3, there are several potential optimisations of the PSD system that could be implemented. Firstly, the application of alternative photodetectors that are free from PMT gain drift would directly improve the results of background subtraction and the least squares corrections, whilst indirectly improving trained neural networks by improving how well their training data matches measured data. Secondly, optimisations that improve the signal to noise ratio of measured signals would improve the accuracy of the least squares corrections and the neural network corrections, given these corrections are analytic in nature. In the literature, optical filtration has been reported to improve the signal to noise ratio of measured PSD and Cerenkov radiation signals. Signal de-noising techniques such as wavelet analysis, Fourier filtering, Wiener filtering, bilateral filtering and non-local means filtering could be applied post-measurement, and may be successful given they attenuate noise while preserving sharp changes in signal.

Given the results using the PSD for MRI-LINAC dosimetry in Chapter 4, further investigations need to be carried out with other PSD systems and other MRI-LINACs to determine whether PSD can be generally considered to be suitable for MRI-LINAC dosimetry. With regards to the experimentally measured PDDs in Chapter 4, it was plausible that detector misalignment was responsible for deviations between the in-house PSD, Farmer chamber and film. For measurements with a point dosimeter, PDDs should be measured using a scanning water tank to mitigate detector misalignment. The PSD system used in Chapter 4 would benefit from the optimisations mentioned in the paragraph above, such that and the PSD would have an improved reproducibility in it's response. The chromatic removal correction may further improve the performance of the PSD given that it has been reported to have an improved performance over background subtraction. With regards to further measurements with such an optimised in-house PSD dosimetry system, the in-house PSD should be modified to make it more reproducible with respect to significant changes in the setup, allowing for the measurement of detector specific correction factors.

The results for the deconvolution correction in Chapter 5 were an important step in the realisation of an *in vivo*, real-time fibre-coupled BeO dosimeter. Future work should aim to optimise and characterise the BeO rtOSL dosimeter for QA dosimetry with brachytherapy sources. Further, the fibre-coupled BeO rtOSL dosimeter should be investigated for it's feasibility as a real-time *in vivo* for brachytherapy treatments. With regards to improving the deconvolution correction, other approaches to LIRF modelling should be investigated with the potential to improve the accuracy of the deconvolution correction. A wealth of alternative LIRF modelling techniques can be found in literature for fluorescence lifetime imaging and analysis. Additionally, such LIRF modelling techniques from fluorescence lifetime imaging may be useful in relating measured luminescence responses to a material's kinetics during irradiation. Optimisation of the dosimetry system to improve the signal to noise ratio is paramount in ensuring that the corrected response is accurate. Aforementioned signal de-noising methods such as wavelet analysis, Fourier filtering, Wiener filtering, bilateral filtering and non-local means filtering should also be explored to further optimise the signal to noise ratio without compromising the time-dependence of the measured rtOSL signal.

Bibliography

[1]G. Delaney, S. Jacob, C. Featherstone, and M. Barton, "The role of radiotherapy in cancer treatment", Cancer **104**, 1129–1137 (2005) 10.1002/cncr.21324.

[2]M. L. Yap, D. L. O'Connell, D. Goldsbury, M. Weber, and M. Barton, "Comparison of four methods for estimating actual radiotherapy utilisation using the 45 and Up Study cohort in New South Wales, Australia", Radiotherapy and Oncology **131**, 14–20 (2019) 10.1016/j.radonc.2018.10.039.

[3]L. Kerkmeijer, C. Fuller, H. Verkooijen, M. Verheij, A. Choudhury, K. Harrington, C. Schultz, A. Sahgal, S. Frank, J. Goldwein, K. Brown, B. Minsky, and M. Vulpen, "The MRI-Linear Accelerator Consortium: Evidence-based clinical introduction of an innovation in radiation oncology connecting researchers, methodology, data collection, quality assurance, and technical development", Frontiers in Oncology **6**, 215 (2016) 10.3389/fonc.2016.00215.

[4]M. A. Schmidt and G. S. Payne, "Radiotherapy planning using MRI", Physics in Medicine & Biology **60**, R323–R361 (2015) 10.1088/0031-9155/60/22/r323.

[5]A. Vickers, N. Thiruthaneeswaran, C. Coyle, P. Manoharan, J. Wylie, L. Kershaw, A. Choudhury, and A. Mcwilliam, "Does magnetic resonance imaging improve soft tissue sarcoma contouring for radiotherapy?", BJR|Open **1**, 20180022 (2019) 10.1259/bjro.20180022.

[6]L. Beaulieu and S. Beddar, "Review of plastic and liquid scintillation dosimetry for photon, electron, and proton therapy", Physics in Medicine & Biology **61**, R305–R343 (2016) 10.1088/0031-9155/61/20/R305.

[7]A. Santos, M. Mohammadi, and S. Afshar, "Investigation of a fibre-coupled beryllium oxide (BeO) ceramic luminescence dosimetry system", Radiation Measurements **70**, 52–58 (2014) 10.1016/j.radmeas.2014.09.007.

[8]E. Podgorsak, *Radiation physics for medical physicists (3rd ed.)* (Springer, 2016), 10.1007/978-3-319-25382-4.

[9]P. R. Almond, P. J. Biggs, B. M. Coursey, W. F. Hanson, M. S. Huq, R. Nath, and D. W. O. Rogers, "AAPM's TG-51 protocol for clinical reference dosimetry of high-energy photon and electron beams", Medical Physics **26**, 1847–1870 (1999) 10.1118/1.598691.

[10]I. Das, C.-W. Cheng, R. Watts, A. Ahnesjö, J. Gibbons, X. Li, J. Lowenstein, R. Mitra, W. Simon, and T. Zhu, "Accelerator beam data commissioning equipment and procedures: Report of the TG-106 of the Therapy Physics Committee of the AAPM", Medical Physics **35**, 4186–4215 (2008) 10.1118/1.2969070.

[11]G. Liney, B. Whelan, B. Oborn, M. Barton, and P. Keall, "MRI-linear accelerator radiotherapy systems", Clinical Oncology **30**, 686–691 (2018) 10.1016/j.clon.2018.08.003.

[12]*Dosimetry of small static fields used in external beam radiotherapy*, Technical Reports Series 483 (IAEA, Vienna, 2017).

[13]J. Birks, edited by J. Birks (Pergamon, 1964), 10.1016/B978-0-08-010472-0.50006-9.

[14]S. McKeever and R. Chen, "Luminescence models", Radiation Measurements **27**, 625–661 (1997) 10.1016/S1350-4487(97)00203-5.

[15]G. Knoll, *Radiation detection and measurement (4th ed.)* (John Wiley, Hoboken, NJ, 2010).

[16]E. Yukihara, "A review on the OSL of BeO in light of recent discoveries: The missing piece of the puzzle?", Radiation Measurements **134**, 106291 (2020) 10.1016/j.radmeas.2020.106291.

[17]G. Kitis, C. Furetta, and V. Pagonis, "Mixed-order kinetics model for optically stimulated luminescence", Modern Physics Letters B **23**, 3191–3207 (2009) 10.1142/S0217984909021351.

[18]T. Yanagida, Y. Fujimoto, K. Watanabe, K. Fukuda, N. Kawaguchi, Y. Miyamoto, and H. Nanto, "Scintillation and optical stimulated luminescence of Ce-doped CaF2", Radiation Measurements **71**, 162–165 (2014) 10.1016/j.radmeas.2014.03.020.

[19]T. Yanagida, "Ionizing radiation induced emission: Scintillation and storage-type luminescence", Journal of Luminescence **169**, 544–548 (2016) 10.1016/j.jlumin.2015.01.006.

[20]E. Yukihara, V. Whitley, J. Polf, D. Klein, S. McKeever, A. Akselrod, and M. Akselrod, "The effects of deep trap population on the thermoluminescence of Al_2O_3:C", Radiation Measurements **37**, 627–638 (2003) https://doi.org/10.1016/S1350-4487(03)00077-5.

[21]A. J. Bos, "Thermoluminescence as a research tool to investigate luminescence mechanisms", Materials **10**, 1357 (2017) 10.3390/ma10121357.

[22]E. G. Yukihara and T. Kron, "Applications of optically stimulated luminescence in medical dosimetry", Radiation Protection Dosimetry **192**, 122–138 (2021) 10.1093/rpd/ncaa213.

[23]T. Kron, P. Lonski, and E. G. Yukihara, "Thermoluminescence dosimetry (TLD) in medicine: Five 'W's and one how", Radiation Protection Dosimetry **192**, 139–151 (2021) 10.1093/rpd/ncaa212.

[24]R. Gaza, S. McKeever, M. Akselrod, A. Akselrod, T. Underwood, C. Yoder, C. Andersen, M. Aznar, C. Marckmann, and L. Bøtter-Jensen, "A fiber-dosimetry method based on OSL from Al_2O_3:C for radiotherapy applications", Radiation Measurements **38**, Proceedings of the 5th European Conference on Luminescent Detectors and Transformers of Ionizing Radiation (LUMDETR 2003), 809–812 (2004) 10.1016/j.radmeas.2003.12.004.

[25]S. Mckeever, M. Akselrod, and B. Markey, "Pulsed optically stimulated luminescence dosimetry using Alpha-Al_2O_3:C", Radiation Protection Dosimetry **65**, 267–272 (1996) 10.1093/oxfordjournals.rpd.a031639.

[26]M. Akselrod and S. Mckeever, "A radiation dosimetry method using pulsed optically stimulated luminescence", Radiation Protection Dosimetry **81**, 167–175 (1999) 10.1093/oxfordjournals.rpd.a032583.

[27]J. M. Edmund, C. E. Andersen, C. J. Marckmann, M. C. Aznar, M. S. Akselrod, and L. Bøtter-Jensen, "CW-OSL measurement protocols using optical fibre Al_2O_3:C dosemeters", Radiation Protection Dosimetry **119**, 368–374 (2006) 10.1093/rpd/nci519.

[28]E. Bulur and A. Yeltik, "Optically stimulated luminescence from BeO ceramics: An LM-OSL study", Radiation Measurements **45**, 29–34 (2010) 10.1016/j.radmeas.2009.08.007.

[29]R. Gaza and S. Mckeever, "A real-time, high-resolution optical fibre dosemeter based on optically stimulated luminescence (OSL) of KBr:Eu, for potential use during the radiotherapy of cancer", Radiation Protection Dosimetry **120**, 14–9 (2006) 10.1093/rpd/nci603.

[30]A. Santos, R. Gowda, E. Bezak, and S. Afshar, "Evaluation of a real-time optically stimulated luminescence beryllium oxide (BeO) fibre-coupled dosimetry system with a superficial 140 kVp X-ray beam", Physica Medica **65**, 167–171 (2019) 10.1016/j.ejmp.2019.08.021.

[31]E. Mones, I. Veronese, A. Vedda, G. Loi, M. Fasoli, F. Moretti, N. Chiodini, B. Cannillo, and M. Brambilla, "Ce-doped optical fibre as radioluminescent dosimeter in radiotherapy", Radiation Measurements **43**, Proceedings of the 15th Solid State Dosimetry (SSD15), 888–892 (2008) 10.1016/j.radmeas.2008.01.031.

[32]I. Veronese, M. C. Cantone, N. Chiodini, C. D. Mattia, M. Fasoli, E. Mones, and A. Vedda, "Radioluminescence dosimetry by scintillating fiber optics: The open challenges", in Hard X-ray, gamma-ray, and neutron detector physics XV, Vol. 8852, edited by M. Fiederle, A. Burger, L. Franks, and R. B. James (International Society for Optics and Photonics, 2013), pp. 262–269, 10.1117/12.2027041.

[33]C. Andersen, C. J. Marckmann, M. Aznar, L. Bøtter-Jensen, F. Kjær-Kristoffersen, and J. Medin, "An algorithm for real-time dosimetry in intensity-modulated radiation therapy using the radioluminescence signal from Al_2O_3:C", Radiation Protection Dosimetry **120**, 7–13 (2006) 10.1093/rpd/nci600.

[34]C. Andersen, S. Damkjær, G. Kertzscher, S. Greilich, and M. Aznar, "Fiber-coupled radioluminescence dosimetry with saturated Al_2O_3:C crystals: Characterization in 6 and 18 MV photon beams", Radiation Measurements **46**, 1090–1098 (2011) 10.1016/j.radmeas.2011.06.063.

[35]S. Magne, S. Deloule, A. Ostrowsky, and P. Ferdinand, "Fiber-coupled, time-gated Al_2O_3:C radioluminescence dosimetry technique and algorithm for radiation therapy with LINACs", IEEE Transactions on Nuclear Science **60**, 2998–3007 (2013) 10.1109/TNS.2013.2263640.

[36]J. Mdhluli, H. Jivan, R. Erasmus, Y. Davydov, V. Baranov, S. Mthembu, B. Mellado, E. Sideras-Haddad, O. Solovyanov, C. Sandrock, G. Peter, S. Tlou, N. Khanye, and B. Tjale, "Neutron induced radiation damage of plastic scintillators for the upgrade of the Tile calorimeter of the ATLAS detector.", Journal of Physics: Conference Series **878**, 012008 (2017) 10.1088/1742-6596/878/1/012008.

[37]J. D. Valentine, W. W. Moses, S. E. Derenzo, D. K. Wehe, and G. F. Knoll, "Temperature dependence of CsI(Tl) gamma-ray excited scintillation characteristics", Nuclear Instruments and Methods in Physics Research Section A: Accelerators, Spectrometers, Detectors and Associated Equipment **325**, 147–157 (1993) 10.1016/0168-9002(93)91015-F.

[38]M. L. Chithambo, *An introduction to time-resolved optically stimulated luminescence*, 2053-2571 (Morgan & Claypool Publishers, 2018), 10.1088/2053-2571/aae5da.

[39]H. Lemmetyinen, N. V. Tkachenko, B. Valeur, J.-i. Hotta, M. Ameloot, N. P. Ernsting, T. Gustavsson, and N. Boens, "Time-resolved fluorescence methods (IUPAC Technical Report)", Pure and Applied Chemistry **86**, 1969–1998 (2014) 10.1515/pac-2013-0912.

[40]V. Pankratova, A. Kozlova, O. Buzanov, K. Chernenko, R. Shendrik, A. Sarakovskis, and V. Pankratov, "Time-resolved luminescence and excitation spectroscopy of Co-doped $Gd_3Ga_3Al_2O_{12}$ scintillating crystals", Scientific Reports **10**, 20388 (2020) 10.1038/s41598-020-77451-x.

[41]R. Datta, T. M. Heaster, J. T. Sharick, A. A. Gillette, and M. C. Skala, "Fluorescence lifetime imaging microscopy: Fundamentals and advances in instrumentation, analysis, and applications", Journal of Biomedical Optics **25**, 1–43 (2020) 10.1117/1.JBO.25.7.071203.

[42]X. Liu, D. Lin, W. Becker, J. Niu, B. Yu, L. Liu, and J. Qu, "Fast fluorescence lifetime imaging techniques: A review on challenge and development", Journal of Innovative Optical Health Sciences **12**, 1930003 (2019) 10.1142/S1793545819300039.

[43]M. Zuker, A. G. Szabo, L. Bramall, D. T. Krajcarski, and B. Selinger, "Delta function convolution method (DFCM) for fluorescence decay experiments", Review of Scientific Instruments **56**, 14–22 (1985) 10.1063/1.1138457.

[44]P. Sarder and A. Nehorai, "Deconvolution methods for 3-D fluorescence microscopy images", IEEE Signal Processing Magazine **23**, 32–45 (2006) 10.1109/MSP.2006.1628876.

[45]"Prescribing, recording, and reporting of stereotactic treatments with small photon beams", Journal of the ICRU **14**, 1–160 (2014) 10.1093/jicru/ndx017.

[46]D. Low, "Dosimetry challenges and opportunities in modern radiation therapy", Journal of Physics: Conference Series **1305**, 012001 (2019) 10.1088/1742-6596/1305/1/012001.

[47]A. Tran, J. Zhang, K. Woods, V. Yu, D. Nguyen, G. Gustafson, L. Rosen, and K. Sheng, "Treatment planning comparison of IMPT, VMAT and 4π radiotherapy for prostate cases", Radiation Oncology **12**, 10.1186/s13014-016-0761-0 (2017) 10.1186/s13014-016-0761-0.

[48]D. Low, J. Moran, J. Dempsey, L. Dong, and M. Oldham, "Dosimetry tools and techniques for IMRT", Medical Physics **38**, 1313–38 (2011) 10.1118/1.3514120.

[49]A. B. Rosenfeld, G. Biasi, M. Petasecca, M. L. F. Lerch, G. Villani, and V. Feygelman, "Semiconductor dosimetry in modern external-beam radiation therapy", Physics in Medicine & Biology **65**, 16TR01 (2020) 10.1088/1361-6560/aba163.

[50]E. Grusell and G. Rikner, "Evaluation of temperature effects in p-type silicon detectors", Physics in Medicine & Biology **31**, 527–534 (1986) 10.1088/0031-9155/31/5/005.

[51]A. S. Saini and T. C. Zhu, "Temperature dependence of commercially available diode detectors", Medical Physics **29**, 622–630 (2002) 10.1118/1.1461842.

[52]M. Petasecca, S. Alhujaili, A. H. Aldosari, I. Fuduli, M. Newall, C. S. Porumb, M. Carolan, K. Nitschke, M. L. F. Lerch, J. Kalliopuska, V. Perevertaylo, and A. B. Rosenfeld, "Angular independent silicon detector for dosimetry in external beam radiotherapy", Medical Physics **42**, 4708–4718 (2015) 10.1118/1.4926778.

[53]S. F. Alhujaili, G. Biasi, F. Alzorkany, G. Grogan, M. A. Al Kafi, J. Lane, B. Hug, A. H. Aldosari, S. Alshaikh, P. R. Farzad, M. A. Ebert, B. Moftah, A. B. Rosenfeld, and M. Petasecca, "Quality assurance of Cyberknife robotic stereotactic radiosurgery using an angularly independent silicon detector", Journal of Applied Clinical Medical Physics **20**, 76–88 (2019) 10.1002/acm2.12496.

[54]R. Alfonso, P. Andreo, R. Capote, M. S. Huq, W. Kilby, P. Kjäll, T. R. Mackie, H. Palmans, K. Rosser, J. Seuntjens, W. Ullrich, and S. Vatnitsky, "A new formalism for reference dosimetry of small and nonstandard fields", Medical Physics **35**, 5179–5186 (2008) 10.1118/1.3005481.

[55]W. U. Laub, T. W. Kaulich, and F. Nüsslin, "A diamond detector in the dosimetry of high-energy electron and photon beams", Physics in Medicine & Biology **44**, 2183–2192 (1999) 10.1088/0031-9155/44/9/306.

[56]H. K. Looe, B. Delfs, D. Poppinga, P. Jiang, D. Harder, and B. Poppe, "The 'cutting away' of potential secondary electron tracks explains the effects of beam size and detector wall density in small-field photon dosimetry", Physics in Medicine & Biology **63**, 015001 (2018) 10.1088/1361-6560/aa9b46.

[57]C. Di Venanzio, M. Marinelli, E. Milani, G. Prestopino, C. Verona, G. Verona-Rinati, M. D. Falco, P. Bagalà, R. Santoni, and M. Pimpinella, "Characterization of a synthetic single crystal diamond Schottky diode for radiotherapy electron beam dosimetry", Medical Physics **40**, 021712 (2013) 10.1118/1.4774360.

[58]A. Ralston, M. Tyler, P. Liu, D. Mckenzie, and N. Suchowerska, "Over-response of synthetic microDiamond detectors in small radiation fields", Physics in Medicine & Biology **59**, 5873–5881 (2014) 10.1088/0031-9155/59/19/5873.

[59]R. Freeman and A. Holmes-Siedle, "A simple model for predicting radiation effects in MOS devices", IEEE Transactions on Nuclear Science **25**, 1216–1225 (1978) 10.1109/TNS.1978.4329516.

[60]R. Ramani, S. Russell, and P. O'Brien, "Clinical dosimetry using MOSFETs", International Journal of Radiation Oncology, Biology, Physics **37**, 959–964 (1997) 10.1016/S0360-3016(96)00600-1.

[61]G. Biasi, F. Su, T. Al Sudani, S. Corde, M. Petasecca, M. L. F. Lerch, V. L. Perevertaylo, M. Jackson, and A. B. Rosenfeld, "On the combined effect of silicon oxide thickness and boron implantation under the gate in MOSFET dosimeters", IEEE Transactions on Nuclear Science **67**, 534–540 (2020) 10.1109/TNS.2020.2971977.

[62]T. Kron, A. Rosenfeld, M. Lerch, and S. Bazley, "Measurements in radiotherapy beams using on-line MOSFET detectors", Radiation protection dosimetry **101**, 445–448 (2002) 10.1093/oxfordjournals.rpd.a006022.

[63]W. L. Jong, J. Wong, N. M. Ung, N. Kh, G. Ho, D. Cutajar, and A. Rosenfeld, "Characterization of MOSkin detector for *in vivo* skin dose measurement during megavoltage radiotherapy", Journal of Applied Clinical Medical Physics **15**, 4869 (2014) 10.1120/jacmp.v15i5.4869.

[64]A. H. Aldosari, M. Petasecca, A. Espinoza, M. Newall, I. Fuduli, C. Porumb, S. Alshaikh, Z. A. Alrowaili, M. Weaver, P. Metcalfe, M. Carolan, M. L. F. Lerch, V. Perevertaylo, and A. B. Rosenfeld, "A two dimensional silicon detectors array for quality assurance in stereotactic radiotherapy: magicplate-512", Medical Physics **41**, 091707 (2014) https://doi.org/10.1118/1.4892384.

[65]V. Borca, M. Pasquino, G. Russo, P. Grosso, D. Cante, P. Sciacero, G. Girelli, M. Porta, and S. Tofani, "Dosimetric characterization and use of GafChromic EBT3 film for IMRT dose verification", Journal of Applied Clinical Medical Physics **14**, 4111 (2013) 10.1120/jacmp.v14i2.4111.

[66]C. Huet, C. Moignier, J. Fontaine, and I. Clairand, "Characterization of the Gafchromic EBT3 films for dose distribution measurements in stereotactic radiotherapy", Radiation Measurements **71**, 364–368 (2014) 10.1016/j.radmeas.2014.05.020.

[67]H. Bouchard, F. Lacroix, G. Beaudoin, J.-F. Carrier, and I. Kawrakow, "On the characterization and uncertainty analysis of radiochromic film dosimetry", Medical Physics **36**, 10.1118/1.3121488 (2009) 10.1118/1.3121488.

[68]E. Y. L. Marroquin, J. A. Herrera González, M. A. Camacho López, J. E. V. Barajas, and O. A. García-Garduño, "Evaluation of the uncertainty in an EBT3 film dosimetry system utilizing net optical density", Journal of Applied Clinical Medical Physics **17**, 466–481 (2016) 10.1120/jacmp.v17i5.6262.

[69]A. Niroomand-Rad, S.-T. Chiu-Tsao, M. P. Grams, D. F. Lewis, C. G. Soares, L. J. Van Battum, I. J. Das, S. Trichter, M. W. Kissick, G. Massillon-JL, P. E. Alvarez, and M. F. Chan, "Report of AAPM Task Group 235 radiochromic film dosimetry: An update to TG-55", Medical Physics **47**, 5986–6025 (2020) 10.1002/mp.14497.

[70]S. F. de Boer, A. S. Beddar, and J. A. Rawlinson, "Optical filtering and spectral measurements of radiation-induced light in plastic scintillation dosimetry", Physics in Medicine and Biology **38**, 945–958 (1993) 10.1088/0031-9155/38/7/005.

[71]J. V. Jelley, "Cerenkov radiation and its applications", British Journal of Applied Physics **6**, 227–232 (1955) 10.1088/0508-3443/6/7/301.

[72]A. S. Beddar, T. R. Mackie, and F. H. Attix, "Cerenkov light generated in optical fibres and other light pipes irradiated by electron beams", Physics in Medicine & Biology **37**, 925–935 (1992) 10.1088/0031-9155/37/4/007.

[73]K. Jang, S. Shin, S. Kim, J. Kim, W. Yoo, Y. Ji, and B. Lee, "Measurement of Cerenkov radiation induced by the gamma-rays of Co-60 therapy units using wavelength shifting fiber", Sensors **14**, 7013–7025 (2014) 10.3390/s140407013.

[74]J. M. Fontbonne, G. Iltis, G. Ban, A. Battala, J. C. Vernhes, J. Tillier, N. Bellaize, C. Le Brun, B. Tamain, K. Mercier, and J. C. Motin, "Scintillating fiber dosimeter for radiation therapy accelerator", IEEE Transactions on Nuclear Science **49**, 2223–2227 (2002) 10.1109/TNS.2002.803680.

[75]A. S. Beddar, T. R. Mackie, and F. H. Attix, "Water-equivalent plastic scintillation detectors for high-energy beam dosimetry: I. Physical characteristics and theoretical considerations", Physics in Medicine & Biology **37**, 1883–1900 (1992) 10.1088/0031-9155/37/10/006.

[76]L. Archambault, A. S. Beddar, L. Gingras, R. Roy, and L. Beaulieu, "Measurement accuracy and Cerenkov removal for high performance, high spatial resolution scintillation dosimetry", Medical Physics **33**, 128–135 (2006) 10.1118/1.2138010.

[77]P. L. Mattem, L. M. Watkins, C. D. Skoog, J. R. Brandon, and E. H. Barsis, "The effects of radiation on the absorption and luminescence of fiber optic waveguides and materials", IEEE Transactions on Nuclear Science **21**, 81–95 (1974) 10.1109/TNS.1974.6498910.

[78]K. J. Jordan, "Evaluation of ruby as a fluorescent sensor for optical fiber-based radiation dosimetry", in Fluorescence detection iv, Vol. 2705, edited by E. R. Menzel and A. Katzir (International Society for Optics and Photonics, 1996), pp. 170–178, 10.1117/12.236190.

[79]M. Clift, P. N. Johnston, and D. V. Webb, "A temporal method of avoiding the Cerenkov radiation generated in organic scintillator dosimeters by pulsed mega-voltage electron and photon beams", Physics in Medicine & Biology **47 8**, 1421–1433 (2002) 10.1088/0031-9155/47/8/313.

[80]B. L. Justus, P. Falkenstein, A. L. Huston, M. C. Plazas, H. Ning, and R. W. Miller, "Gated fiber-optic-coupled detector for *in vivo* real-time radiation dosimetry", Applied Optics **43**, 1663–1668 (2004) 10.1364/ao.43.001663.

[81]J. Lambert, Y. Yin, D. R. McKenzie, S. Law, and N. Suchowerska, "Cerenkov-free scintillation dosimetry in external beam radiotherapy with an air core light guide", Physics in Medicine & Biology **53**, 3071–3080 (2008) 10.1088/0031-9155/53/11/021.

[82]A. Darafsheh, J. E. Melzer, J. A. Harrington, A. Kassaee, and J. C. Finlay, "Radiotherapy fiber dosimeter probes based on silver-only coated hollow glass waveguides", Journal of Biomedical Optics **23**, 1–7 (2018) 10.1117/1.JBO.23.1.015006.

[83]M. Goulet, M. Rilling, L. Gingras, S. Beddar, L. Beaulieu, and L. Archambault, "Novel, full 3D scintillation dosimetry using a static plenoptic camera", Medical Physics **41**, 082101 (2014) 10.1118/1.4884036.

[84]S. Beddar, "Real-time volumetric scintillation dosimetry", Journal of Physics: Conference Series **573**, 012005 (2015) 10.1088/1742-6596/573/1/012005.

[85]P. Brůža, D. Gladstone, J. Cammin, O. Green, and B. W. Pogue, "4D scintillation dosimetry for the MRI-LINAC: proof of concept", Journal of Physics: Conference Series **1305**, 012015 (2019) 10.1088/1742-6596/1305/1/012015.

[86]L. F. Nascimento, D. Verellen, J. Goossens, L. Struelens, F. Vanhavere, P. Leblans, and M. Akselrod, "Two-dimensional real-time quality assurance dosimetry system using μ-Al_2O_3:C,Mg radioluminescence films", Physics and Imaging in Radiation Oncology **16**, 26–32 (2020) https://doi.org/10.1016/j.phro.2020.09.008.

[87]M. A. Clift, R. A. Sutton, and D. V. Webb, "Water equivalence of plastic organic scintillators in megavoltage radiotherapy bremsstrahlung beams", Physics in Medicine & Biology **45**, 1885–1895 (2000) 10.1088/0031-9155/45/7/313.

[88]A. S. Beddar, T. R. Mackie, and F. H. Attix, "Water-equivalent plastic scintillation detectors for high-energy beam dosimetry: II. Properties and measurements", Physics in Medicine & Biology **37**, 1901–1913 (1992) 10.1088/0031-9155/37/10/007.

[89]L. Wang, D. Klein, and A. Beddar, "Monte Carlo study of the energy and angular dependence of the response of plastic scintillation detectors in photon beams", Medical Physics **37**, 5279–86 (2010) 10.1118/1.3488904.

[90]A. Dimitriadis, I. S. Patallo, I. Billas, S. Duane, A. Nisbet, and C. Clark, "Characterisation of a plastic scintillation detector to be used in a multicentre stereotactic radiosurgery dosimetry audit", Radiation Physics and Chemistry **140**, 373–378 (2017) 10.1016/j.radphyschem.2017.02.023.

[91]J. B. Birks, "Scintillations from organic crystals: specific fluorescence and relative response to different radiations", Proceedings of the Physical Society. Section A **64**, 874–877 (1951) 10.1088/0370-1298/64/10/303.

[92]J. B. Christensen and C. E. Andersen, "Relating ionization quenching in organic plastic scintillators to basic material properties by modelling excitation density transport and amorphous track structure during proton irradiation", Physics in Medicine & Biology **63**, 195010 (2018) 10.1088/1361-6560/aadf2d.

[93]A. Beierholm, C. Behrens, and C. Andersen, "Dosimetric characterization of the Exradin W1 plastic scintillator detector through comparison with an in-house developed scintillator system", Radiation Measurements **69**, 50–56 (2014) 10.1016/j.radmeas.2014.08.005.

[94]C. M. M. Wells, T. R. Mackie, M. B. Podgorsak, M. A. Holmes, N. Papanikolaou, P. J. Reckwerdt, J. Cygler, D. W. Rogers, A. F. Bielajew, D. G. Schmidt, and J. K. Muehlenkamp, "Measurements of the electron dose distribution near inhomogeneities using a plastic scintillation detector", International Journal of Radiation Oncology, Biology, Physics **29**, 1157–1165 (1994) 10.1016/0360-3016(94)90413-8.

[95]D. Flühs, M. Heintz, F. Indenkämpen, C. Wieczorek, H. Kolanoski, and U. Quast, "Direct reading measurement of absorbed dose with plastic scintillators-The general concept and applications to ophthalmic plaque dosimetry", Medical Physics **23**, 427–434 (1996) 10.1118/1.597736.

[96]L. Archambault, T. M. Briere, F. Pönisch, L. Beaulieu, D. A. Kuban, A. Lee, and S. Beddar, "Toward a real-time *in vivo* dosimetry system using plastic scintillation detectors", International Journal of Radiation Oncology, Biology, Physics **78**, 280–287 (2010) 10.1016/j.ijrobp.2009.11.025.

[97]D. Klein, T. M. Briere, R. Kudchadker, L. Archambault, L. Beaulieu, A. Lee, and S. Beddar, "In-phantom dose verification of prostate IMRT and VMAT deliveries using plastic scintillation detectors", Radiation Measurements **47**, 921–929 (2012) 10.1016/j.radmeas.2012.08.005.

[98]C. McKerracher and D. I. Thwaites, "Assessment of new small-field detectors against standard-field detectors for practical stereotactic beam data acquisition", Physics in Medicine & Biology **44**, 2143–2160 (1999) 10.1088/0031-9155/44/9/303.

[99]C. Martens, C. D. Wagter, and W. D. Neve, "The value of the PinPoint ion chamber for characterization of small field segments used in intensity-modulated radiotherapy", Physics in Medicine & Biology **45**, 2519–2530 (2000) 10.1088/0031-9155/45/9/306.

[100]F. Haryanto, M. Fippel, W. Laub, O. Dohm, and F. Nüsslin, "Investigation of photon beam output factors for conformal radiation therapy-Monte Carlo simulations and measurements", Physics in Medicine & Biology **47**, N133–N143 (2002) 10.1088/0031-9155/47/11/401.

[101]E. Pappas, T. G. Maris, A. Papadakis, F. Zacharopoulou, J. Damilakis, N. Papanikolaou, and N. Gourtsoyiannis, "Experimental determination of the effect of detector size on profile measurements in narrow photon beams", Medical Physics **33**, 3700–3710 (2006) 10.1118/1.2349691.

[102]P. Francescon, W. Kilby, and N. Satariano, "Monte Carlo simulated correction factors for output factor measurement with the CyberKnife system-Results for new detectors and correction factor dependence on measurement distance and detector orientation", Physics in Medicine & Biology **59**, N11–N17 (2014) 10.1088/0031-9155/59/6/N11.

[103]Y. Kamio and H. Bouchard, "Correction-less dosimetry of nonstandard photon fields: a new criterion to determine the usability of radiation detectors", Physics in Medicine & Biology **59**, 4973–5002 (2014) 10.1088/0031-9155/59/17/4973.

[104]P. Papaconstadopoulos, F. Tessier, and J. Seuntjens, "On the correction, perturbation and modification of small field detectors in relative dosimetry", Physics in Medicine & Biology **59**, 5937–5952 (2014) 10.1088/0031-9155/59/19/5937.

[105]J. Archer, E. Li, J. Davis, M. Cameron, A. Rosenfeld, and M. Lerch, "High spatial resolution scintillator dosimetry of synchrotron microbeams", Scientific Reports **9**, 10.1038/s41598-019-43349-6 (2019) 10.1038/s41598-019-43349-6.

[106]L. Madden, J. Archer, E. Li, U. Jelen, B. Dong, N. Roberts, L. Holloway, and A. Rosenfeld, "First measurements with a plastic scintillation dosimeter at the Australian MRI-LINAC", Physics in Medicine & Biology **64**, 175015 (2019) 10.1088/1361-6560/ab324b.

[107]P. Mobit, E. Agyingi, and G. Sandison, "Comparison of the energy-response factor of LiF and Al_2O_3 in radiotherapy beams", Radiation Protection Dosimetry **119**, 497–9 (2006) 10.1093/rpd/nci676.

[108]S. B. Scarboro and S. F. Kry, "Characterisation of energy response of Al_2O_3:C optically stimulated luminescent dosemeters (OSLDs) using cavity theory", Radiation Protection Dosimetry **153**, 23–31 (2012) 10.1093/rpd/ncs086.

[109]J. Polf, E. Yukihara, M. Akselrod, and S. McKeever, "Real-time luminescence from Al_2O_3 fiber dosimeters", Radiation Measurements **38**, 227–240 (2004) 10.1016/j.radmeas.2003.10.005.

[110]A. M. C. Santos, M. Mohammadi, and S. Afshar V., "Energy dependency of a water-equivalent fibre-coupled beryllium oxide (BeO) dosimetry system", Radiation Measurements **73**, 1–6 (2015) 10.1016/j.radmeas.2014.12.006.

[111]A. M. C. Santos, M. Mohammadi, and S. Afshar V., "Evaluation of a real-time BeO ceramic fiber-coupled luminescence dosimetry system for dose verification of high dose rate brachytherapy", Medical Physics **42**, 6349–6356 (2015) https://doi.org/10.1118/1.4931968.

[112]N. Council, D. Studies, B. Toxicology, C. Toxicology, and C. Exposures, *Managing health effects of beryllium exposure* (National Academies Press, 2008).

[113]K. Walsh and E. Vidal, *Beryllium chemistry and processing* (ASM International, 2009).

[114]I. Chetty, B. Curran, J. Cygler, J. DeMarco, G. Ezzell, B. Faddegon, I. Kawrakow, P. Keall, H. Liu, C.-M. C. Ma, D. Rogers, J. Seuntjens, D. Bagheri, and J. Siebers, "Report of the AAPM Task Group No. 105: Issues associated with clinical implementation of Monte Carlo-based photon and electron external beam treatment planning", Medical Physics **34**, 4818–4853 (2008) 10.1118/1.2795842.

[115]J. Allison, K. Amako, J. Apostolakis, P. Arce, M. Asai, T. Aso, E. Bagli, A. Bagulya, S. Banerjee, G. Barrand, B. Beck, A. Bogdanov, D. Brandt, J. Brown, H. Burkhardt, P. Canal, D. Ott, S. Chauvie, K. Cho, and H. Yoshida, "Recent developments in Geant4", Nuclear Instruments and Methods in Physics Research Section A: Accelerators, Spectrometers, Detectors and Associated Equipment **835**, 186–225 (2016) 10.1016/j.nima.2016.06.125.

[116]D. M. Santos, J. St-Aubin, B. Fallone, and S. Steciw, "Magnetic shielding investigation for a 6 MV in-line linac within the parallel configuration of a LINAC-MR system", Medical Physics **39**, 788–797 (2012) 10.1118/1.3676692.

[117]D. Constantin, L. Holloway, P. Keall, and R. Fahrig, "A novel electron gun for in-line MRI-LINAC configurations", Medical Physics **41**, 022301 (2014) 10.1118/1.4860660.

[118]J. St-Aubin, S. Steciw, and B. Fallone, "Magnetic decoupling of the linac in a low field biplanar LINAC-MR system", Medical Physics **37**, 4755–4761 (2010) 10.1118/1.3480482.

[119]S. Kolling, B. Oborn, and P. Keall, "Impact of the MLC on the MRI field distortion of a prototype MRI-LINAC", Medical Physics **40**, 121705 (2013) 10.1118/1.4828792.

[120]B. Burke, B. Fallone, and S. Rathee, "Radiation induced currents in MRI RF coils: Application to LINAC/MRI integration", Physics in Medicine & Biology **55**, 735–46 (2010) 10.1088/0031-9155/55/3/013.

[121]B. Burke, A. Ghila, B. G. Fallone, and S. Rathee, "Radiation induced current in the RF coils of integrated linac-MR systems: the effect of buildup and magnetic field", Medical Physics **39**, 5004–5014 (2012) 10.1118/1.4737097.

[122]B. Raaymakers, J. Lagendijk, J. Overweg, J. Kok, A. Raaijmakers, E. Kerkhof, R. van der Put, I. Meijsing, S. Crijns, F. Benedosso, M. Vulpen, C. Graaff, J. Allen, and K. Brown, "Integrating a 1.5 t MRI scanner with a 6 MV accelerator: Proof of concept", Physics in Medicine & Biology **54**, N229–37 (2009) 10.1088/0031-9155/54/12/N01.

[123]B. Fallone, "The rotating biplanar LINAC-magnetic resonance imaging system", Seminars in Radiation Oncology **24**, 200–202 (2014) 10.1016/j.semradonc.2014.02.011.

[124]P. J. Keall, M. Barton, and S. Crozier, "The Australian magnetic resonance imaging-linac program", Seminars in Radiation Oncology **24**, 203–206 (2014) 10.1016/j.semradonc.2014.02.015.

[125]J. J. Lagendijk, B. W. Raaymakers, and M. van Vulpen, "The magnetic resonance imaging–linac system", Seminars in Radiation Oncology **24**, 207–209 (2014) 10.1016/j.semradonc.2014.02.009.

[126]S. Mutic and J. F. Dempsey, "The ViewRay system: Magnetic resonance–guided and controlled radiotherapy", Seminars in Radiation Oncology **24**, 196–199 (2014) 10.1016/j.semradonc.2014.02.008.

[127]A. J. E. Raaijmakers, B. W. Raaymakers, and J. J. W. Lagendijk, "Integrating a MRI scanner with a 6 MV radiotherapy accelerator: dose increase at tissue-air interfaces in a lateral magnetic field due to returning electrons", Physics in Medicine & Biology **50**, 1363–1376 (2005) 10.1088/0031-9155/50/7/002.

[128]G. P. Liney, B. Dong, J. Begg, P. Vial, K. Zhang, F. Lee, A. Walker, R. Rai, T. Causer, S. J. Alnaghy, B. M. Oborn, L. Holloway, P. Metcalfe, M. Barton, S. Crozier, and P. Keall, "Technical Note: Experimental results from a prototype high-field inline MRI-LINAC", Medical Physics **43**, 5188–5194 (2016) 10.1118/1.4961395.

[129]A. J. E. Raaijmakers, B. W. Raaymakers, and J. J. W. Lagendijk, "Experimental verification of magnetic field dose effects for the MRI-accelerator", Physics in Medicine & Biology **52**, 4283–4291 (2007) 10.1088/0031-9155/52/14/017.

[130]S. J. Alnaghy, J. Begg, T. Causer, T. Alharthi, L. Glaubes, B. Dong, A. George, L. Holloway, and P. Metcalfe, "Technical Note: Penumbral width trimming in solid lung dose profiles for 0.9 and 1.5 T MRI-LINAC prototypes", Medical Physics **45**, 479–487 (2018) 10.1002/mp.12680.

[131]B. M. Oborn, Y. Ge, N. Hardcastle, P. E. Metcalfe, and P. J. Keall, "Dose enhancement in radiotherapy of small lung tumors using inline magnetic fields: A Monte Carlo based planning study", Medical Physics **43**, 368–377 (2016) 10.1118/1.4938580.

[132]J. Begg, S. Alnaghy, T. Causer, T. Alharthi, A. George, L. Glaubes, B. Dong, G. Goozee, P. Keall, U. Jelen, G. Liney, and H. L., "Experimental characterization of the dose deposition in parallel MRI-LINACs at various magnetic field strengths", Medical Physics **46**, 5152–5158 (2019) 10.1002/mp.13767.

[133]N. F. Roberts, E. Patterson, U. Jelen, T. Causer, L. Holloway, G. Liney, M. Lerch, A. B. Rosenfeld, B. M. Cutajar Dean amd Oborn, and P. Metcalfe, "Experimental characterization of magnetically focused electron contamination at the surface of a high-field inline MRI-linac", Medical Physics **46**, 5780–5789 (2019) 10.1002/mp.13847.

[134]U. Jelen, B. Dong, J. Begg, N. Roberts, B. Whelan, P. Keall, and G. Liney, "Dosimetric optimization and commissioning of a high field inline MRI-LINAC", Frontiers in Oncology **10**, 136 (2020) 10.3389/fonc.2020.00136.

[135]H. K. Looe, B. Delfs, D. Poppinga, D. Harder, and B. Poppe, "Magnetic field influences on the lateral dose response functions of photon-beam detectors: MC study of wall-less water-filled detectors with various densities", Physics in Medicine & Biology **62**, 5131–5148 (2017) 10.1088/1361-6560/aa6ca0.

[136]U. Jelen and J. Begg, "Dosimetry needs for MRI-LINACs", Journal of Physics: Conference Series **1305**, 012010 (2019) 10.1088/1742-6596/1305/1/012010.

[137]D. J. O'Brien, J. Dolan, S. Pencea, N. Schupp, and G. O. Sawakuchi, "Relative dosimetry with an MR-LINAC: Response of ion chambers, diamond, and diode detectors for off-axis, depth dose, and output factor measurements", Medical Physics **45**, 884–897 (2018) 10.1002/mp.12699.

[138]S. J. Woodings, J. W. H. Wolthaus, B. van Asselen, J. H. W. de Vries, J. G. M. Kok, J. J. W. Lagendijk, and B. W. Raaymakers, "Performance of a PTW 60019 microDiamond detector in a 1.5 T MRI-LINAC", Physics in Medicine & Biology **63**, 05NT04 (2018) 10.1088/1361-6560/aaa1c6.

[139]P. A. Jursinic, "Angular dependence of dose sensitivity of surface diodes", Medical Physics **36**, 2165–2171 (2009) 10.1118/1.3125644.

[140]K. Smit, B. van Asselen, J. G. M. Kok, A. H. L. Aalbers, J. J. W. Lagendijk, and B. W. Raaymakers, "Towards reference dosimetry for the MR-LINAC: Magnetic field correction of the ionization chamber reading", Physics in Medicine & Biology **58**, 5945–5957 (2013) 10.1088/0031-9155/58/17/5945.

[141]D. J. O'Brien, D. A. Roberts, G. S. Ibbott, and G. O. Sawakuchi, "Reference dosimetry in magnetic fields: Formalism and ionization chamber correction factors", Medical Physics **43**, 4915–4927 (2016) 10.1118/1.4959785.

[142]D. J. O'Brien and G. O. Sawakuchi, "Monte Carlo study of the chamber-phantom air gap effect in a magnetic field", Medical Physics **44**, 3830–3838 (2017) 10.1002/mp.12290.

[143]S. Hackett, B. van Asselen, J. Wolthaus, J. Kok, S. Woodings, J. Lagendijk, and B. Raaymakers, "Consequences of air around an ionization chamber: Are existing solid phantoms suitable for reference dosimetry on an MR-LINAC?", Medical Physics **43**, 3961–3968 (2016) 10.1118/1.4952727.

[144]I. Meijsing, B. Raaymakers, A. Raaijmakers, J. Kok, L. Hogeweg, B. Liu, and J. Lagendijk, "Dosimetry for the MRI accelerator: The impact of a magnetic field on the response of a Farmer NE2571 ionization chamber", Physics in Medicine & Biology **54**, 2993–3002 (2009) 10.1088/0031-9155/54/10/002.

[145]C. K. Spindeldreier, O. Schrenk, A. Bakenecker, I. Kawrakow, L. Burigo, C. Karger, S. Greilich, and A. Pfaffenberger, "Radiation dosimetry in magnetic fields with Farmer-type ionization chambers: Determination of magnetic field correction factors for different magnetic field strengths and field orientations", Physics in Medicine & Biology **62**, 6708–6728 (2017) 10.1088/1361-6560/aa7ae4.

[146]M. Reynolds, B. G. Fallone, and S. Rathee, "Dose response of selected ion chambers in applied homogeneous transverse and longitudinal magnetic fields", Medical Physics **40**, 042102 (2013) 10.1118/1.4794496.

[147]X. Chen, E. S. Paulson, E. Ahunbay, A. Sanli, S. Klawikowski, and X. A. Li, "Measurement validation of treatment planning for a MR-Linac", Journal of Applied Clinical Medical Physics **20**, 28–38 (2019) 10.1002/acm2.12651.

[148]J. E. Snyder, J. St-Aubin, S. Yaddanapudi, A. Boczkowski, D. A. Dunkerley, S. A. Graves, and D. E. Hyer, "Commissioning of a 1.5T Elekta Unity MR-LINAC: A single institution experience", Journal of Applied Clinical Medical Physics **21**, 160–172 (2020) 10.1002/acm2.12902.

[149]M. Reynolds, B. Fallone, and S. Rathee, "Dose response of selected solid state detectors in applied homogeneous transverse and longitudinal magnetic fields", Medical Physics **41**, 092103 (2014) 10.1118/1.4893276.

[150]M. Gargett, B. Oborn, P. Metcalfe, and A. Rosenfeld, "Monte Carlo simulation of the dose response of a novel 2D silicon diode array for use in hybrid MRI-LINAC systems", Medical Physics **42**, 856–865 (2015) 10.1118/1.4905108.

[151]S. Wegener, S. Weick, and O. A. Sauer, "Influence of a transverse magnetic field on the response of different detectors in a high energy photon beam near the surface", Zeitschrift für Medizinische Physik **29**, 22–30 (2019) 10.1016/j.zemedi.2018.07.001.

[152]M. Gargett, B. Oborn, S. J. Alnaghy, T. Causer, M. Petasecca, A. B. Rosenfeld, and P. Metcalfe, "A high resolution 2D array detector system for small-field MRI-LINAC applications", Biomedical Physics & Engineering Express **4**, 035041 (2018) 10.1088/2057-1976/aabd08.

[153]S. Alnaghy, T. Causer, N. Roberts, B. Oborn, U. Jelen, B. Dong, M. Gargett, J. Begg, G. Liney, M. Petasecca, A. Rosenfeld, L. Holloway, and P. Metcalfe, "High resolution silicon array detector implementation in an inline MRI-LINAC", Medical Physics **47**, 1920–1929 (2020) 10.1002/mp.14016.

[154]A. Houweling, J. Vries, J. Wolthaus, S. Woodings, J. Kok, B. van Asselen, K. Smit, A. Bel, J. Lagendijk, and B. Raaymakers, "Performance of a cylindrical diode array for use in a 1.5 T MR-LINAC", Physics in Medicine & Biology **61**, N80–N89 (2016) 10.1088/0031-9155/61/3/N80.

[155]J. Cammin, A. Curcuru, H. Li, S. Mutic, and O. Green, "TH-AB-BRA-06: MOSFET-based dosimetry in an MR image-guided radiation therapy system: Comparison with and without a static 0.3 T magnetic field", Medical Physics **43**, 3854–3855 (2016) 10.1118/1.4958057.

[156]N. Knutson, V. Rodriguez, Y. Hu, R. Kashani, H. Wooten, K. Tanderup, S. Mutic, and O. Green, "SU-E-T-494: A MOSFET-based *in-vivo* dosimetry system for MR image-guided radiation therapy (MR-IGRT)", Medical Physics **41**, 340–340 (2014) 10.1118/1.4888827.

[157]P. Yadav, A. Hallil, D. Tewatia, D. Dunkerley, and B. Paliwal, "MOSFET dosimeter characterization in MR-guided radiation therapy (MRgRT) LINAC", Journal of Applied Clinical Medical Physics **21**, 127–135 (2019) 10.1002/acm2.12799.

[158]N. Thorpe, A. Rosenfeld, P. Metcalfe, D. Cutajar, and M. Cai, "Development of quality assurance dosimetry systems for MRI brachytherapy and MRI-LINAC technology", in (2014), 10.1594/ranzcr2014/R-0280.

[159]I. Billas, H. Bouchard, U. Oelfke, and S. Duane, "The effect of magnetic field strength on the response of Gafchromic EBT-3 film", Physics in Medicine & Biology **64**, 06NT03 (2019) 10.1088/1361-6560/ab0503.

[160]B. Delfs, A. A. Schoenfeld, D. Poppinga, R.-P. Kapsch, P. Jiang, D. Harder, B. Poppe, and H. K. Looe, "Magnetic fields are causing small, but significant changes of the radiochromic EBT3 film response to 6 MV photons", Physics in Medicine & Biology **63**, 035028 (2018) 10.1088/1361-6560/aa9bd5.

[161]D. Cusumano, S. Teodoli, F. Greco, A. Fidanzio, L. Boldrini, M. Massaccesi, F. Cellini, V. Valentini, M. De Spirito, and L. Azario, "Evaluation of dose calculation accuracy at lung-tissue interface in presence of magnetic field with Gafchromic EBT3", Physica Medica **56**, 140–141 (2018) 10.1016/j.ejmp.2018.04.135.

[162]G. Gungor, L. Korkmaz, N. Kayalilar, G. Aydin, B. Yapıcı, T. Zoto, B. Atalar, and E. Ozyar, "Multichannel film dosimetry for quality assurance of intensity modulated radiotherapy treatment plans under 0.35 T magnetic field", Cureus **12**, e7334 (2020) 10.7759/cureus.7334.

[163]D. L. J. Barten, D. Hoffmans, M. A. Palacios, S. Heukelom, and L. J. van Battum, "Suitability of EBT3 GafChromic film for quality assurance in MR-guided radiotherapy at 0.35 T with and without real-time MR imaging", Physics in Medicine & Biology **63**, 165014 (2018) 10.1088/1361-6560/aad58d.

[164]F. Therriault-Proulx, Z. Wen, G. Ibbott, and S. Beddar, "Effect of magnetic field strength on plastic scintillation detector response", Radiation Measurements **116**, 10–13 (2018) 10.1016/j.radmeas.2018.06.011.

[165]S. Stefanowicz, H. Latzel, L. Lindvold, C. Andersen, O. Jäkel, and S. Greilich, "Dosimetry in clinical static magnetic fields using plastic scintillation detectors", Radiation Measurements **56**, 357–360 (2013) 10.1016/J.RADMEAS.2013.03.012.

[166]J. Yoon, J.-I. Kim, C. H. Choi, and J. M. Park, "Characteristics of the Exradin W1 scintillator in the magnetic field", Journal of Applied Clinical Medical Physics **20**, 149–156 (2019) 10.1002/acm2.12707.

[167]D. A. Alexander, R. Zhang, P. Brůža, B. W. Pogue, and D. J. Gladstone, "Scintillation imaging as a high-resolution, remote, versatile 2D detection system for MR-LINAC quality assurance", Medical Physics **47**, 3861–3869 (2020) 10.1002/mp.14353.

[168]L. Madden, J. Archer, E. Li, D. Wilkinson, and A. Rosenfeld, "Temporal separation of cerenkov radiation and scintillation using a clinical LINAC and artificial intelligence", Physics in Medicine & Biology **63**, 225004 (2018) 10.1088/1361-6560/aae938.

[169]M. Yasin, S. Harun, and H. Arof, *Selected topics on optical fiber technology* (IntechOpen, 2012).

[170]R. Carroll, D. Ruppert, L. Stefanski, and C. Crainiceanu, *Measurement error in nonlinear models: A modern perspective, (2nd ed.)* Chapman & Hall/CRC Monographs on Statistics & Applied Probability (CRC Press, 2006).

[171]G. Cybenko, "Approximation by superpositions of a sigmoidal function", Mathematics of Control, Signals and Systems **2**, 303–314 (1989) 10.1007/BF02551274.

[172]K. Hornik, "Approximation capabilities of multilayer feedforward networks", Neural Networks **4**, 251–257 (1991) 10.1016/0893-6080(91)90009-T.

[173]S. Ioffe and C. Szegedy, "Batch normalization: Accelerating deep network training by reducing internal covariate shift", ArXiv **abs/1502.03167** (2015).

[174]A. L. Maas, "Rectifier nonlinearities improve neural network acoustic models", in (2013).

[175]L. Madden, J. Archer, E. Li, D. Wilkinson, and A. Rosenfeld, "Temporal separation of Cerenkov radiation and scintillation using artificial neural networks in Clinical LINACs", Physica Medica **54**, 131–136 (2018) 10.1016/j.ejmp.2018.10.007.

[176]N. M. Nawi, W. H. Atomi, and M. Rehman, "The effect of data pre-processing on optimized training of artificial neural networks", Procedia Technology **11**, 4th International Conference on Electrical Engineering and Informatics, ICEEI 2013, 32–39 (2013) 10.1016/j.protcy.2013.12.159.

[177]N. Husin, N. Salim, and A. Ahmad, "Modeling of dengue outbreak prediction in Malaysia: A comparison of neural network and nonlinear regression model", 2008 International Symposium on Information Technology **3**, 1–4 (2008) 10.1109/ITSIM.2008.4632022.

[178]J. Archer, L. Madden, E. Li, D. Wilkinson, and A. Rosenfeld, "2D photon dosimetry with a scintillation fibre optic dosimeter", Radiation Physics and Chemistry **166**, 108490 (2020) 10.1016/j.radphyschem.2019.108490.

[179]X. Glorot and Y. Bengio, "Understanding the difficulty of training deep feedforward neural networks", in AISTATS (2010).

[180]A. Krizhevsky, I. Sutskever, and G. E. Hinton, "ImageNet classification with deep convolutional neural networks", Communications of the ACM **60**, 84–90 (2012) 10.1145/3065386.

[181]K. Simonyan and A. Zisserman, "Very deep convolutional networks for large-scale image recognition", CoRR **abs/1409.1556** (2015).

[182]G. Yang, J. Pennington, V. Rao, J. Sohl-Dickstein, and S. Schoenholz, "A mean field theory of batch normalization", ArXiv **abs/1902.08129** (2019).

[183]N. Srivastava, G. E. Hinton, A. Krizhevsky, I. Sutskever, and R. Salakhutdinov, "Dropout: A simple way to prevent neural networks from overfitting", J. Mach. Learn. Res. **15**, 1929–1958 (2014).

[184]K. He, X. Zhang, S. Ren, and J. Sun, "Delving deep into rectifiers: Surpassing human-level performance on ImageNet Classification", 2015 IEEE International Conference on Computer Vision (ICCV), 1026–1034 (2015) 10.1109/ICCV.2015.123.

[185]P. E. Galavis, L. Hu, S. Holmes, and I. J. Das, "Characterization of the plastic scintillation detector Exradin W2 for small field dosimetry", Medical Physics **46**, 2468–2476 (2019) 10.1002/mp.13501.

[186]A.-M. Frelin, J.-M. Fontbonne, G. Ban, J. Colin, M. Labalme, A. Batalla, A. Isambert, A. Vela, and T. Leroux, "Spectral discrimination of Cerenkov radiation in scintillating dosimeters", Medical Physics **32**, 3000–3006 (2005) 10.1118/1.2008487.

[187]L. Madden, J. Archer, E. Li, U. Jelen, B. Dong, L. Holloway, and A. Rosenfeld, "MRI-LINAC beam profile measurements using a plastic scintillation dosimeter.", Physica Medica **73**, 111–116 (2020) 10.1016/j.ejmp.2020.04.016.

[188]L. Madden, N. Roberts, U. Jelen, B. Dong, L. Holloway, P. Metcalfe, A. Rosenfeld, and E. Li, "In-line MRI-LINAC depth dose measurements using an in-house plastic scintillation dosimeter", Biomedical Physics & Engineering Express **7**, 025012 (2021) 10.1088/2057-1976/abe295.

[189]E. Simiele, N. Viscariello, and L. DeWerd, "Monte Carlo modeling of the influence of strong magnetic fields on the stem-effect in plastic scintillation detectors used in radiotherapy dosimetry", Medical Physics **48**, 1381–1394 (2021) doi.org/10.1002/mp.14637.

[190]A. Chalkley and G. Heyes, "Evaluation of a synthetic single-crystal diamond detector for relative dosimetry measurements on a CyberKnife™", The British Journal of Radiology **87**, 20130768 (2014) 10.1259/bjr.20130768.

[191]A. Niroomand-Rad, C. R. Blackwell, B. M. Coursey, K. P. Gall, J. M. Galvin, W. L. McLaughlin, A. S. Meigooni, R. Nath, J. E. Rodgers, and C. G. Soares, "Radiochromic film dosimetry: Recommendations of AAPM Radiation Therapy Committee Task Group 55", Medical Physics **25**, 2093–2115 (1998) 10.1118/1.598407.

[192]S.-Q. Tang, Y.-M. Jen, and J.-M. Wu, "An empirical model for describing the small field penumbra in radiation therapy", BioMed Research International **2019**, 1–13 (2019) 10.1155/2019/7584743.

[193]N. Roberts, B. Oborn, U. Jelen, B. Dong, J. Begg, A. George, S. J. Alnaghy, T. Causer, T. Alharthi, L. Holloway, and P. Metcalfe, "Modelling the X-ray source for the Australian MRI-Linac", Journal of Physics: Conference Series **1154**, 012025 (2019) 10.1088/1742-6596/1154/1/012025.

[194]B. Whelan, L. Holloway, D. Constantin, B. Oborn, M. Bazalova-Carter, R. Fahrig, and P. Keall, "Performance of a clinical gridded electron gun in magnetic fields: Implications for MRI-Linac therapy", Medical Physics **43**, 5903–5914 (2016) 10.1118/1.4963216.

[195]S. Kolling, B. M. Oborn, P. J. Keall, and J. Horvat, "Magnetization curves of sintered heavy tungsten alloys for applications in MRI-guided radiotherapy", Medical Physics **41**, 061707 (2014) 10.1118/1.4873679.

[196]B. M. Oborn, S. Kolling, P. E. Metcalfe, S. Crozier, D. W. Litzenberg, and P. J. Keall, "Electron contamination modeling and reduction in a 1 T open bore inline MRI-LINAC system", Medical Physics **41**, 051708 (2014) 10.1118/1.4871618.

[197]M. Hussein, C. Clark, and A. Nisbet, "Challenges in calculation of the gamma index in radiotherapy-Towards good practice", Physica Medica **36**, 1–11 (2017) 10.1016/j.ejmp.2017.03.001.

[198]B. Taylor, *Guidelines for evaluating and expressing the uncertainty of NIST measurement results (rev. ed.)* (DIANE Publishing Company, 2009), 10.6028/NIST.TN.1297.

[199]M. Reynolds, S. Rathee, and B. G. Fallone, "Technical Note: Ion chamber angular dependence in a magnetic field", Medical Physics **44**, 4322–4328 (2017) 10.1002/mp.12405.

[200]E. Podgorsak and I. A. E. Agency, *Radiation oncology physics: a handbook for teachers and students* (International Atomic Energy Agency, 2005).

[201]B. Koger, R. Price, D. Wang, D. Toomeh, S. Geneser, and E. Ford, "Impact of the MLC leaf-tip model in a commercial TPS: Dose calculation limitations and IROC-H phantom failures", Journal of Applied Clinical Medical Physics **21**, 82–88 (2020) 10.1002/acm2.12819.

[202]Y. Roed, D. O'Brien, H. J. Lee, L. Pinsky, and G. Ibbott, "Comparison of measurements in small fields from an MR-LINAC", International Journal of Radiation Oncology Biology Physics **99**, 3705 (2017) 10.1016/j.ijrobp.2017.06.2327.

[203]G. Khelashvili, J. Chu, A. Diaz, and J. Turian, "Dosimetric characteristics of the small diameter Brainlab™ cones used for stereotactic radiosurgery", Journal of Applied Clinical Medical Physics **13**, 4–13 (2012) 10.1120/jacmp.v13i1.3610.

[204]J. F. Williamson, J. F. Dempsey, A. S. Kirov, J. I. Monroe, W. R. Binns, and H. Hedtjärn, "Plastic scintillator response to low-energy photons", Physics in Medicine and Biology **44**, 857–871 (1999) 10.1088/0031-9155/44/4/004.

[205]C. A. Whittaker, A. M. Santos, C. A. Kalnins, H. Ebendorff-Heidepriem, D. Ottaway, and N. A. Spooner, "Evaluating the energy dependence of various polystyrene based plastic scintillators", Radiation Measurements **122**, 57–62 (2019) https://doi.org/10.1016/j.radmeas.2019.01.007.

[206]A. S. Beddar, T. M. Briere, F. A. Mourtada, O. N. Vassiliev, H. H. Liu, and R. Mohan, "Monte carlo calculations of the absorbed dose and energy dependence of plastic scintillators", Medical Physics **32**, 1265–1269 https://doi.org/10.1118/1.1897465.

[207]M. Sommer, R. Freudenberg, and J. Henniger, "New aspects of a BeO-based optically stimulated luminescence dosimeter", Radiation Measurements **42**, Proceedings of the 6th European Conference on Luminescent Detectors and Transformers of Ionizing Radiation (LUMDETR 2006), 617–620 (2007) 10.1016/j.radmeas.2007.01.052.

[208]M. Sommer, A. Jahn, and J. Henniger, "Beryllium oxide as optically stimulated luminescence dosimeter", Radiation Measurements **43**, Proceedings of the 15th Solid State Dosimetry (SSD15), 353–356 (2008) 10.1016/j.radmeas.2007.11.018.

[209]L. Madden, A. Santos, E. Li, R. Gowda, E. Bezak, V. S.Afshar, and A. Rosenfeld, "Temporal modelling of beryllium oxide ceramics' real-time OSL for dosimetry with a superficial 140 kVp X-ray beam", Physica Medica **80**, 17–22 (2020) 10.1016/j.ejmp.2020.10.003.

[210]D. U. Campos-Delgado, O. Gutierrez-Navarro, R. Salinas-Martinez, E. Duran, A. R. Mejia-Rodriguez, M. J. Velazquez-Duran, and J. A. Jo, "Blind deconvolution estimation by multi-exponential models and alternated least squares approximations: Free-form and sparse approach", PLOS ONE **16**, 1–29 (2021) 10.1371/journal.pone.0248301.

[211] A. Kruzhalov, I. Ogorodnikov, and S. Kudyakov, "Radiative relaxation of low-energy electron excitations and point defects in beryllium oxide", Russian Physics Journal **39**, 1067–1088 (1997) 10.1007/BF02436150.

[212] E. G. Yukihara, "Luminescence properties of BeO optically stimulated luminescence (OSL) detectors", Radiation Measurements **46**, 580–587 (2011) https://doi.org/10.1016/j.radmeas.2011.04.013.

[213] L. Reichel and Q. Ye, "Simple square smoothing regularization operators", Electronic Transactions on Numerical Analysis **33**, 63–83 (2009).

[214] M. Abramowitz, *Handbook of mathematical functions, with formulas, graphs, and mathematical tables* (Dover Publications, Inc., USA, 1974).

[215] D. V. Lindley and A. F. M. Smith, "Bayes estimates for the linear model", Journal of the Royal Statistical Society. Series B (Methodological) **34**, 1–41 (1972).

[216] G. Cowan, *Statistical data analysis*, Oxford science publications (Clarendon Press, 1998).

[217] T. A. Johansen, "On Tikhonov regularization, bias and variance in nonlinear system identification", Automatica **33**, 441–446 (1997) 10.1016/S0005-1098(96)00168-9.

[218] P. Hansen, *Rank-deficient and discrete ill-posed problems: Numerical aspects of linear inversion*, Mathematical Modeling and Computation (Society for Industrial and Applied Mathematics, 2005).

[219] F. Walker, L. Colyott, N. Agersnap Larsen, and S. McKeever, "The wavelength dependence of light-induced fading of thermoluminescence from alpha-Al_2O_3:C", Radiation Measurements **26**, 711–718 (1996) 10.1016/S1350-4487(97)82885-5.

[220] V. H. Whitley and S. W. S. McKeever, "Photoionization of deep centers in Al_2O_3", Journal of Applied Physics **87**, 249–256 (2000) 10.1063/1.371853.

[221] G. Polymeris, S. Çoskun, E. Tsoutsoumanos, P. Konstantinidis, E. Aşlar, E. Şahiner, N. Meriç, and G. Kitis, "Dose response features of quenched and reconstructed, TL and deconvolved OSL signals in BeO", Results in Physics **25**, 104222 (2021) 10.1016/j.rinp.2021.104222.

[222] M. L. Chithambo, "The analysis of time-resolved optically stimulated luminescence: I. Theoretical considerations", Journal of Physics D: Applied Physics **40**, 1874–1879 (2007) 10.1088/0022-3727/40/7/006.

[223] M. L. Chithambo, "The analysis of time-resolved optically stimulated luminescence: II. Computer simulations and experimental results", Journal of Physics D: Applied Physics **40**, 1880–1889 (2007) 10.1088/0022-3727/40/7/007.

Appendix A

MATLAB code

A.1 OLS correction MATLAB code

```
function [OLS_dose] = OLS_analysis(PSD_signal,stem_signal)
%%PSD_signal is the measured PSD signal, and stem_signal is the ...
    measured reference probe signal. PSD_signal and stem signal ...
    are m by n arrays, consistning of n column vectors, each ...
    with a length of m samples.
[m1, n1] = size(PSD_signal);
[m2, n2] = size(stem_signal);

% Align mean background voltage with zero assuming beam on does ...
    not occur in the first 500 samples
Cerenkov_fit = stem_signal - ones(m2, 1) * ...
    mean(stem_signal(1:500, 1:n2));
Combined_fit = PSD_signal - ones(m1, 1) * mean(PSD_signal(1:500, ...
    1:n1));

tau_d = 285 / 1.6; % set decay constant to 285 ns. Division by ...
    1.6 accounts for the 1.6 ns/sample of the digital oscilloscope
tau_r = 19.5 / 1.6; % set rise constant to 19.5 ns.

LIRF = exp(-(1:1500) ./ tau_d) - exp(-(1:1500) ./ tau_r); % ...
    Calculate LIRF, h(t)

model_scint = zeros(m2, n2); % initialise the modelled scintillation
M2 = 1:m2;

for N2 = 1:n2
    dummy_scint = conv(Cerenkov_fit(M2, N2), LIRF); % calculate ...
        the modelled scintillation as the convolution of the ...
```

```
        LIRF and stem signal
20      model_scint(M2, N2) = (dummy_scint(M2) - ones(m2, 1) * ...
        mean(dummy_scint(1:500))) ./ (max(dummy_scint) - ...
        mean(dummy_scint(1:500))); % apply min-max normalisation ...
        to modelled scintillation to improve computational speed ...
        of gradient descent
21
22      Cerenkov_fit(M2, N2) = (Cerenkov_fit(M2, N2) - ones(m2, 1) * ...
        mean(Cerenkov_fit(1:500, N2))) ./ (max(Cerenkov_fit(M2, ...
        N2)) - mean(Cerenkov_fit(1:500, N2))); % also min-max ...
        normalise the stem signal to improve computational speed ...
        of gradient descent
23  end
24
25  % define parameters for LS algorithm
26  lr = 0.01; % initialise the step length with a value of 0.01
27  c_param = 0.5; % parameter used in backtracking line search
28  lr_limit = sqrt(eps); % parameter used to break line search if ...
        lr < limit, prevents infinite loops.
29
30  OLS_dose = zeros(n1, 1);
31
32  for N1 = 1:n1
33      if N1==1 && (m1≠m2 || n1≠n2)
34          disp('Error: PSD signal array has different size to stem ...
                signal array!')
35          break
36      end
37
38      fitS = model_scint(1:m1, N1); % column vector form of ...
        modelled scintillation
39      fitC = Cerenkov_fit(1:m1, N1); % column vector form of ...
        measured stem signal
40      fitT = Combined_fit(1:m1, N1); % column vector form of ...
        measured PSD signal
41
42      X = [fitS fitC ones(m1, 1)]; % Ordinary least squares ...
        variables used to calculate first estimate of parameters
43      beta = (X' * X) \ X' * Combined_fit; % Ordinary least ...
        squares analytical solution
44      a = beta(1); % initial estimate of the scaling parameter for ...
        scintillation
45      b = beta(2); % initial estimate of the scaling parameter for ...
        stem signal
46      c = beta(3); % initial estimate of the scaling parameter for ...
        voltage offset
47
```

```
48      old_err = inf; % initialise the SSE_0 with value of infinity
49
50      while true % Gradient descent algorithm
51          est = a * fitS + b * fitC + c*ones(m1, 1); % calculate ...
               estimate, y^(t)
52          err = 0.5*sum((fitT - est).^2); % calculate SSE
53
54          if err ≥ 0.9999*old_err % stopping criterion
55              break
56          else % Acceptable improvement made, record improved ...
               parameters
57              best_a = a;
58              best_b = b;
59              best_c = c;
60              old_err = err; % also update the current fit error
61          end
62
63          % Backpropagate for derivatives
64          d_err_d_est = - 2* (fitT - est)';
65
66          % derivatives of the SSE with respect to the fitting ...
               parameters
67          d_err_d_a = d_err_d_est * fitS;
68          d_err_d_b = d_err_d_est * fitC;
69          d_err_d_c = sum(d_err_d_est);
70
71          % do backtracking line search
72          seach_dir = - [d_err_d_a d_err_d_b d_err_d_c];
73          grad_mag = norm(seach_dir);
74
75          while true
76              new_err = 0.5*sum((fitT - ((a - lr * d_err_d_a) * ...
                   fitS + (b - lr * d_err_d_b) * fitC + (c - lr * ...
                   d_err_d_c) * ones(m1, 1))).^2);
77
78              if old_err - new_err ≥  lr * grad_mag * c_param
79                  break; % condition satisfied, don't need to ...
                       modify lr
80              elseif lr ≤ lr_limit % step length is below ...
                   specified limit
81                  break % no improvements made, parameters are ...
                       optimised and gradient descent loop will end ...
                       at next evaluation of SSE
82              end
83              lr = lr * 0.5; % halve the step length and try again
84          end
85
```

```
86          % Update fitting parameters
87          a = a - lr * d_err_d_a;
88          b = b - lr * d_err_d_b;
89          c = c - lr * d_err_d_c;
90      end
91
92      OLS_dose(N1) =  0.5 * sum(fitT - best_b * fitC - best_c * ...
            ones(m1, 1) + best_a * sum(fitS)); % calculate integral ...
            response
93  end
94  end
```

A.2 NLLS correction MATLAB code

```
1   function [OLS_dose] = NLLS_analysis(PSD_signal,stem_signal)
2   %%PSD_signal is the measured PSD signal, and stem_signal is the ...
        measured reference probe signal. PSD_signal and stem signal ...
        are m by n arrays, consistning of n column vectors, each ...
        with a length of m samples.
3
4   [m1, n1] = size(PSD_signal);
5   [m2, n2] = size(stem_signal);
6
7   % Align mean background voltage with zero assuming beam on does ...
        not occur in the first 500 samples
8   Cerenkov_fit = stem_signal - ones(m2, 1) * ...
        mean(stem_signal(1:500, 1:n2));
9   Combined_fit = PSD_signal - ones(m1, 1) * mean(PSD_signal(1:500, ...
        1:n1));
10
11  tau_d = 285 / 1.6; % initialise decay constant to 285 ns. ...
        Division by 1.6 accounts for the 1.6 ns/sample of the ...
        digital oscilloscope
12  tau_r = 19.5 / 1.6; % initialise rise constant to 19.5 ns.
13
14  LIRF = exp(-(1:1500) ./ tau_d) - exp(-(1:1500) ./ tau_r); % ...
        Calculate LIRF, h(t)
15  model_scint = zeros(m2, n2); % initialise the modelled scintillation
16      M2 = 1:m2;
17
18  for N2 = 1:n2
```

```
19      dummy_scint = conv(Cerenkov_fit(M2, N2), LIRF); % calculate ...
            the modelled scintillation as the convolution of the ...
            LIRF and stem signal
20      model_scint(M2, N2) = (dummy_scint(M2) - ones(m2, 1)* ...
            mean(dummy_scint(1:500))) ./ (max(dummy_scint) - ...
            mean(dummy_scint(1:500))); % apply min-max normalisation ...
            to modelled scintillation to improve computational speed ...
            of gradient descent
21
22      Cerenkov_fit(M2, N2) = (Cerenkov_fit(M2, N2) - ones(m2, 1) * ...
            mean(Cerenkov_fit(1:500, N2))) ./ (max(Cerenkov_fit(M2, ...
            N2)) - mean(Cerenkov_fit(1:500, N2))); % also min-max ...
            normalise the stem signal to improve computational speed ...
            of gradient descent
23  end
24
25  % define parameters for LS algorithm
26  lr = 0.01; % initialise step length with a value of 0.01
27  c_param = 0.5; % parameter used in backtracking line search
28  lr_limit = sqrt(eps); % parameter used to break line search if ...
        lr < limit, prevents infinite loops.
29
30  OLS_dose = zeros(n1, 1);
31
32  for N1 = 1:n1
33      if N1==1 && (m1≠m2 || n1≠n2)
34          disp('Error: PSD signal array has different size to stem ...
                signal array!')
35          break
36      end
37
38      fitS = model_scint(1:m1, N1);
39      fitC = Cerenkov_fit(1:m1, N1);
40      fitT = Combined_fit(1:m1, N1);
41
42      X = [fitS fitC ones(m1, 1)]; % Ordinary least squares ...
            variables as first estimate
43      beta = (X' * X) \ X' * fitT;
44      a = beta(1);
45      b = beta(2);
46      c = beta(3);
47
48      old_err = inf; % initialise the SSE_0 with value of infinity
49
50      while true % Gradient descent algorithm
51          est = a * fitS + b * fitC + c*ones(m1, 1); % calculate ...
                estimate, y^(t)
```

```
52          err = 0.5*sum((fitT - est).^2); % calculate SSE
53
54          if err ≥ 0.9999*old_err % stopping criterion
55              break
56          else % Acceptable improvement made, record improved ...
                parameters
57              best_a = a;
58              best_b = b;
59              best_c = c;
60              best_tau_d = tau_d;
61              best_tau_r = tau_r;
62              old_err = err; % also update the current fit error
63              best_S = fitS;
64          end
65
66          % Backpropagate for derivatives
67          d_err_d_est = 2 * (est - fitT)';
68
69          % derivatives of the SSE with respect to the fitting ...
                parameters
70          d_err_d_a = d_err_d_est * fitS;
71          d_err_d_b = d_err_d_est * fitC;
72          d_err_d_c = sum(d_err_d_est);
73
74          d_est_d_tau_d = (1:m1)' ./ tau_d.^2 .* exp(-(1:m1)' ./ ...
                tau_d);
75          d_est_d_tau_r = -(1:m1)' ./ tau_r.^2 .* exp(-(1:m1)' ./ ...
                tau_r);
76          d_err_d_tau_d = d_err_d_est * d_est_d_tau_d;
77          d_err_d_tau_r = d_err_d_est * d_est_d_tau_r;
78
79          % do backtracking line search
80          seach_dir = -[d_err_d_a d_err_d_b d_err_d_c ...
                d_err_d_tau_d d_err_d_tau_r];
81          grad_mag = norm(seach_dir); % gradient magnitude by ...
                steepest descent
82
83          while true
84              new_impulse = exp(-(1:1500) ./ (tau_d - lr * ...
                    d_err_d_tau_d)) - exp(-(1:1500) ./ (tau_r - lr * ...
                    d_err_d_tau_r));
85              newS = conv(fitC, new_impulse);
86              newS = (newS(1:m1) - mean(newS(1:500))) ./ ...
                    (max(newS(1:m1)) - mean(newS(1:m1)));
87
88              new_a = a - lr * d_err_d_a;
89              new_b = b - lr * d_err_d_b;
```

```
90              new_c = c - lr * d_err_d_c;
91
92              new_err = 0.5*sum((fitT - (new_vs * newS + new_vc * ...
                    fitC + new_v0 * ones(m1, 1))).^2);
93
94              if old_err - new_err ≥ lr * grad_mag * c_param
95                  break; % condition satisfied, don't need to ...
                        modify lr
96              elseif lr ≤ lr_limit % step length is below ...
                    specified limit
97                  break % no improvements made, parameters are ...
                        optimised and gradient descent loop will end ...
                        at next evaluation of SSE
98              end
99              lr = lr * 0.5; % halve the step length
100         end
101
102         % Update fitting parameters
103         a = a - lr * d_err_d_a;
104         b =  b - lr * d_err_d_b;
105         c = c - lr * d_err_d_c;
106         tau_d = tau_d - lr * d_err_d_tau_d;
107         tau_r = tau_r - lr * d_err_d_tau_r;
108         fitS = newS; % need to update the scintillation vectors ...
                as exponential rise and decay constants have changed
109     end
110
111     OLS_dose(N1) =  0.5 * sum(fitT - best_b * fitC - best_c * ...
            ones(m1, 1) + best_a * sum(best_S)); % calculate ...
            integral response
112 end
113
114 end
```

A.3 LIRF calculation MATLAB code

```
1  function [LIRF,nnls_dist] = LIRF_fit(rtOSL_signal, stem_sig, ...
       time_ind)
2  %%rtOSL_signal is the measured rtOSL signal, stem_sig is the ...
       measured stem+RL signal and time_ind are times when the ...
       rtOSL signals was measured, e.g. (0, 0.5, 1, ...)s. Each of ...
       these inputs are assumed to be column vectors with equal length.
```

```
3
4  decay_lib = [eps 1:1:700]; % set decay constants to eps, 1, 2, ...
       ..., M
5  stem_toe = tril(toeplitz(stem_sig)); % initialise toeplitz ...
       matrix for linear convolution
6  conv_lib = zeros(length(rtOSL_signal), length(decay_lib));
7  exp_lib = exp(- time_ind * (1 ./ decay_lib)); % initialise the ...
       library of M exponentials
8
9  for el = 1:length(decay_lib)
10     conv_lib(:,el) = stem_toe * exp(- time_ind ./ decay_lib(el));
11 end
12
13 nnls_dist = lsqnonneg(conv_lib, rtOSL_signal); % nonnegative ...
       least squares solution for distribution of lifetimes
14 LIRF = exp_lib * nnls_dist; % optimal estimate of the LIRF
15 end
```

A.4 Deconvolution rtOSL correction MATLAB code

```
1  function [deconv_signal] = GD_deconv(rtOSL_signal,LIRF)
2  %%rtOSL_signal is the measured rtOSL signal, and LIRF is the ...
       estimated LIRF. Both are assumed to be column vectors, and ...
       it is assumed that the rtOSL signal is longer than the LIRF.
3  if length(LIRF) < length(rtOSL_signal) % pad the LIRF with zeros ...
       if shorter than the measured rtOSL signal
4  LIRF = [LIRF; zeros(length(rtOSL_signal) - length(LIRF),1)];
5      end
6  S_toe = tril(toeplitz(LIRF)); % precalculate lower triangular ...
       toeplitz matrix for linear convolution
7  DR = pinv(S_toe' * S_toe) * S_toe' * rtOSL_signal; % OLS ...
       analytical solution to deconvolution
8
9  % Calculate first order finite difference matrix
10 L1 = zeros(size(S_toe));
11 [La,¬] = size(L1);
12 for l1 = 1:length(La)-1
13     L1(l1, l1) = 0.5;
14     L1(l1, l1+1) = -0.5;
15 end
16 L1(La, La) = 0.5;
17
```

```
18 alpha = var(rtOSL_signal - S_toe * DR) ./ var(L1 * DR); % ...
       optimal alpha parameter
19 deconv_signal = (S_toe' * S_toe +  alpha .* L1' * L1) \ S_toe' * ...
       rtOSL_signal; % RLS solution for deconvolved signal
20 end
```